ADVISORY COMMITTEE

EDITORIAL BOARD

[1] The Faculty of Civil Engineering, Wrocław University of Technology
Wybrzeże Wyspiańskiego 27, 50-370 Wrocław, Poland
Tel. +48 71 320 41 35, Fax. +48 71 320 41 05, E-mail: jan.kmita@pwr.wroc.pl

[2] The Faculty of Civil Engineering, Wrocław University of Technology
Wybrzeże Wyspiańskiego 27, 50-370 Wrocław, Poland
Tel. +48 71 320 34 04, E-mail: wojciech.glabisz@pwr.wroc.pl

[3] The Faculty of Mechanical Engineering, Wrocław University of Technology
ul. Łukasiewicza 5, 50-371 Wrocław, Poland
Tel. +48 71 320 21 73, Fax. +48 71 320 34 22, E-mail: metalplast@pwr.wroc.pl

Archives of Civil and Mechanical Engineering is indexed and abstracted in the following:
- Science Citation Index Expanded (also known as SciSearch®),
- Journal Citation Reports/Science Edition.

POLISH ACADEMY OF SCIENCES – WROCŁAW BRANCH
WROCŁAW UNIVERSITY OF TECHNOLOGY

ARCHIVES OF CIVIL AND MECHANICAL ENGINEERING

Quarterly
Vol. XI, No. 4

WROCŁAW 2011

EDITOR IN CHIEF

ZBIGNIEW GRONOSTAJSKI

EDITORIAL LAYOUT AND PROOF-READING

WIOLETTA GÓRALCZYK

TYPESETTING

SEBASTIAN ŁAWRUSEWICZ

SECRETARY

WIOLETTA GÓRALCZYK

Publisher: Committee of Civil and Mechanical Engineering
of Polish Academy of Sciences – Wrocław Branch,
Faculty of Civil Engineering and Faculty of Mechanical Engineering
of Wrocław University of Technology

OFICYNA WYDAWNICZA POLITECHNIKI WROCŁAWSKIEJ
Wybrzeże Wyspiańskiego 27, 50-370 Wrocław
http://www.oficyna.pwr.wroc.pl
e-mail: oficwyd@pwr.wroc.pl

ISSN 1644-9665

Drukarnia Oficyny Wydawniczej Politechniki Wrocławskiej. Zam. nr 1203/2011.

Contents

Spis treści

ARCHIVES OF CIVIL AND MECHANICAL ENGINEERING

Vol. XI 2011 No. 4

Weld line behaviour during uniaxial tensile testing of tailor welded blanks

V. CIUBOTARIU, G. BRABIE
University of Bacau, 157 Marasesti Street, 5500 Bacau, Romania.

The quality of weld line in a tailor welded blank (TWB) is an important factor that can affect the quality of the deep drawing process and resulted drawn parts. Hence, the behaviour of weld line during forming must be made with responsibility and by applying different physical testing methods in order to obtain useful and accurate information. For example, the mechanical properties of TWB and weld line, that give information concerning yield limit and ultimate strength, can be generally determined by applying the following techniques: parallel tensile testing or normal tensile testing. But, since the welding process can induce specific properties in the weld joint and heat – affected zone, the simple tensile test is not enough to obtain the needed information concerning such properties. The present paper investigates the behaviour and mechanical properties of the weld line in a tailor welded blank during and after its tensile testing by applying the following testing methods: parallel tensile test, micro-hardness testing, thermography, EDX and microscopy.

Keywords: *tailor welded blank, weld line, parallel tensile test, thermography, microscopy, micro-hardness testing*, *EDX testing*

1. Introduction

The behaviour of weld line during cold forming of a tailor welded blank (TWB) is one of factors that can contribute to the success of the forming process and quality of obtained parts. It is well known that the welding process leads to the stiffness of the achieved joint and heat affected zone and hence to the formability modification in such zones [3]. The difference between the formability of base materials and weld line or heat affected zone can influence the accuracy and quality of the drawn parts made from tailor welded blanks. The variations in thickness and formability of metal sheets joined in a TWB can also cause an uncontrolled movement of the blank component materials during drawing process. Thus, the weld line will be moved towards the thicker material because the thinner/softer material may undergo more deformations than the thicker/stronger material in the formed TWB [4, 6]. The difference in strength between the TWB component materials can also cause the concentration of deformations in the softer material that will increase the probability of fractures or of a considerable springback for the high strength material [4]. Due to the poorer mechanical properties of the weld line by comparing to base materials, the splitting will occur across or parallel and immediately adjacent to the weld line as a function of thickness

or strength material combinations [4–5]. The above mentioned behaviours of the weld line during TWB forming are caused by specifically factors and phenomena induced by different technologies used to achieve the welded blanks. Such behaviours are also determined by the blank forming and require different and specific conditions in the design of tools, forming processes and equipment. Hence, the determination of the weld line behaviour by applying different physical testing methods must be made with responsibility in order to obtain useful and accurate information.

The mechanical properties of the TWB and weld line can be generally determined by applying the following techniques: parallel tensile testing or normal tensile testing [1–2]. But, because the welding process can induce specific properties in the weld line and heat – affected zone, the simple tensile testing is not enough to obtain the needed information concerning such properties. The present paper investigates the behaviour and mechanical properties of the weld line in a tailor welded blank, during and after its tensile testing, by applying the following testing methods: parallel tensile test, micro-hardness testing, infrared thermography and electronic microscopy.

2. Experimental methodology

The tailored welded blanks used in the present study were made by laser welding of two steel sheets having different chemical compositions, thicknesses and mechanical properties. The welding was done along rolling direction of sheets. The chemical compositions of the base materials used in TWB are presented in Table 1.

Table 1. Chemical composition of the steels used as base materials in TWB

Thickness	steel 1							
0.75 mm	C	Si	Mn	P	S	Al	Ti	N
	0.002	0.006	0.097	0.01	0.01	0.029	0.057	0.0032
Thickness	steel 2							
0.72 mm	C	Si	Mn	P	S	Al	Ti	–
	0.028	0.009	0.25	0.029	0.011	0.053	0.001	

The parallel tensile testing was made by using specimens whose geometries were established according to ASTM standard recommendations [8]. The specimen dimensions are indicated in Figure 1.

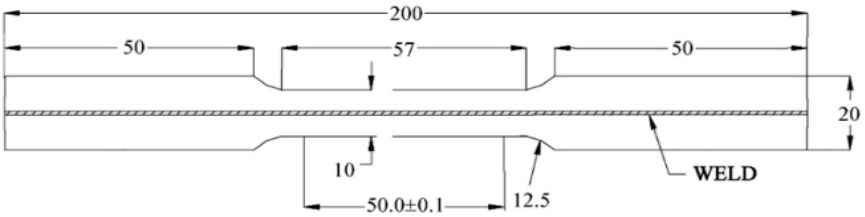

Fig. 1. Dimensional parameters of test specimens according to ASTM E8 [8]

The experiments were performed on a universal testing machine Lloyd EHZ and the engineering strains were measured by using EPSILON extensometers. The specimens were deformed till failure using the following two testing speeds: 5 mm/min and 25 mm/min. The engineering stresses / strains were converted into true stresses/strains according to following equations:

$$\varepsilon = \ln(1 + E), \tag{1}$$

$$\sigma = S(1 + E), \tag{2}$$

where:

ε – the true strain,

σ – the true stress,

E – the engineering strain,

S – the engineering stress.

The infrared thermography was performed in order to determine the TWB specimen and weld line behaviour as a function of variation and distribution of temperature along and across of weld line or TWB components during tensile testing. The analysis was made according to ISO instructions [8] by using for thermographic measurements a FLIR – A325 infrared video camera and an OMEGA OS-3572 pyrometer for the temperature measurement in different points of TWB specimens or weld line. The temperature in the testing zone and of the not deformed specimens was equal to 21 °C. In order to emphasize the temperature variation in a more precise manner and to achieve an emissive exponent equal to 1, all specimens were painted in black. The thermographic measurements were simultaneously activated at the start of the parallel tensile testing and the specific data were collected with a speed equal to 5 data points/second.

The micro-hardness examination was performed in order to establish and prove the influence of base metals, heat affected zones and weld line on the general behaviour of the TWB samples deformed by tensile. The examination of hardness distribution along and across the deformed and not deformed specimens was made according to ASTM E 384-09 standards [7], by using METKON MH3 micro-hardness testing equipment controlled by computer.

The SEM (scanning electron microscopy) and EDX (Energy-dispersive X-ray) examinations were performed in order to obtain the behaviour of TWB specimen and weld line as a function of surface structure and chemical composition of materials along and across weld line and HAZ zones, before and after testing. The specimens subjected to SEM or EDX analysis were cut away from the initial specimens (rectangles having dimensions equal to ≈ 10/10 mm) prior and after deformation and without initial preparation. The analysis of the specimen surface was made on the basis of the SEM method by using a VEGA-II LMH scanning electron microscope having a magnification between 4× to 500.000×, a maximum resolution of 2 μm and a power accel-

erator of 200 V–30 kV on 10 V steps. The elemental analysis and chemical characterization of the weld line and HAZ zones of the tested TWB sample was performed by applying the EDX analytical technique.

3. Results and discussions

Analysis by parallel tensile test. The mechanical properties of the tested materials are indicated in Table 2 and the true strain/stress curves obtained from parallel tensile test are presented in Figure 2.

Table 2. Mechanical properties of the base metals and TWB

Material properties/Specimens material		Steel 1	Steel 2	TWB
Young modulus	[MPa]	163174	204175	211995
Yield stress	[MPa]	140.46	191.43	230.35
Ultimate tensile stress	[MPa]	370.95	378.47	392.88
Total elongation	[%]	37.22	26.51	25.82
Plastic strain ratio, r	–	1.79	2.21	2.69
Strain hardening exponent, n	–	0.25	0.19	0.17

The analysis of the above presented results emphasizes some important and expected aspects concerning the weld line influence and behaviour. Thus, the presence of weld line determines the following mechanical properties of the TWB assembly by comparing to those of basic materials: highest Young modulus, yield stress, ultimate stress and plastic strain ratio and smallest total elongation and strain hardening coefficient. From such properties we can conclude that, because of higher strength and low total elongation or work hardening coefficient, TWB formability will be reduced, the risk of springback, creasing and wrinkling will be greater, material forming will need higher forming forces, during forming the tool will be subjected to higher stress and wear or material work hardening will be smaller.

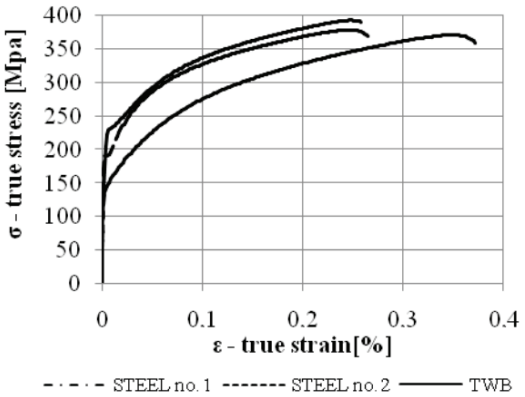

Fig. 2. True stress/strain curves

By comparing the stress/strain curves it can be observed that TWB stress/strain curve presents the highest level because the weld line makes the TWB specimens more resistant to axial tensile loads. The same curve presents the shorter yielding and ultimate tensile stress zones and hence the TWB specimen will fail before the specimens from the basic materials but at a higher value of the applied stress.

Analysis by infrared thermography. The maximum values of the temperatures resulted during different testing stages for both base materials and weld line are presented in Table 3.

Table 3. Maximum temperatures rise during different testing stages

TWB components material	Steel 1		Weld line		Steel 2	
Testing speed	5 mm/min	25 mm/min	5 mm/min	25 mm/min	5 mm/min	25 mm/min
Forming stages	Maximum temperatures [°C]					
Elastic stage 1	21.8	22	21.4	21.6	21.6	21.8
Elastic stage 2	21.8	21.9	21.4	21.6	21.6	21.8
Yielding stage	21.8	21.8	21.4	21.5	21.5	21.7
Ultimate tensile stage	24.8	31.1	24.4	30.9	24.6	31.1
Necking before fracture stage	27.3	42	26.9	41.5	27.3	43.1

The thermographs obtained from the parallel tensile testing of TWB specimens are presented in Figures 3 and 4 for the both testing speeds applied in investigation. The length of specimens represented in images is the maximum length recorded by the IR video camera and not the calibrated length of the specimens.

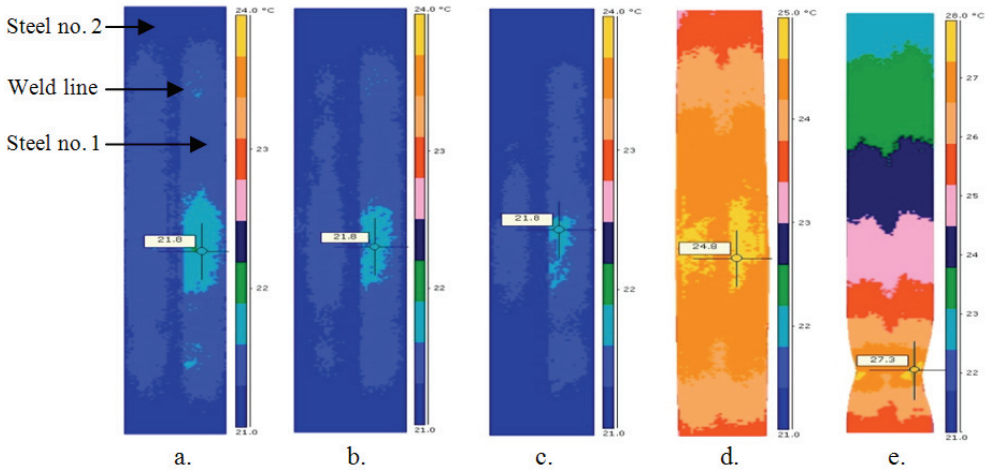

Fig. 3. Thermographs of each deformation stage – testing speed equal to 5 mm/min: a) elastic stage 1, b) elastic stage 2, c) yielding stage, d) ultimate tensile stage, e) necking before fracture stage

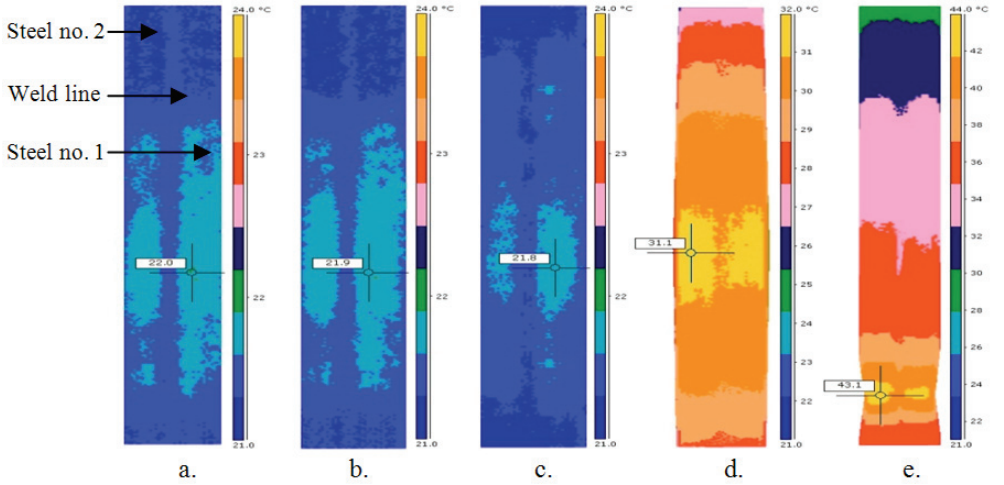

Fig. 4. Thermographs of each deformation stage – testing speed equal to 25 mm/min: a) elastic stage 1, b) elastic stage 2, c) yielding stage, d) ultimate tensile stage, e) necking before fracture stage

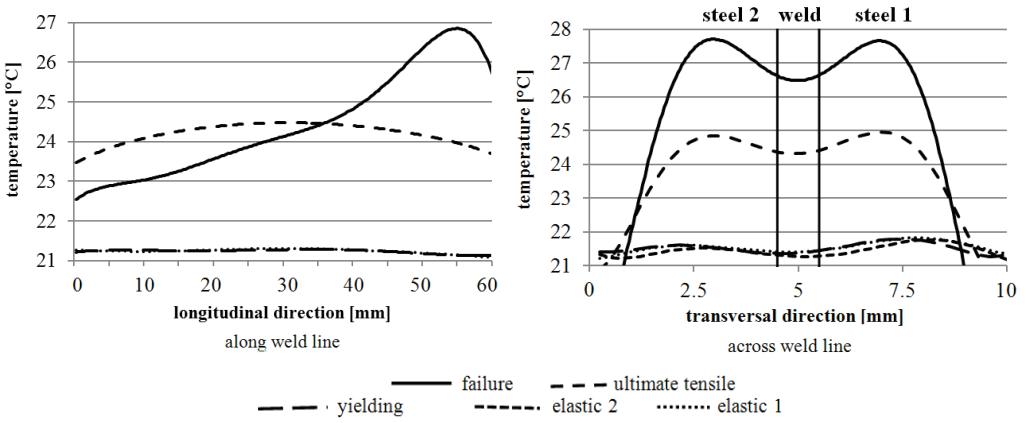

Fig. 5. Weld line temperature variation on longitudinal and transverse directions (testing speed equal to 25 mm/min)

The analysis was performed for the following five stages of deformation: elastic stage 1 (0.26% strain level), elastic stage 2 (0.78% strain level), yielding stage (1.37% strain level), ultimate tensile stage (96.42% strain level) and necking before fracture stage (99.99% strain level). The analysis the above presented results emphasizes different aspects concerning the temperature variation on the weld line, base materials and TWB tested samples. Thus, the temperature varies on the TWB components during tensile testing with very small values in the elastic and yielding stages and with highest values in the ultimate and necking before failure stages. In every stage, the

weld line presents lower values of temperature rise by comparing to the base materials, but in spite of fact that this temperature is not high, its increase can permit to maintain the TWB yield stress to an appropriate value by the yield stress of the stronger steel (Figure 2).

The variations of temperature values on weld line are presented in Figure 5. From the analysis of the diagrams it can be observed that after yielding stage the temperature increases and varies on both directions of weld line as follows: on longitudinal direction, where the temperature tends to decrease from middle of sample to its ends and on transverse direction, where the temperature has maximum values at the middle of each base materials width and smaller values on weld line width. It can be also observed that between the weld line and the two sheet margins there are some differences in temperature.

The influence of the testing speed on the weld line temperature in the last two stages of the TWB testing is presented in Figure 6.

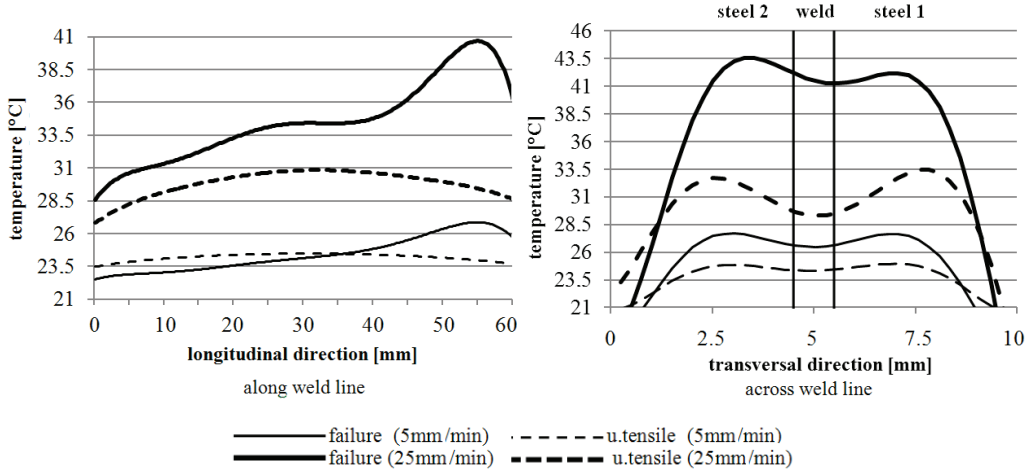

Fig. 6. Variation of the weld line temperature in the last two stages of tensile testing

From the analysis of the diagrams presented in Figure 6 it can be observed that weld line temperature has higher values in the last two testing stages of the TWB assembly: the ultimate tensile stress stage and the necking before fracture stage. The testing speed has a high impact on temperature variation. Thus, the increase of the weld line temperature from testing start till failure can touch, like the temperature rise in the case of base materials that compose the TWB assembly, 6 degrees for lower testing speed (5 mm/min) and 20 degrees for higher testing speed (25 mm/min).

The variations of temperature values on the TWB specimen as a function of time and loading force are presented in Figures 7 and 8, respectively. The analysis of the diagrams confirms the before presented aspects concerning the temperature variation on the TWB specimen. In addition, from Figure 7 it can be observed that the tem-

perature of the TWB specimen increases faster once the yielding point is exceeded. From Figure 8 it can be observed that if the loading force which deforms the TWB specimen increases, the temperature will also increases till the ultimate stress stage. But, between the ultimate stress stage and necking before fracture stage, when the junction between grains starts to be interrupted, in spite of fact that the loading force decreases the temperature increases.

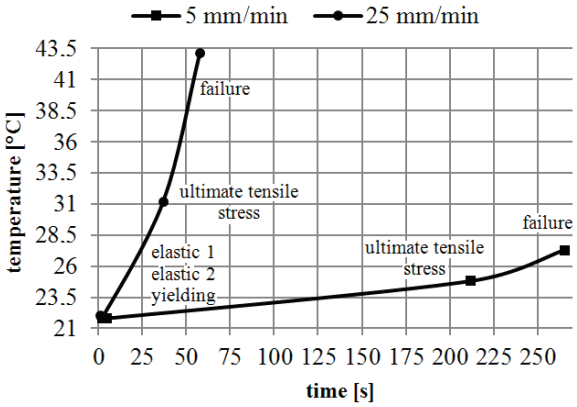

Fig. 7. Variation of TWB specimen temperature as a function of forming time

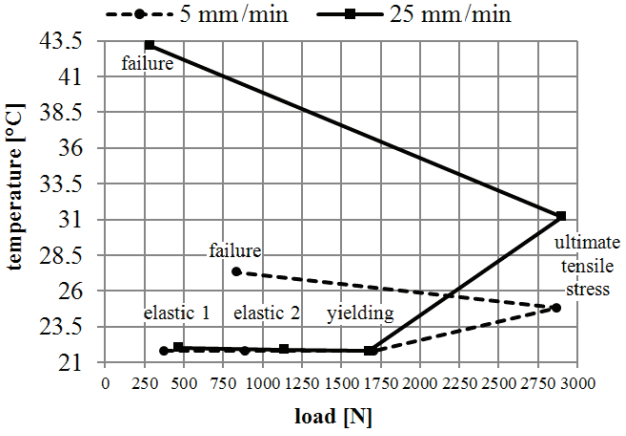

Fig. 8. Variation of TWB specimen temperature as a function of loading force

Analysis by hardness testing. The mean values of hardness measured on each component of the TWB specimen are presented in Table 4. The hardness variations along and across weld line on its both sides, prior and post tested, are presented in Figures 9 and 10.

Table 4. Mean values of the hardness on the TWB components

Measurement moment	Hardness (HV1)				
	Steel 1	HAZ 1	Weld line	HAZ 2	Steel 2
Prior to deformation	93.72	154.97	246.95	201.07	171.41
Post deformation	103.34	195.32	330.32	260.23	198.89
Increasing level [%]	10.26	26.03	33.75	29.42	16.03

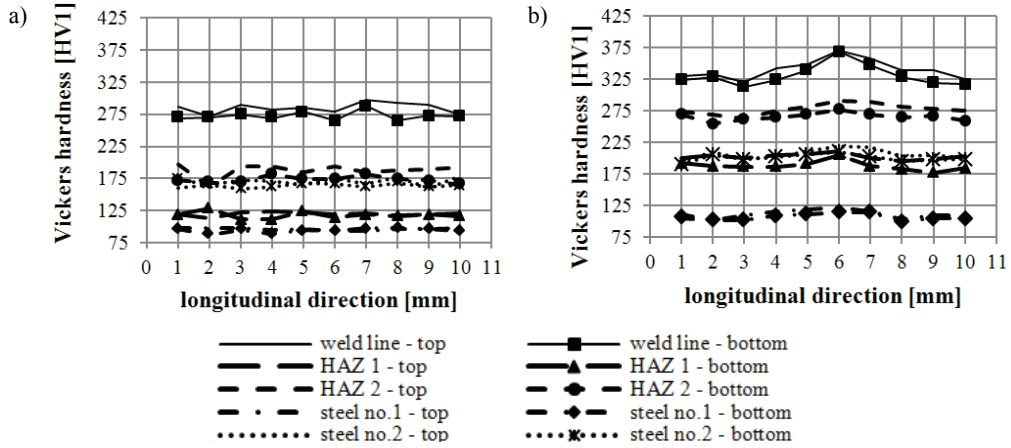

Fig. 9. Hardness variation along the weld line prior and post deformation:
a) prior to deformation, b) post deformation

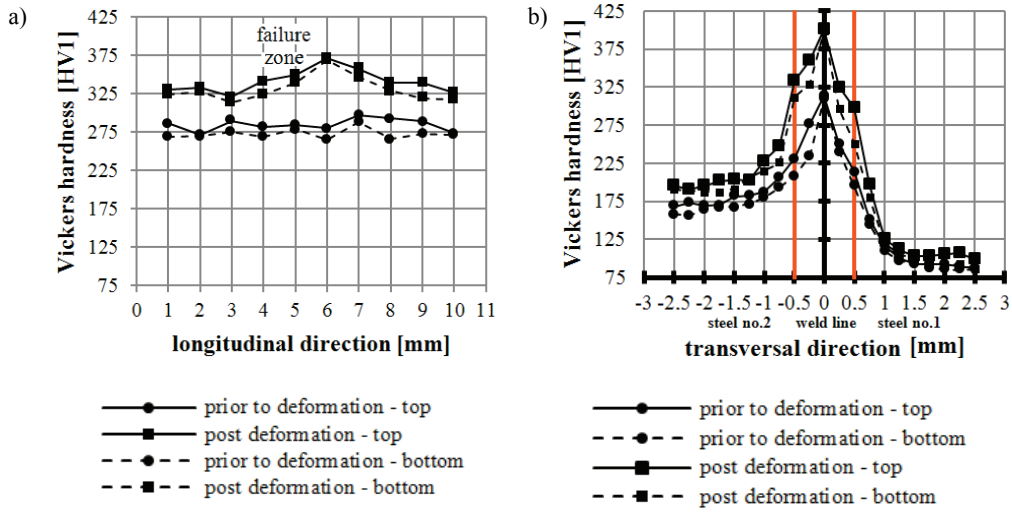

Fig. 10. Hardness distribution prior/post deformation of the specimens:
a) along the welding line, b) across the TWB specimen

From Figure 9 and Table 3 it can be remarked that the hardness of the weld line presents an increase of about 33.75% in the case of post deformation measurement by comparing to prior deformation. The increase of the weld line hardness is of about 77% by comparing to the increase of hardness of the stronger steel that compose the TWB specimen (usually, the increase of the hardness after laser welding is of about 120% by comparing to the mean hardness of the stronger material used in the welded structure [2]). The level of the curves of hardness variation along the weld line is always higher by comparing to the same curves resulted for the TWB components. From Figure 10 and Table 3 it can be remarked that post deformation the weld line hardness presents a considerable increase especially in the proximity of failure zone. The analysis of hardness variation across TWB specimen emphasizes not only the highest hardness values in the case of weld line but also it put into evidence the existence of heat affected zones having a width approximately equal to 0.5 mm.

Analysis by SEM microscopy. The analysis of the weld line surface structure by using the SEM microscopy was applied prior and post TWB specimens testing. A comparison between an optical microscopic image and a SEM image of the untested weld line is presented in Figure 11. The images of the untested and post tested components of the TWB specimens obtained from SEM are presented in Figure 12.

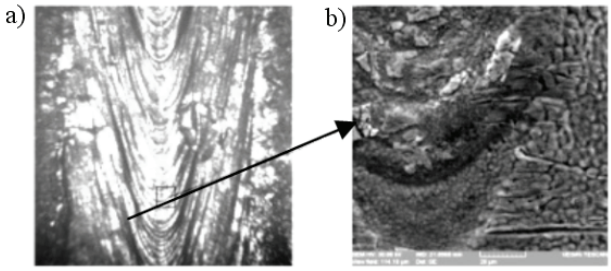

Fig. 11. Surface structure of the untested weld line: a) mag. 400×, b) mag. 2500×

The surface structure of the untested weld line clearly presents the orientation of the material in the welding direction. It also can be remarked a nonuniform distribution of the material on the weld line that certainly will cause its nonuniform deformation. The surface structure of the post tested weld line is changed by comparing to untested ones, in the sense of its reorientation according to forming direction. The surface structures of the untested heat affected zones (HAZ 1and HAZ 2) are different and they conserve the type of macrostructures from their base materials. The surface structures of the post tested heat affected zones are not essentially changed by comparing to the structures of post tested base materials and untested HAZ zones. Some modification of the surface structures can be observed in the case of base materials and especially in the case of steel 1, where the surface structure receives an orientation in the direction of the forming force.

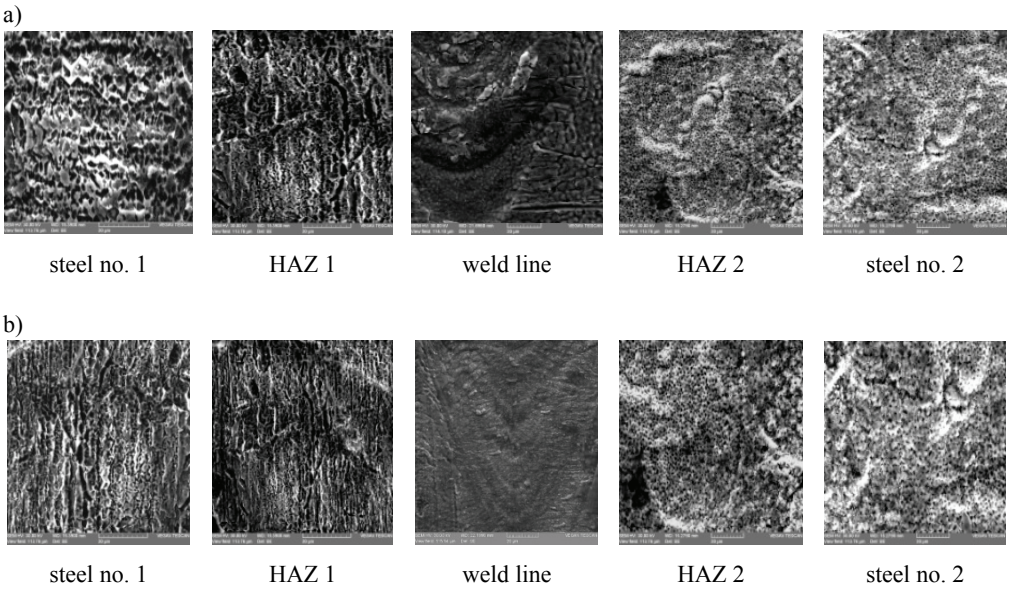

Fig. 12. Surface structure of the not deformed and post deformed TWB components:
a) Surface structure of the untested TWB components – SEM imaging at 2500×,
b) Surface structure of the post tested TWB components – SEM imaging at 2500×

Analysis by energy-dispersive X-ray spectroscopy (EDX). The X – ray spectrum resulted from spectroscopy analysis for a not deformed weld line and HAZ zones is presented in Figure 13.

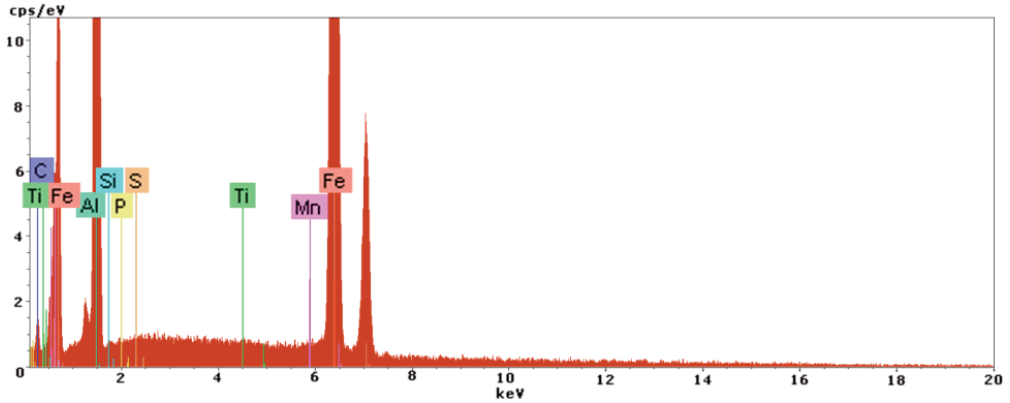

Fig. 13. X-ray spectrum of not deformed weld line and HAZ

The analysis of the weld line behaviour by using the SEM – EDX spectroscopy was also applied prior and post testing of TWB specimens. The elemental composition

and chemical characterization of the not deformed and post deformed weld lines and HAZ zones of the TWB specimens, obtained from EDX technique, are presented in Figure 14.

a)

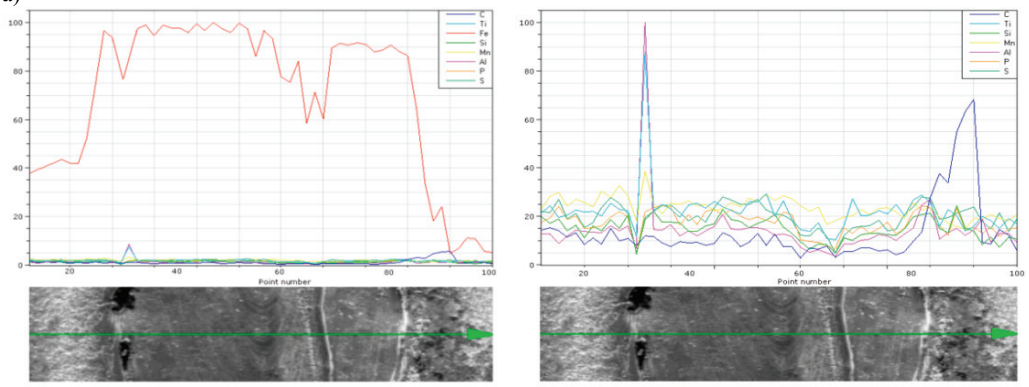

Fe elemental analysis C and other components elemental analysis

b)

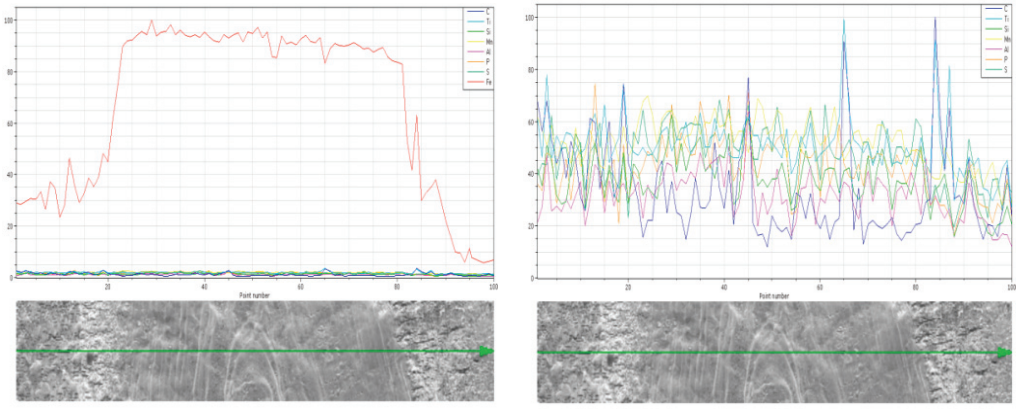

Fe elemental analysis C and other components elemental analysis

Fig. 14. Elemental analysis of the weld line and HAZ zones obtained from EDX technique: a) not deformed weld line and HAZ zone, b) post deformed weld line and HAZ zone

The main aspects remarked from the elemental analysis based on EDX technique are that all chemical components of base materials are also emphasized into weld line and HAZ zones and the composition in Fe, C, Si or other elements on specimen cross section is different in the case of post-deformed specimens by comparing to not deformed ones.

4. Conclusions

The classic parallel testing of TWB specimens emphasizes the following expected behaviours of the TWB assembly that are mainly determined by the presence of the weld line: because of its higher strength and low total elongation or work hardening coefficient the TWB formability will be reduced and the material forming will need higher forming forces; the weld line makes the TWB specimens more resistant to axial tensile loads and hence the TWB stress/strain curve presents the highest level, the shorter yielding and ultimate tensile stress zones; the TWB specimens will fail before specimens made from the base materials but at a higher value of the applied stress.

The performed additional analyses present interesting aspects concerning the behaviour and influence of the weld line during TWB testing. Thus, from the thermographic analysis the following main conclusions can be presented concerning the behaviours of the TWB assembly and weld line: the temperature rises during tensile on weld line, heat affected zones and TWB assembly and this is due to plastic deformation work and to frictional heating that increase after yielding; the temperature rise on weld line presents lower values by comparing to base materials, aspect that is connected to the fact that the deformation of weld line starts later than those of base materials; the differences in temperature between weld line and sheets margins can affect the distribution of residual stresses generated in material during its forming and hence, the material uniform elongation or the location of necking and fracture.

From hardness analysis the following main conclusions can be presented concerning the behaviours of the TWB assembly and weld line: the level of the hardness variation curves along weld line is always higher by comparing to the same curves resulted for the TWB components; the hardness variation across TWB specimen emphasizes the existence of the heat affected zones having a width approximately equal to 0.5 mm, aspect that is very important because many studies concerning the TWB formability not emphasize or neglect the HAZ zone.

From SEM microscopy analysis, the following main conclusions can be presented concerning the behaviour of TWB assembly and weld line: on the weld line surface it can be observed a nonuniform distribution of material that certainly will cause its nonuniform deformation; the surface structure of the post tested weld line will be reoriented in the forming direction by comparing to untested ones, but the post tested heat affected zones present surface structures that are not essentially changed by comparing to structures of post tested base materials and untested HAZ zones.

From the elemental analysis based on EDX technique, the following main conclusions can be presented concerning the behaviours of the TWB assembly and weld line: the weld line and HAZ zones are composed by the same chemical components of the base materials but in a different concentration; the concentration in Fe and especially in C and Si of the post deformed weld lines seems to be reoriented by tensile across weld line and HAZ zones by comparing to the not deformed ones, aspect that can be connected to variation of hardness along and across the post deformed weld line and HAZ zones.

Acknowledgments

The present research was performed with the financial support from the Romanian Ministry of Education and Research CNCSIS, TE/256 project.

References

[1] Abdullah K., a.o.: *Tensile testing for weld deformation properties in similar gage TWBs using the rule of mixture*, J. of Mat. Proc. Tech., Vol. 112, 2001, pp. 91–97.
[2] Brabie G., Chirita B., Chirila C.: *Determination of the weld metal properties and behaviour in the case of tailor-welded blanks using the parallel tensile test and image-analysis method*, Archives of Civil and Mechanical Engineering, Vol. 4, No. 2, 2004, pp. 41–47.
[3] Kinsey B., Cao J.: *An analytical model for tailor welded blanks forming*, Journal of Manufacturing Science and Engineering, Vol. 125, No. 2, 2001, pp. 344–351.
[4] Lee K.J, Chun B.K.: *Numerical investigation of TWB forming and springback*, Simulation of Materials Processing: Theory, Methods and Applications, ed. Mori, 2001.
[5] Min K.B., Kang S.S., Kim K.S.: *A study on resistance welding in steel sheets using a tailor welded blank (1st report). Evaluation of upset weldability and formability*, Journal of Materials Processing Technology, Vol. 101, 2000, pp. 186–192.
[6] Park K.C., Shan S., Kim K.S., Kwon O.: *Forming characteristics of laser welded tailored blanks*, Journal of the Korean Society for Technology of Plasticity, Vol. 7, 1998, pp. 23–35.
[7] *** ASTM E384-09: *Standard test methods for microidentation hardness of materials*.
[8] *** ASTM E8/E8M – 09: *Standard test methods for tension testing of metallic materials*.
[9] *** ISO 18434-1 2008: *Condition monitoring and diagnostics of machines – Thermography*. Part 1: *General procedures*.

Zachowanie się spoiny liniowej w próbie jednoosiowego rozciągania w elementach typu *tailor blanks*

Jakość spoiny w blachach typu *tailor blanks* jest istotnym parametrem, który może wpływać na przebieg procesu tłoczenia i jakość wyrobu. Zachowanie się spoiny podczas formowania musi być określone w różnych testach, aby uzyskać przydatne informacje. W artykule przedstawiono badania dotyczące zachowania się i właściwości mechanicznych spoiny liniowej w blachach typu *tailor blanks* podczas i po próbie rozciągania stosując między innymi pomiary mikrotwardości i mikrostruktury.

ARCHIVES OF CIVIL AND MECHANICAL ENGINEERING

Vol. XI 2011 No. 4

Influence of constructive and operating parameters on a modified Trombe wall efficiency

S. DRAGIĆEVIĆ
University of Kragujevac, Technical faculty Cacak, Svetog Save 65, 32000 Cacak, Serbia.

M. LAMBIC
University of Novi Sad, Technical faculty "M. Pupin" Zrenjanin, Dj. Djakovica bb, 23000 Zrenjanin, Serbia.

The paper presents an analysis of efficiency of the modified Trombe wall with forced convection that could be operating in four different modes. The analyzed system comprises a double glass glazing, and a massive wall with an opening and central channel in it. In order to increase the efficiency, a fan is provided at the bottom vent of the wall. It is more advanced as compared with simple Trombe solar wall with a relatively low thermal resistance, which is taken as a reference in experimental analysis. The mathematical model, composed for the massive solar wall efficiency, is usually very complicated and assessment of the thermal behaviour requires the use of thermal simulation techniques. This paper presents steady-state and one-dimensional mathematical model for simplified analysis of thermal efficiency of modified Trombe solar wall that is working in heating mode. The results from presenting model were analyzed to predict the effects of variations in the constructive and operating parameters on the efficiency. The obtained results were used for simple and fast running design tools that designers can use in the early phases of the design process for calculations of efficiency of the active solar heating systems.

Keywords: *modified Trombe wall; solar air heating, energy efficiency*

1. Introduction

The passive solar systems are well-know method for use of solar energy as sources of heating in buildings. In practice buildings with passive solar system are still rare because there is the lack of available information about the efficiency of passive solar systems. The modified Trombe wall system consists of a transparent cover (two glasses) and the massive wall with a central channel in it (Figure 1). At the bottom and the top of the massive wall, there are vents for allowing an air circulation between entrance duct (air gap between transparent cover and the wall), central channel and room space. At the bottom vent there is a fan so the air circulates through a wall by forced convection. In order to approve that analyzed type of the wall has better temperature effects in relation to the classic Trombe wall the experimental testing has been done.

Depending on the position of the valve, the wall can work in the four different modes. A-C modes are used for heating and storage energy when the wall is exposed

to sunlight (A-Room heating by hot air circulation from the entrance duct; B-Intensive heat storage, by the direct absorption and conduction, and by hot air circulation from the entrance duct into the channel space; C-Room heating and heat storage by simultaneous air circulation from the entrance duct into the room and the channel space). The mode D is used to send storage heat into the room, when there is no sun (the room being heated by both radiation and natural convection from the inside wall, and hot air circulation from the central channel).

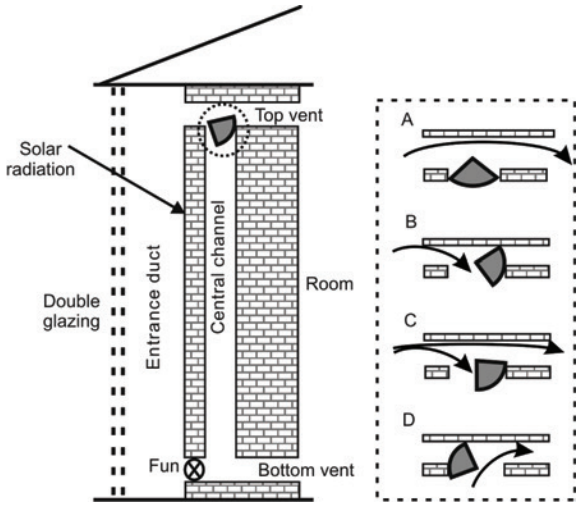

Fig. 1. Schematic representations of the modified Trombe wall and modes of operation

The Trombe wall has been the subject of numerous experiments and papers. Many theoretical and experimental studies have shown that indoor comfort is improved due to well-designed Trombe walls. The results from [3] yield some insights into the performance of passive solar collectors, by varying the heat input and channel depth. In the paper [5] PV-Trombe wall installed in a fenestrated room with heat storage is investigated to approach the practical application of this type of solar wall. Glazed building wall as a solar thermal collector that transmits, absorbs and accumulates solar energy was investigated by [8]. The paper [7] investigates the performance of a new configuration of Modified Trombe Wall named the Partially-Glazed Modified Trombe Wall, which aims to decrease heat accumulation, induce higher natural ventilation and provide daylight for housing. The paper [10] presents the application of Finite Element Method for the analysis of energy transfer in Trombe – Mitchell's solar wall.

Research efficiency analysis of the efficiency of the Modified Trombe wall was carried out in all modes. Part of the results are given in [4], when the wall was worked with mode C, so results presents an efficiency of the solar wall that is used for heating room and simultaneous thermal energy storage. The study presents the effect of constructive and operating parameters, such as entrance duct width, solar radiation, wind

velocity, air velocity in entrance duct and wall height, on the thermal efficiency of the analyzed air heating system when the wall is used for heating.

2. The modified Trombe wall description

The heat transfer modes and heat transfer exchanges in the system are presented in Figure 1. Analyzed solar wall is divided and the external part, acting as a partition, and the internal one, acting as a massive wall. From the view of decreasing heat losses, appropriate solution of the solar wall is based on application of a special absorber and thermo-insulation over the outside wall surface. This construction of the wall provides heat storage in the part of the wall that are closer to the inside surface of the wall. This paper analyzes the case when the air temperature in the room is below a specified level, so it is necessary that heated air from the entrance duct circulate only in the heated room (Figure 2). In this case efficient heat transfer from the zone where are intensive heat losses are provided, while the influence of the interior massive wall can be neglected.

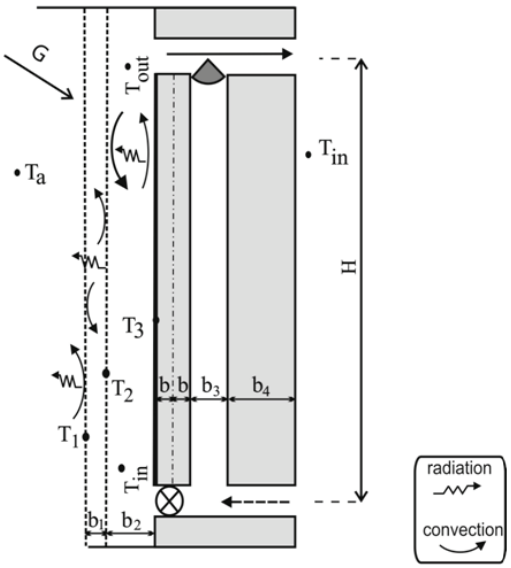

Fig. 2. Definition of heat transfer modes and parameters of the wall

The glazing, which is in contact with the outside air, is at a constant temperature of Ta. The energy input to the system is from the solar radiation received on the absorber surface. The air in the entrance duct is heated in contact with the external wall surface, rises and circulates towards the central channel of the wall and the room (when the vents are open). The net losses from the system are due to convection and radiation losses from the absorber surface. The wall is cooled by forced convection of the air in

the gap between wall and glazing (entrance duct). At the top and bottom of the wall, vents are provided for thermo circulation of air with constant heat flux into the adjacent room. Cooler room air, drawn through the bottom vent, is heated at it passes up the entrance duct and then delivered into the room through the top vent. The Trombe wall is especially suited to higher latitudes, where the winter sun is lower in the sky and thus falls more directly on the wall. The change in sun's trajectory during the year enables the wall to be shaded, using overhangs or eaves, during the summer when the sun's altitude is greater, and heating is not required.

The geometrical and thermo-physical parameters of the system are:

1. Double glass glazing unit: distance between glazing $b_1 = 2$ cm, emissivity $\varepsilon_{1,2} = 0.95$, glass transmittance $\tau = 0.85$;

2. Solar wall (concrete wall): length $Y = 3$ m, thicknesses $b = 5$ cm, $b_3 = 5$ cm, $b_4 = 10$ cm, emissivity $\varepsilon_3 = 0.95$, absorptivity $\alpha = 0.95$.

3. Experimental analysis of test cells

The experiments were carried out on a test cell of the classical Trombe wall and modified Trombe wall provided with vents for the flow of hot air from the entrance zone in the central channel, in order to analyze their thermal characteristics. Test cells were located on the roof of the Technical faculty at the University of Novi Sad. Testing models with equal collecting surfaces and transmittance-absorptance characteristics are placed vertically and south-oriented. Rear surfaces are open to the outside environment. For a given models comparison of different temperature measurements were carried out: t_a – ambient temperature, t_1, t_2 – glazing glasses, t – air in the entrance zone, t_3 – absorber, t'_3, t_4, t_5 – inside wall temperature.

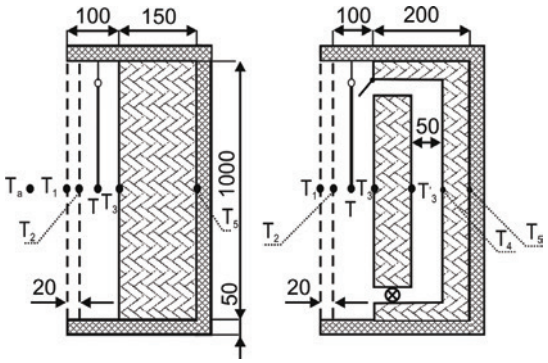

Fig. 3. Scheme of test cells with location of measurement points

The walls are constructed of concrete with absorbing surfaces painted with matt black paint. The external wall surface is shielded from the environment by two panes of 3 mm thick commercial glass. The walls are thermo-insulated from the lower side

and all wall sides (except the front and rear ones) along with glass girders are covered with a mineral 50 mm thick wall of thermal conductivity 0.037 W/mK, and specific density 27 kg/m^3. All surfaces of both test cells with installed thermal insulation are covered with tin housing.

Comparative testing of both walls included measures of distinctive temperatures at both the time when the radial fan (20 W, 1450 min^{-1}) at modified Trombe wall was running (by day/in the sunshine) and when it was not running (when the wall was not exposed to sun rays/by day and at night). Temperature of ambient air and temperature of air in entrance zone was measured using a mercurial thermometer. The thermometers were calibrated over the range 0 – 100 °C (class of accuracy ±0.2 °C). All temperatures of glass and wall were measured with digital apparatus MDL-910, with temperature range from –5 °C to 70 °C (class of accuracy ±0.1 °C). Figure 4 shows measured temperatures at both test cells, for one of many days of testing.

The experimental results show that the temperature in the mid-zone of transparent and absorbing wall surface of the composite wall is higher than the one of the classic Trombe wall in the morning, and lower in the afternoon. The temperature of the rear surface of the composite wall during the day (in the sunshine) is slightly higher than the one of the classic wall.

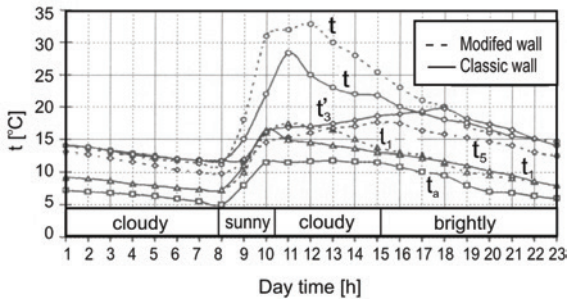

Fig. 4. Comparative measured temperatures for both types of wall for January 2

Based on the experimental results of the test cells, the advantages of the modified Trombe solar wall compared to the classical Trombe wall are presented. Other researches have been done on the structure renovation of the Trombe wall system, and show that the modified Trombe wall works more effectively than the classical Trombe wall [6, 13]. In the next section of this paper numerical calculations for the evaluation of the efficiency of the modified Trombe wall from Figure 2 will be carried out, which work in real conditions.

4. Mathematical model

Mathematical model of the modified Trombe wall, from Figure 2, is derived for the case when the air temperature in the heating room is below a specified level, so it is

necessary to achieve the circulation of heated air from the receiving area to the room. In this case, the fan is turned on and the valve takes the position as shown in Figure 2. Heated air circulates from the entrance duct into the room, and back up through the opening in the lower part of the wall. The energy potential of the return air is insignificant compared to the potential of air that circulates between the absorbing surface and the glass covers of the wall. In this case the heat flux of the return air could be ignored in the energy balances.

In this investigation, the following simplified assumptions have been made: the model is steady state, heat transfer through the system is one-dimensional, different layers of wall construction to be at uniform temperature at any given time, thermo physical properties of air and all materials involved constant and independent of temperature, the resistance of conduction heat exchange through glazing is neglected, air is considered as a nonparticipating medium in radiation heat exchange, the entire system is well insulated so there are no heat lateral losses, two horizontal boundaries are adiabatic, the temperature of the adjacent room is constant. As in all steady-state methods, the role of the storage capacity of the massive wall was not considered [2, 12, 14–15]. According to these assumptions the mathematical model of the wall is developed.

The solar radiation transmitted through the glazing and transformed into heat by the absorber is:

$$S = \tau\alpha G, \tag{1}$$

where:

τ – glass transmittance,

α – absorptivity of the wall surface,

G – solar radiation incident on vertical surface (W/m^2).

Energy losses from both glazing at temperatures T_1 and T_2 and from the external surface of the wall at temperature T_3 are [12]:

$$q = h_w (T_1 - T_a) + \varepsilon_{1,2}\,\sigma (T_1^4 - T_a^4), \tag{2}$$

$$q = h_{1,2} (T_2 - T_1) + \frac{1}{\dfrac{2}{\varepsilon_{1,2}} - 1}\sigma (T_2^4 - T_1^4), \tag{3}$$

$$q = h_{2,3} (T_3 - T_2) + \frac{1}{\dfrac{1}{\varepsilon_{1,2}} + \dfrac{1}{\varepsilon_3} - 1}\sigma (T_3^4 - T_2^4), \tag{4}$$

where:

$\varepsilon_{1,2}$ – emissivity of glazing,

ε_3 – emissivity of wall,

σ – Stefan-Boltzmann constant (W/m^2 K^4),

T_a – ambient temperature (K).

When heat effects of the sun radiation activity are considered over a sufficiently long period, an essential equation form is used for the obtained useful energy:

$$q_f = S - q. \tag{5}$$

The energy balances for the airflow in an entrance duct is:

$$q_f = \frac{\rho \dot{V} c_p (T_{\text{out}} - T_{in})}{A_w}, \tag{6}$$

where:

T_{in} =20 °C is the room air temperature,

ρ – air density (kg/m^3),

c_p – specific heat of air at constant pressure (J/kgK),

A_w – massive wall area (m^2).

The volume flow rate of air is given as $\dot{V} = C_d A_v \sqrt{2 g H \beta (T_{\text{out}} - T_{in})}$, and discharge coefficient of two rows of vents in series with similar cross-section areas is C_d = 0.57 [1], where are A_v – vent cross section area (m^2), β – volume coefficient of expansion of air (1/K).

The air temperature at the upper vent is calculated from [2]:

$$T_{\text{out}} = T_{in} \exp(-\theta H) + T_3 \left[1 - \exp(-\theta H)\right], \; \theta = \frac{h_{2,3} b_2}{\dot{m} c_p}. \tag{7}$$

where:

m – mass flow rate (m^3/s),

b_2 – distance between glazing and massive wall (m).

The efficiency of the system could be defined as the relation of the useful heat delivered by the solar wall to the total energy input:

$$\eta = \frac{q_f}{S + q_{el}} = \frac{q_f}{\tau \alpha G + \dfrac{v^3 \rho b_2}{H \eta_f}}. \tag{8}$$

Electrical energy can be found if the kinetic energy of the entrance air and useful fan's effectiveness are known ($\eta_f = 0.95$) [9].

Average convection coefficients ($h_{i,j}$) used in Equations (2–4) are used from literature references. The average convection coefficient due to wind on glazing from McAdams expression is [15]:

$$h_w = 5.7 + 3.8 \cdot w, \tag{9}$$

where w stands for uniform wind velocity.

The average convection coefficient between glazings was calculated from [11]:

$$N_{u1,2} = 0.062\, G_r^{0.327} \quad \Rightarrow \quad h_{1,2} = 0.82 \frac{(T_2 - T_1)^{0.327}}{b_1^{0.019}} \left[1 - 0.018 \left(\frac{T_1 + T_2}{2} - 283 \right) \right]. \tag{10}$$

Equation (10) holds in the range $1.5 \cdot 10^5 < G_r < 10^7$.

The average convective coefficient in the entrance duct between the wall and the glazing for forced airflow over a vertical plane surface is [1]:

$$h_{2,3} = 5.68 + 4.1 \cdot v, \tag{11}$$

where v stands for uniform air velocity in the entrance duct.

System (1–8) is one-dimensional steady-state mathematical model of the modified Trombe wall. These equations accompanied by properly selected correlation equation for convective and radiation heat transfer coefficient has to be solved using iteration numerical technique to calculate unknown values: S, q, q_f, T_1, T_2, T_3, T_{out}, η.

5. Results and discussion

A series of numerical calculations have been done for the evaluation of the efficiency of the heating system from Figure 2. The thermal analysis of such system is very complicated, because of possible variations of constructive, operating and ambient climatic parameters. Therefore, in the efficiency studies conducted for modified Trombe wall certain parameters are considered as constant, while influence of two parameters was analyzed.

The effects of the air velocity in the entrance duct on the system efficiency, for different distances between glazing and massive wall (width of the entrance duct), are illustrated in Figure 5. While the width of the entrance duct is 2.5 cm, efficiency of the system increases with increasing air velocity in the entrance duct. For larger entrance duct width of 5 cm to 10 cm efficiency increase to the maximum, after which it decreased with increasing air velocity at the entrance duct.

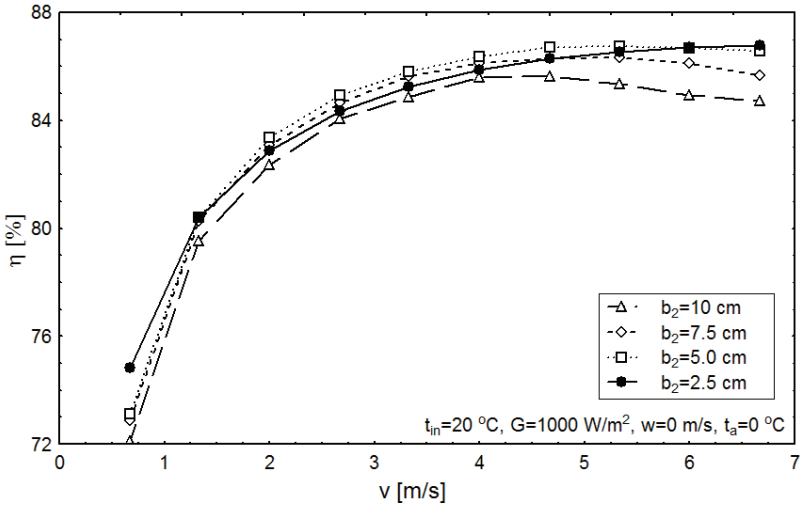

Fig. 5. Variation of efficiency with air velocity in the entrance duct for different distance between glazing and solar wall

Figure 6 shows that the efficiency decreases with increase of inlet air temperature in the entrance duct for different solar radiation. In this case the temperature of the absorber and glazings increase, causing an increase of heat losses. For inlet air temperature in the entrance duct of 20 °C efficiency varies from 65% for solar radiation of 400 W/m^2, to 72% for solar radiation of 1000 W/m^2.

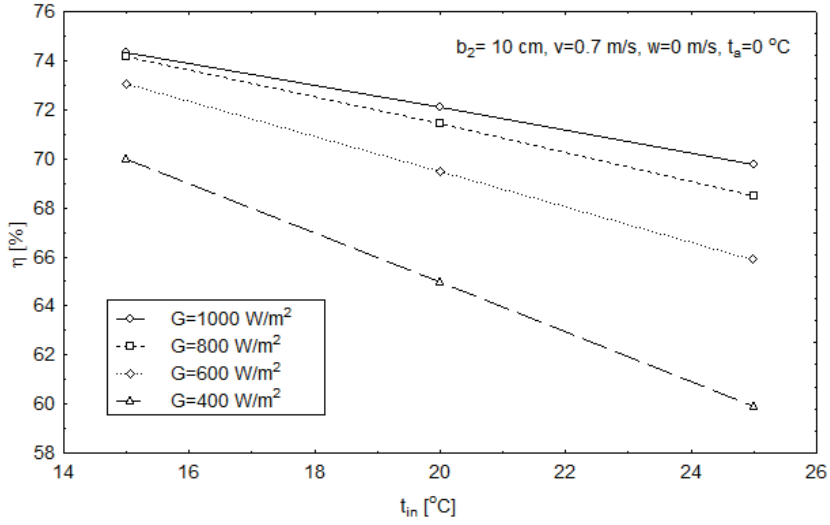

Fig. 6. Variation of efficiency with inlet air temperature in the entrance duct for different solar radiation

Results from the Figure 7 shows that the decrease in inlet air temperatures in the entrance duct causes the efficiency to rise. If the inlet air temperature in the entrance duct is 20 °C, 75% efficiency is obtained for the duct width of 2.5 cm, and 72% for duct width of 10 cm. In this case, influence of duct width is negligible, but bearing in mind that the large width of entrance duct includes a risk of convection loops thinner ducts are recommended.

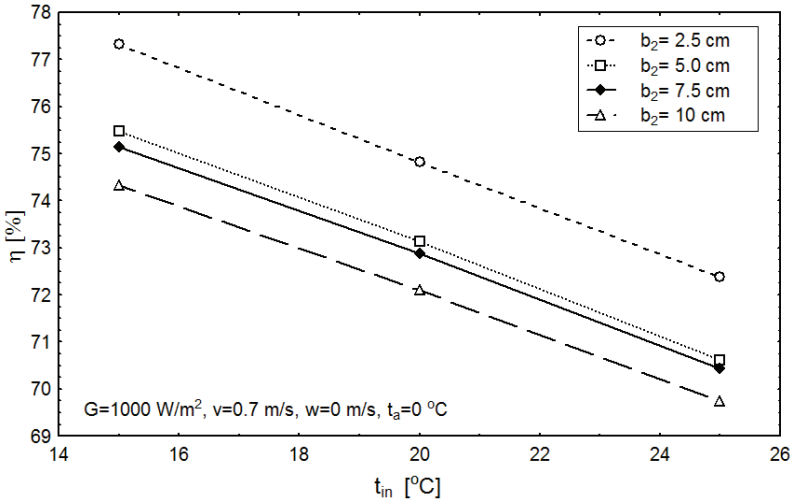

Fig. 7. Variation of efficiency with inlet air temperature in the entrance duct for different distance between glazing and massive wall

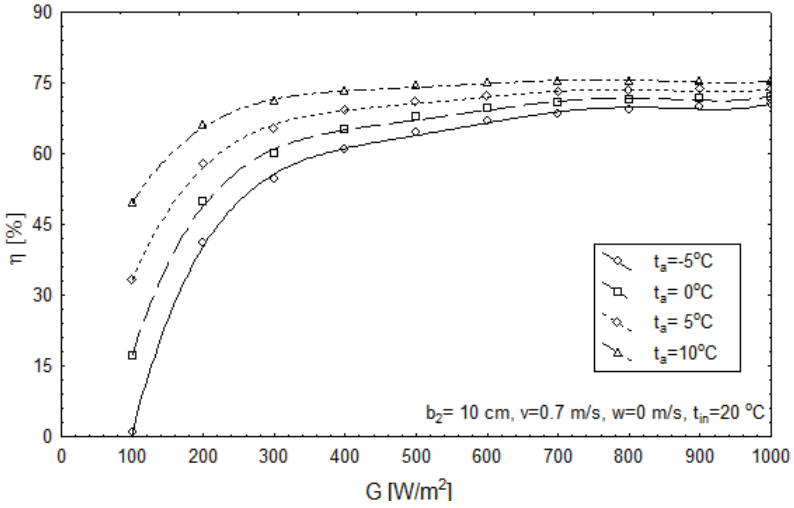

Fig. 8. Variation of efficiency with solar radiation for different ambient temperature

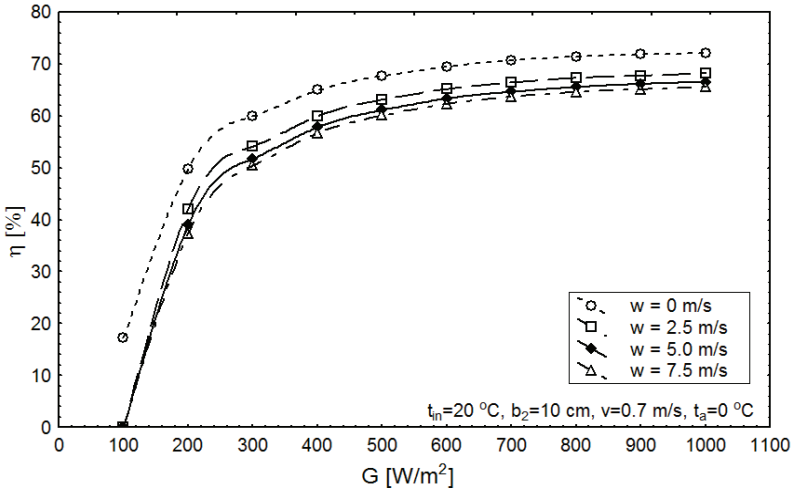

Fig. 9. Variation of efficiency with solar radiation for different wind velocity

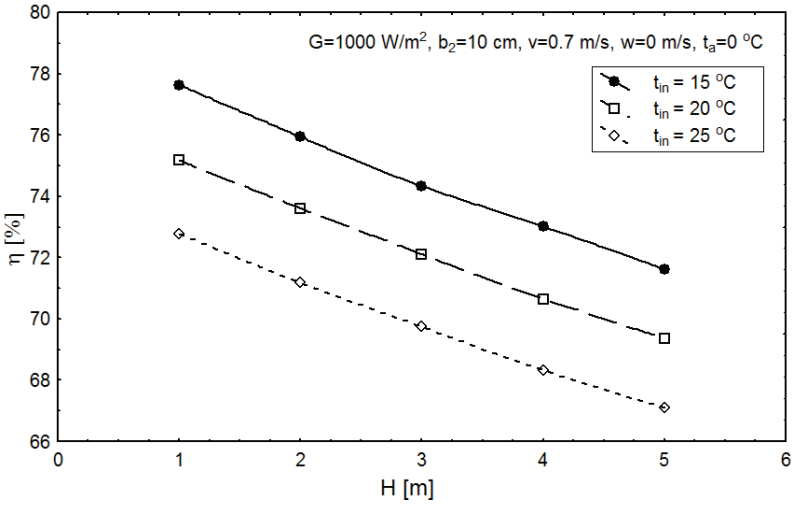

Fig. 10. Variation of efficiency with height of solar wall for different inlet air temperature in the entrance duct

The effects of solar radiation and ambient temperature variation in efficiency are illustrated in Figure 8. Results show that efficiency increases with increasing of solar radiation, significantly up to 600 W/m^2, after increasing of global solar radiation cause an insignificant increase of system efficiency. For ambient temperature of 5 °C efficiency varies from 33% for solar radiation of 100 W/m^2, to 72% for solar radiation of 1000 W/m^2. For locations with cold winter season with ambient temperature below 0 °C, maximum efficiency of present solar air heating system is about 15%.

Figure 9 shows the variations of efficiency of the system as a function of the solar radiation for various wind velocities. It should be noted that efficiency increases with increasing of solar radiation, significantly up to 500 W/m^2, after increasing of global solar radiation cause an insignificant increase of system efficiency. For global solar radiation up to 300 W/m^2, efficiency has very close values for all cases when there is wind. Also, the results show that for a wind velocity greater than 5 m/s efficiency has very close values. The obtained results are close to the result given for Trombe wall by Bhandari and Bansal [2].

Figure 10 shows decreasing of system efficiency with increase of solar wall's height, for different inlet air temperature in the entrance duct. When the wall height is greater, temperatures of the absorbing surface and both glazings are also greater, which caused an increase of system heat loss and decrease of efficiency. With increasing of wall height of 1 m, efficiency decreases by 2%. Ong [12] found similar results for the solar chimney because its physical model is similar to the Trombe wall.

6. Conclusion

In the present study, numerical calculations are performed for analysis of the modified Trombe wall efficiency. Analyzed wall is used for space heating in the times of day when the wall is exposed to the sun. In order to increase the efficiency, an active control (fan) is integrated, which is the innovation compared to the analyzed modified Trombe wall. The data from this investigation yields some insights into the efficiency of the solar air heating, for different constructive and operating parameters of the wall. Because of the large number of parameters and the wide range of weather conditions, which influence the operation of the wall, the effect of varying velocity and temperature of the air in the entrance duct, solar radiation, wind velocity, wall height and ambient temperature on the efficiency of the heating system is presented.

Based on the results of numerical study, if the room temperature is 20 °C, following conclusions can be drawn:

- The maximum efficiency obtained for an entrance duct width of 2.5 cm and air velocity in the entrance duct up to 2 m/s, which can be expected in real conditions of the wall operation,
- Results show that efficiency increases with increasing of solar radiation, significantly up to 600 W/m^2, then it can be considered to have nearly constant value,
- For winter weather conditions with maximum solar radiation of 400 W/m^2 and ambient temperature of 0 °C, without wind, maximum efficiency is about 60%. For lower values of solar radiation and wind velocity of 5 m/s, efficiency significantly decreases,
- In climates with cold winters, when ambient temperatures are below –5 °C, the present system is not efficient for air heating.

This method enables users to evaluate the efficiency of the present air heating system of several options and to make comparison and predictions of thermal behaviour

of the solar wall under various conditions. It should be clear, however, that a different maximum efficiency could be expected when the constructive and operating parameters of the wall are modified.

References

[1] Akbarzadeh A., Charters W.W.S., Lesslie D.A.: *Thermo circulation characteristics of a Trombe wall passive test cell*, Solar Energy, Vol. 28, No. 6, 1982, pp. 461–468.
[2] Bhandari M.S., Bansal N.K.: *Solar heat gain factors and heat loss coefficients for passive heating concepts*, Solar Energy, Vol. 53, No. 2, 1994, pp. 199–208.
[3] Burek S.A.M., Habeb A.: *Air flow and thermal efficiency characteristics in solar chimneys and Trombe walls*, Energy and Buildings, Vol. 39, 2007, pp. 128–135.
[4] Dragicevic S., Lambic M.: *Numerical study of a modified Trombe wall solar collector system*, Thermal Science, Vol. 13, No. 1, 2009, pp. 195–204.
[5] Jie J., Hua Y., Gang P., Jianping L.: *Study of PV-Trombe wall installed in a fenestrated room with heat storage*, Applied Thermal Engineering, Vol. 27, 2007, pp. 1507–1515.
[6] Jie J., Luo C.L., Wei S., HanCheng Y., Wei H., Gang P.: *An improved approach for the application of Trombe wall system to building construction with selective thermo insulation façades*, Chinese Sci Bull, Vol. 54, 2009, pp. 1949–1956.
[7] Khedari J., Pongsatirat C., Puangsombut W., Hirunlabh J.: *Experimental performance of partially-glazed modified Trombe wall*, International Journal of Ambient Energy, Vol. 26, No. 1, 2005, pp. 27–36.
[8] Kisilewicz T.: *Glazed building wall as a solar thermal collector*, Archives of Civil and Mechanical Engineering, Vol. 9, No. 1, 2009, pp. 83–99.
[9] Lambic M.: *Solar walls – The passive solar heating*, 1 eds. University of Novi Sad, Technical faculty Zrenjanin, Serbia, 2000.
[10] Lenik K., Wójcicka-Migasiuk D.: *FEM applications to the analysis of passive solar wall elements*, Journal of Achievements in Materials and Manufacturing Engineering, Vol. 43, No. 1, 2010, pp. 333–340.
[11] Matuska T.: *A simple Trombe wall: comparsion of different glazings*, in 3rd ISES Congress Eurosun 2000, Copenhagen, Denmark, 19–21 June, 2000.
[12] Ong K.S.: *A mathematical model of a solar chimney*, Renewable Energy, Vol. 28, 2003, pp. 1047–1060.
[13] Shen J., Lassue S., Zalewski L., Huang D.: *Numerical study of classical and composite solar walls by TRNSYS*, Journal of Thermal Science, Vol. 16, No. 1, 2007, pp. 46–55.
[14] Zomorodian A.A., Woods J.L.: *Modelling and testing a new once-through air solar energy collector*, J. Agric. Sci. Technol., Vol. 5, 2003, pp. 11–19.
[15] Zrikem Z., Bilgen E.: *Theoretical study of a composite Trombe–Michel wall solar collector the system*, Solar Energy, Vol. 39, No. 5, 1987, pp. 409–419.

Wpływ konstrukcyjnych i operacyjnych parametrów na wydajność zmodyfikowanej ściany Trombe'a

W artykule przedstawiono analizę efektywności zmodyfikowanej ściany Trombe'a z wymuszonym obiegiem, która może działać w czterech różnych trybach. Analizowany system

składa się z podwójnych szyb i masywnej ściany z otworem oraz centralnym kanałem. W celu zwiększenia efektywności systemu, wentylator został usytuowany w dolnym otworze ściany. Przedstawiony system jest bardziej zaawansowany w porównaniu z konwencjonalną ścianą Trombe'a o stosunkowo niskiej odporności termicznej, która przyjęta jest w pracy, jako punkt odniesienie w analizie eksperymentalnej. W artykule przedstawiono jednowymiarowy model matematyczny w stanie stacjonarnym i zastosowano go w celu przeprowadzenia uproszczonej analizy sprawności cieplnej zmodyfikowanej ściany Trombe'a. Wyniki uzyskane z zaprezentowanego modelu analizowano pod kątem określenia wpływu zmian konstrukcyjnych i operacyjnych parametrów na efektywność systemu. Uzyskane rezultaty zostały wykorzystane jako proste i efektywne narzędzia projektowe, które mogą służyć we wczesnych fazach procesu projektowania do obliczeń wydajności aktywnych solarnych systemów grzewczych.

ARCHIVES OF CIVIL AND MECHANICAL ENGINEERING

Vol. XI 2011 No. 4

Study on fatigue cracks in steel-concrete shear connection with composite dowels

W. DUDZIŃSKI, G. PĘKALSKI, P. HARNATKIEWICZ, A. KOPCZYŃSKI, W. LORENC, M. KOŻUCH, S. ROWIŃSKI
Wrocław University of Technology, Wybrzeże Wyspiańskiego 27, 50-370 Wrocław, Poland.

In recent years many research on composite beams with innovative shear transmission with composite dowels have been conducted (mainly within PreCo-Beam project [15]) and innovative composite constructions have been designed and built. As this shear connection is to be applied mainly for bridges, problems concerning fatigue behaviour appear [1, 16]. Composite dowels behaviour in aspect of fatigue resistance and fatigue cracks investigations is extremely complex. It is caused not only by complicated stress distribution from external loads but also by eigenstresses which are released during beam cutting and cutting technology itself as well. It will be proved in detail macroscopic studies how production and cutting process may influence the fatigue crack initiation and propagation process. This paper presents investigations undertaken after finished PreCo-Beam project [15] which is part of the research to be conducted years 2009–2011 at Wrocław University of Technology. Results of detailed metallographic inspections of fatigue cracks obtained during full-scale tests, and schedule of next full-scale tests to be performed at Wroclaw University of Technology are presented. Described researches are carried out in order to determine fatigue lifespan of composite beams with shear transmission realized with composite dowels of MCL shape [5, 10]. MCL shape is currently the most often used shape of steel dowel because of its fatigue behaviour as well as technological aspects of its production process and therefore all foreseen research will focus mainly on this shape. The MCL shape is shown in Figures 33–38.

Keywords: *composite dowel, composite structures, continuous shear connection, metallographic inspection, fatigue cracks, FE analysis, FE fatigue analysis, laboratory tests*

1. Cyclic test

In scope of realized Precobeam Project [15] full-scale beam tests were performed under cyclic loads. The span of tested beams was 3.6 m and was determined with adjusting the loading frequency (f = 1.1–1.3 Hz), hence overall time needed to accomplish tests, to project's schedule. Load varied from 120 to 280 kN, boundary conditions – single supported beam subjected to four-point bending (Figure 1). Pictures, which present testing condition, took during testing are also presented in Figure 2a and 2b.

All technical data about specific conditions and test's process, like values measured and frequency of taken measurements, can be found in [1, 15–16]. In report [1] also calculation and test evaluation in aspect of static values can be found. Force value was chosen this way to ensure that stress range is high enough to cause fatigue damage

within 2e6 cycles. It was chosen as the reference number of cycles which was suitable to timeframe of the project as well. During tests, beam with low web (shear connection level far in the tensile zone – Figure 1) underwent fatigue damages which caused its total failure at 1.26e6 cycle. Crack was propagated throughout all web and eventually caused fracture of lower flange of steel T – section being tensile part of composite

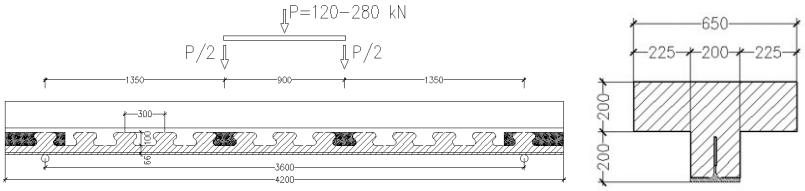

Fig. 1. Side view and test setup of considered beam (left) and cross section (right)

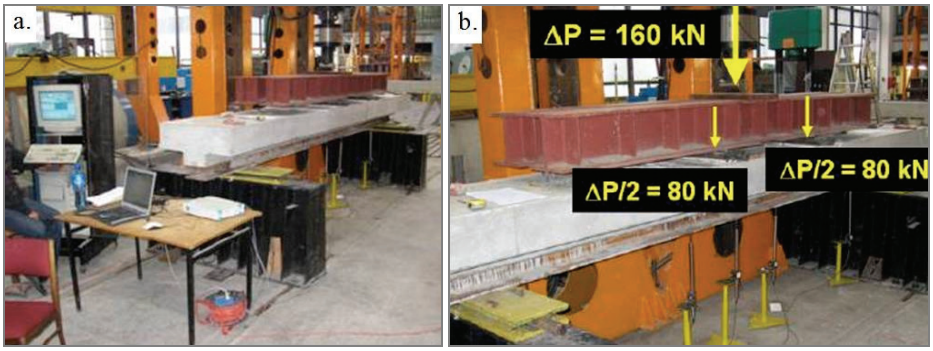

Fig. 2. a) Testing stand, b) Load applied to the beam

Fig. 3. Pattern of cracks on concrete part of beam after cycling tests and failure of beam caused by fatigue crack in steel flange (marked with circle)

beam. Detail pictures presenting fatigue crack being described is shown in Figures 3 and 4a,b. The region of fatigue crack was cut out from the beam and metallographic inspections were carried out.

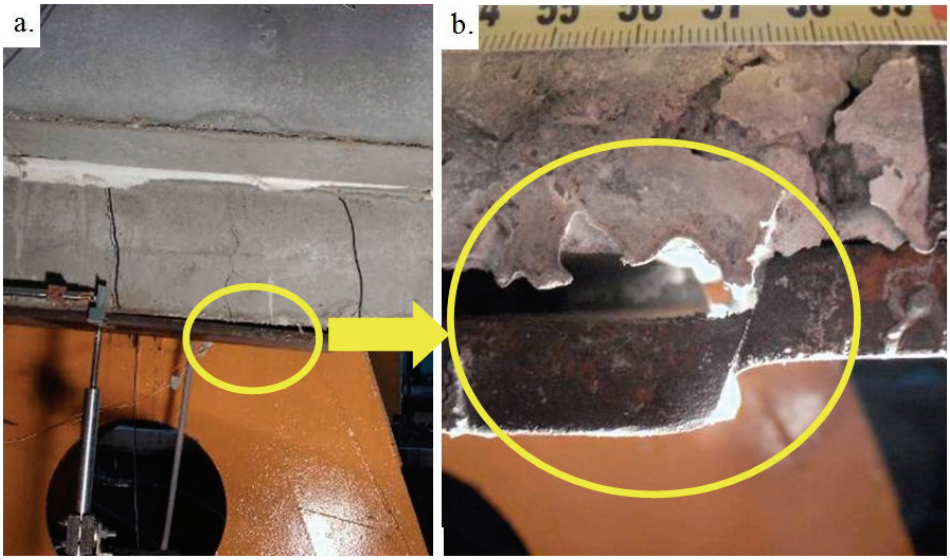

Fig. 4. a) Place where flange was cracked, b) Zoom into crack zone

Concrete was removed from composite beam and steel part was separated. It turned out that there were fatigue cracks in most of active steel dowels. Length of cracks propagation as well as direction of crack was confirmed by FE analysis. Crack pattern in concrete slab and in steel part of the beam is presented in Figure 5. After removing the concrete, region where crack propagated throughout the flange (Figure 6) was cut out and put to detail analysis. Characteristic of presented fatigue crack with conclusions about its affecting factors is subject of following part of this paper.

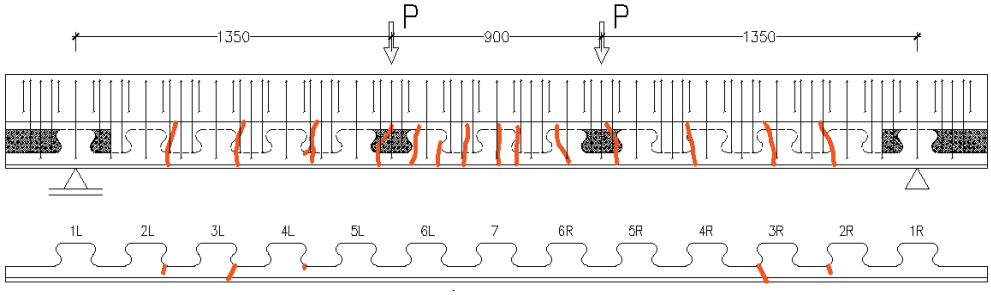

Fig. 5. Cracks on concrete slab (upper part of picture) and on steel section (down)

Fig. 6. Considered crack after concrete is partially removed

2. Cracks investigation

The cracks propagation and initiation mechanism generally can be assumed to be independent on cutting line shape [11–12]. The basis for fatigue calculations are presented in [2–3] and FE approach is presented in [9]. It means that the stress fluctuation and its layout influence the number of cycles resulting in crack appearance and crack propagation speed, but the basis of the phenomenon is the same [4]. Hence detailed microscopic studies [6, 8] of cracked specimens were conducted and the results were presented herein.

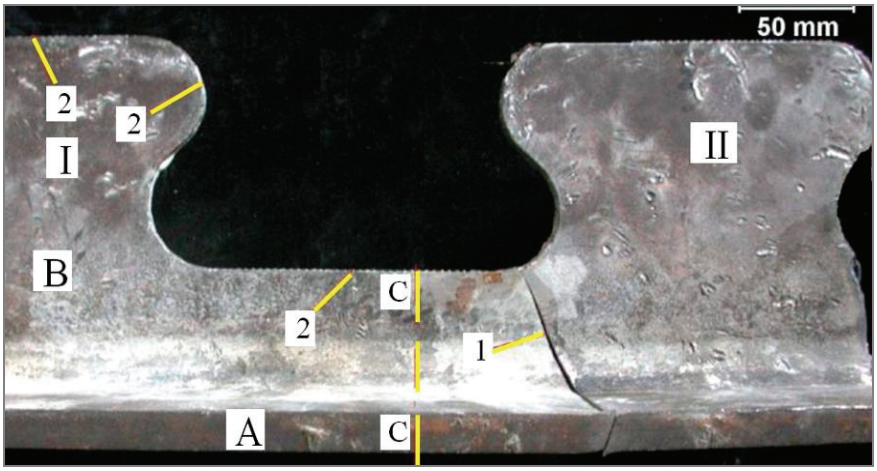

Fig. 7. Macroscopic photo of the supplied specimen for testing. The view from side. A – Flange of a steel section. B – Steel web. C-C – intersecting plane with an aim to gain a macroscopic cross section. I – The left part of the cracked beam. II – The right part of the cracked beam. 1 – A crack throughout the entire cross section. 2 – The outer surface parts of the web B with evidence of grinding

A beam fragment (beam with a low web and the PZ shape of the cut) has been tested experimentally (Figures 7 and 8) within the scope of the Precobeam project. The geometry, test setup and results were presented in detail in the Precobeam report [15] and shortly described above. A T-bar shape specimen (A – flange of steel section and B – web of steel section) underwent fatigue testing resulting in the appearance of the crack on the entire cross-section (Figure 9). The profile of the web B was shaped with the use of thermal method (gas cut) whereas its exterior surface had been roughly grinded.

The results of observation in the area of the cross section C–C (Figure 7) indicate that the beam was shaped using the ductile alteration method (Figure 9). There were no macroscopic defects in this section with an exception of a local vertical discontinuity 4 mm long and 0.2 mm wide, showing up in the vertical part of the steel section (B).

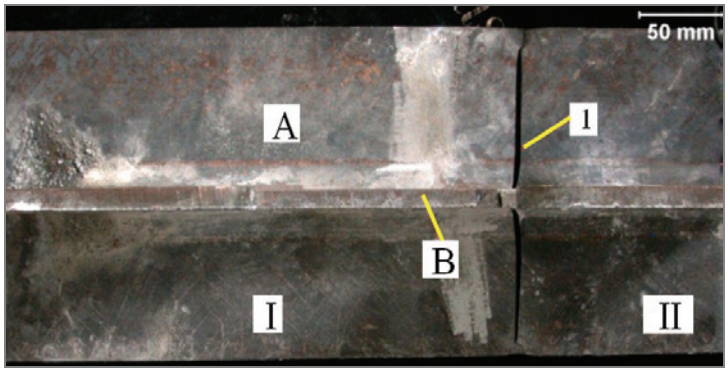

Fig. 8. Macroscopic photo of the tested specimen. View from side. I – The left part of the cracked beam. II – The right part of the cracked beam. 1 – crack. A – Flange of steel section. B – Web of steel section

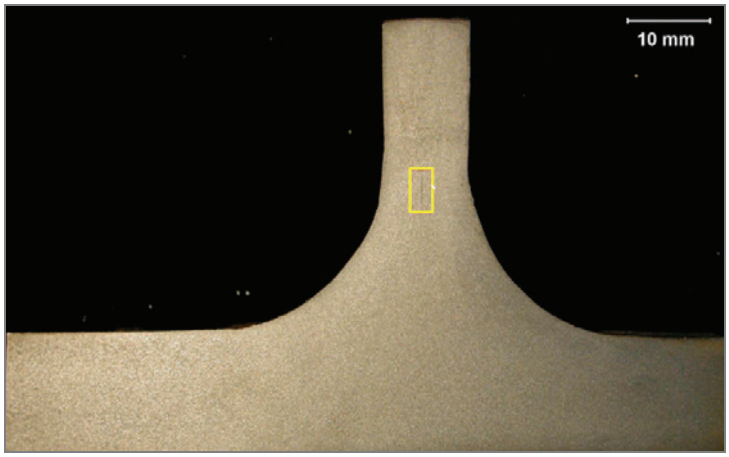

Fig. 9. Cross section across the plane C – C marked in Figure 7.
The discontinuity is marked with a frame in the steel web

In order to carry out further macro and microscopic tests of both fragments of the cracked beam (marked as I and II on Figure 7) five samples were taken and marked with letters A, B, E, F, G. The places the samples were taken from were schematically shown in Figure 10. The investigated beam was made out of steel grade S460M.

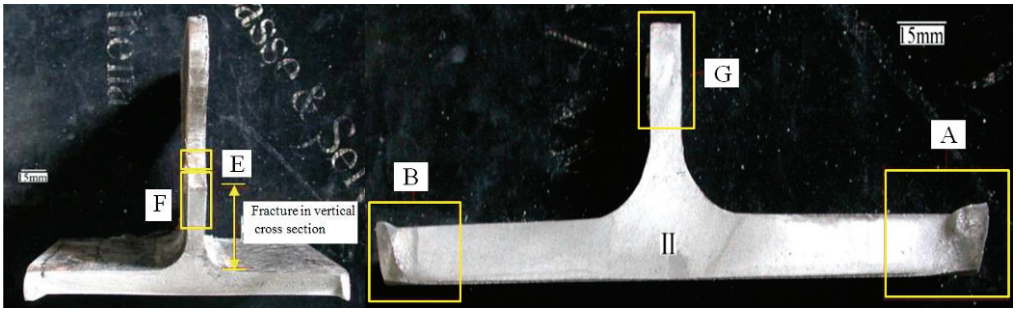

Fig. 10. General view in parts I and II with marked areas of the samples

The base values of the S460M mechanical properties are as the following: yield strength $R_e \geq 460$ MPa; tensile strength $R_m = 540–720$ MPa; elongation $A_5 \geq 17\%$.

A chemical analysis of the beam material was done with the use of the gravimetrical method. Chips for chemical analysis were taken for testing from the entire width of the vertical part of cross section (web) that was previously cleaned from pollutants and colouring agents. In addition, a microanalysis of the chemical composition of the sample G microsection surface was done employing an EDX (Energy-dispersive X-ray spectroscopy) device coupled with a scanning microscope type JEOL JSM 5800LV. The energy spectrum of the X-radiation (Figure 11).

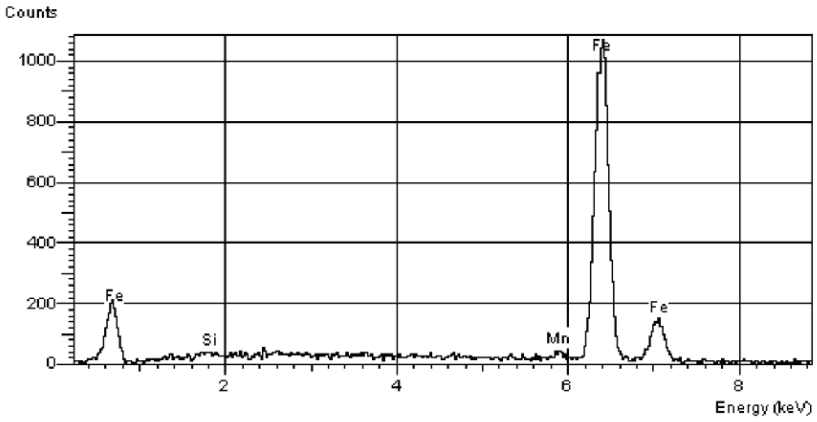

Fig. 11. The energy radiation of the spectrum in the X-ray from sample G

The examined fracture covered the entire flange of beam cross section as well as 30% of its web, marked in Figure 10. About 95% of the surface of the fracture has a temporary and fine-grained character and its surface does not show an extended topography. Two areas, different than above mentioned, were found at the end of the fracture in the flange of the beam (Figure 12 and 13). The areas were marked as A and B in Figure 10. The zone in area A is 14 mm wide and leaned at an angle of 45 degrees in relation to the rest of the fracture. In zone B, the width is 5 mm and is bent at an angle of 30 degrees. In the described surfaces the traces of plastic deformations as well a differential surface topography were observed.

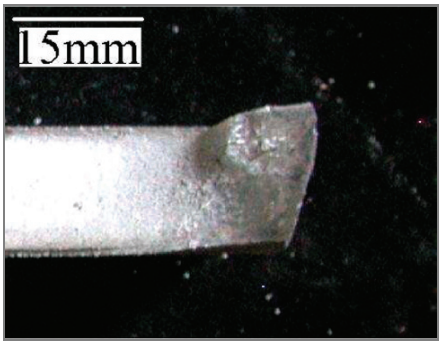

Fig. 12. Enlarged fragment of the broken part shown in Fig. 10, area A.

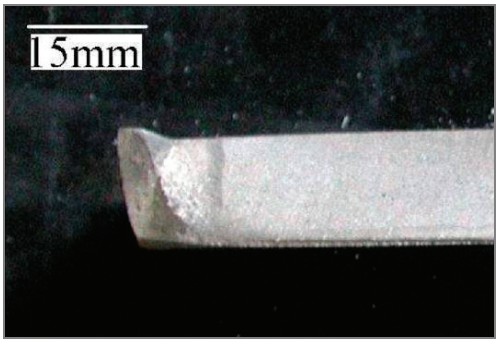

Fig. 13. Enlarged fragment of the broken part shown in Fig. 10, area

The observations of the web show that rolling and cutting of profile and then rough grinding could result in the future local stresses accumulation and cause initiation and propagation of the fatigue cracks. The state of the outer surfaces on the web of the beam – samples E and F (Figure 10) is presented at Figure 14. Numerous deep scratches resulting from cutting process of the beam are seen.

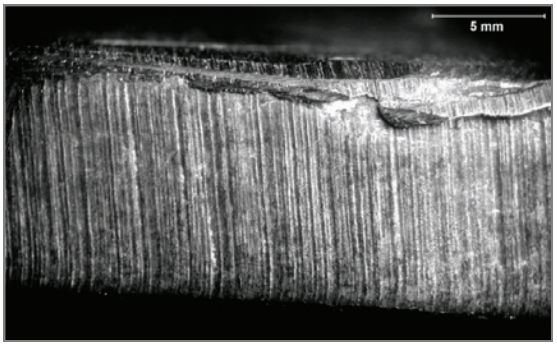

Fig. 14. Numerous deep scratches seen on the outer part of the surface of the web of the beam (areas E and F were marked at Figure 10)

Observations of the surface fractures conducted for samples G, A and B with the help of a scanning electron microscope have shown the presence of initiation places in fatigue fractures of the tested beam. The structure of these fracture fragments (Figures 15–20) reveals the characteristics of the fatigue fractures. The initiation of the fatigue fracture in the sample G took place in the bottom of the notch that resulted from grinding (Figures 15 and 16). Starting in the corner of the sample, the occurrence of micro-fractures that penetrate into the small fatigue zone in the rest of the fracture in the bottom of the notch was found. Enlarged zone of the place showed on the Figure 15 and 16.

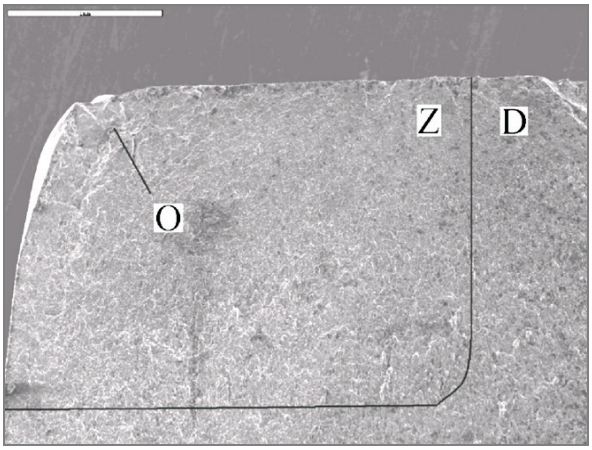

Fig. 15. Sample G in Figure 10. The fragment of a fracture with fatigue zone – Z. Rapid fracture – D. As well as the places of fracture initiation – O. Zoom 35×, SEM

Fig. 16. Sample G. Enlarged fragment of the fracture surface in Figure 10 that includes the fatigue zone (Z) as well as the places of fracture initiation – O. SEM

In the samples A and B (end of the horizontal part of the beam showed on Figure 10) the fracture fatigue zones appear in the steel section corners as well as on the entire width near the outer surfaces. They are more smooth than observed in the sample G and show signs of invariant lines. There is ductile fracture predominating in rapid fracture zones. The topography of these fractures is presented in Figures 17–20.

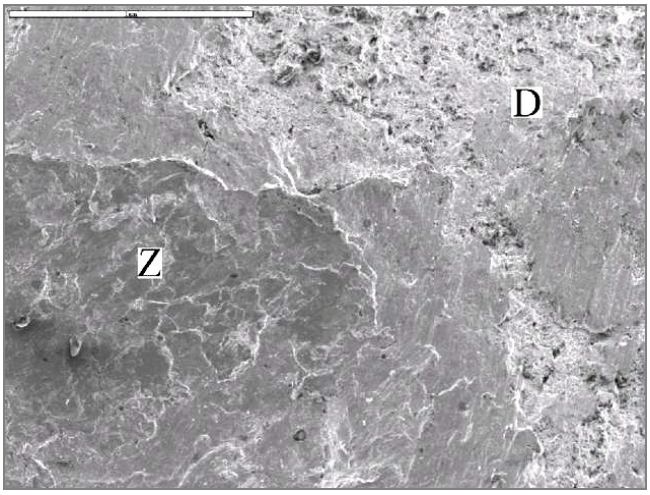

Fig. 17. Sample A in Figure 10 – fragment of the fracture that includes the fatigue part – Z and rapid fracture part – D. SEM

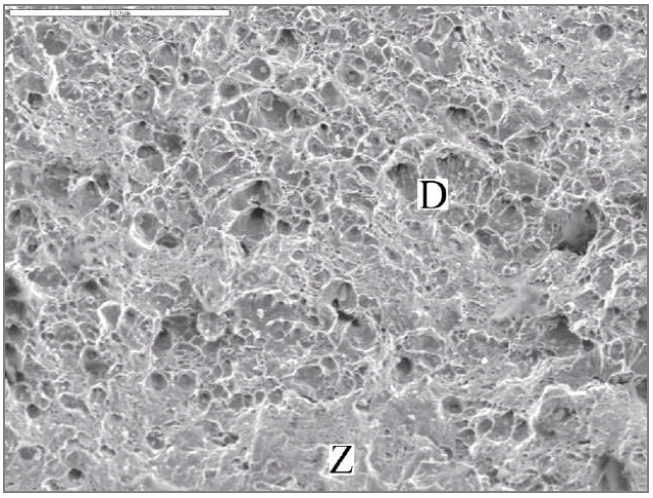

Fig. 18. Sample A. The enlarged fragment of the topography of the fracture shown in Figure 17 that includes mostly its rapid fracture – D as well as a small part of the fatigue fracture – Z, which exhibits the character of ductile fracture. SEM

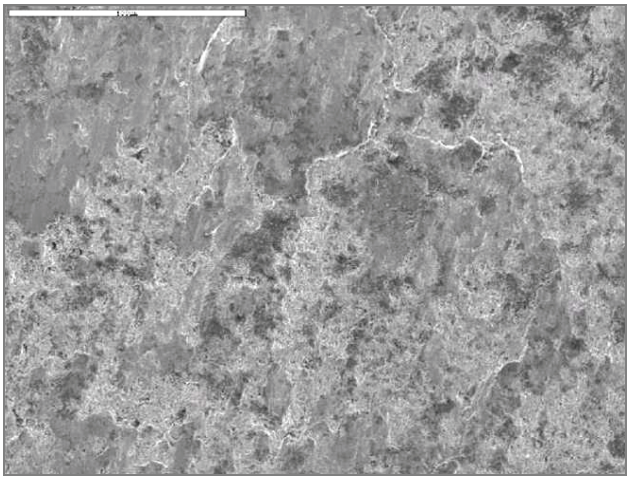

Fig. 19. Sample B in Figure 10. The fatigue fracture part. SEM

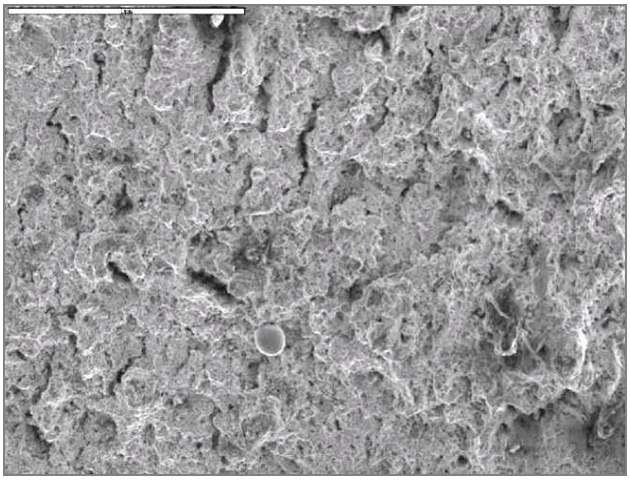

Fig. 20. Sample B. The rapid fracture at ductile area. Zoom 50×, SEM

The results of the fractures observation shows they have a character of multi-pocket fatigue fractures initiated in the vertical part of the tested beam (web) as well as on the extremity of its horizontal part (edges of flange). In the area of the vertical part (area of the sample G) focus of breakage located in the surface zone in areas of stresses concentration triggered by the presence of grinding grooves were identified. In the horizontal part (areas of samples A and B) research on fractures did not yet allow for the establishment of breakage initiation causes, therefore metallographic microsection on perpendicular and parallel planes in relation to the surface of the fractures were carried out for these samples.

A metallographic samples parallel to the fracture surface (zone A – Figure 10) of the specimen was investigated. In the unattached state of the tested material, the occurrence of a significant amount of non-metallic inclusions situated mostly in the surface layer was proven.

After etching of 3% Nital was finding of non-equilibrium pearlite -ferrite structure with fine carbide after coagulation. Furthermore, the presence of micro-fractures course passing through the borders of former austenite grains was noticed. In Figure 21 and 22 an example of inclusions done by non-metallic pollutants is shown as well as the structure of the material of the tested beam from the area of sample A.

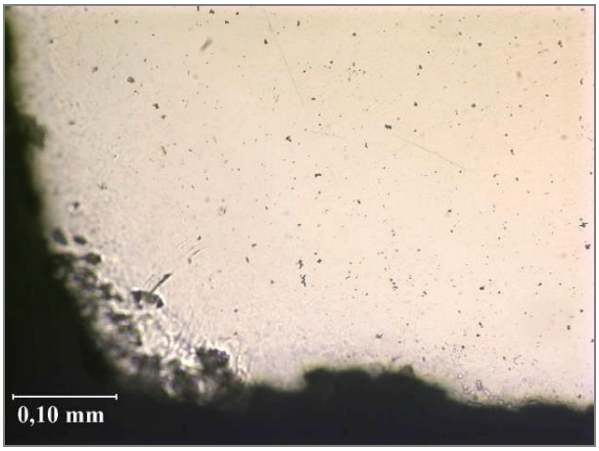

Fig. 21. Sample A. Non-metallic inclusion in the fatigue zone of the sample. The unetched state

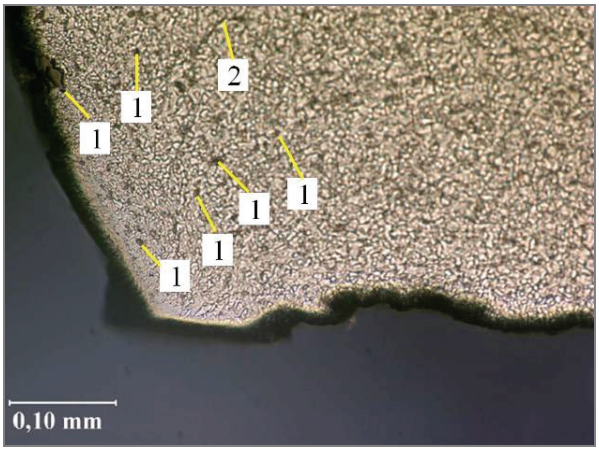

Fig. 22. Sample A. Non-metallic inclusions (marked with arrows) as well as micro-fractures on the border of the previous austenite grain on the background of non-equilibrium of pearlite-ferrite structure. Mi1Fe etching. Light microscopy

During the microscopic investigations of the samples F and G (taken from the vertical part of the beam) it was proven that they have a nonuniform structure in the layer construction. The extent of the structural changes reaches the depth of 3.5 mm. In the surface layer that has a thickness of about 1 mm, zones with a pearlite-ferrite equilibrium structure was observed. Under this layer, an area of 1.5 mm thickness martensite structure appears and non-equilibrium pearlite with ferrite zone (Figures 23–26).

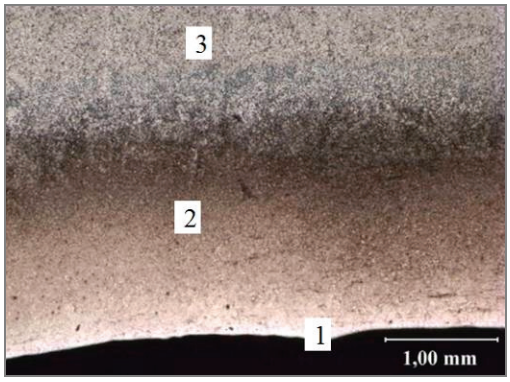

Fig. 23. Sample F. Changes in structure inside the surface zone in the vertical part of the beam. 1 – Ferrite – pearlite zone, 2 – Martensite structure zone. 3 – Pearlite – ferrite zone. Mi1Fe etching. LM

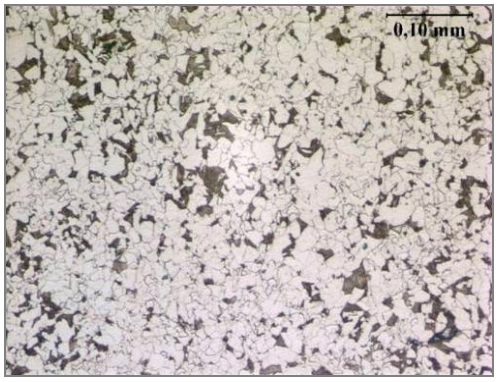

Fig. 24. Sample G. Ferrite – pearlite zone. Mi1Fe etching. LM

Fig. 25. Sample G. – martensite structure zone. The arrows indicate the micro fractures on the previous austenite grains**.** Mi1Fe etching. LM

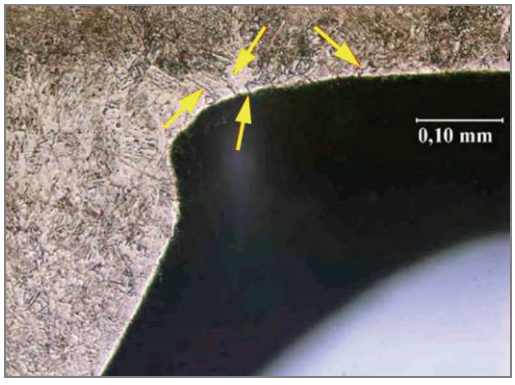

Fig. 26. Sample G. Changes in structure in the near surface zone. The arrows presence of micro fractures. Mi1Fe etching. LM

Microscopic testing of the metallographic microsection showed the presence of multifocus fatigue scraps. They are initiated in areas where stress concentrations appeared: the bottom of grooves that appeared when grinding, nonmetallic inclusions and areas where martensite structure occurs. The zone construction of the surface layer of the

vertical part of the beam is most likely caused by its profiling technology. Cooling after thermal cutting caused the appearance of low-carbon martensite in the material structure. During this process, partial decarburization of the surface layer occurred (Figure 26). Subsequently, intensive grinding led to the creation of a zone with a pearlite-ferrite structure.

Hardness tests were carried out with the Vickers method in conditions compliant with PN EN ISO 6507-1; 1999. A hardness tester, Zwick 321, was using the load 10 kG (98.07 N) working in a 15 second time frame. The hardness was performed along two lines A-B, C-D shown in Figure 27. The layout of hardness appropriate for lines A-B and C-D are show at Figures 28 and 29. The distance between the surface and the first impression is about 1 mm while subsequent impressions were done in about 5 mm distances.

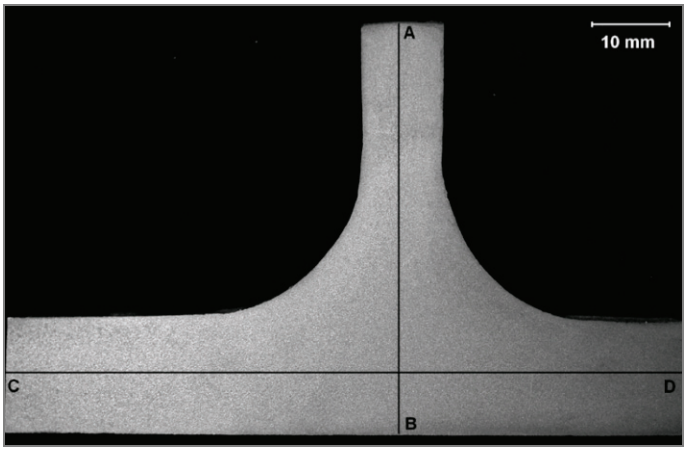

Fig. 27. The horizontal cross section with marked lines A-B and C-D, along which the hardness testing was done

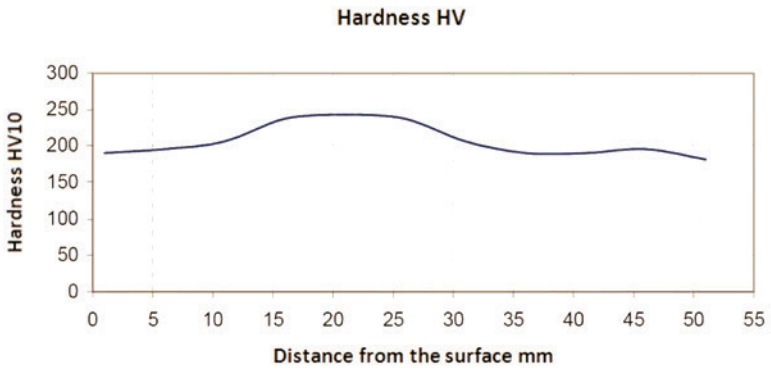

Fig. 28. The layout of hardness of line A-B

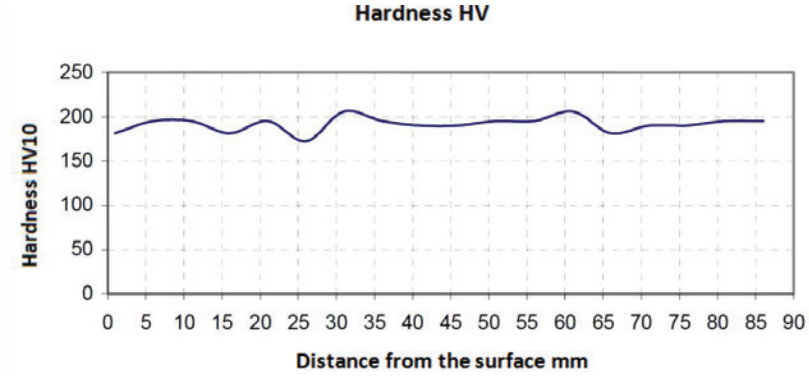

Fig. 29. The layout of hardness for line C-D

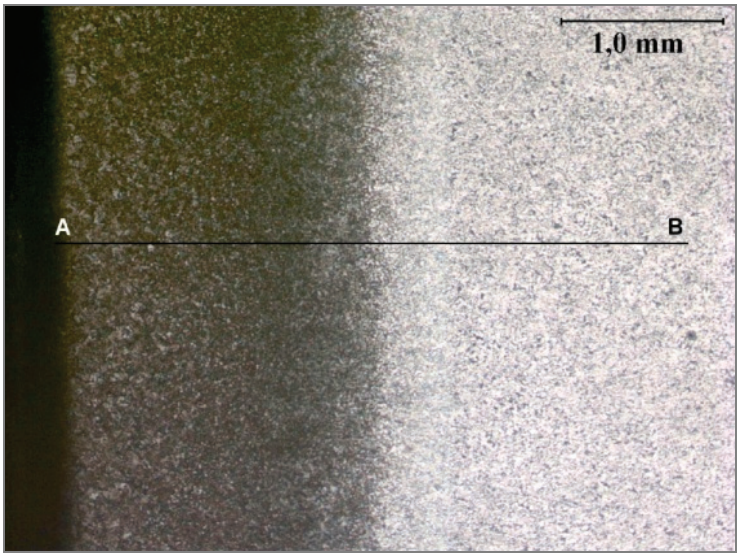

Fig. 30. Sample E. The hardness testing line

The hardness of the tested beam is in the 172 to 243 HV10 range in the area of the material with no near surface area structure changes. However, in areas with various microstructures within the vertical beam fragment the testing was done after removing the pearlite- ferrite layer like shown in Figure 30. The results of the hardness measurements of this region are illustrated in Figure 31. The maximum hardness that appeared in the zone with a martensite structure is 453 HV10. Only in distances about 2.5 mm (including the 2-coal 3.5 mm zone) from the surface of the hardness of the tested material the hardness reaches the level of 200 HV10, meaning it is closer to the average of the hardness of the material.

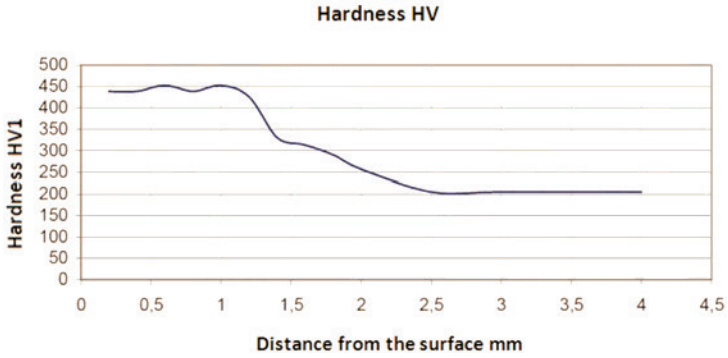

Fig. 31. Sample E. The results of the hardness measurements of the surface layer across the line A-B

The above testing verifies the occurrence of the fatigue fracture effect as well as crack propagation that led to the damage of the construction. The presented microscopic analysis allows for the assumption as to what the character of the effect is like. The presented results show the numeral values that will be taken under consideration in further testing in theoretical analysis of the propagation of the cracks. This analysis will be important especially since on its basis, it will be possible to choose the method of estimation as well as a partial factor according to table 3 in the [7].

3. Tests to be conducted

In order to verify the correctness of shear connector dimensioning methods accepted by the authors durability testing are conducted [4]. Full-sized composite beams were put under static and cyclic loads. One of the conducted trials within the Precobeam project was the four-point bending of a beam with a PZ shape shear connection. During these tests, the strain layouts in the steel dowels were measured with the help of electro-resistant strain gauges [15]. This trial was described in a Precobeam report. [15]. The PZ-CD testing was done within the frame of the accomplished testing [1, 15], currently the CL-CD testing is being planned. The scheme of the beams intended for damage testing in the Wrocław University of Technology is shown in Figures 32 and 33, however, sample strain gauges arrangements are presented in Figures 34 and 35. General testing procedures are described in [13].

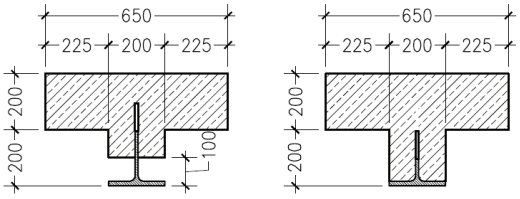

Fig. 32. Basic beam's cross sections subjected to 4-point-bending tests

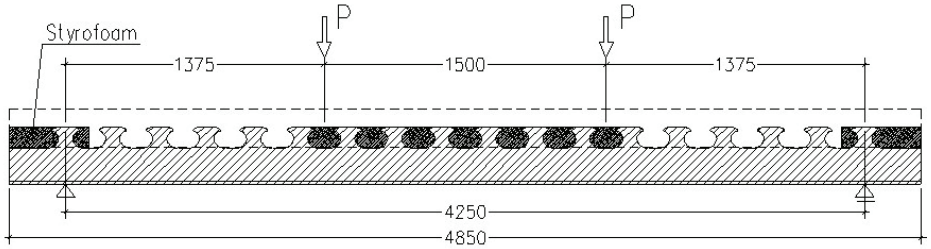

Fig. 33. General view of static system for 4-point-bending tests

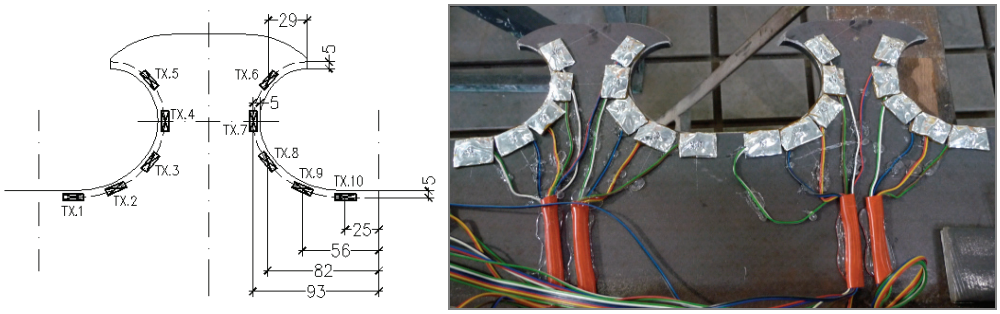

Fig. 34. Localization and numbering of strain gauges on steel dowels (left) and picture of placed SG

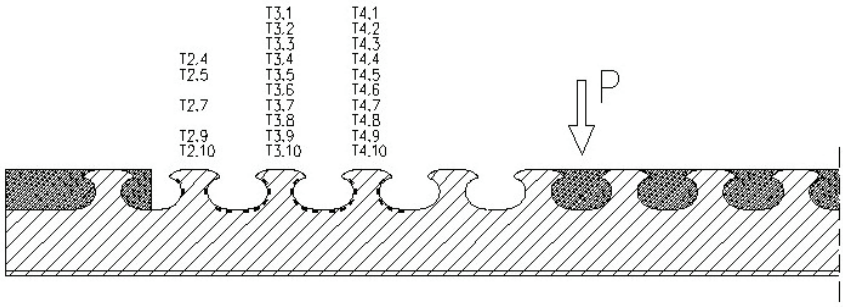

Fig. 35. Proposal of placing SGs on steel dowels

Basing on the results obtained from the strain measurements acquired from the proposed strain gauges layout a calibration of the beams numerical models will be performed. The map of strains will be readable in discreet points of the numerical model and will be used for elastic resistance interactive formulas determination. In areas of geometric notches, in beams subjected for cyclic testing, rosettes were used to confirm the values and direction of main stresses. In tests that are currently being realized of composite beams with different (than previously tested) connector shapes, it is planned to use at base of the connector shield pipes, creating observational channels

for beams subjected for cyclic loads. During the time of the cyclic testing, continual measurement will be done in the channels with a highly sensitive thermal imaging camera with frequent scanning. Thanks to this, it will be possible to observe the initiation time of the fatigue fracture through the observation of temperature changes of the tested surface as well as propagation rate. Places where channels are built-in are presented in Figure 36.

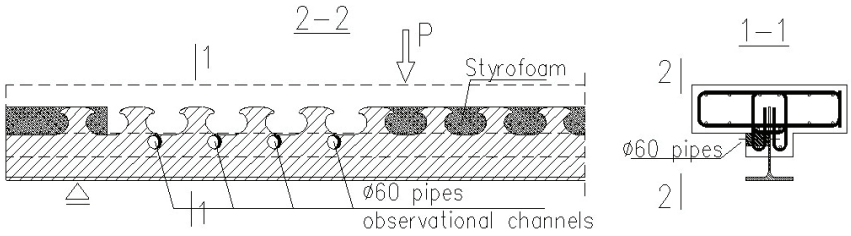

Fig. 36. Places arrangements for observational channels

These channels are built-in at the one side of steel connectors, while on the second side strain gauges and rosettes are put. During the test it is possible both measurement of strains hence calculation of stresses in the dowel and observation of cracks arisen. Erected at Wroclaw University of Technology beams with described channels are presented in Figures 37 and 38.

Fig. 37. Steel beam with observational channels

Fig. 38. Channel before concreting and view through the channel after concrete is casted

As separate research there will be cyclic tested many simple tensioned specimens cut from a steel plate with different methods – oxy, plasma and water cutting. According to results, it is planned to create determine notch category for a straight plate under tension which edges are of quality that can be got in an industrial fabrication with adequately method.

4. Conclusions

The newest studies concerning fatigue durability of composite dowel shear connectors were presented. Detailed analysis of fatigue crack obtained in frame of PreCo-Beam project is a necessary step in direction of good understanding the fatigue behaviour of composite dowels. It was proven how important is the technology of fabrication of steel part subjected to use in composite construction. Technological aspects like way of I-sections rolling, cutting them into halves and preparing the outer surfaces can significantly affect fatigue lifespan of composite beam with shear connection with composite dowels. Crack investigated was coming from PZ steel dowel which is nowadays not used in structures (but realized bridges with PZ steel dowels exist), but crack propagation and initiation mechanism generally can be assumed to be independent on cutting line shape. It means that the stress fluctuation and its layout influence the number of cycles needed for crack initiation and influence crack propagation rate as well, but the basis of the phenomenon is the same. Nevertheless further researches with currently used MCL shape of steel connector are being realized at present. It is planned to achieve the result of the research studies in form of the evaluation method as well as the values of partial factors for fatigue durability that should be ascribed in accordance with the EN 1993-1-9:2005. It is very important to state clearly if fatigue design should be based on tolerated damages or unconditional lifespan method. Both observation of crack propagation through channels embedded into concrete and strains measurements throughout all testing time should give the answer about stress state and it changes caused by crack as well as rate and direction of propagating crack. On basis of these results and research on edges fatigue category it is expected to solve definitely problem of fatigue design in composite dowels shear connectors and consciously choose proper way of cutting technology to minimize possibility of crack initiation caused by technological damages.

Acknowledgement

The presented research is undertaken on the basis of results and conclusions obtained during international research project Precobeam financed by European Commision (RFCS). Thus, the authors representing Dept. of Civil Engineering of Wrocław University of Technology appreciate the work of all partners involved in Precobeam [15] established as a state-of-the-art and starting point for current research. Especially, the input of Jacques Barthellemy from SETRA concerning fatigue has great importance for current research. Cooperation with Guenter Seidl from SSF Ingenieure conducting research concerning fatigue behaviour of composite dowels at spring 2010 in Germany together with professor Mensinger from TU Muenchen is also acknowledged.

The work is realized in the frame of MNiSW national project no. 2502/B/T02/2009/37. Financial support of MNiSW of the Polish government is gratefully acknowledged.

References

[1] Berthellemy J., Hechler O., Lorenc W., Seidl G., Viefhues E.: *Premiers résultats du projet de recherche européen Precobeam de connexion par découpe d'une tôle*, Construction métallique, Vol. 46, No. 3, 2009, pp. 3–26.

[2] Berthellemy J., Lorenc W., Mensinger M., Ndogmo J., Seidl G.: *Zum Tragverhalten von Verbunddübeln, Teil 2: Ermüdungsverhalten*. Stahlbau, Vol. 80, No. 4, 2011, pp. 256–267.

[3] Berthellemy J., Lorenc W., Mensinger M.R., Seidl G.: *Zum Tragverhalten von Verbunddübeln.Teil 1: Tragverhalten unter statischer Belastung*. Stahlbau, Vol. 80, No. 3, 2011, pp. 172–184.

[4] Bobyr M., Yakhno B., Rusinski E., Harnatkiewicz P.: *Damage in the complex low-cycle fatigue*, Archives of Civil and Mechanical Engineering, Vol. 8, 2008, pp. 23–31.

[5] Budka E., Lorenc W., Rabiega J.: *Causes of cracks and the realized repair of main girder of steel railway viaduct*, Steel bridges: advanced solutions & technologies, 7th International Conference on Steel Bridges, Conference proceedings, [Eds] Paulo J.S. Sruz, Luis Simoes da Silva, Falko Schroter, Guimaraes, Portugal, 4–6 June, 2008, Brussels: ECCS-European Convention for Constructional Steelwork, 2008, pp. 301–307.

[6] Dudziński W.: *Metalographic inspection of part of welded steel structure damaged after strength tests* (in Polish), Report of Institute of Material Engineering and Technical Mechanics, Wrocław University of Technology, Wrocław, 2008.

[7] EN 10025-4:2004.

[8] Frydman S., Konat Ł., Pękalski G.: *Structure and hardness changes in welded joints of Hardox and HTK steels*, Archives of Civil and Mechanical Engineering, Vol. 8, 2008, pp. 15–27.

[9] Harnatkiewicz P., Kopczyński A., Kożuch M., Lorenc W., Rowiński S.: *Research on fatigue cracks in composite dowel shear connection*, Engineering Failure Analysis, Vol. 18, 2011, pp. 1279–1294.

[10] Hechler O., Berthellemy J., Lorenc W., Seidl G., Viefhues E.: *Continuous shear connectors in bridge construction*, ASCE Conf. Proc., Vol. 396, No. 7, 2008, DOI:10.1061/41142.

[11] Kubica E., Rykaluk K., Lorenc W., Kożuch M.: *Cutting of T-section from rolled beams in aspect of realisation composite girders* (in Polish), Composite bridge structures, Kraków, 2009, pp. 289–300.

[12] Lorenc W., Ignatowicz R., Kubica E., Seidl G.: *Numerical model of shear connection by concrete dowels*, Recent Developments in Structural Engineering Mechanics and Computation, Millpress, 2007, Rotterdam, Netherlands, pp. 1139–1144.

[13] Lorenc W., Kubica E., Kożuch M.: *Testing procedures in evaluation of resistance in innovative shear connection with composite dowels*, Archives of Civil and Mechanical Engineering, Vol. 10, No. 3, 2010, pp. 51–63.

[14] Lorenc W.: *Boundary approach in shape study of composite dowel shear connector*, Wrocław, Archives of Civil and Mechanical Engineering, Vol. 9, 2009, pp. 55–66.

[15] Preco-Beam: *Prefabricated enduring composite beams based on innovative shear transmission* RFSR-CT-2006-00030, Final report. Project carried out with the financial grant of the Research Programme of the Research Fund for Coal and Steel, 2009.

[16] Seidl G.: *Behaviour and load bearing capacity of composite dowels in steel-concrete composite girders*, Report PRE 4.2009, Doctoral Thesis, Wrocław University of Technology, 2009.

Analiza pęknięć zmęczeniowych w łącznikach zespalających typu *composite dowel*

W ostatnich latach przeprowadzono wiele badań dotyczących belek zespolonych z ciągłymi łącznikami otwartymi typu *composite dowels* oraz zaprojektowano i wybudowano innowacyjne obiekty stosując omawiane łączniki. Ze względu na adresowanie tego typu zespolenia przede wszystkim do budownictwa mostowego istotnym okazuje się problem zmęczenia. Bardzo złożony problem zmęczenia w łącznikach zespalających jest wynikiem nie tylko skomplikowanego stanu naprężeń w łączniku od obciążeń zewnętrznych, ale również wpływami naprężeń walcowniczych, które zostają uwolnione podczas rozcinania kształtowników oraz wpływem samego cięcia i przygotowania powierzchni. W artykule przedstawiono analizę pęknięć zmęczeniowych biorąc pod uwagę aspekty technologiczne wytwarzania części stalowej belki zespolonej oraz przedstawiono plan dalszych badań przybliżających autorów do rozwiązania problemu żywotności rozważanych belek zespolonych w aspekcie projektowania na podstawie aktualnych norm.

ARCHIVES OF CIVIL AND MECHANICAL ENGINEERING

Vol. XI 2011 No. 4

Spool valve leakage behaviour

D. GORDIĆ, M. BABIĆ, D. MILOVANOVIĆ, S. SAVIĆ
University of Kragujevac, Faculty of Mechanical Engineering, Sestre Janjic 6, 34000 Kragujevac, Serbia.

A four-way axial spool servovalve has such a design that flows through its restrictions can be presented by means of a hydraulic bridge. The characteristics analytically describe the fluid flow through spool orifices in the most of working regimes. The exceptions are regimes around the null characterised by an overlap existence when internal leakages dominate. Several mathematical models for the calculation of the internal leakage flows are presented in this paper including theoretical model worked out by authors. Modelling results are compared with appropriate experimental.

Keywords: *spool valve, leakage*

1. Introduction

Theoretical, ideal stationary characteristics of spool control valves that include the following assumptions: no volumetric losses, equal and symmetrical spool orifices, turbulent flow regime through the spool orifices, equal zero lap conditions on all spool orifices are presented in detail in standard literature [1–2]. Mentioned mathematical expressions describe the characteristics of working fluid flow through axial spool valve orifices in the most of working regimes. The exceptions are the working regimes characterised by the existence of overlap where fluid flows between the spool and bushing (valve body) significantly affect the valve behaviour. In these regimes the mentioned characteristics does not precisely describe the flow of working fluid through the spool valve orifices. Therefore, models of the valve for the regimes should include additional terms for the flow of internal leakage. This internal leakage flow is one of the key parameters in designing the precise positioning of the hydraulic actuator. Due to the internal leakage, pressure difference on hydraulic load exists, which affects the behaviour of the system in several ways: crawling of a loaded actuator in open loop systems, position error of a P-controlled loaded actuator and increase of the system damping [2].

2. Mathematical models of internal leakage flow

Following equations:

$$Q_{L1} = Q_{t1} - Q_{t4} + Q_{l1} - Q_{l4}, \tag{1}$$

$$Q_{L2} = Q_{t3} - Q_{t2} + Q_{l3} - Q_{l2}, \tag{2}$$

can be written using denotes in Figure 1, where:

- Q_{L1} [m^3/s] – volumetric flow through the right actuator port,
- Q_{L2} [m^3/s] – volumetric flow through the left actuator port,
- Q_{li} [m^3/s] – internal leakage volumetric flow through i-th spool orifice, i = (1, 2, 3, 4),
- Q_{ti} [m^3/s] – volumetric flow through i-th spool orifice, i = (1, 2, 3, 4),

Volumetric flow through i-th spool orifice can be calculated as:

$$Q_{ti} = \begin{cases} Q_{ti} & x \cdot (-1)^{i+1} \geq x_{0\,i} \\ 0 & x \cdot (-1)^{i+1} < x_{0\,i} \end{cases} \text{ and } Q_{li} = \begin{cases} 0 & x \cdot (-1)^{i+1} \geq x_{0\,i} \\ Q_{ti} & x \cdot (-1)^{i+1} < x_{0\,i} \end{cases}, \tag{3}$$

where x [m] – spool displacement, x_{0i} [m] – null lap condition of i-th spool orifice.

Several mathematical models for the calculation of the internal leakage flow through a spool orifice can be found in literature [3–5]. It is necessary to know the experimental spool valve static characteristics for their use.

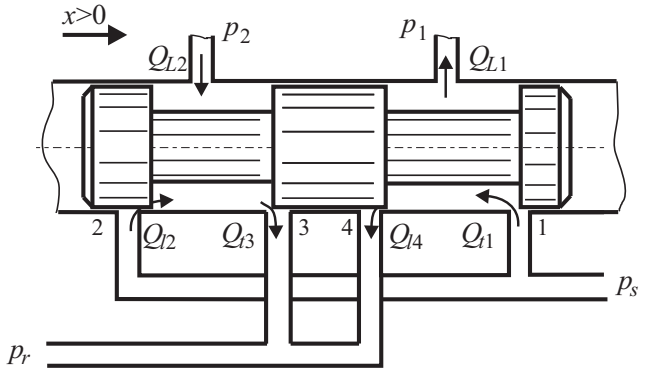

Fig. 1. Analysis of internal leakage flow through axial spool valve

Ellman & Virvalo presented the model which assumed laminar leakage flow and symmetric valve configuration [2]. The model also assumes small positive or zero overlap for each orifice. It is valid only for small positive spool displacements limited to approximately 2% of maximal spool displacement. The authors propose that internal leakage flow should be calculated according to:

$$Q_{li} = \frac{Q_{l0}}{2 \cdot p_s} \cdot \left(1 - \frac{x}{x_a} \operatorname{sgn}(x)\right) \cdot \Delta p_i, \quad Q_{li} \geq 0, \tag{5}$$

where:

– Q_{l0} [m^3/s] – internal leakage flow at null (zero spool displacement),

– p_s [Pa] – supply pressure,

– x_a [m] – relative opening of the spool where the load pressure equals supply pressure,

– $Q_{L\max}$ [m^3/s] – nominal volumetric flow through the valve (measured at full opening – max spool displacement $x_{\max}$ and supply pressure p_s).

and where (using denotes on Figure 1) pressure difference on each spool orifice Δp_i can be written as:

$$\Delta p_{ti} = \begin{cases} p_s - p_1, & i = 1 \\ p_s - p_2, & i = 2 \\ p_2 - p_r, & i = 3 \\ p_1 - p_r, & i = 4 \end{cases}, \tag{6}$$

where:

– p_r [Pa] – atmospheric (reservoir) pressure,

– p_1 [Pa] – pressure in right actuator chamber,

– p_2 [Pa] – pressure in left actuator chamber.

According to the model, flow through *i*-th spool orifice is:

$$Q_{ti} = \frac{Q_{l0}}{2 \cdot p_s} \cdot \left(1 + \frac{x}{x_a} \cdot \operatorname{sgn}(x) \right) \cdot \Delta p_i + x \cdot \frac{Q_{L\max}}{\sqrt{p_s}} \cdot \sqrt{\Delta p_i}, \tag{7}$$

Values for Q_{l0}, x_a and $Q_{L\max}$ can be obtained from the valve experimental static characteristics (Figure 2).

Ellman presented an improved model that can include a valve asymmetry [1]. Unlike the previous, the model provides a ”smooth” transition from the internal leakage flow to flow through the spool orifice. According to the model, internal leakage flow can be written as:

$$Q_{li} = \frac{k_{EL2}}{2} \left[\sqrt{\left(\frac{k_{EL2}}{k_{EL1}} \right)^2 x^2 + 4\Delta p_i} - \frac{k_{EL2}}{k_{EL1}} x \right], \tag{8}$$

In addition to static pressure gain characteristic, it is necessary to know experimental curves of flow characteristics for both actuator ports to determine the parameters k_{EL1} and k_{EL2}. For obtaining the mentioned curves non-standard measurements are required and therefore this model was omitted from further analysis due its complexity for practical application.

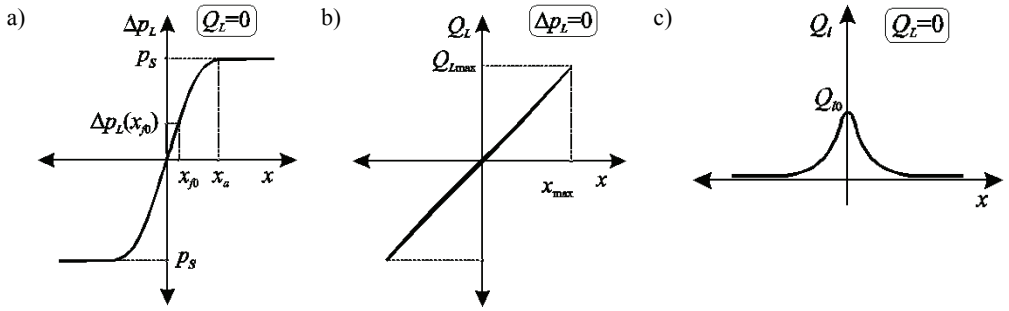

Fig. 2. Static characteristics of axial spool valve a) pressure gain characteristic, b) no-load static flow characteristic, c) internal leakage flow characteristic

Eryilmaz & Wilson presented the model where the internal leakage flow is turbulent, whereby the cross-section area is inversely proportional to the length of the overlap between the spool and the body of the valve [3]. The model only assumes valve with zero overlap in null and it is valid for all possible spool positions. The authors suggest that the internal leakage flow can be calculated by:

$$Q_{li} = K_{EWi} \cdot \sqrt{\Delta p_i} \cdot \frac{x_{f0i}^2}{x_{f0i} + k_{EWi} \cdot x}, \tag{9}$$

where the flow through the orifice is:

$$Q_{ti} = K_{EWi} \cdot \sqrt{\Delta p_i} \cdot (x_{f0i} + x), \tag{10}$$

where the term x_{f0i} [m] denotes "fictive overlap" of i-th orifice. This parameter takes into account turbulent leakage flow at zero spool displacement. It should be mentioned that x_{f0i} corresponds to a spool displacement that would result in the same amount of flow in a non-leaking valve as the leakage flow rate in a leaking valve with zero lap at null.

For valves with symmetric and matched spool orifices, parameters K_{EWi}, k_{EWi} and x_{f0i} are equal for all orifices so subscript i can be omitted. In this case, the parameters can be determined from the experimental static characteristics (Figure 2) according to:

$$K_{EW} = \frac{Q_{L\max} \cdot \sqrt{2}}{\sqrt{(p_s - p_r)} \cdot x_{\max}}, \tag{11}$$

3. Theoretical mathematical model of internal leakage flow

The authors of the paper propose usage of a mathematical model in which all parameters are physical quantities. The model is based on theoretical analysis performed by Mookherjee et al. [6]. This model includes pressure-flow relations for the

following orifices: short (based on inflow and outflow along the spool edge), intermediate (based on boundary layer analysis of steady, incompressible developing flow) and long (based on fully developed steady laminar flow through an annular orifice). As a result, the group of implicit equations for internal leakage flow determination is obtained [4]:

$$\begin{aligned}
&q \cdot Q_{li}^2 = \Delta p_i \quad \text{for } \left| x \cdot (-1)^{\mathrm{i}} + x_{0i} \right| < (q/s)^2 \cdot Q_{li}, \\
&s \cdot \left| x \cdot (-1)^{\mathrm{i}} + x_{0i} \right|^{1/2} \cdot Q_{li}^{3/2} = \Delta p_i \quad \text{for } (q/s)^2 \cdot Q_{li} \le \left| x \cdot (-1)^{\mathrm{i}} + x_{0i} \right| < x_{tli}, \\
&s \cdot x_{tli}^{1/2} \cdot Q_{li}^{3/2} + w \cdot \left(\left| x \cdot (-1)^{i} + x_{0i} \right| - x_{tli} \right) \cdot Q_{li} = \Delta p_{\mathrm{i}} \quad \text{for } \left| x \cdot (-1)^{\mathrm{i}} + x_{0i} \right| \ge x_{tli},
\end{aligned} \tag{14}$$

where:

- $q = \dfrac{\rho}{2 \cdot K_{ti}^2 \cdot f^2 \cdot (\sqrt{(\delta + h)^2 + h^2} - h)^2 \cdot \delta^2}$,
- $s = \dfrac{23 \cdot (\rho \cdot \eta)^{1/2}}{f^{3/2} \cdot \delta^{5/2}}$, and $w = \dfrac{12 \cdot \eta}{f \cdot \delta^3}$,

and where:

- ρ [kg/m^3] – fluid density,
- η [Pa·s] – fluid dynamic viscosity,
- K_{ti} [–] – flow coefficient of i-th spool orifice,
- f [m] – spool valve area gradient,
- δ [m] – spool in bushing radial clearance,
- h [m] – sum of radiuses of bushing and spool control edges.

In Equation (14) the term x_{tli} [m] denotes large transition length. It presents the distance from the entrance at which boundary layers on spool and bushing meet at the mid-plane. It can be obtained as:

$$x_{tli} = \frac{0.075 \cdot \delta \cdot Q_{li}}{\pi \cdot d_s \cdot \nu}, \tag{15}$$

where ν [m^2/s] is fluid kinematic viscosity nad d_s [m^2/s] is spool diameter.

Considering the spool in bushing radial clearance, round corners of control edges and lapping conditions of spool orifices the volumetric flow through i-th spool valve orifice can be written as:

$$Q_{ti} = K_{ti} \cdot f \cdot \sqrt{(\delta + h)^2 + [(x - x_{0i} \cdot (-1)^{i+1}) + h]^2} - h) \cdot \sqrt{\frac{2}{\rho}} \cdot \sqrt{\Delta p_i}. \tag{16}$$

4. Comparative analysis of the models

In order to determine the accuracy of proposed models for internal leakage flow calculation, the results of numerical calculation should be compared with appropriate experimental results. Estimation of model accuracy was done by comparing the numerical results obtained using the software package Matlab, with experimental pressure gain and internal leakage flow characteristics of servovalve B.31.210.12.1000.U2V, produced by PPT, Trstenik, Serbia (Figure 3).

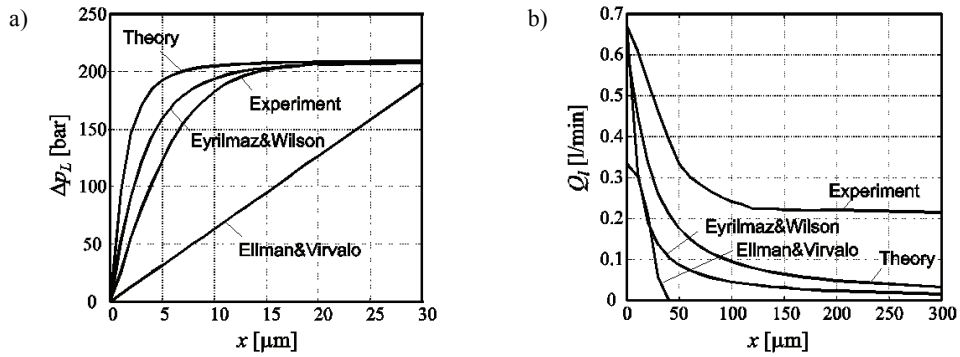

Fig. 3. Comparative review of a) pressure gain and b) internal leakage characteristics

The values of quantities and parameters used in numerical simulation are presented in Table 1.

Table 1. Initial date for numerical calculations

Symbol	Value	Unit
p_s	210	bar
p_r	0	bar
ρ	871	kg/m^3
ν	$14 \cdot 10^{-6}$	m^2/s
η	0,012	Pa s
d_s	4,62	mm
f	2·2.4	mm
h	20	μm
δ	4	μm

Symbol	Value	Unit
x_{0i}	0	mm
K_t	0.611	–
Q_{l0}	0.672	l/min
x_a	33	μm
Q_{Lmax}	12	l/min
x_{max}	0.5	mm
K_{EW}	$1.237 \cdot 10^{-4}$	m^2·s^{-1}·Pa$^{-0.5}$
k_{EW}	2.793	–
x_{f0}	0.7	μm

Static experimental analyses of the servovalve were performed on the standard servovalve testing equipment MOOG-PLOTTERSTAND D046-030 (Figure 4).

It can be noticed that pressure gain characteristic calculated by the Ellman & Virvalo model by its trend completely deviates from the experimentally determined characteristic. Pressure gain characteristic determined with proposed theoretical model gives somewhat higher values then values obtained by Eryilmaz &Wilson model and experimental until saturation.

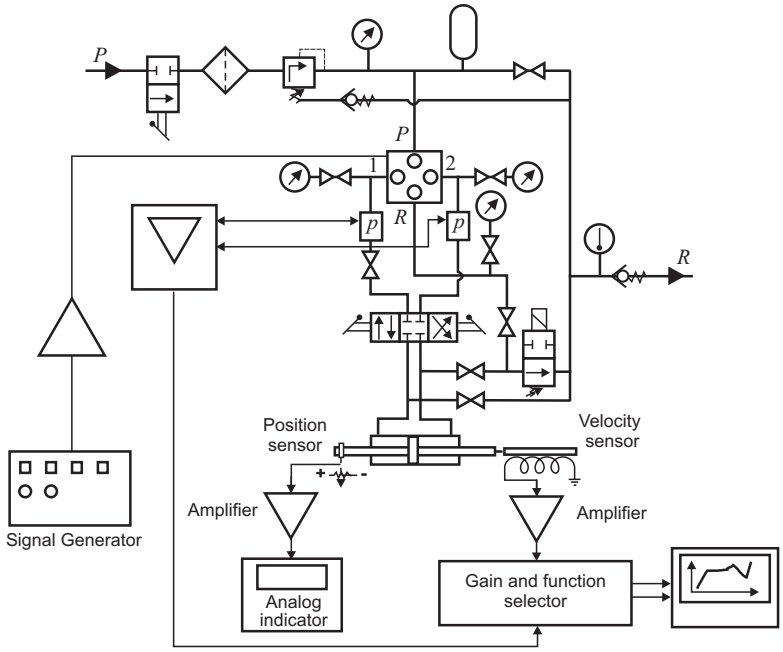

Fig. 4. Experimental test stand for static experimental analyses

Internal leakage characteristics obtained using Ellman & Virvalo model qualitatively follows experimentally obtained curve for small positive spool displacements limited to approximately 2% of maximal spool displacement as it was denoted in chapter 2. For bigger spool displacements it has negative values. This interval was not shown in Figure 3 because of compliance with graphical presentations of other methods. Internal leakage characteristics obtained using Eyrilmaz & Wilson model and the theoretical one by its trend correspond to experimental. They have the same values as experimental at null, but for other possible spool positions they had lover values. It is important to emphasize that in regimes with relative big spool displacements orifice flows dominates instead of leakage flows, so the mentioned difference does not have significant influence on valve flow characteristics.

5. Conclusion

Fluid flows between the spool and bushing (internal leakage flows) in working regimes characterised by the existence of overlap principally affect the valve behaviour. Several models for the calculation of internal leakage flow in axial spool valve can be found in relevant literature. The use of these models is limited to the knowledge of experimental static characteristics of a valve. The best result compared to experimental characteristics provides the model proposed by Eryilmaz and Wilson. The theoretical model presented in the paper, based on the valve geometry and physical properties

of working fluid, correctly predicts the internal leakage flow rates. It may present a good basis for predicting the behaviour of axial spool valve in regimes close to spool zero position. Since all its parameters are easily determinable physical quantities it can be a useful design tool.

References

[1] Ellman A.: *Leakage behaviour of four-way servovalve*, Proceedings of the ASME Fluid Power Systems and Technology, Vol. 5, 1998, pp. 163–167.
[2] Ellman A., Virvalo T: *Formation of pressure gain in hydraulic servovalves and its significance in system behavior*, Proceedings of the ASME Fluid Power Systems and Technology, Vol. 3, 1996, pp. 77–81.
[3] Eryilmaz B., Wilson B.H.: *Combining leakage and orifice flows in a hydraulic servovalve model*, Journal of Dynamic Systems, Measurement and Control, Vol. 122, No. 3, pp. 576–579.
[4] Gordić D., Babić M., Jovičić N.: *Modelling of spool position feedback servovalves*, International Journal of Fluid Power, Vol. 5, No. 1, 2004, pp. 37–50.
[5] Merritt H.: *Hydraulic control systems*, John Wiley & Sons, New York, 1967.
[6] Mookherjee J.L., et al.: *Static-performance based computer-aided design of a DDV and its sensitivity analyses*, International Journal of Fluid Power, Vol. 2, No. 2, 2001, pp. 47–63.
[7] Watton J.: *Modelling, monitoring and diagnostic techniques for fluid power systems*, Springer-Verlag, London, 2007.

Model teoretyczny wyznaczania wewnętrznych przecieków w rozdzielaczu hydraulicznym

Czterodrogowy rozdzielacz hydrauliczny ma budowę, w której przepływ przez jego kanały może być przedstawiony (opisany) za pomocą tzw. mostku hydraulicznego. Z reguły charakterystyki zaworu opisują przepływ cieczy przez szczeliny dla większości stanów jego pracy. Wyjątkiem są stany pracy, w których dominują wewnętrzne przecieki. W pracy przedstawiono modele matematyczne do obliczeń wewnętrznych przecieków. Przedstawiono propozycję modelu teoretycznego opracowanego przez autorów. W pracy przedstawiono również porównanie wyników badań symulacyjnych z odpowiednimi badaniami eksperymentalnymi.

ARCHIVES OF CIVIL AND MECHANICAL ENGINEERING

Vol. XI 2011 No. 4

Stable algorithm to simulate dynamic undercarriage loads of tracked vehicles

J. HARTLEB
Münster University of Applied Sciences – Faculty of Mechanical Engineering, Germany.

M. KETTING
IBAF – Institut für Baumaschinen, Antriebs- und Fördertechnik GmbH Bochum and Department of Mechanical Engineering at Ruhr-University Bochum, Germany.

The loads acting on the undercarriage of a tracked vehicle are composed from multiple operation situations which result in dynamic loads. These loads are influenced by different variables and also combinations of these. Within this paper a method is described to simulate the loads acting on the undercarriage taking into consideration the multitude of critical combinations of influencing variables. Priority is given to the description of a calculation algorithm which allows to dynamically simulate how an excavator runs over an obstacle considering numerous parameters like obstacle height, running speed, track deformation and response behaviour of the overall system.

Keywords: *construction equipment, dynamic simulation, loads on tracked vehicle, lumped mass model*

1. Complex load and boundary conditions of the undercarriage system

The running gear of an undercarriage of a tracked vehicle is in interaction with the upper structure and soil systems which are connected with the undercarriage through interfaces of the rotary joint and the track (Figure 1).

Fig. 1. Crawler excavator in operation

The loads acting on the undercarriage are composed of loads from operations like digging, pulling, grabbing, turning and mass forces mainly initiated by travelling motions. While the operational loads may quasi-statically be defined rather precisely by means of maximum cylinder forces and positions, the determination of mass and inertia forces is more complex [8]. They form dynamic load curves which mainly depend on the following factors:

- Running speed v,
- Soil properties:
  Soil profile: $h(x)$
  Friction angle: φ
  Cohesion: c
  Density: γ
- Specific resistance: k_S
- Roller arrangement a_{Lfr}.

Mass and stiffness distribution of upper structure and undercarriage.

This provides a multitude of critical combinations of influencing variables which are to be analyzed for their effects on the loading of the undercarriage so that construction machinery can be designed according to specific operating requirements.

Though fundamental questions of operational behaviour, lifetime and wear mechanisms are substantiated by empirical values, these values must constantly be verified while simultaneously the structural components are subject to continuous improvements. This is only possible by measurements on original vehicles or by computer simulation. As comprehensive series of measurements, in particular on construction machinery, present a considerable cost factor (expenditure and non-productive time during measurements), the use of a computer is indispensable.

2. Calculation of dynamic system loads

To support design criteria, empiricism shall be replaced by analysis. Subject of the subsequent explanations is a method to simulate the loading process under consideration of the above mentioned influencing variables. In addition to the interactions already discussed in [6], priority is given here to the description of the algorithm for the calculation of the lumped-mass model. In connection with an exemplary application, the load curves resulting from the dynamics are analyzed for their major influencing variables. Based on that, the causes of the impact and vibration factors which are characteristic for the operational behaviour may be determined [3].

3. Generation of a specific simulation algorithm

The focal point of the structure-dynamic problem is the vibratory model of a track-type undercarriage which is influenced by geometric and dynamic initial and boundary conditions. The significant path excitation generated when running over an obstacle

can be defined as path function over a time-variant track curve. Due to the interactions between running gear, track and soil, it is recommended to use an iterative time-increment procedure for this purpose. This is described in detail in [5].

The corresponding flow chart represents the sequence of main modules of the algorithm for the calculation of the forces (here roller loads) of a time increment.

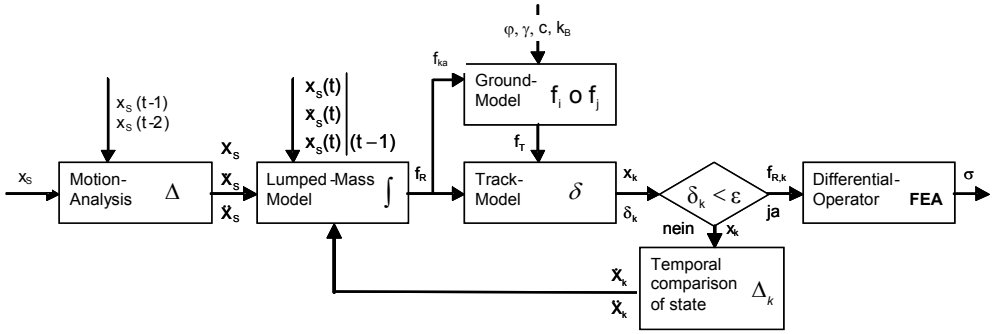

Fig. 2. Flowchart for the calculation of dynamic forces and stresses for a time increment [6]

The chart illustrates the interaction between kinematics, structural dynamics, soil mechanics and strength (not subject of this article):

3.1. Motion analysis (Δ)

The kinematic values $x, \dot{x}, \ddot{x}$ resulting from the motion analysis indicate the excitation for the structural model (e.g. lumped-mass model) which delivers the resulting roller loads f_R. Together with the traction forces $f_T = f\,(c, j, g, k_S, f_{Ka})$ calculated by means of the ground model, they generate the shape x_k of the track curve whereby the path excitation x of the roller supported at this moment at point x_R is calculated by numerical differentiation on the basis of two previous values:

$$\begin{aligned} x(Lfr) &= x_k(x_R, t), \\ \dot{x}(Lfr) &= \frac{x_k(x_R, t) - x_k(x_R, t-1)}{\Delta t}, \\ \ddot{x}(Lfr) &= \frac{x_k(x_R, t) - 2x_k(x_R, t-1) + x_k(x_R, t-2)}{\Delta t^2}. \end{aligned} \tag{1}$$

(The reverse differentiation quotient requires two previous time increments).

In this way the dynamic boundary conditions $x_1, \dot{x}_1, \ddot{x}_1$ are known in the partitioned equation system of the lumped-mass model:

(Indices 1: known path variables, 2: searched path variables, R: roller, a: external)

$$\begin{vmatrix} \mathbf{M_{11}} & 0 \\ 0 & \mathbf{M_{11}} \end{vmatrix} \begin{vmatrix} \ddot{x}_1 \\ \ddot{x}_2 \end{vmatrix} + \begin{vmatrix} \mathbf{D_{11}} & \mathbf{D_{12}} \\ \mathbf{D_{21}} & \mathbf{D_{22}} \end{vmatrix} \begin{vmatrix} \dot{x}_1 \\ \dot{x}_2 \end{vmatrix} + \begin{vmatrix} \mathbf{K_{11}} & \mathbf{K_{11}} \\ \mathbf{K_{21}} & \mathbf{K_{22}} \end{vmatrix} \begin{vmatrix} x_1 \\ x_2 \end{vmatrix} = \begin{vmatrix} f_1 \\ f_2 \end{vmatrix} = \begin{vmatrix} f_R \\ f_a \end{vmatrix}. \tag{2}$$

So partitioning was done according to path excitation $x_1, \dot{x}_1, \ddot{x}_1$ and force excitation f_a.

3.2. Integration of the lumped-mass model

The matrixes **M** and **K** in Equation (2) are the result of system discretization according to element catalogues [11], applicable to the lumped-mass model [12], for diagonal matrixes (**M**) and band matrixes (**K**). With an assumed viscous material damping (no active dampers on the undercarriage), a damping system is used which is proportionate to the stiffness to keep the lower effective frequencies. This gives the following damping matrix:

$$\mathbf{D} = \frac{2\xi_{\min}}{\omega_{\min}} \cdot \mathbf{K}, \tag{3}$$

where:

$\xi_{\min}$ – Lehr's damping measure of basic vibration given in the tables,

$\omega_{\min}$ – fundamental frequency of the non-damped system from vector iteration.

The external forces f_a are basically restricted to the known weight of the lumped masses. Vectors $x_2, \dot{x}_2, \ddot{x}_2$ are calculated by means of a direct, implicit single-step integration procedure with unconditional stability.

For that purpose the considered procedures according to *Wilson-Θ-* and *Newmark-β-γ* [2, 7] were compared with each other. The major difference is in the respective assumptions of the acceleration curve $\ddot{x}(t)$ during Δt as demonstrated in Figure 3.

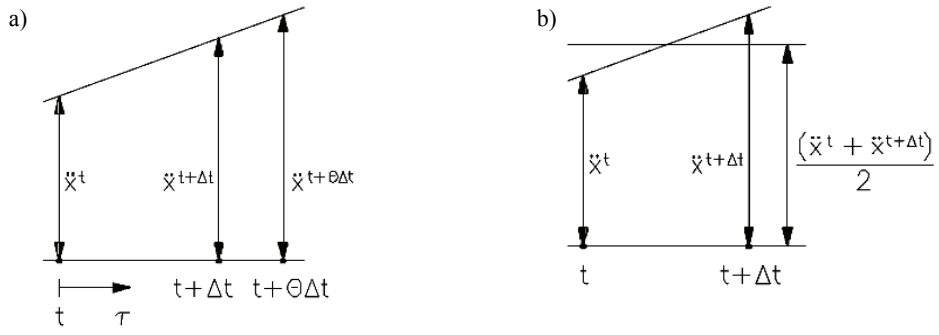

Fig. 3. Basic values for integration according to: a) Wilson, b) Newmark

Newmark assumes a constant average acceleration while Wilson proceeds from a linear acceleration. Since however the assumption of a linear acceleration function over a period Δt only leads to a conditional stability, Wilson assumes a linear behaviour over a time $\tau = \Theta \cdot \Delta t$ with $\Theta \geq 1.37$ to achieve an unconditional stability. The searched variables of solution for Δt are derived from that by interpolation.

The Wilson-Θ-method has the disadvantage that it eliminates both wrong vibration frequencies caused by an excessive increment but also correct higher vibration frequencies as a consequence of which only the lower natural frequencies are integrated correctly while other system behaviours are neglected [4]. Even when considering further properties, the Newmark-β-γ method proved to be more suitable in particular from the computing point of view. The test functions are:

$$\begin{aligned} \dot{x}(t) &= \dot{x}(t-\Delta t) + \left[(1-\gamma)\ddot{x}(t-\Delta t) + \gamma \ddot{x}(t)\right]\Delta t, \\ x(t) &= x(t-\Delta t) + \dot{x}(t-\Delta t)\Delta t + \left[\left(\frac{1}{2} - \beta\right)\ddot{x}(t-\Delta t) + \beta \ddot{x}(t)\right]\Delta t^2 \end{aligned} \tag{4}$$

with $\gamma = ½$ and $\beta = ¼$ for unconditional stability (proof, see [5]).

As each partial equation i of an equation system like the present one requires a different step size Δt_i, the relevant modal forms are integrated in the period with varying error. Low natural frequencies ω_i, for instance, require small step sizes Δt_i for accurate results. If unconditionally stable algorithms induce the assumption of big step sizes, there is a risk of very high errors at high natural frequencies.

To stipulate a suitable time step size (increment) Δt for Equation (4), it is therefore necessary to assess the maximum natural frequency of the considered system. Assuming that the natural behaviour of the damped system differs only insignificantly from that of the non-damped system, the following natural value function is to solve to determine a suitable time increment:

$$\left[\omega^2 M - K\right] x = 0. \tag{5}$$

For a numerical solution, the vector iteration is used:

$$M x^{(k+1)} = K x^{(k)}. \tag{6}$$

Inserting its solution $x(k)$ and/or $x(k + 1)$ in Schwarz' constant delivers an upper bound for the natural frequencies:

$$\omega_{\max}^{(k)} = \sqrt{\frac{x^{(k)T}\, K\, x^{(k)}}{x^{(k)T}\, M\, x^{(k)}}} = \sqrt{\frac{x^{(k)T}\, M\, x^{(k+1)}}{x^{(k)T}\, M\, x^{(k)}}}, \tag{7}$$

with $k = 1, ..., n$ and n – number of iteration loops.
So the increment suitable for integration according to Newmark results from the function (see Table 1 given in [1]):

$$\Delta t = \frac{\vartheta}{\omega_{\max}^{(n)}}; \qquad e.g.\ \Delta t = \frac{0.6}{\omega_{\max}^{(n)}}. \tag{8}$$

Table 1. Increment bounds with regard to stability (($\vartheta_{\lim}$) and accuracy (($\vartheta_{1\%}$, $\vartheta_{3\%}$), Argyris

$\beta, \gamma = 0.5$	$\vartheta_{\lim} = \omega_{\max} \Delta t$	$\vartheta_{1\%}$	$\vartheta_{3\%}$
0 (explicit)	2.0	0.48	0.83
0.09	2.5	1.68	2.00
0.10	2.58	2.05	2.25
0.15	3.16	0.55	0.98
0.167 (linear)	3.46	0.48	0.87
0.25 (average)	∞	0.35	0.60

3.3. Soil model (f_i o f_j)

With the first solution for f_R in Equation (2), the traction force f_T absorbed by the soil is calculated according to Rankine's and Terzaghi's earth pressure theory [10]. Figure 4 shows the interaction between the roller load – supposed as linear line load – for each track link and the resulting traction force per track link bar f_{TK} against the friction angle.

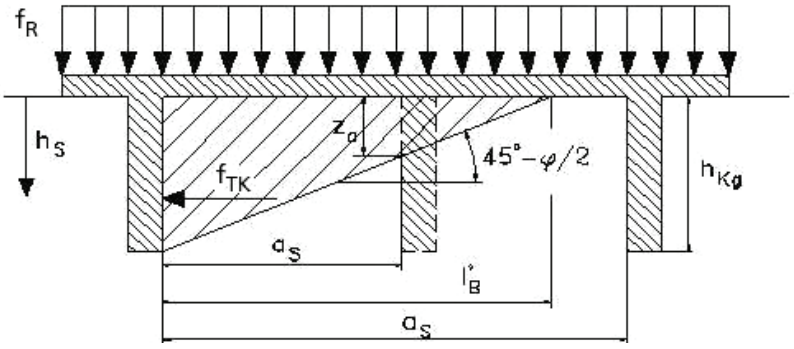

($f_T = \Sigma f_{TK}$)

Fig. 4. Resulting traction force at track link bar

This force influences the geometry of the track curve and in this way provides a new input variable for the second calculation of f_R [9].

From the local components of roller load and traction force, the geometric track curve is iteratively developed. Only if the track curve x_K reaches a value below a defined limit E:

$$\lim_{\delta_K \to \varepsilon} \quad f(\delta_K) = x_K ,$$

the roller load resulting from the track-soil-interaction f_R is recorded for this time step and the calculation continues with the next time step.

4. Summary and prospect

Due to the application of an iterative time-increment procedure, it was possible to dynamically simulate how an excavator runs over an obstacle taking into consideration numerous parameters like obstacle height, running speed, track deformation and response behaviour of the overall system. For that purpose the track curve is adapted for each time increment to the current running condition up to a stop criterion ε and used as new path variable for the path excitation of the system. To shorten the computing time, a direct, unconditionally stable working integration algorithm is used which was adjusted by two parameters, i.e. Newmark's β-γ algorithm.

The program was applied in form of simulation runs with crossing of a defined obstacle and the variation of running speed and obstacle height. In addition to a qualitative increase of the dynamic load factor, it was also possible to obtain quantitative information on the considered running gear loads. So an increase of speed by 59% led to an increase of the dynamic amplitude (raising of static roller loads) by at last 55%. Doubling the obstacle height resulted in a dynamic raising of 30%.

For a systematic development concept of track-type undercarriages, the presented algorithm could be combined with modules to describe other operating conditions (turning, working with attachments, etc.). Controlled by a framework program, operating loads could be recorded, standardized and classified for any complete working cycle in this way.

References

[1] Argyris J.: Mlejnek H.-P.: *The method of finite elements in elementary structural mechanics*, Part 3, Introduction into Dynamics, Viehweg & Sohn, Braunschweig, 1988.

[2] Bathe K.-J.: *Finite element procedures in engineering analysis*, Prentice-Hall, Inc., Englewood Cliffs, New Jersey 07632, 2002.

[3] Dresig H., Holzweißig F.: *Dynamics of machines*, Springer Verlag, 9th Edition, Berlin, 2009.

[4] Dukkipati R.V., Rao M.A., Bhat R.: *Computer aided analysis and design of machine elements*, New Age International, Pvt Ltd Publishers, 2nd Edition, New Delhi, 2007.

[5] Hartleb J.: *Dynamic wheel loads of unsuspended tracked vehicles, taking into account structure-specific properties*, Series of the Institute for Design Engineering at Ruhr-University Bochum, Book 97.5.

[6] Hartleb J., Ketting M.: *Simulation of dynamic undercarriage loads resulting from interactions between excavator and soil* (in preparation), Journal of Terramechanics, published on behalf of The International Society for Terrain-Vehicle Systems.

[7] Klein B.: *FEM – Fundamentals and applications of the finite element method in mechanical and vehicle-engineering*, 6th Edition, 2005.
[8] Magnus K., Popp K.: *Oscillations*, 8th Edition, Vieweg+Teubner Verlag, Wiesbaden, 2008.
[9] Rankine W.J.M.: *On the stability of loose earth*, Philosophical Transactions of the Royal Society of London, Vol. 147, 1857.
[10] Terzaghi K., Peck R.B., Mesri G.: *Soil mechanics in engineering practice*, 3rd Edition, John Wiley & Sons, Inc., New York, 1996.
[11] Waller H., Krings W.: *Methods for matrices of machine- and building dynamics*, B.I.-Wissenschaftsverlag, Zürich, 1975.
[12] Waller H., Schmidt R.: *Vibration studies for engineers*, Springer-Verlag, Berlin, 1989.

Stabilny algorytm do symulowania dynamicznych sił występujących w podwoziu pojazdu gąsienicowego

Siły działające na podwozie pojazdu gąsienicowego są wynikiem jego złożonych działań. Siły te są spowodowane przez różne zmienne i ich kombinacje. W artykule została opisana metoda symulacji sił działających na podwozie, uwzględniając różne kombinacje krytycznych parametrów. Sprawą nadrzędną było opisanie algorytmu, który pozwala modelować dynamicznie pokonywanie przez koparkę przeszkód biorąc pod uwagę różne parametry takie jak: wysokość przeszkody, prędkość pojazdu, jego deformację.

ARCHIVES OF CIVIL AND MECHANICAL ENGINEERING

Vol. XI 2011 No. 4

Strength analysis of the kinematic pairs of a mobile collapsible bridge

A. ILUK, E. RUSIŃSKI
Institute of Machines Design and Operation, Wrocław University of Technology, Poland.

The paper presents a strength analysis of kinematic pairs made of high-yield point steel. Simulations of the behaviour of the joint in the elastoplastic range were carried out and the effect of the amplitude of the successive load cycles on the state of internal stress after the exceedance of the yield point in the joint's crucial points was determined. A prestressing procedure applied to increase the strength of the kinematic pair elements through the introduction of beneficial plastic strains is presented.

Keywords: *collapsible bridge, kinematic joints, plastic deformation, overload*

1. Introduction

In our age the requirements which steel constructions must meet change as new technologies of producing materials are developed. This particularly applies to modern grades of steel, which owing to modern production technologies acquire ever better strength properties at relatively small alloy addition content. Examples here are increasingly popular high-strength weldable steels with a yield point in the order of 1000 MPa.

Steels of this kind seem to be especially suitable for structures which must be both strong and lightweight. This is required of, for example, load-bearing structures mounted on vehicles and the bearing elements of the vehicles themselves. In this case, lightweight means lower fuel consumption, which is advantageous, but not essential for the functioning of the system. However, there is a class of structures in which the dead load is critical for their operation. An example here is a mobile collapsible bridge. This structure must satisfy two contradictory requirements. On hand, there is a limit on its dead load and outside dimension, while on the other hand, it is expected to carry ever greater working loads.

2. Problem description

The bridge enables sets of vehicles with a weight of up to 127 ton to overcome obstacles as wide as 40 m. Two class MLC 70 (military nomenclature) tracked vehicles each weighing 63.5 T constitute the maximum design load of the bridge. The dimensions of the contact area between vehicle and the bridge are shown in Figure 1. Position of vehicles on the bridge is presented in Figure 2.

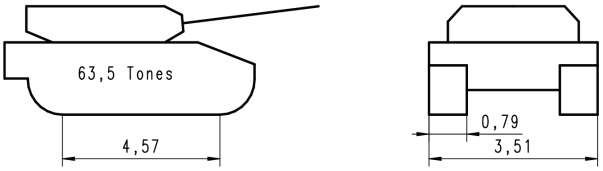

Fig. 1. Bridge load: class MLC 70 vehicle – dimension of contact area between vehicle and the bridge

The bridge design is shown in Figure 2. The bridge span is made up of many sections connected by articulated joints. When in service the bridge rests on two supports (one fixed and one movable) with a spacing of 43 m.

Because of the relatively long span of the bridge at a limited height of the span, great tensile forces occur in the bottom flanges of the bridge girders, which must be carried by the temporary pin joint indicated by the red arrow in Figure 2.

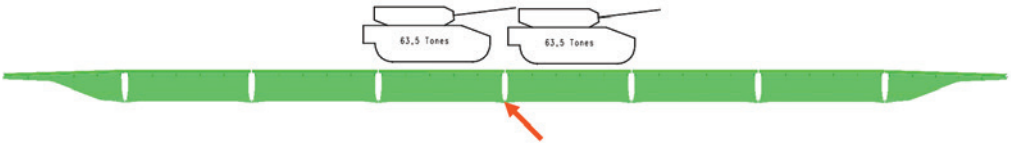

Fig. 2. Point at which bridge's bottom flanges are connected – place where maximum tensile forces occur

The required safety factor for this structure is 2.25. In addition, one needs to take into account a possible 20% increase in load [5] due to the dynamic loads generated by passing vehicles, which means that the safety factor should amount to 2.7. It would be extremely difficult to achieve this even if high-strength steel were used. The joint working under such an overload in the elastic range would have very large dimensions and would be very heavy. Therefore an attempt was made to exploit to some degree the plastic range in the material [2] from which the pin joint was made.

3. Material model

Computations in the elastoplastic range were performed for the following material data (conforming to the steel XABO1100 specifications): R_e = 1100 MPa, R_m = 1200 MPa, A_5 = 8%.

A typical stress-strain curve for a similar material, i.e. XABO 960QL, with a slightly lower yield point is shown in Figure 3.

For the analysis of the joint the behaviour of the material in the elastoplastic range needs to be simulated, which means that the work hardening of the material must be taken into account in the model [7]. The material work hardening curve according to the classic Johnson-Cook work hardening model (1), leaving out the modules relating to strain and temperature because of the static character of the load, was used for the computations.

$$\sigma = A + B\left(\varepsilon^{p}\right)^{n}. \tag{1}$$

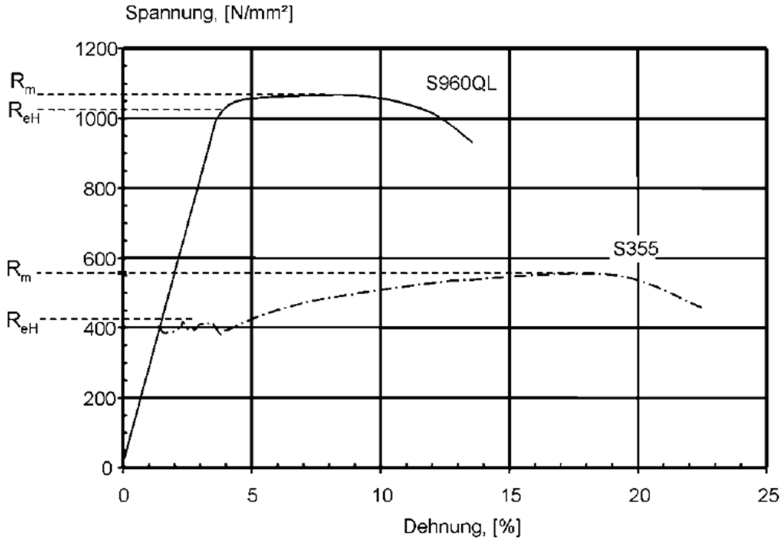

Fig. 3. Typical stress-strain curve for steel S960QL compared with that for steel S355 [3]

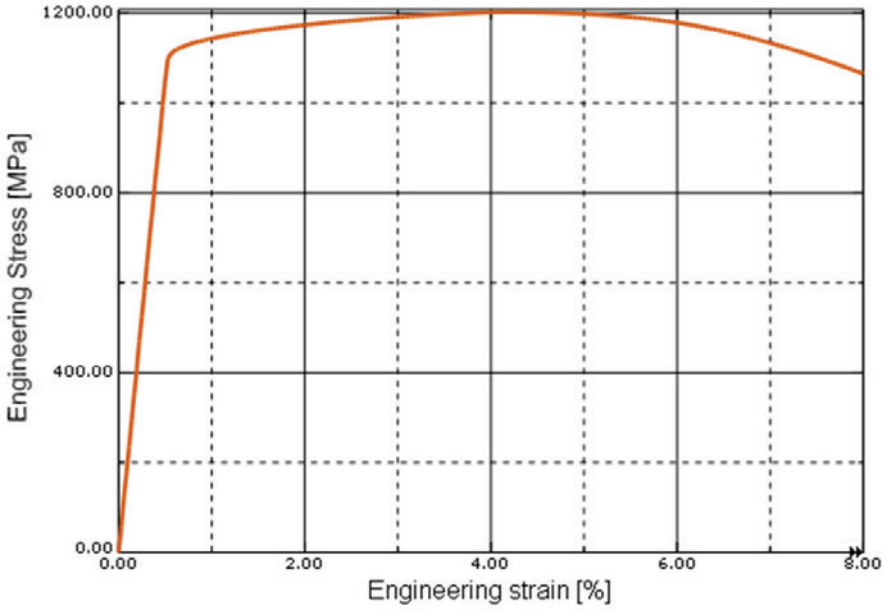

Fig. 4. Stress-strain curve for material XABO 1100, obtained by fitting Johnson-Cook work hardening model parameters to technical specifications

The model parameters were experimentally fitted to the catalogue specifications for material XABO 1100 and they amounted to A = 1090 MPa, B = 440 MPa, n = 0.4. When the parameter values are applied to the material model subjected to the classic tensile test, the (nominal) stress-strain curve shown in Figure 4, satisfying the minimal catalogue requirements, is obtained. A model of the specimen used to determine the material model parameters immediately before failure is shown in Figure 5.

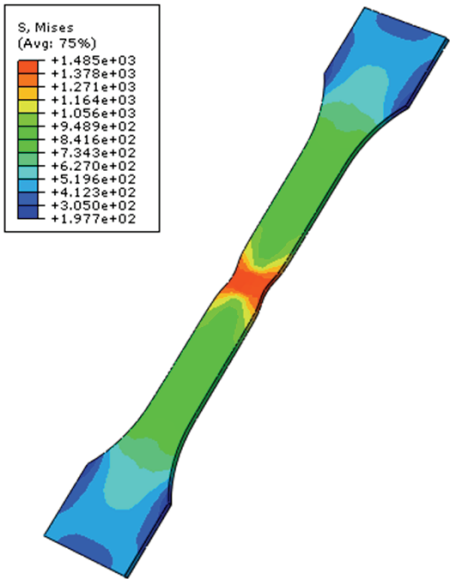

Fig. 5. Model of specimen used to determine material properties. Visible distribution of equivalent stress [MPa] immediately before failure

4. Computational models of the joint

In order to examine the state of stress in the pin joint between the bridge's bottom flanges one must determine the forces acting on this joint. For this purpose a computational model and a set of boundary conditions corresponding to the most hazardous load cases need to be developed [4, 6]. In order to check the strength of the joint it was necessary to most accurately determine the forces acting on it. For this purpose a FE shell model of the span, consisting of 380 000 shell elements (about 2 million degrees of freedom), was built. The computations were performed using ABAQUS/Standard [1]. The discrete computational model is shown in Figure 6.

Through the FEM simulation of the behaviour of the span one can reliably determine the loading of the bridge's structural components [6], in particular that of the bridge's bottom flange pin joint. The maximum force in the bottom flange for the asymmetric (at the deck's edge) passage of a set of tracked vehicles amounted to 4800 kN.

5. Simulation of the behaviour of the eyes connecting the bottom flanges

The behaviour of the pin joint was simulated using a local model to which the forces obtained from the full span simulation were applied. A solid model of the whole unit (consisting of two sets of eyes and the pin joining them) was developed. The geometry of the joint is shown in Figure 7. The force tensioning the joint was applied to the fragments of the bottom flanges of the neighbouring sections.

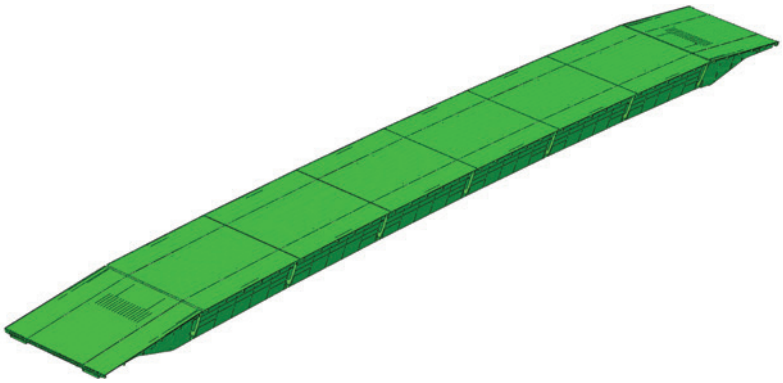

Fig. 6. Discrete shell model of bridge span

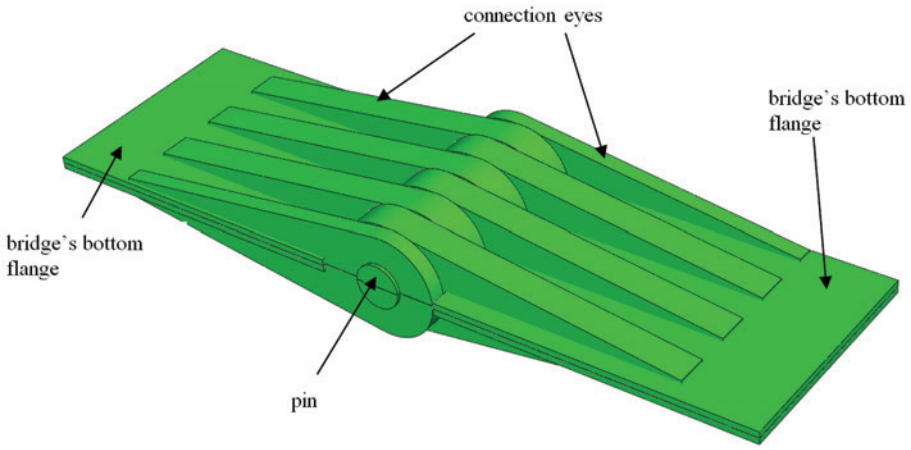

Fig. 7. Geometry of pin joint connecting bottom flanges of span

The aim of the simulation was to determine the joint's overload strength in the plastic range and the effect of the first (e.g. strength test) overload cycle on the subsequent state of stress and strain in the joint. For this purpose simulations were run for two types of joint load cycles:

A cycle without overload, consisting of the following stages:
1. preloading (clearance removal),
2. loading with force $F1$= 8500 kN,
3. relaxation to 0 kN,
4. loading with force $F2$ = 8500 kN,
5. unloading to 0 kN.

A cycle with overload, consisting of the following stages:
1. preloading (clearance removal),
2. overloading with force $F1 = F_{max}$ = 12 960 kN,
3. relaxation to 0 kN,
4. loading with force $F2$ = 8500 kN,
5. unloading to 0 kN.

The maximum load in the cycle with overload had the form of tensile force F_{max} = 12 960 kN in the bottom flange, which for the asymmetric passage of tracked set 2 × MLC70 was tantamount to an overload factor of 2.7 for the more loaded flange. The state of stress and strain in the selected cycles is shown in the figures below.

The first-cycle overloading of the joint with a force causing transition into the plastic range has a significant effect on the state of stress and strain in the eyes. After the plastic limit is exceeded in the maximally strained zone large compressive stresses appear there when the load is removed. As a result, the average stress value in the subsequent load cycles is shifted close to zero (the zone is alternately compressed and tensioned).

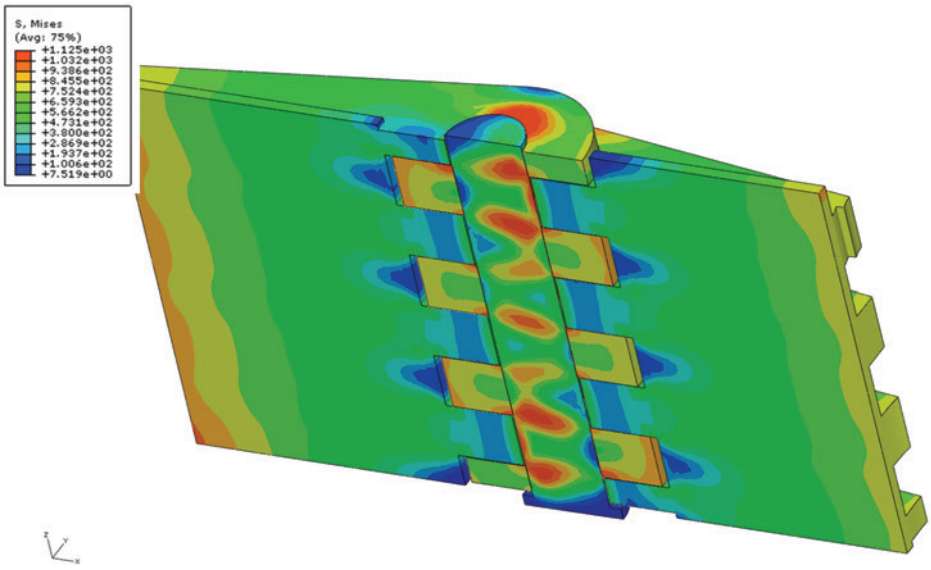

Fig. 8. Contour lines of equivalent stress (acc. to H-M-H [MPa]) in joint, maximum value 1125 MPa at force 12 960 kN (overload)

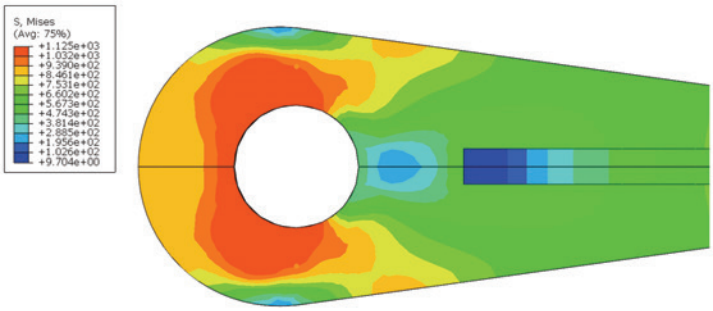

Fig. 9. Equivalent stress (max. 1125 MPa), overloading with force of 12960 kN in first cycle

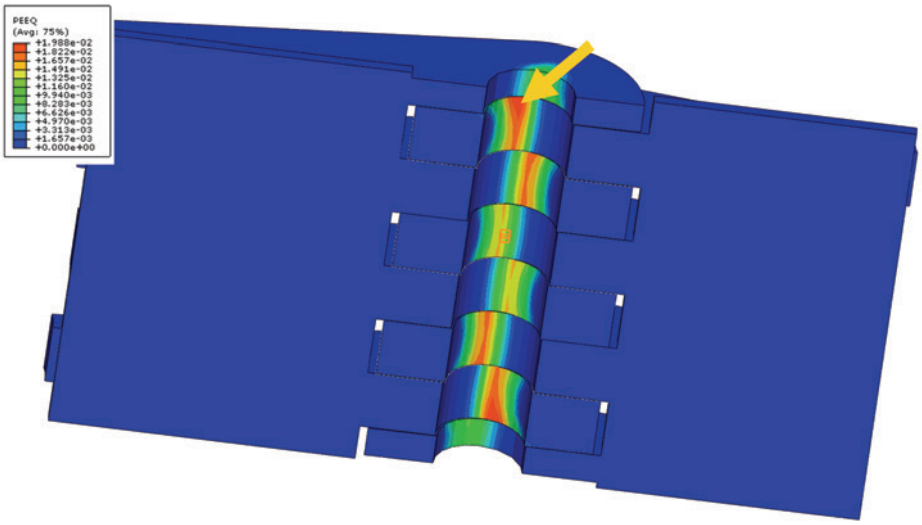

Fig. 10. State of strain in connection eyes after overload. Cross section of joint with pin removed. Visible maximum overload-cycle plastic strain of 1.98% under force of 12 960 kN (overload factor of 2.7) at eye/pin interface

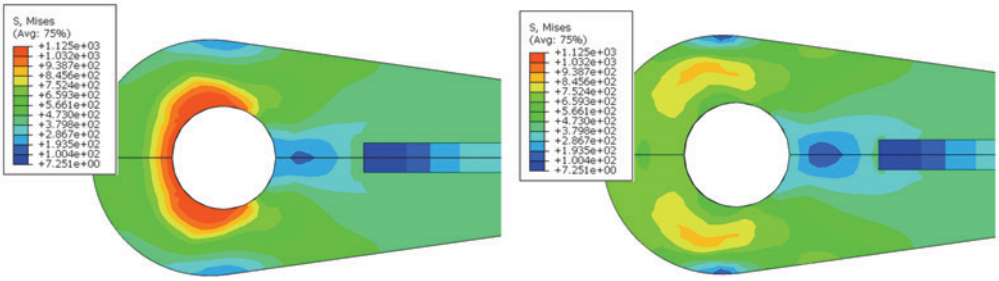

Fig. 11. Distribution of equivalent stress in eye loaded with force of 8500 kN for:
left – cycle without overload, right – cycle with overload (same colour scale in both cases)

In order to illustrate the above, the stress component along the connection for an eye point where the maximum stress occurs is shown in Figure 13.

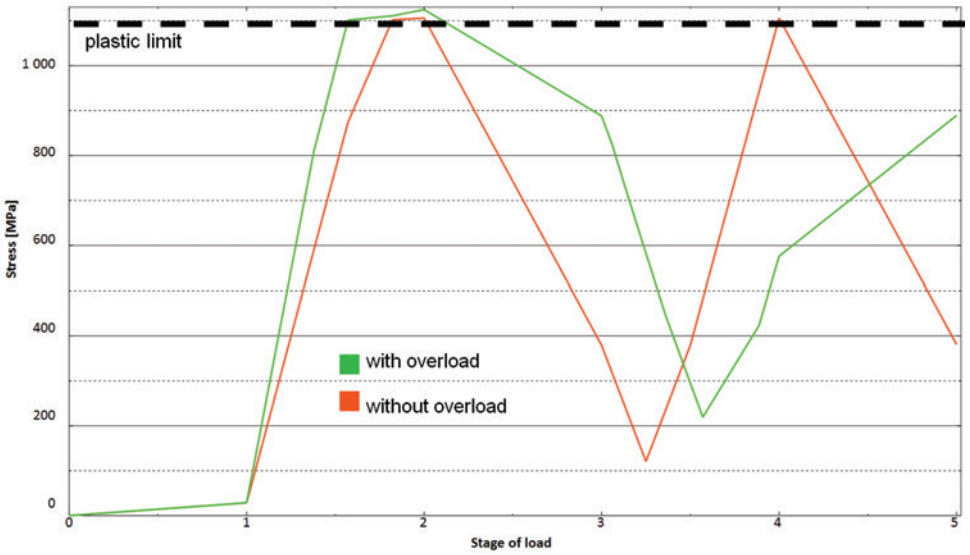

Fig. 12. Maximum equivalent stress during connection loading [MPa]. X-axis corresponds to successive stages: 1 – minimum load, clearance removal, 2 – loading with force of 8500 kN (cycle without overload) or 12 960 kN (cycle with overload), 3 – unloading (no tensile force), 4 – loading with force of 8500 kN, 5 – unloading (no tensile force)

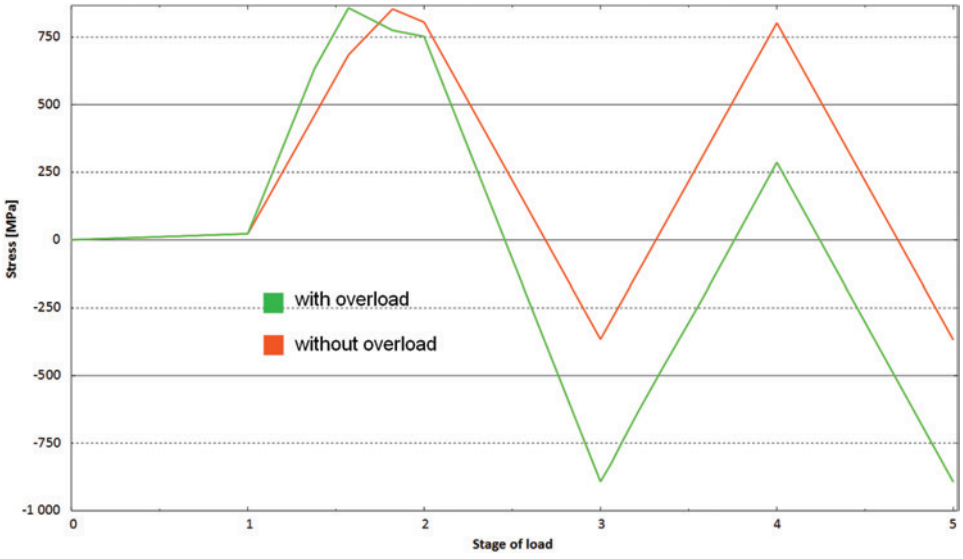

Fig. 13. Longitudinal stress in axis of bottom bridge flange [MPa] in successive stages

Table 1. Results of eye performance simulation for cycle with and without overload

	Equivalent stress			Longitudinal stress (negative values – compression)		
	σ_{max} [MPa]	σ_{min} [MPa]	range [MPa]	σ_{max} [MPa]	σ_{min} [MPa]	range [MPa]
Without overload	1105	121	1004	–366	+805	1171
With overload in first cycle	890	218	672	–892	+286	1175

The joint was also subjected to a failure test. The joint was loaded until a plastic hinge formed and extended over the whole cross section of the eye. Then the joint completely lost its load capacity. The maximum plastic strain at the instant of load capacity loss amounted to 3.25%. The joint loses its load capacity under the force of 14 235 kN, i.e. under about a triple overload relative to the maximum force for the asymmetric passage of the set of tracked vehicles.

6. Conclusions

After the first load, a 2% yield occurs (stage 2), generating large compressive stresses (stage 3) after unloading. As a result, no yield stress occurs in the next cycle and the maximum stress is much lower in the subsequent load cycles, which may have a highly beneficial effect on the durability of the joint (Figure 11).

The changes in the state of stress, introduced by the first load cycle bear resemblance to the overstraining procedure applied to pressure vessels to relax welding stresses and raise the plastic limit through material work hardening.

In order to apply such a procedure one must:

- very accurately determine the material properties,
- precisely compute the plasticizing force,
- precisely control the load.

In order to introduce an advantageous state of stress, the yield point needs to be clearly exceeded, which is very risky in the case of high-strength steel because of the very short interval between the yield point and the ultimate strength. Overstraining was conducted up to an overload 2.7 times greater than the nominal load (the total failure of the joint occurs at an overload of 3).

It is much more difficult to carry out this procedure in the considered case than in the case of a structure made of plastic steel (characterized by high elongation A_s). Nevertheless, as the simulation showed, by introducing an advantageous state of stress and strain into the joint one can obtain equally beneficial results.

References

[1] ABAQUS – *theory manual*, Hibbitt, Karlsson & Sorensen, Inc., 1080 Main Street, Pawtucket, RI 02860-4847, U.S.A. 1997.

[2] Chen S., Chen J.: *Steel bridge columns with pre-selected plastic zone for seismic resistance*, Thin-Walled Structures, Vol. 47, No. 1, 2009, pp. 31–38.
[3] Hamme U., Hauser J., Kern A., Schriever U.: *Einsatz hochfester Baustahle im Mobilkranbau*, Stahlbau, Vol. 69, No. 4, 2000, pp. 295–305.
[4] Kim S., Cho K., Won J., Kim J.: *A study on thermal behaviour of curved steel box girder bridges considering solar radiation*, Archives of Civil and Mechanical Engineering, Vol. 9, No. 3, 2009, pp. 59–76.
[5] Kim Y., Tanovic R.: *Load configuration and lateral distribution of NATO wheeled military trucks for steel I-Girder bridges*, Journal of Bridge Engineering, Vol. 15, 2010, pp. 740–748.
[6] Krasoń W.: *Simulation of the behaviour of scissors bridge in special conditions* (in Polish), Modelowanie inżynierskie, Vol. 9, No. 40, 2010, pp. 125–132.
[7] Roll K., Faust A.: *Forming simulation of high-strength steels with direction-specific hardening modelling*, Archives of Civil and Mechanical Engineering, Vol. 8, No. 3, 2008, pp. 107–115.
[8] Zienkiewicz O.C.: *The finite element method*, McGraw-Hill, London, Third Edition, 1977.

Analiza wytrzymałościowa par kinetycznych składanego mostu mobilnego

W artykule przedstawiono analizę wytrzymałościową par kinematycznych wykonanych z stali o wysokiej granicy plastyczności. Przeprowadzono symulacje pracy elementów połączenia w zakresie sprężysto-plastycznym oraz zaprezentowano wpływ amplitudy kolejnych cykli obciążenia na stan naprężeń wewnętrznych po przekroczeniu granicy plastyczności w newralgicznych punktach połączenia. Przedstawiona została procedura wstępnego przeciążenia połączenia, której celem było zwiększenie wytrzymałości elementów pary kinematycznej poprzez wprowadzenie korzystnych odkształceń plastycznych.

ARCHIVES OF CIVIL AND MECHANICAL ENGINEERING

Vol. XI 2011 No. 4

Load capacity and stiffness of angular cross section reinforced concrete beams under torsion

M. KAMIŃSKI, W. PAWLAK
Wrocław University of Technology, Wybrzeże Wyspiańskiego 27, 50-370 Wrocław, Poland.

The paper presents the results of tests, numerical analyses and theoretical analyses of reinforced concrete beams loaded with a torsional moment as well as a shearing force and a bending moment, carried out in the Research Laboratory of the Institute of Building Engineering at Wrocław University of Technology. The research focused on the load capacity and stiffness of such elements. Beams angular (in the shape of the inverted letter L) and rectangular in cross section were investigated. The tests were carried out in two series. In the first test series the elements were loaded with solely a torsional moment. In the second test series the beams were subjected to the combined load of a torsional moment, a shearing force and a bending moment. The behaviour of the beams with the different cross sectional shapes was compared. The experimental results and the ones yielded by numerical analyses were compared with theoretical and standard results.

Keywords: *beam, crack, experimental research, L-beam, load capacity, reinforced concrete, stiffness, torsion*

1. Introduction

A torsional moment in building structures always arises when the resultant force acts eccentrically relative to the longitudinal axis of an element. Although this happens quite often, in most cases the torsional moment is slight and has a smaller effect (in comparison with the other types of loading) on the ultimate limit state. Torsion usually occurs together with a bending moment and a shearing force. Generally, it is the bending moment which is decisive. In building engineering the loading of an element with a torsional moment alone (pure torsion) is a wholly theoretical case. In most cases, the reinforced concrete elements under torsion are simultaneously loaded with a bending moment and a shearing force (sometimes also with a longitudinal force, as in prestressed reinforced concrete elements). Examples of reinforced concrete elements often loaded with a torsional moment are: edge floor joists, balcony slab ring beams, spatial frames, spiral stairs and reinforced concrete arches loaded perpendicularly to their plane (Figure 1).

Structural components have been the subject of extensive research for over a hundred years of the history of reinforced concrete. Most of the experimental research has been on beams rectangular or circular in cross section (the latter were investigated mainly at the beginning of the 20th century). Simultaneously, theories describing the behaviour of reinforced concrete elements under torsional loads have been developed.

Two main theoretical models describing the behaviour of cracked reinforced concrete elements under torsional moment, i.e. the Rausch space truss model (1929) [18] and the Lessig spatial cross section model (1959) [13], were created. Since then the models have been modified and refined in order to bring them closer to reality. The most comprehensive monograph on torsion was written by T.T.C. Hsu [4].

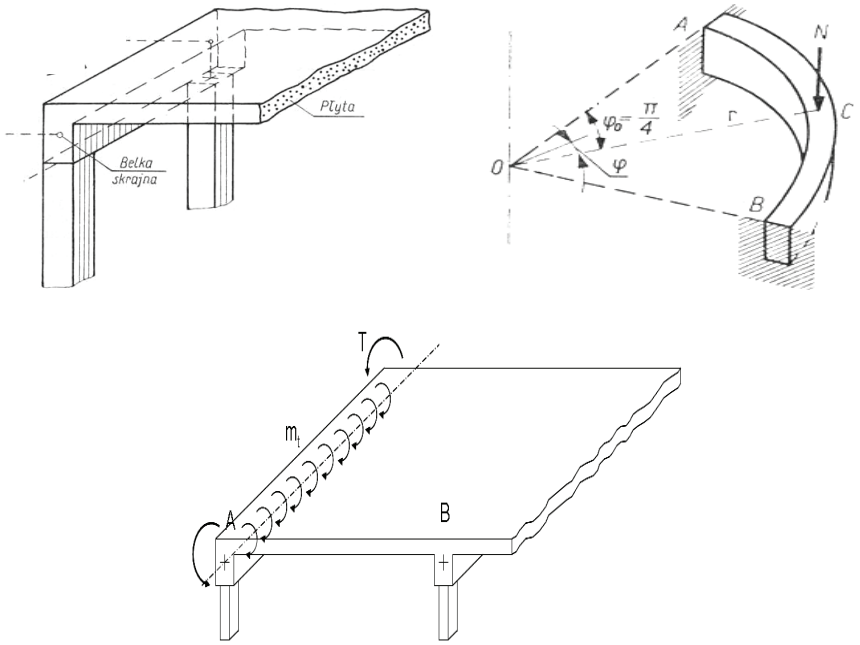

Fig. 1. Examples of reinforced concrete elements in which torsion occurs

Selected conclusions emerging from the experimental studies and theoretical analyses found in the literature on the subject are presented below:

- the cracking moment for elements with and without reinforcement is basically the same (the cracking moment is mainly determined by the strength of the concrete, the influence of the reinforcement being almost imperceptible);
- the longitudinal reinforcement and the lateral reinforcement of elements subjected to pure torsion should have a similar "strength" (for strength and economic reasons spiral reinforcement with the spiral direction consistent with that of element torsion under same-sign torsional moment is most preferable);
- after cracking the stiffness and the load-bearing capacity are determined mainly by the amount and type of reinforcement, not by the strength of the concrete;
- spiral reinforcement is better utilized (but it has many drawbacks, such as workmanship defects and possible errors in laying the spiral consistently with the direction of the twist);

- the stiffness of elements sharply decreases under the combined action of a torsional moment, a bending moment and a shearing force ($T + M + V$);
- the use of concrete of a higher grade results only in a greater cracking moment;
- regardless of whether the cross section is solid or hollow, only the outer concrete shell takes part in the transmission of torsion;
- both longitudinal and lateral reinforcement (unless spiral reinforcement is employed) must be used in elements loaded with a torsional moment;
- when $T + V$, the first crack appears on the wall where shear stresses and torsional stresses add up ($\tau_T + \tau_M$);
- the highest stresses in the lateral reinforcement (stirrups) occur at half the height of the longer side; in the case of a compound load (torsion plus shearing $T + V$), the highest stresses occur in the stirrups at half of the longer side where torsion stresses and shearing stresses add up.

Despite the extensive research and numerous analyses not all the questions have been answered. One of the still unexplored problems is the behaviour of reinforced concrete elements with a cross section other than rectangular or circular. Therefore the authors undertook research on reinforced concrete beams with an angular (in the shape of the inverted letter L) cross section. This paper deals in detail with the load capacity and stiffness of such elements.

Similar tests of reinforced concrete structures are described in the works Kobielak et al. [10] and Jansen, Łapko [7].

2. Load capacity and stiffness of elements under torsion

2.1. Load capacity of elements under torsion

First, theories describing the load capacity of elements under torsion in stage 1 (uncracked elements) were developed. Obviously, they were unsuitable for investigating the behaviour of cracked reinforced concrete elements. Elasticity analyses could be applied to uncracked reinforced concrete elements (treated as homogenous materials), but only to a limited extent of their behaviour.

Later inelastic theories, which better represent the behaviour of reinforced concrete elements loaded with a torsional moment and take into account their specificity, were developed. Two main models: the Rausch space truss model and the Lessig space cross section were elaborated. In their initial version the theories predicted torsional load capacity well, but they did not describe accurately enough the behaviour of reinforced concrete elements under any other load level. The original theories have been successively improved by other researchers. The spatial truss theory has undergone the largest number of modifications and improvements.

In real elements torsion practically always occurs together with bending and shearing. The two most advanced theories describing jointly the torsion, bending and shearing of reinforced concrete elements are the Vecchio and Collins modified com-

pression field theory (MCFT) [19–20] and the Hsu softened truss model theory (STMT) [6].

The two theories are based on the analysis of a rectangular cross section reinforced concrete element under biaxial stress.

In order to accurately determine the behaviour (load capacity, deformation) of reinforced concrete elements under combined bending and shearing at each load level one should take into account equations of equilibrium, strain inseparability conditions and constitutive laws for concrete and steel.

There is also the Rahal and Collins model [14–15] (based on the Vecchio and Collins MCFT) – the only existing model for the analysis of reinforced concrete elements under combined torsion and shearing. In this method the spatial behaviour of the element was additionally taken into account through the introduction of a condition of curvatures inseparability.

2.2. Stiffness of elements under torsion

The stiffness of an uncracked reinforced concrete element (in stage 1) can be expressed by the formula:

$$K_T^I = G \cdot I_T = \frac{T}{\vartheta}, \tag{1}$$

where:

G – a material constant (for concrete) called (Kirchhoff) shear modulus $G = \dfrac{E}{2 \cdot (1+\nu)}$,

I_T – a torsional moment of inertia (a quantity characterizing the cross section depending on the latter's geometry),

ϑ – rotation per length unit,

E – a modulus of longitudinal deformability,

υ – a Poisson ratio (a coefficient of transverse deformability),

T – a torsional moment.

Torsional strength in stage 2 (after cracking) is usually expressed as the product of stage 1 stiffness (for the uncracked element) and a reducing coefficient(s) (e.g. denoted as C in Equation 2) which takes into account the influence of cracking and reinforcement. This can be written as:

$$K_T^{II} = C \cdot \left(G \cdot I_T\right)^I. \tag{2}$$

The full formulas are highly complex since coefficient C in Equation (2) depends on many factors. The problem has been investigated by Hsu [5], Lampert and Thürlimann [12], Rahlwes [16], Karlsson [9] and others.

3. Experimental research

3.1. Preparation for tests

After a survey of the literature on torsion, a test plan was developed. In the first test series, one beam with an angular cross section (BK-T) and one beam with a rectangular cross section (BP-T) were tested solely under a torsional moment. Then eight beams (four L-beams (BK-TVM and four beams rectangular in cross section (BP-TVM)) under a combined load of a torsional moment, a bending moment and a shearing force were tested. The elements in the second test series were loaded with different values of the bending moment M – torsional moment T ratio (M/T = 1, 2, 3, 4). The beams rectangular in cross section were tested as a reference since such beams had been much better explored.

The beams to be tested were made in house in the laboratory Institute of Building Engineering (IBE) at Wrocław University of Technology. For this purpose formworks made of waterproof plywood OSB Special 21 had been prepared. The beams were made from concrete C20/25 reinforced with steel (BSt500S and 18G2-b in the case of respectively longitudinal elements #16 and stirrups #8). The test stand shown in Figure 2. The geometry of the tested beams and the span reinforcement are shown in Figures 3 and 4.

Fig. 2. Tested beam on test rig

The concrete had been ordered from a readymix concrete plant. The beams to be tested were compacted using a 38 mm ϕ poker vibrator. During their casting, samples were taken to determine the strength properties of the concrete. The preparation for the tests, the formworks, the test beam reinforcement and the testing of the samples to determine the strength of the concrete and the steel are described in detail in a report from the research [8].

The torsional moment in the beam span was produced by applying a concentrated force to reinforced concrete brackets situated at the ends of the beam. The force was located eccentrically (at an eccentricity of 0.6 m) relative to the beam's longitudinal axis. In top view the beam had the shape of a letter Z (Figure 3).

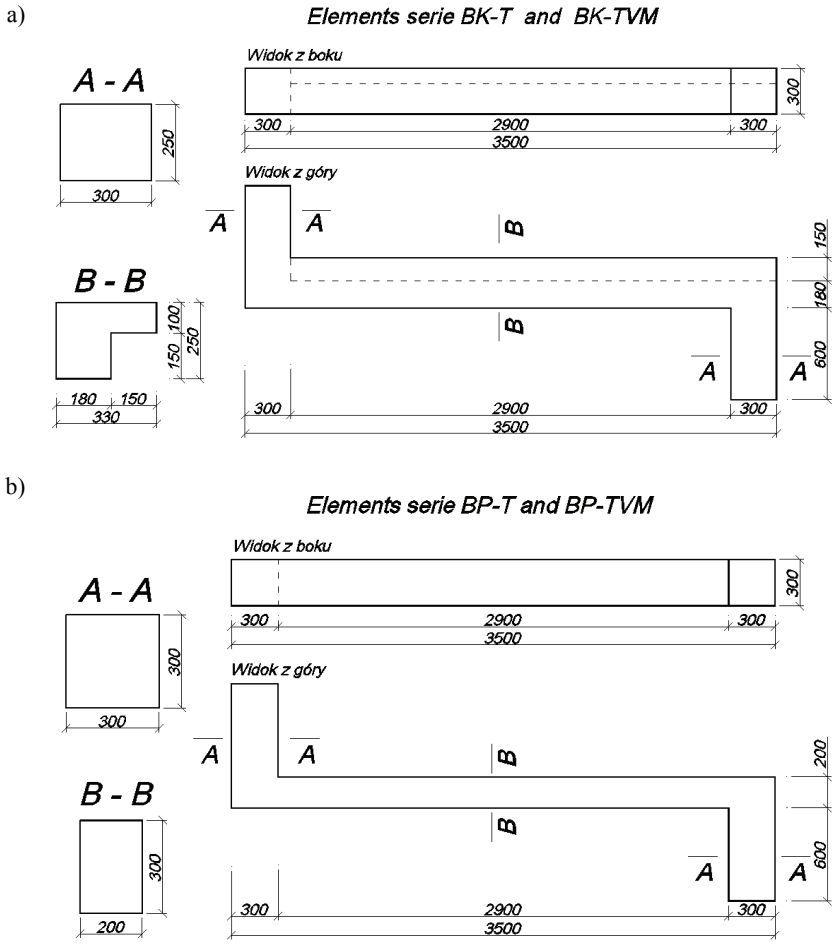

Fig. 3. Geometry of tested beams – series BK (a) and BP (b)

Although difficult to execute, this shape was chosen because of the method of transmitting the load. In the case of torsion or shearing tests, strains may be seriously disturbed locally by concentrated forces (or support reactions). Regions of serious strain disturbances (referred to as discontinuity regions in the literature, e.g. [17]) occur in

the concentrated force application area. In such regions neither the principle of plane sections nor strain inseparability conditions hold good. It would be much simpler to make the tested beams without the brackets and to transmit the torsion producing force through a steel beam situated above the tested beam and perpendicular to the longitudinal axis of its span. Many tests employing a steel beam to produce torsion in fact have been carried out, but then discontinuity regions in the places where the brackets are mounted appeared.

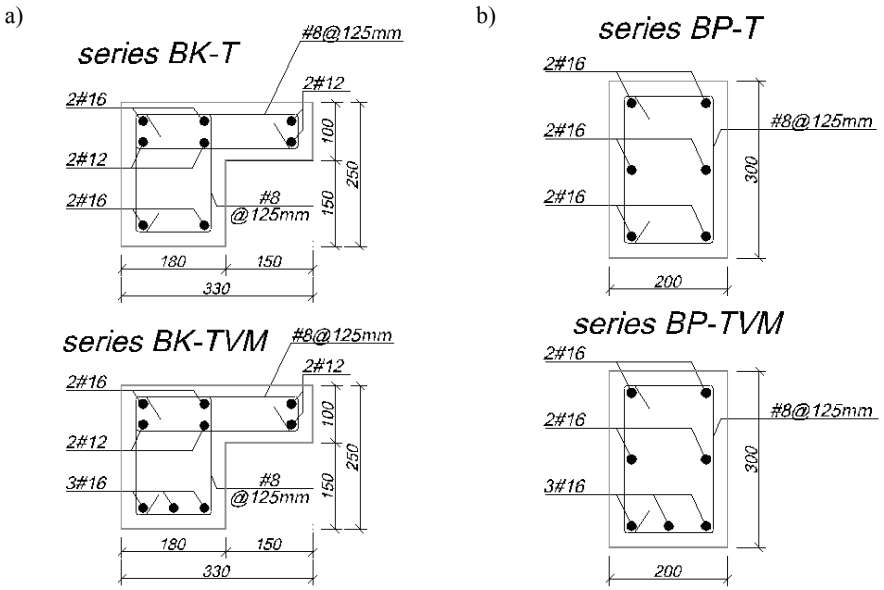

Fig. 4. Reinforcement in tested beams – series BK (a) and BP (b)

One should treat with caution the results of such tests. For this reason, according to Hsu [4], the load should be introduced into the tested element via reinforced concrete brackets. Then the concentrated load from the cross-beam is transferred to the main beam through the shearing stress uniformly distributed along the entire height of the cross section of the tested beam and only slight strain disturbances limited to a very small area occur in the place of load transfer. Because of the reasons stated above it was decided to make beams with brackets.

3.2. Description of tests

The strength properties of the concrete and the reinforcement steel are shown in Tables 1 and 2. The concrete was tested on the same day as the beams. The reinforcement steel was tested on the same day as the series T (BK-T and B-PT) beams. All the

tested beams were made using steel from one batch. The samples for the strength tests were cured and stored in the same way as the beams.

Table 1. Characteristics of concrete from which beams were made

Characteristics of concrete					
Elements	Age of concrete [days]	Compressive strength f_c [MPa]	Tensile strength f_{ct} [MPa]	Module of elasticity E_c [GPa]	Poission's factor 8_c [–]
BK-T BP-T	54	27.1	2.77	26.41	0.19
BK-TVM_1 BP-TVM_1	47	27.5	2.59	24.55	0.19
BK-TVM_2 BP-TVM_2	74	37.6	3.08	26.05	0.19
BK-TVM_3 BP-TVM_3	62	30.4	3.11	24.57	0.19
BK-TVM_4 BP-TVM_4	49	29.4	2.07	25.21	0.19

Table 2. Characteristics of reinforcement steel from which beams were made

Characteristics of reinforcement steel					
#16 (BSt500S)			#8 (18G2-b)		
Yield f_y [MPa]	Tensile strength f_t [MPa]	Module of elasticity E_s [GPa]	Yield f_y [MPa]	Tensile strength f_t [MPa]	Module of elasticity E_s [GPa]
576	762	204	435	584	203

The beams were subjected to static loading. In the first stage of testing (under pure torsional moment), the series T beams were loaded with a force applied by a hydraulic actuator to the reinforced concrete bracket (at an eccentricity of 60 cm relative to the longitudinal axis of the beam). The force was increased in steps of 2.0 kN (in the first loading-unloading cycle the step was 1.0 kN in order to better identify the cracking force and the propagation of cracks) up to about 60% of failure load $P_u = 0.6\ P_N$. Failure force P_N was set to 30 kN (which corresponds to torsional moment $T_R = 18$ kNm) and so $P_u = 18$ kN. After loading up to this level the beam was unloaded down to level $P \approx 0.2$ kN at the same step as during loading. The loading-unloading cycle was repeated six times. After the seventh loading to level $P_u = 0.6\ P_N$ the beam was loaded (at a step of 1.0 kN) until it failed. The failure of the beams was observed. The loading of the TVM series beams in the second stage of testing (under torsional moment, bending moment and shearing force) consisted in applying a force by one hydraulic actuator located on a reinforced concrete bracket (at an eccentricity of 60 cm relative to the longitudinal axis of the element), producing a torsional moment while the other hydraulic actuator situated on the beam span generated a shearing force and a bending moment. The other actions during the loading of the beams were the same as for the series T beams. The forces producing the loads were so located that force P_T situated at an eccentricity of 0.6 m relative to the beam's longitudinal

axis produced torsional moment $T = P_T$ 0.6 [kNm]. Force P_M generated bending moment $M = 0.6\ P_M$ [kNm]. This means that as force P_T or P_M was increased, the respective moments increased by the same value.

At each load level the following were measured: the unit torsional angle of the beam, the unit strain of the longitudinal and lateral reinforcement, the unit strain of the concrete's surface, the crack opening width and the propagation of cracks. All the measurements were read off and recorded by a PC with a multichannel measuring system UPM100 made by Hottinger Baldwin Messtechnik, except for crack propagation which was measured by the authors by means of a magnifier. Moreover, the entire course of the tests was photographically documented and partially recorded by a digital video camera.

3.3. Empirical results

The load capacities of all the tested beams are shown in Table 3 below.

Table 3. Load capacities of beams T and TVM

Beams	Breaking force P_n [kN]	Breaking torsional moment T_R [kNm]
BK-T	28.0	16.8
BP-T	25.0	15.0
BK-TVM_1	31.0	18.6
BP-TVM_1	30.0	18.0
BK-TVM_2	21.0	12.6
BP-TVM_2	26.0	15.6
BK-TVM_3	22.0	13.2
BP-TVM_3	24.0	14.4
BK-TVM_4	20.0	12.0
BP-TVM_4	26.0	15.6

As the table shows, beam BK-T (L-beam) failed under torsional moment T = 16.8 kNm while beam BP-T (rectangular in cross section) failed under T = 15.0 kNm. This seems to support the thesis that the flange of angular elements loaded with pure shear has a beneficial effect on their load capacity. Elements loaded with both a torsional moment and a bending moment (the latter being dominant) failed at a lower load level (the bending moment/torsional moment ratio ≥2).

As the table shows, beam BK-T (L-beam) failed under torsional moment T = 16.8 kNm while beam BP-T (rectangular in cross section) failed under T = 15.0 kNm. This seems to support the thesis that the flange of angular elements loaded with pure shear has a beneficial effect on their load capacity. Elements loaded with both a torsional moment and a bending moment (the latter being dominant) failed at a lower load level (the bending moment/torsional moment ratio ≥2).

The figures below show the dependence between torsional moment T and torsional angle Θ, determined at midspan. Figure 5 shows this for the elements loaded solely with a torsional moment (the first test series).

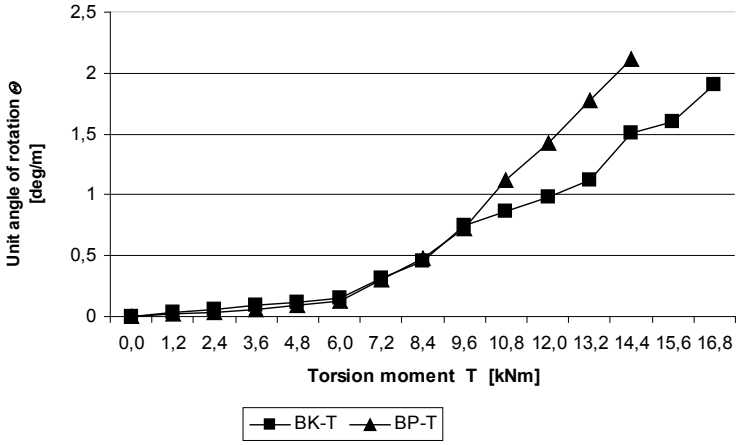

Fig. 5. Torsional moment T versus unit torsional angle Θ for elements under pure torsion – beams BK-T and BP-T

A considerable decrease in stiffness is observed at higher load levels. Until cracking (T_{cr} = 5.0 kNm) the dependence is nearly linear (stiffness decreased only slightly: by ~3% for the angular element and ~3.5% for the rectangular element). In stage 2, stiffness sharply decreases and immediately before failure the angle of rotation of the element is very large and rapidly growing. It is apparent that the serviceability limit state (SLS) may be decisive in the case of such elements. Although the element's load capacity is still not exceeded, its angle of rotation may disqualify it from further use. The L-beam (BK-T) was characterized by a greater torsional stiffness at higher load levels than the rectangular beam (BP-T), despite the fact that the torsional moment of inertia I_T of the BK-T beam's cross section is lower. This may be attributed to the beneficial effect of the cross section's flange which limits the torsion of the element's web.

Figures 6 and 7 show the elements (with respectively the L-shaped cross section and the rectangular cross section) in the second stage of testing, i.e. loaded with a torsional moment, a bending moment and a shearing force. All the graphs are for the midspan cross section.

One can see that until cracking the dependence is nearly linear. After cracking the angle of rotation significantly increases. The graphs are similar for both the rectangular elements and the angular elements. At the same load levels the values of angle Θ are similar for the angular elements and the rectangular elements. It is apparent that for the same load level the torsion of the angular element and that of the rectangular element are similar, with the angular elements showing a smaller torsion and the rectangular elements showing a considerably higher torsional moment of inertia (I_T). One may attribute this to the beneficial effect of the beam's flange on its stiffness.

The decrease in the stiffness of the tested elements was understood as a change in unit torsion angle Θ with increasing torsional moment T.

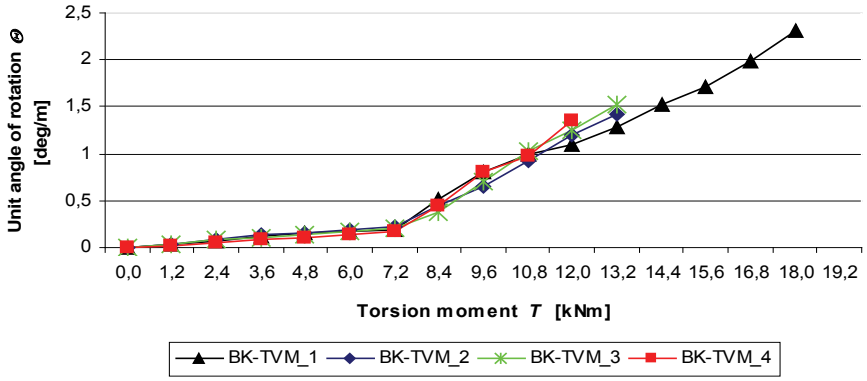

Fig. 6. Torsional moment T versus unit torsional angle Θ for angular (in shape of letter L) elements – beams BK-TVM

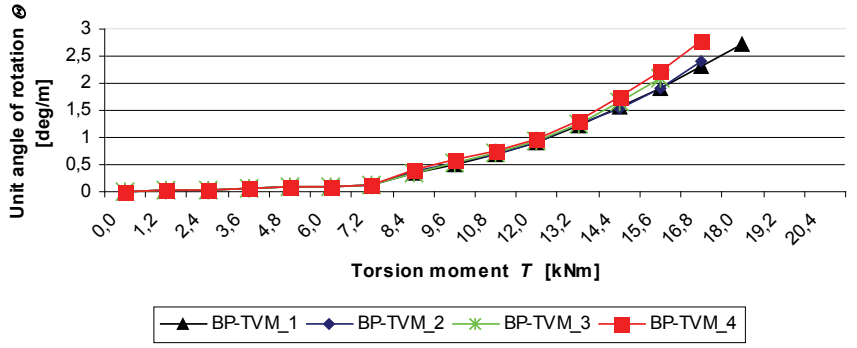

Fig. 7. Torsional moment T versus unit torsional angle Θ for rectangular elements – beams BP-TVM

In the elements loaded with both a torsional moment and a bending moment the decrease in stiffness was larger than in the elements loaded solely with a torsional moment (especially in the elements with the dominant effect of bending at a bending moment/torsional moment ratio ≥2).

4. Comparison of empirical and numerical results

Also numerical analyses were carried out using program DIANA® based on the finite element method (FEM) [1]. In order to model the structure, 20-node cuboidal finite elements with 24 degrees of freedom were used to model the concrete and 3-node spatial bar finite elements with two Gaussian integration points were used to model the reinforcement bars. Interaction between the concrete and the steel was ensured through agreement between the displacements of the solid finite elements' nodes (concrete) and those of the bar finite elements' (reinforcement) nodes. The smeared crack model was used to model the concrete elements. According to this model, crack

initiation occurs in any point where the stress in the concrete reaches one of the cracking surfaces (i.e. then longitudinal modulus of elasticity $E = 0$ and Poisson ratio $\nu = 0$ are assumed in the direction perpendicular to the cracking surface). The concrete/steel interaction between cracks, where the concrete enters into interaction with the tensioned reinforcement (which in the literature is referred to as the reinforcement stiffening effect) was modelled through the assumption that the loss of tensile strength by the concrete does not occur abruptly as in concrete elements without reinforcement, i.e. the tensile strength linearly decreases to zero and the slope of the apparent strength decline curve depends on the reinforcement strain value. This is a common practice in such computations. The Hsu softened concrete model with softening coefficient $\zeta = 0.5$ was used in the analyses.

The experimentally and numerically determined load capacities (Table 4) and stiffnesses of the elements (Figures 8–12) are compared below.

Table 4. Comparison of load capacity T_R values (EMP – empirical and MES – numerical)

Elements	Load capacity T_R		
	Empirical T_r^{MES} [kNm]	MES – numerical T_R^{MES} [kNm]	Percentage difference [%]
BK-T	16.8	18.5	9.2
BP-T	15.0	18.0	16.7
BK-TVM_1	18.6	20.0	7.0
BP-TVM_1	18.0	20.0	10.0
BK-TVM_2	12.6	16.0	21.3
BP-TVM_2	15.6	17.5	10.9
BK-TVM_3	13.2	14.5	9.0
BP-TVM_3	14.4	16.0	10.0
BK-TVM_4	12.0	13.5	11.1
BP-TVM_4	15.6	17.0	8.2

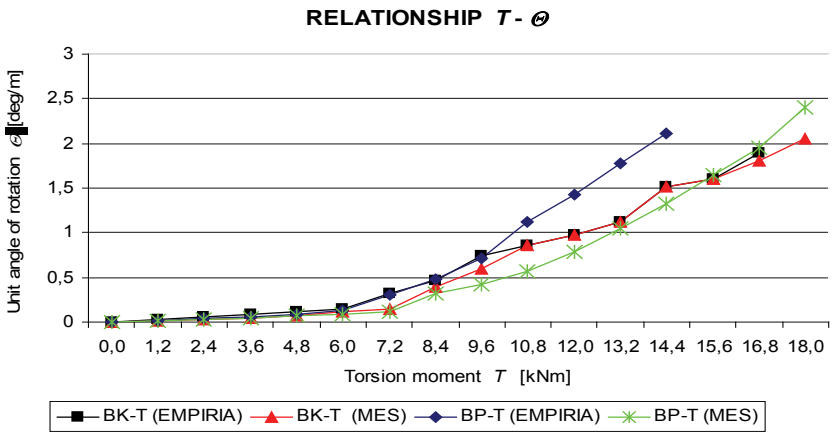

Fig. 8. Comparison of torsional stiffness $T - \Theta$ for BK-T and BP-T elements

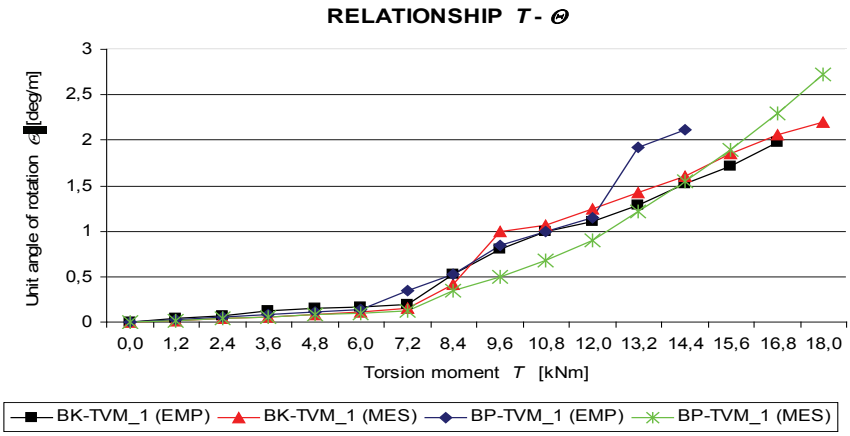

Fig. 9. Comparison of torsional stiffness $T - \Theta$ for BK-TVM_1 and BP-TVM_1 elements

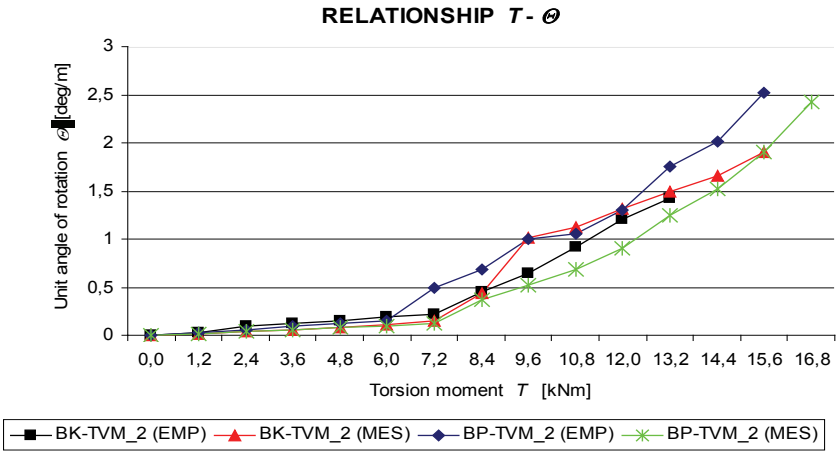

Fig. 10. Comparison of torsional stiffness $T - \Theta$ for BK-TVM_2 and BP-TVM_2 elements

One can see that the numerical FEM analyses yielded much higher torsional load capacity values T_R. In each case the higher value comes from the numerical analysis. The load capacities calculated by the (FEM) program were on average ~10% higher, except for the BP-T and BK-TVM_2 elements for which they were even higher (by about 20%).

According to the graphs shown in the figures, the same elements showed a higher torsional strength in the numerical analyses (at a lower unit torsional angle Θ for a given torsional moment load T). Cracking point T_{cr} is much more distinct (the bend in the graph is much sharper). Until the moment of cracking, the graphs remain almost rectilinear. After cracking, the torsional angle markedly increases. The shape of the graphs

is similar for the experimental and numerical results. At the same load levels, the experimental and numerically determined values of cross section torsion Θ are quite close (but the torsional angle is smaller for the numerical results). Also the torsion of the L-beam and that of the beam rectangular in cross section are similar at the same load level or sometimes the angular element is characterized by a smaller cross sectional torsion while the rectangular element shows a much higher torsional moment of inertia (I_T). This may be attributed to the beneficial effect of the beam's flange on its stiffness.

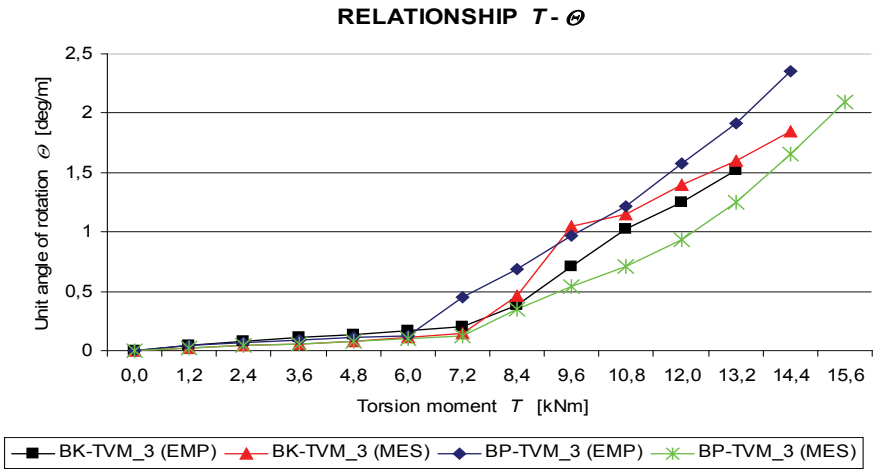

Fig. 11. Comparison of torsional stiffness $T - \Theta$ for BK-TVM_3 and BP-TVM_3 elements

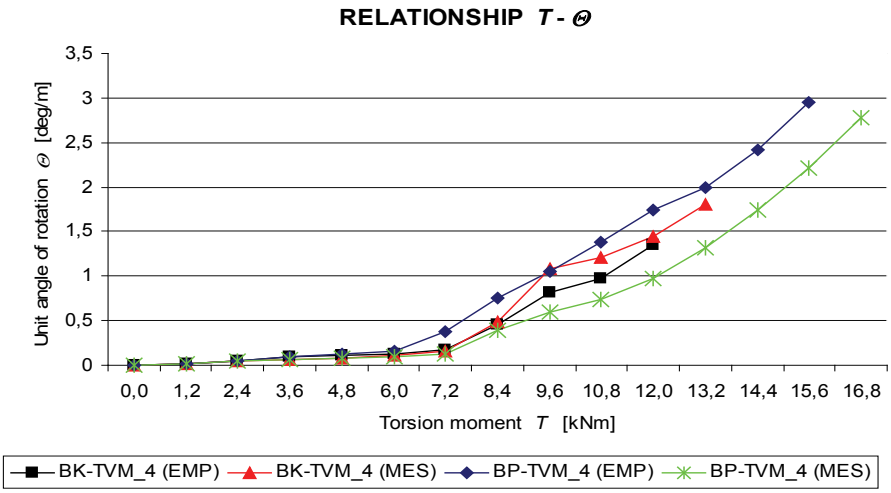

Fig. 12. Comparison of torsional stiffness $T - \Theta$ for BK-TVM_4 and BP-TVM_4 elements

5. Comparison of empirical, numerical and theoretical results

Also the experimentally determined beam load-bearing capacities T_R were compared with the ones calculated from equations based on the well-known theories concerning reinforced concrete elements cracked under torsional moment load. The load-bearing capacities are shown in Table 5. The particular T_R values were calculated from the formulas for breaking torsional moment, presented below.

Table 5. Comparison of experimental and calculated torsional load-bearing capacities T_R

Elements		Torsional load-bearing capacities T_R						
		Experience	EC-2 [19]	Eq. (3)	Eq. (4)	Eq. (5)	Eq. (6)	Eq. (7)
		T_R^{emp}	T_R^{std}	HSU	KUYT		LAMPERT&THURLIMANN	
		[kNm]	[kNm]	[kNm]	[kNm]	[kNm]	[kNm]	[kNm]
Reinforced concrete beams	BK-T	16.8	22.0	17.8	42.2	21.7	19.9	23.0
	BP-T	15.0	23.6	15.1	42.2.	20.8	16.3	23.6
	BK-TVM_1	18.6	22.0	21.1	42.2	26.5	29.9	23.0
	BP-TVM_1	18.0	23.6	18.4	42.2	25.5	24.5	23.6
	BK-TVM_2	12.6	22.0	21.8	42.2	26.5	29.9	23.0
	BP-TVM_2	15.6	23.6	19.1	42.2	25.5	24.5	23.6
	BK-TVM_3	13.2	22.0	21.3	42.2	26.5	29.9	23.0
	BP-TVM_3	14.4	23.6	18.6	42.2	25.5	24.5	23.6
	BK-TVM_4	12.0	22.0	21.3	42.2	26.5	29.9	23.0
	BP-TVM_4	15.6	23.6	18.6	42.2	25.5	24.5	23.6
	– closest to the result of the theoretical results with experimental studies							

The Hsu [5] formula for breaking torsional moment (based on his extensive experimental studies and analyses):

$$T_R = \frac{1.015}{\sqrt{b}} \cdot b^2 \cdot h \cdot \sqrt{f_c} + \left(0.66 \cdot m \cdot \frac{f_{yd}}{f_{\mathrm{ywd}}} + 0.33 \cdot \frac{h_j}{b_j} \right) \cdot \frac{A_{sw} \cdot f_{\mathrm{ywd}} \cdot h_j \cdot b_j}{s}, \tag{3}$$

where:

h_j, b_j – respectively the cross-sectional width and height in the axis of the stirrups,

coefficient m – expressed by the formula: $m = \dfrac{A_s \cdot s}{2 \cdot (b_j + h_j) \cdot A_{sw}}$.

According to Kuyt [11] who derived the above equation from his theory (similar to the Lessig theory), the breaking torsional moment can be calculated from the following two equations:

$$\text{for stirrups } T_R = A_{sw} \cdot f_{\mathrm{ywd}} \cdot \frac{2 \cdot A_c}{s} \cdot \cot\theta, \tag{4}$$

for longitudinal reinforcement $T_R = 2 \cdot b_j \cdot h_j \cdot \sqrt{\frac{A_s \cdot f_{yd}}{2 \cdot (b_j + h_j)} \cdot \frac{A_{sw} \cdot f_{ywd}}{s}}$. (5)

Moreover, the load-bearing capacity was calculated on the basis of the (Lampert & Thurlimann [12]) spatial truss theory

for longitudinal reinforcement $T_R = \frac{2 \cdot A_k \cdot A_{sl} \cdot f_y}{u_k} \cdot tg\theta$, (6)

for stirrups $T_R = \frac{2 \cdot A_k \cdot a_{sw} \cdot f_{yw}}{s} \cdot ctg\theta$. (7)

Table 6. Comparison of stiffness K_T

Stiffness K_T [kNm^2]					
	$K_{T,I}$	$K_{T,cr}^{empiria}$	$K_{T,cr}^{MES}$	$K_{T,I}/K_{T,cr}^{empiria}$	$K_{T,I}/K_{T,cr}^{MES}$
	[MNm^2]	[MNm^2]	[MNm^2]	[–]	[–]
BK-T	3.3	3.4	3.5	0.97	0.94
BP-T	5.2	3.7	4.9	1.41	1.06
BK-TVM_1	3.1	3.2	3.3	0.97	0.94
BP-TVM_1	4.9	4.3	4.8	1.14	1.02
BK-TVM_2	3.3	2.8	3.8	1.18	0.87
BP-TVM_2	5.1	3.6	4.8	1.42	1.06
BK-TVM_3	3.1	3.25	3.8	0.95	0.82
BP-TVM_3	4.9	4.5	4.8	1.09	1.02
BK-TVM_4	3.2	4.6	3.3	0.70	0.97
BP-TVM_4	5.0	3.4	4.8	1.47	1.04

In the above formulas:
A_k – the area bounded by the centre line of the thin-walled element cross section,
A_{Sl} – the area of the longitudinal reinforcement,
A_{Sw} – the area of the lateral reinforcement (a single reinforcement set),
T – the torsional moment,
b – the width of the element cross-section,
f_c – the compressive strength of the concrete,
f_{ct} – the tensile strength of the concrete,
f_y – the yield point of the reinforcement steel,
h – the height of the element cross section,
s – the (longitudinal) spacing of the stirrups,
t – the wall thickness of the equivalent thin-walled cross section,
u – the parameter of the concrete cross section,
u_k – the perimeter of area A_k,

α – the angle of lateral reinforcement inclination to the longitudinal axis of the element,

θ – the angle of inclination of the compressed concrete cross braces.

Table 6 shows stiffnesses K_T theoretically calculated for stage 1 (uncracked). The theoretical results were compared with the experimental results and the ones yielded by the numerical analyses. The theoretical results were calculated using equations found in the literature [e.g. 3, 4]. It is apparent that the theoretical stiffness was about 10% higher than the experimentally determined one. The FEM results were closer to the theoretical ones. It should be noted, however, that the stiffness theoretically calculated for the angular elements is lower than the empirical and numerical stiffnesses. This may be due to the beneficial effect of the flange on the stiffness of the beams.

6. Conclusion

On the basis of the results obtained from the tests and the numerical analyses and their comparison with the theoretical results one can formulate the following observations and conclusions:

a) The flange was found to have a beneficial effect on the torsional stiffness of the L-beams (BK). The BK beams were characterized by a smaller torsional angle than the beams rectangular in cross section (BP), even though the torsional moment of inertia (I_T) of the BP beams was higher. Percentage wise, the decrease in stiffness in the BK elements was about 0.5–10% smaller than in the corresponding (compared) BP elements.

b) The angular elements (BK) loaded with solely torsional moment T (pure torsion) showed only slightly greater load capacity than the corresponding rectangular elements rectangular (BP). In the tests the BK-T element showed load capacity 2% greater than the BP-T element. In the numerical analyses the BK-T element showed load capacity 3% greater than the BP-T element.

c) In the case of the elements subjected to combined bending, torsion and shearing, the angular elements showed lower load capacity than the corresponding rectangular elements. This was due to the effect of bending, in the case of which the height of the cross section plays a more decisive role.

d) In the elements subjected to both a torsional moment and a bending moment the decrease in stiffness was larger than in the elements loaded with solely a torsional moment (especially in the elements with the greater influence of bending at a bending moment/torsional moment ratio ≥ 2).

e) The experimental (load capacity, stiffness) values were mostly lower than the ones calculated from the standard formulas and the ones yielded by the numerical analyses. The differences between the numerical results and the experimental ones were in the order of ten to twenty per cent. Whereas the difference between the results yielded by standard calculations and the experimental ones was larger, reaching as much as a few tens of per cent.

It should be added that generally the load capacity of elements under torsion has been explored quite well whereas their stiffness still needs to be investigated, especially that it is the second most important aspect to be taken into account in the design of reinforced concrete elements subject to torsional moment. It often happens that an element with sufficient load capacity can no longer remain in service because its torsional stiffness has decreased so much that it disqualifies the element from further service.

It should be noted that the problem of the load capacity and limit states of angular elements under torsion has not been fully explored by this experimental research. Moreover, the number of elements tested by other researchers is not large enough to draw any general conclusions. A larger number of elements should be tested, taking into account a larger number of variables having an influence on the load capacity and deformability of reinforced concrete elements under torsion.

References

[1] *DIANA finite element analysis, users manual, release 9.0 – TNO building and construction researche*, Delft, The Netherlands, 2006.
[2] European Standard PN-EN 1992-1-1: September, 2008. *Eurocode 2. Design of concrete structures. Part 1–1: general rules and rules for buildings* (in Polish).
[3] Godycki-Ćwirko T.: *The mechanics of concrete* (in Polish), Arkady, Warsaw, 1982.
[4] Hsu T.T.C.: *Torsion of reinforced concrete*, Van Nostrand Reinhold Company, Inc., New York, 1984.
[5] Hsu T.T.C.: *Torsion of structural concrete*, ACI SP-18, 1968.
[6] Hsu T.T.C.: *Unified theory of reinforced concrete*, CRC Press, Inc., Boca Raton, Florida, 1993.
[7] Jensen B.Ch., Łapko A.: *On shear reinforcement design of structural concrete beams on the basis of theory of plasticity*, Journal of Civil Engineering and Management, Vol. 16, No. 1, 2010, pp. 395–403.
[8] Kamiński M., Pawlak W.: *Load-bearing capacity of reinforced concrete beams angular in cross section, subjected to torsion* (in Polish), Appendix 2 to Final Research Report. Report SPR No. 9, 2008, Institute of Building Engineering at Wrocław University of Technology.
[9] Karlsson J.: *Torsional stiffness of reinforced concrete structures in pure torsion*, Chalamers University of Technical, Report 71, Goeteborg, 1971.
[10] Kobielak S., Tatko R., Piekarz R.: *Method for approximate analysis of cracking effect on lateral stiffness of reinforced concrete framed-tube structures*, Archives of Civil and Mechanical Engineering, Vol. X, No. 1, 2010, pp. 43–57.
[11] Kuyt B.: *The ultimate torsional resistance of rectangular reinforced concrete beams*, Concrete Beams, Concrete, Vol. 12, 1968.
[12] Lampert P., Thurlimann B.: *Torsionsversuche an Stalbetonbalken*, Inst. für Baustatik ETH, Zurych, 1968.
[13] Lessig N.N.: *Determination of load-carrying capacity of rectangular reinforced concrete elements subjected to flexure and torsion* (in Russian), Trudy, No. 5, Concrete and Reinforced Concrete Institute, Moscow, 1959, pp. 5–28.

[14] Rahal K.N., Collins M.P.: *Analysis of sections subjected to combined shear and torsion – a theoretical model*, ACI Structural Journal, Vol. 92, No. 4, 1995.
[15] Rahal K.N., Collins M.P.: *Effect of thickness of concrete cover on shear-torsion interaction – an experimental investigation*, ACI Structural Journal, Vol. 92, No. 3, 1995.
[16] Rahlews K.: *Zur Torsionssteifigkeit von Stahlbetonrechtquerschnitten*, Bethon und Stalhbeton, Vol. 9, 1970.
[17] Ramirez J.A., Breen J.E.: *Evaluation of a modified truss-model approach for beams in shear*, ACI Structural Journal, Vol. 88, No. 5, 9–10, 1991.
[18] Rausch E.: *Berechnung des Eisenbetons Genge Verdrehung*, Technische Hochschule, Berlin, 1929.
[19] Vecchio F.J., Collins M.P.: *The modified compression-field theory for reinforced concrete Elements subjected to shear*, ACI Structural Journal, Vol. 83, No. 2, 1986.
[20] Vecchio F.J., Collins M.P.: *The response of reinforced concrete to in-plane shear and normal stresses*, Publication 82–03, Department of Civil Engineering, University of Toronto, Toronto, 1982.

Nośność i sztywność żelbetowych belek skręcanych o kątownikowym kształcie przekroju poprzecznego

W artykule przedstawiono wyniki badań doświadczalnych, analiz numerycznych oraz analiz teoretycznych żelbetowych belek obciążonych momentem skręcającym oraz siłą tnącą i momentem zginającym, które przeprowadzono w Laboratorium Badawczym Instytutu Budownictwa Politechniki Wrocławskiej. W artykule skoncentrowano się na nośności i sztywności tych elementów. Badane elementy miały różny przekrój poprzeczny: kątownikowy (w kształcie odwróconej litery L) lub prostokątny. Sposób obciążania elementów podzielił badania na dwie serie badań. Pierwsza seria – badane elementy obciążano tylko momentem skręcającym. Druga seria – belki były obciążone momentem skręcającym, siłą tnącą i momentem zginającym. W pracy porównano zachowanie się belek o różnym kształcie przekroju poprzecznego. Porównano także wyniki uzyskane doświadczalne i otrzymane w analizach numerycznych z rezultatami teoretycznymi i normowymi.

ARCHIVES OF CIVIL AND MECHANICAL ENGINEERING

Vol. XI 2011 No. 4

Construction optimization of hydrodynamic torque converter with application of genetic algorithm

A. KĘSY
Technical University of Radom, Malczewskiego 29, 26-600 Radom, Poland.

A. KĄDZIELA
Technical University of Łódź, Faculty of Mechanical Engineering, S. Żeromskiego 116, Łódź, Poland.

This paper describes multi-objective construction optimization of hydrodynamic torque converter with the application of a genetic algorithm. The main optimization criteria were: torque ratio, efficiency, permeability and a range of high efficiencies. Overall 16 variables were selected as main optimized parameters. Among them were: active diameter, parameters of meridional cross section, blade angles on core and shell. Value ranges of these variables were obtained from the analysis of constructed prototypes. Mathematical model based on multiple streams was applied. Sample calculations were provided for hydrodynamic torque converter type PH 410. The results of these calculations provided a set of suboptimal parameters that were utilized as a basis for further consideration. In addition, influence of range limitations of optimized parameters into optimization results was analyzed. The influence varies significantly.

Keywords: *Construction optimization, hydrodynamic torque converter, genetic algorithm*

1. Introduction

Hydrodynamic torque converters (HTC) are widely used in vehicle power transmission systems. HTC construction is simple, reliable and long lasting. Major disadvantages of HTC are low efficiency, necessity of delivering working fluid and relatively low torque ratio. Due to low torque ratio the HTC works together with a mechanical transmission creating a hydrodynamic power transmission system. The main advantage of hydrodynamic power transmission system application is its smooth, quiet and long lasting reliable performance.

In order to select best suitable construction of HTC an application of mathematical modelling to construction optimization calculations is necessary. Mathematical models based on average stream theory are still applied. In order to increase modelling accuracy additional parameters such as working fluid temperature [9], or considering the working fluid flow through as a set of individual streams and diligent parameter estimation for the mathematical model [8] are introduced. HTC model estimation calculations apply stochastic methods. In order to perform proper estimation empirical testing of the considered HTC is required.

2. Construction optimization of the hydrodynamic torque converter

Construction optimization of the particular HTC to be included in the analyzed hydrodynamic power transmission system relies on optimal selection of values of preselected parameters of HTC working area.

2.1. Hydrodynamic torque converter quality indicators

In order to determine quality of HTC working in the hydrodynamic power transmission system, HTC quality indicators were introduced [8, 15]. These indicators evaluate steady-state characteristic, implementation properties, production and HTC ability to fulfil traction requirements of a vehicle where it is applied. Construction optimization uses quality indicators sorted into four groups:

- related to load type,
- related to power transfer type,
- related to condition of engine operation,
- economical.

Method of selecting parameters to define HTC quality indicators are shown on Figure 1. HTC loading properties are characterized by torque factors in pump impeller $\lambda_{M,1}$ and turbine impeller $\lambda_{M,2}$:

$$\lambda_{M,1} = M_1 / \rho\omega_1^2 D^5; \qquad \lambda_{M,2} = M_2 / \rho\omega_1^2 D^5, \tag{1}$$

where:

M_1, M_2 – torque of input and output shaft, respectively,
ω_1, ω_1 – angular speed of input and output shaft, respectively,
ρ – density of working fluid,
D – HTC active diameter.

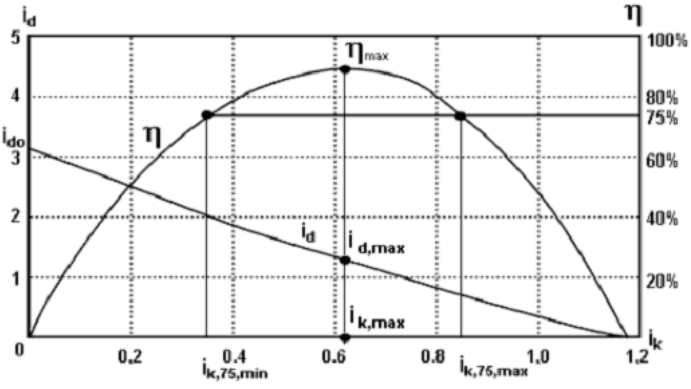

Fig. 1. Method of defining HTC quality indicators i_{do}, d_{75} and η_{max}

HTC power transferring properties are characterized by torque ratio $i_d = M_2/M_1$ defined for this purpose as:

$$i_d = \lambda_{M,1} / \lambda_{M,2}, \tag{2}$$

and value of torque ratio i_{do} for $i_k = \omega_2/\omega_1 = 0$.

Conditions of engine operation are characterized by permeability p:

$$p = \lambda_{M,1\max} / \lambda'_{M,1}, \tag{3}$$

where:

$\lambda_{M,1\max}$ – maximum value of torque factor,

$\lambda'_{M,1}$ – torque factor for $i_d = 1$.

HTC economical properties are characterized by the range of high efficiencies d_{75}:

$$d_{75} = \frac{i_{k,75,\max}}{i_{k,75,\min}}, \tag{4}$$

and by maximum efficiency $\eta_{\max}$ defined by equation $\eta_{\max} = (i_k i_d)_{\max}$. (5)

The HTC quality indicators applied during optimization proceedings depend on:

- geometric parameters of HTC working area,
- working fluid selection,
- construction of other HTC components.

During steady-state motion of hydrodynamic power transmission system HTC quality indicators are constant.

2.2. Optimization method

Selection of HTC optimization method depends on mathematical representation of this optimization problem. Due to:

- non-linearity and sophisticated form of applied HTC mathematical models,
- number of limitations with various magnitude and form,
- number of optimized parameters,

up to now HTC optimization utilizes primarily stochastic methods such as Monte Carlo or combinatorial and heuristic method Linja [1, 8, 11, 15].

2.3. Optimization criteria

Construction optimization contains three groups of optimization criteria as follows:

- criteria of highest rigidity,
- criteria of constant strength,
- criteria of minimum cost.

Rigidity and strength of impellers is determined by construction technology. Typical construction technologies provide blades and walls of core and shell with thickness from 3 to 4 mm for caste impellers and from 0.8 to 1.2 mm for impellers made from pressed steel metal sheets. Therefore the most important HTC design criterion is minimization of cost. This criterion is tied to vehicular performance where the hydrodynamic power transmission system is applied [8]. Production cost and transportation of worked-on media were taken as a construction optimization criteria of HTC applied to heavy duty work machinery [15]. These criteria were defined as a maximization of an average efficiency of each working cycle in work [15]. Other works such as [10] recommend using range of economical HTC performance – d_{75}, this criterion should lead to maximum performance.

Also in practice as optimization criteria the following quality indicators are used [15]:

- HTC efficiency – $\eta_{\max}$,
- torque ratio for zero speed ratio – i_{do},
- permeability – p,
- HTC range of high efficiencies – d_{75}.

These indicators also should reach the highest possible values.

2.4. Optimized parameters

Optimized parameters required during construction optimization of HTC should be selected from a set of all HTC parameters. All selected parameters have to be present in the applied optimization mathematical model. During HTC optimization geometrical parameters of working area are primarily considered such as: HTC working area meridional cross section shape [5, 12, 18] number of blades [16], profile of stator blades [14], and additional mass moments of inertia and rigidity of impellers shafts [17].

Stochastic calculation methods tend to significantly increase the number of required iterations with increased number of variables. Therefore variables with the most significant influence on optimization criteria should be selected to become the optimized parameters. Work [15] recommends selecting 6 optimized parameters for construction optimization of HTC such as blade angles on average line on inlet and exit of impellers – β_{ij}. Works such as [2] selected the following 10 parameters as optimized parameters:

- HTC active diameter D,
- 6 mean path blade angles,
- 3 dimensionless coefficients that are included in mathematical description of geometrical working area shape.

2.5. Optimization model

The mathematical model of hydrodynamic torque converter applied to optimization should be [8]: simple, accurate, and it should allow estimation of model parameters. Such model is called multi-stream model and is described in chapters 2.51 and 2.52.

2.5.1. Multi-stream model assumptions

The multi-stream model designated for optimization was developed based on the following assumptions:

- entire through flow in HTC working area consists of n_o independent streams,
- a torque carried by HTC is equal to a sum of all streams torques carried by each individual stream,
- the contribution of each individual stream to carry out the torque differs and depends on assumed torque function $y = f(x)$,
- each individual stream is described by a single-dimensional average stream model [8, 9, 13, 15],
- the result of the modelling of the entire through flow in HTC working area consists of the sum of the flow results for each individual stream included in the entire through flow in HTC working area.

Based on the analysis of actual velocity ranges in the HTC working area [2, 4] it was assumed that the torque function $y = f(x)$ is sloping upward, is measurable, differentiable, and continuous in the range of $0 < x \le 1$ and that the torque function is characterized by values of three constant coefficients a, b, c obtained from the assumed range of change. The independent variable x in the torque function is a consecutive number n for each corresponding stream divided by the number of all streams in the considered through flow n_o ($0 < x \le 1$) but the contribution factor of the torque carrying through y in the range of ($0 \le y \le 1$) is taken as the dependent variable. Usually values of torque calculated with the average stream model are smaller than the values obtained from empirical measurements. This fact is considered as a major disadvantage of the average stream model [8–9, 13] therefore these parameters are multiplied by a constant z for every stream ($z > 1$).

2.5.2. Model equations

The main purpose of the model is a calculation of the non-dimensional steady-state characteristic of HTC for pre-selected values of speed ratio i_k with utilization of numerical methods, therefore it is considered to be as a discrete numerical model. The model equations are as follows:

$$i_d(i_k) = \frac{M_2}{M_1}, \qquad \lambda(i_k) = \frac{M_1}{\rho D^5 \omega_1^2}, \qquad \eta(i_k) = i_d i_k, \tag{6}$$

where:

$$M_1(i_k) = z\sum_{n=1}^{n_o} y_n M_{1,n}, \qquad M_2(i_k) = z\sum_{n=1}^{n_o} y_n M_{2,n},$$

$$M_{1,n} = \rho k_{12/32,n} Q^2 + \rho r_{12,n}^2 \omega_1 Q,$$

$$M_{2,n} = \rho k_{12/22,n} Q^2 + \rho r_{12,n}^2 \omega_1 Q + \rho r_{22,n}^2 \omega_2 Q,$$

$$a_{1,n}\omega_1^2 + a_{2,n}\omega_2^2 + a_{3,n}Q^2 + a_{4,n}\omega_1 Q + a_{5,n}\omega_2 Q = 0$$

and

$$k_{a/b} = \frac{r_a}{F_m} ctg\,\beta_a - \frac{r_b}{F_m} ctg\,\beta_b,$$

$$a_{1,n} = \frac{1}{2}\left((2r_{12,n}^2 - r_{11,n}^2 - \frac{r_{12,n}^4}{r_{21,n}^2} \right),$$

$$a_{2,n} = \frac{1}{2}\left((2r_{22,n}^2 - r_{21,n}^2 - \frac{r_{22,n}^4}{r_{31,n}^2} \right),$$

$$a_{3,n} = -\frac{1}{2}\left(\frac{1}{r_{11,n}^2} k_{32/11,n}^2 + \frac{1}{r_{21,n}^2} k_{12/21,n}^2 + \frac{1}{r_{31,n}^2} k_{22/31,n}^2 \right) -$$

$$-\frac{\psi}{F_{m,n}} \left(ctg^2 \beta_{12,n} + ctg^2 \beta_{22,n} + ctg^2 \beta_{32,n} + 3 \right),$$

$$a_{4,n} = k_{12/32,n} + k_{32/11,n} - \frac{r_{12}^2}{r_{21}^2} k_{12/21,n},$$

$$a_{5,n} = -k_{12/22,n} - k_{12/21,n} + \frac{r_{22,n}^2}{r_{31,n}^2} k_{22/31,n},$$

$$F_{m,n} = \frac{\pi (r_{gz}^2 - r_{gw}^2)}{n_o},$$

where i is impeller number ($i = 1$ – impeller of the pump, $i = 2$ – impeller of the turbine, $i = 3$ – impeller of the stator), j is inlet or exit of impeller ($j = 1$ inlet, $j = 2$ exit),

$$r_{11,n} = \sqrt{\frac{n}{n_o} r_{dz}^2 + \left(1 - \frac{n}{n_o}\right) r_{dw}^2}, \qquad r_{12,n} = \sqrt{\frac{n}{n_o} r_{gz}^2 + \left(1 - \frac{n}{n_o}\right) r_{gw}^2},$$

where n changes from 0 to n_o and $\bar{r}_{1j,n} = \sqrt{\frac{r_{1j,n}^2 + r_{1j,n1}^2}{2}}$, where n changes from 1 to n_o determining a stream number.

$$\beta_{ij,n} = \frac{(\beta_{ijz} - \beta_{ijw})(\bar{r}_{ij,n} - r_w)}{r_z - r_w},$$

where: for the inlet $r_w = r_{gw}$, $r_z = r_{gz}$, and for the outlet $r_w = r_{dw}$, $r_z = r_{dz}$.

Remaining radii of the mean path streams were obtained as follows:

- for impeller of the turbine – the inlet radius equal to the exit radius of the pump impeller,
- for impeller of the stator – the inlet and the exit radius equal to the radius of the inlet of the pump impeller.

The radii determining impellers dimensions are shown in Figure 2.

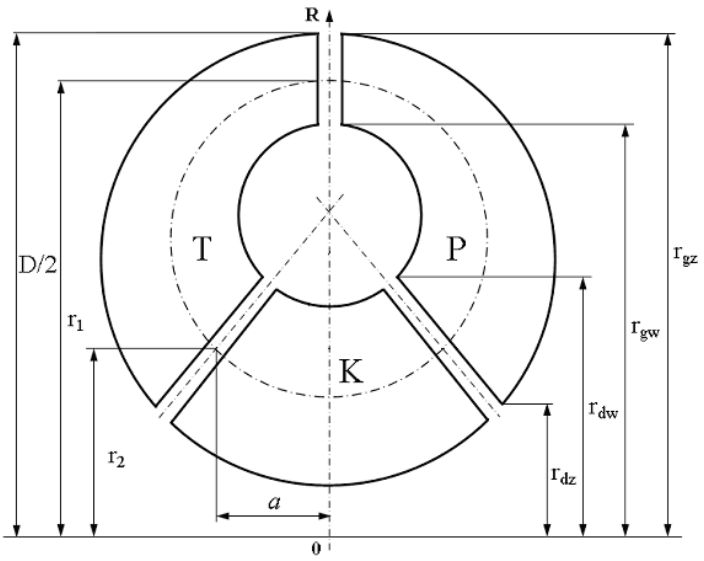

Fig. 2. Proposed method of impellers radii marking

The following were provided as the input data to the model:

- parameters of HTC operation point – i_k and ω_1,
- model parameters: a number of speed ratio values k_o, a number of streams n_o, value of flow losses factor ψ, an increasing torque factor z,
- geometric dimensions of HTC working area – D, $r_{gz}=D/2$, r_{gw}, r_{dz}, r_{dw}, $\beta_{ij,z}$, $\beta_{ij,w}$,
- torque function $y = f(x)$ and its parameters: a, b, c.

The calculated results are: torques obtained on HTC inlet and exit shafts that allow obtaining non-dimensional steady-state characteristic of HTC (acc. to formulae (6)).

3. Construction optimization of the pre-selected hydrodynamic torque converter

Construction optimization was performed for HTC type PH 410. It is a HTC containing three impellers: pump, turbine, stator, Figure 2, with active diameter D = 0.41 m. Basic data pertaining to geometry of working area within this HTC are shown in Table 1.

Table 1. HTC type PH 410 data; D, r [m], β [°]

$D = 2r_{gz} = 0.41$	$r_{gw} = 0.177$	$r_{dz} = 0.098$	$r_{dw} = 0.134$
$\beta_{11w} = 96$	$\beta_{11z} = 94$	$\beta_{12w} = 133$	$\beta_{12z} = 131$
$\beta_{21w} = 33$	$\beta_{21z} = 30$	$\beta_{22w} = 156$	$\beta_{22z} = 149$
$\beta_{31w} = 74$	$\beta_{31z} = 85$	$\beta_{32w} = 20$	$\beta_{32z} = 23$

3.1. Estimation of the model parameters

The parameter estimation calculations of the multi-stream HTC type PH 410 model was performed through comparison of empirical measurement data with the results obtained from the model. As an accuracy criterion the average relative error of modelling points from the non-dimensional steady-state characteristic of HTC was considered [8]. This criterion, calculated for all considered values of i_k should obtain minimal values.

3.1.1. Empirical analysis and measurements

In order to estimate model parameters the empirical analysis and measurements were performed on the special testing rig that allowed loading the HTC with various torque continuously controlled under different rotational velocities of inlet and exit shafts. The analysis was performed under constant angular velocity of the inlet shaft equal to $\omega_1 = 210$ rad/s. The measured parameters were values of speed ratio i_k within a range 0 to 1. Twenty four measurement points were taken ($k_o = 24$). For each measurement point a measurement of angular velocity on exit and torque on inlet and exit shaft were taken. Based on this measurement an empirical non-dimensional steady-state characteristic of HTC type PH 410 was created.

3.1.2. Estimating calculations

For estimation calculations the following were selected: a torque function in the form of $y = |a/(b + cx^3)|$, a, b, c parameters: z, ψ and a number of streams n_o. Values of the model parameters obtained based on calculations are shown in Table 2. Figure 3 shows a torque function curve.

Table 2. Parameter values obtained from estimation calculations

a	b	c	ψ	z	n_o
1.43792766	1.09677419	1.99902248	0.39970674	2.74193548	30

3.2. Optimization procedure

The performed construction optimization of HTC type PH 410 was multi-objective. One optimization criteria was selected as the main one, the rest was converted to limits. The following main criteria were selected for the optimization quality of HTC:

- value of torque ratio i_{do} for $i_k = 0$,

- HTC permeability – p,
- HTC range of high efficiencies – d_{75}.

A multi-stream model was selected as a mathematical representation.

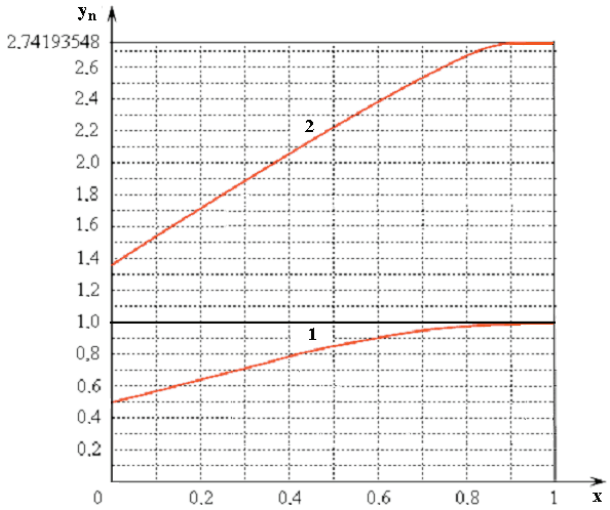

Fig. 3. Torque function curve $y=|a/(b + cx^3)|$ with values of a, b, c per Table 2:
1 – curve after recalculation of function range to $0 \le y_n \le 1$, 2 – function curve after multiplying by z

Among many parameters the following variables were selected as optimized parameters:

- HTC active diameter – D,
- dimensionless parameters describing meridional cross section of HTC [8], Figure 2:

$$\rho_1 = \frac{2r_1}{D}, \qquad \rho_2 = \frac{2r_2}{D}, \qquad \chi = \frac{2a}{D}, \tag{7}$$

- blade angles on core and shell of HTC impellers (on core β_{ijw} and on shell β_{ijz}, 12 parameters).

Overall 16 parameters were selected as optimized parameters. Ranges of each optimized parameter values assumed based on the parameter values obtained from the actual constructions of HTC [6] as shown in Table 3.

Table 3. Assumed ranges of optimized parameters, D [m], β [°]

$0.38 \ge D \ge 0.44$	$0.93 \ge \rho_1 \ge 0.945$	$0.547 \ge \rho_2 \ge 0.626$	$0.15 \ge \chi \ge 0.18$
$90 \ge \beta_{11w} \ge 130$	$90 \ge \beta_{11z} \ge 130$	$75 \ge \beta_{12w} \ge 150$	$75 \ge \beta_{12z} \ge 150$
$30 \ge \beta_{21w} \ge 75$	$30 \ge \beta_{21z} \ge 75$	$129 \ge \beta_{22w} \ge 160$	$129 \ge \beta_{22z} \ge 160$
$70 \ge \beta_{31w} \ge 140$	$70 \ge \beta_{31z} \ge 140$	$20 \ge \beta_{32w} \ge 50$	$20 \ge \beta_{32z} \ge 50$

A simple genetic algorithm method was applied to optimization. The genetic algorithm is based on the natural process of selection. Genetic selection occurring in nature is mathematically modelled. Random selection is applied to find the minimum value of quality criteria. Crossing over parts of the coded strings, coding of solution range, multiplication of code strings and generation of pseudorandom numbers are applied in these models with using computer programming. In order to apply this method to parameter estimation, rescaling to range of 0 to 1 has to be performed. The parameters are binary coded with the resolution of ten binary places. The fitness function is defined as converging to the minimum. Different methods are used to obtain the optimal parameter selection and various probabilities of crossing and mutation are given. As a result a set of parameters providing minimum quality criteria value are obtained. The genetic algorithm parameter values applied during calculations are shown in Table 4.

Table 4. Genetic algorithm parameters recommended for further calculations

Initial random value	Crossover probability	Mutation probability	Population size	Number of generations
0.45	0.9	0.01	100	5000

In order to limit involvement inside of the genetic algorithm structure it was assumed that the fitness function value is decreased through its division by a constant s whenever the required conditions by optimization criteria modified to limits are not met. The decrease of the fitness function value creates significantly increased probability of the elimination of such set of parameters from the optimization calculations. Since three criteria are converted to limits the fitness function is divided by s^3 in the worst case scenario. Based on the initial calculations the value $s = 10$ was assumed.

3.3. Optimization calculations for hydrodynamic torque converter

The main goal of optimization calculations is to find a set of values of the optimized parameters (16 selected parameters of HTC), where the main criteria obtains maximum and the criteria converted into limits fulfil the assumed limits at the same time. Beside calculations of the optimized parameters a numerical analysis of the limit influence and the range of the optimized parameters values on the results of the optimization were performed. During this consideration the HTC maximum efficiency $\eta_{\max}$ was added as an additional criterion.

3.3.1. Calculation of a set of values of the optimized parameters

During the construction of the actual HTC the limits are determined by the constructor based on the technical requirements. In calculations of criteria converted into limits the assumed range of limits was determined based on construction recommendations [8, 15]. The limit ranges are shown in Table 5.

Table 5. The main criteria and the criteria converted into limits during HTC optimization

No.	Main criteria	The optimal value obtained	Criteria converted into the limits
1	i_{do}	Maximum	$d_{75} \geq 1.8$; $p \geq 1.3$
2	d_{75}		$i_{do} \geq 2$; $p \geq 1.3$
3	p		$i_{do} \geq 2$; $d_{75} \geq 1.8$

Calculations were performed based on custom computer programs written in Turbo Pascal high level programming language. The obtained results of maximal values of main criteria, values of limits and values of optimized parameters are shown in Table 6.

Table 6. Values of the decisive variables obtained during HTC optimization

No.	Main criteria	Values of limits	Set of the optimized parameters D [m], β [°]			
1	$i_{do} = 3.49$	$d_{75} = 1.80$ $p = 1.30$	$D = 0.4192$	$\rho_1 = 0.9448$	$\rho_2 = 0.5749$	$\chi = 0.1687$
			$\beta_{11w} = 100.5$	$\beta_{11z} = 91.4$	$\beta_{12w} = 119.1$	$\beta_{12z} = 140.6$
			$\beta_{21w} = 30.1$	$\beta_{21z} = 30.0$	$\beta_{22w} = 144.4$	$\beta_{22z} = 151.6$
			$\beta_{31w} = 122.2$	$\beta_{31z} = 139.3$	$\beta_{32w} = 27.6$	$\beta_{32z} = 22.6$
2	$p = 2.0$	$i_{do} = 2.00$ $p = 1.30$	$D = 0.4020$	$\rho_1 = 0.9335$	$\rho_2 = 0.5553$	$\chi = 0.1638$
			$\beta_{11w} = 126.6$	$\beta_{11z} = 121.7$	$\beta_{12w} = 110.5$	$\beta_{12z} = 90.1$
			$\beta_{21w} = 37.2$	$\beta_{21z} = 35.9$	$\beta_{22w} = 158.9$	$\beta_{22z} = 146.0$
			$\beta_{31w} = 84.7$	$\beta_{31z} = 73.9$	$\beta_{32w} = 29.1$	$\beta_{32z} = 21.5$
3	$d_{75} = 3.77$	$i_{do} = 2.00$ $d_{75} = 1.80$	$D = 0.4366$	$\rho_1 = 0.9432$	$\rho_2 = 0.5474$	$\chi = 0.1664$
			$\beta_{11w} = 100.9$	$\beta_{11z} = 100.9$	$\beta_{12w} = 75.4$	$\beta_{12z} = 75.0$
			$\beta_{21w} = 30.2$	$\beta_{21z} = 30.0$	$\beta_{22w} = 160.0$	$\beta_{22z} = 153.5$
			$\beta_{31w} = 122.2$	$\beta_{31z} = 140.0$	$\beta_{32w} = 23.1$	$\beta_{32z} = 49.2$

3.3.2. Influence of the limits

Numerical analysis of the influence of the limits on possible values of the main criteria that can be obtained was performed for the criteria converted into the limit values as listed in Table 6. Initially, the values of the main criteria without consideration of the limits were calculated based on data listed in Table 3. The obtained results are shown in Table 7. Next, the limits were introduced and the maximum value of the main criteria was looked for while fulfilling conditions of the criteria converted into the limits. The desire was to obtain the maximum value of the main criteria under the largest possible values of the limits. Sample calculation results are shown in Table 8.

From a comparison of the results shown in Tables 7 and 8 it can be concluded that the limits have significant influence on the value of the main criteria with the exception of HTC range of high efficiencies – d_{75}. In case of criteria i_{do} and p the influence is more significant. On the other hand the influence on the maximum efficiency $\eta_{\max}$ is negligible.

Table 7. Maximum values of the main criteria calculated without limits

No.	Main criteria	Criteria value
1	i_{do}	4.27
2	$\eta_{\max}$	0.92
3	d_{75}	2.0
4	p	4.31

Table 8. Values of the main criteria obtained with the assumed values of the criteria converted into limits

Value of the main criteria	Value of limits	Value of the main criteria	Value of limits
$i_{do} = 3.17$	$\eta_{max} = 0.83$ $d_{75} = 1.85$ $p = 1.3$	$d_{75} = 2.0$	$i_{do} = 2.00$ $\eta_{max} = 0.80$ $p = 2.50$
$\eta_{\max} = 0.90$	$i_{do} = 2.30$ $d_{75} = 1.85$ $p = 1.80$	$p = 3.77$	$i_{do} = 2.00$ $\eta_{max} = 0.85$ $d_{75} = 1.80$

3.3.3. Influence of the optimized parameters

In order to analyze the influence of the optimized parameters on the optimization results, calculations for blade angles were performed. These variables according to literature [2–3] have significant influence on the HTC characteristics. Two blade angle ranges were selected: wide and narrow. The blade angle values for such ranges are shown in Table 9. Optimization was performed for the pre-selected main criteria i_{do}, $\eta_{\max}$, d_{75}, p for the angle ranges provided from the actual construction according to Table 9. The obtained optimal result values of main criteria are shown in Table 10.

Table 9. Angle ranges β [°] selected to optimization calculations

	β_{11w} β_{11z}	β_{12w} β_{12z}	β_{21w} β_{21z}	β_{22w} β_{22z}	β_{31w} β_{31z}	β_{32w} β_{32z}
Wide angle range	60–130	60–150	30–100	120–160	60–150	10–60
Narrow angle range	95–120	110–120	50–70	135–140	80–100	30–40

Table 10. Values of the main criteria for angle ranges taken from actual HTC constructions for wide and narrow angle range

Angle Range	Optimization criteria			
	i_{do}	$\eta_{\max}$	d_{75}	p
Actual contractions per Table 3	4.27	0.92	2.0	4.31
Narrow angle range per Table 9	2.75	0.89	2.0	1.67
Wide angle range per Table 9	4.33	0.93	2.0	7.32

After comparing the results shown in Table 10 it can be concluded that the range variation of blade angles has a significant influence on the values of the main criteria

with the exception of the HTC range of high efficiencies – d_{75}. The influence of the angle value range on the optimal value of the main permeability criteria p is very significant. In case of criteria i_{do}, the influence is less significant, but it is negligible for maximum efficiency $\eta_{\max}$ and d_{75}.

Based on these results it can be concluded that there is a certain blade angle value range where good efficiencies can be obtained.

3.3.4. Calculations time

Time required for one optimization calculation cycle for a number of 5000 generations and a population size equal to 100 with 16 parameters on Pentium IV, 3.1 GHz computer was about 12 hours.

In order to shorten calculation time a parallel genetic algorithm was also applied. The parallel genetic algorithm calculates evolution of two populations at the same time. After a certain number of generations an exchange of some parameters values occurs and further evolution calculation takes place. Such procedure lasts until optimal value is obtained. Application of the parallel genetic algorithm neither provided better results nor shortened the time of calculations. Based on this analysis it can be concluded that the application of evolution methods other than a genetic algorithm to the optimization of HTC construction is not necessary, because the genetic algorithm allows to provide satisfactory results in reasonable time much shorter than other random numerical methods.

4. Evaluation of optimization calculations

During the optimization of the HTC construction sets of sub-optimal parameters required to fabrication initiation were obtained. From the calculated sets of parameters shown in Table 6 one set needs to be chosen. The parameter values should be convenient from technological aspects, providing higher value of the main criteria and satisfactory values of criteria converted to limits at the same time. For example, an HTC impeller blade with small inlet angle is easier to fabricate than a blade with large inlet angle. Furthermore it is desired to obtain the proper shape of the flow channel with limited curvature, small length and small hydraulic radius (small ratio of channel cross section area and its circumference). Based on the selected set of optimized parameters the shape of the HTC working area is determined through blade core and shell profiles. This data allows building a 3-D model of HTC impellers using the available CAD software [5].

From the analysis of the construction process of the HTC working area it can be concluded that the determination of the optimized parameters is not sufficient but necessary in order to obtain the optimal HTC working area construction. An optimal working area is considered as area that provides minimal flow through losses and the least technological problems during fabrication. The working area geometrical shape also

depends on: curvature angle of the inlet blade edge, an angle along the blade edge and a bending angle along the inlet blade length [8, 15].

Based on the analysis of the influence of blade angle range changes it can be concluded that HTC construction with high values of d_{75} and $\eta_{\max}$ criteria can be obtained under limited range of blade angles. It concurs with conclusions provided in [8, 15] dissertations that selection of angle values beyond the typically applied range in the existing HTC constructions almost always leads to worse construction quality. The optimization calculations also confirm opposite influence of maximum efficiency $\eta_{\max}$ and dynamic ratio i_{do} on HTC characteristics (for HTC construction with high values of i_{do} the maximum efficiency $\eta_{\max}$ HTC is smaller).

The application of genetic algorithm allows to obtain accurate results within several hours, the genetic algorithm is efficient, calculative and determinative [3]. Furthermore genetic algorithm is universal and it can be applied to estimation and optimization calculations of HTC with more accuracy and certainty of obtaining global optimum than other previously applied optimization methods.

5. Conclusions

In this paper construction optimization of HTC with application of genetic algorithm was described. The scope of this optimization contains optimization of HTC impeller working area. Multi-objective type of optimization was applied. As main optimization criteria was selected: a value of torque ratio for $i_k = 0$, therefore i_{do}, HTC efficiency – $\eta_{\max}$, HTC permeability – p and HTC range of high efficiencies – d_{75}. These criteria should obtain maximum value. As optimized parameters the following were selected: HTC active diameter, HTC meridional cross section and blade angles on core and shell, overall 16 parameters. The ranges of value for these parameters were selected based on values obtained from fabricated HTC constructions. A model of multiple streams was used as the mathematical model. Sample calculation for HTC type HTC 410. Selected parameters of the model were estimated based on analysis of HTC type HTC 410. As a result of these calculations sub-optimal set of parameters were obtained. These parameters are the output data for further construction.

References

[1] Bazhenov N.S. et al.: *Design of follow-up hydraulic transmission systems for flying machines*, Mashinostroenie, Moscow, 1981.

[2] Brun K., Flack R.D.: *Laser velocimeter measurements in the turbine of an automotive torque converter*. Part I – *average measurements*, Transactions of the ASME, Journal of Turbomachinery Vol. 119, 1997, pp. 646–654.

[3] Goldberg D.: *Genetic algorithms in search, optimization, and machine learning*, Addison-Wesley Publishing Company, Inc. Massachusetts, USA, 1989.

[4] Gruver J.K., Flack R.D., Brun K.: *Laser velocimeter measurements in the pump of an automotive torque converter*. Part I – *average measurements*, Transactions of the ASME, Journal of Turbomachinery, Vol. 118, July 1996, pp. 562–569.
[5] Ishihara T. et al.: *An experimental analysis of fluid flow in a torque converter*, SAE Paper 830571, 1983, pp. 67–76.
[6] Kęsy A.: *Development of impellers with optimal parameters for hydrodynamic transmission systems of transportation means* (in Russian), DSc Thesis, MADI Technical State University, Moscow, 1999.
[7] Kęsy A.: *Mechatronic design of impellers of hydrodynamic element in automobiles*, Int. J. Vehicle Design, Vol. 38, No. 2–3, 2005, pp. 234–239.
[8] Kęsy A.: *Numerical identification and optimization of means of transport hydrodynamic power transmission system* (in Polish), Monograph, Technical University of Radom Press, Radom, 2004.
[9] Kęsy Z.: *Hydrodynamic torque converter control through properties of working fluid* (in Polish), Monograph, Technical University of Radom Press, Radom, 2003.
[10] Kęsy Z., Kęsy A., Madeja J.: *Identification of hydrodynamic torque converter controlled by physical properties of working fluid*, Int. Conference "Modern Practice in Stress and Vibration Analysis", Dublin, 1997, pp. 557–572.
[11] Martyna M., Kardasz R.: *Multi-objective optimization of new type working system of loader* (in Polish), Problemy Maszyn Roboczych, Vol. 6, No. 6, 1995, pp. 12–17.
[12] Minato K., Sakamoto K., Takagi M., Fujitani K.: *Performance prediction of a hydrodynamic torque converter*, Japan Automobile Research Institute Society of Automotive Engineers, Japan, 1990, pp. 740–747.
[13] Pawelski Z.: *Investigation of hydrodynamic torque converter characteristics for unsteady-state of load* (in Polish), PhD Thesis, Technical University of Łódź, 1980.
[14] Stesin S.P.: *Method of objective function determination for design optimisation of hydrodynamic torque converter*, Sbornik Nauchnykh Trudov MADI, Moscow, 1983.
[15] Stesin S.P.: *Parameters optimisation of hydraulic transmission for building and road machines systems*, Mashinostroenie, Moscow, 1996.
[16] Stesin S.P.: *Selection of mathematical method for parameter optimisation of hydraulic machines and mechanisms*, Sbornik Nauchnykh Trudov MADI, Moscow, 1990.
[17] Stesin S.P., Yakovenko Ye.A.: *Blade machines and hydrodynamic transmission systems*, Mashinostroenie, Moscow, 1990.
[18] Yamaguchi J.: *Super-flow torque converter improves acceleration*, Automotive Engineering, Vol. 96, No. 12, 1988, pp. 83–84.

Optymalizacja konstrukcji przekładni hydrokinetycznej z użyciem algorytmu genetycznego

W artykule opisano wielokryterialną optymalizację konstrukcji przekładni hydrokinetycznej z użyciem algorytmu genetycznego. Jako główne kryteria optymalizacji wybrano: przełożenie dynamiczne, sprawność, przenikalność oraz zakres wysokich sprawności. Na zmienne decyzyjne przyjęto: średnicę czynną, parametry przekroju merydionalnego oraz kąty łopatek na torusach, razem 16 parametrów. Zakresy zmienności tych parametrów ustalono na podstawie analizy rzeczywistych konstrukcji. Jako model matematyczny zastosowa-

no model wielu strug. Wykonano przykładowe obliczenia dla przekładni hydrokinetycznej typu PH 410. W wyniku obliczeń otrzymano suboptymalne zestawy parametrów, będące danymi wyjściowymi do dalszych rozważań. Ponadto zbadano wpływ ograniczeń oraz zakresów zmian zmiennych decyzyjnych na rezultaty optymalizacji. Stwierdzono, że wpływ tych zmian jest różny.

ARCHIVES OF CIVIL AND MECHANICAL ENGINEERING

Vol. XI 2011 No. 4

Static and dynamic response of cost effective unreinforced brick masonry buildings

I.K. KHAN
Department of Civil Engineering, Aligarh Muslim University, Aligarh 202 002, India.

H. ABBAS
Specialty Units for Safety and Preservation of Structures, College of Engineering,
King Saud University, Riyadh 11421, Saudi Arabia.

Besides the buildings with conventional one-brick thick solid masonry walls, two cost effective masonry wall constructions, viz. reduced thickness and cavity wall, have been studied for their lateral load resistance. The reduced thickness of wall was constructed with a combination of bricks on bed and bricks on edge; whereas the cavity wall was constructed with bricks on edge in Flemish bond using solid fired-earth bricks. Single storey one-room building models were subjected to static lateral load and shake table tests. The study shows that there is considerable reduction in shear strength of buildings with cost effective masonry and the reduction is more than the saving in the material, which is due to increase in the vertical mortar joints in both masonry types. The base isolation system, using Teflon sheet, shows great promise for adoption in conventional as well as the cost effective building construction as a measure of earthquake safety.

Keywords: *brick masonry, cost effective, shake table, lateral load, fired-earth brick*

1. Introduction

Fired-earth brick masonry is being used in the construction industry from the time immemorial and even today it is one of the most common and popular cost-effective construction materials in the third-world countries. The cost of housing is no more affordable by the common man and thus providing shelter to everyone is becoming difficult. Though some cost effective methods are available, especially for brick masonry construction, but these have never been thoroughly tested. Thus there is an urgent need for research in this area for making safe and at the same time affordable homes for the common man.

Some of the prevalent low cost brick masonry construction techniques involve the construction of brick masonry cavity walls (one brick thick i.e. thickness of wall = L) using bricks on edge and reduced thickness walls (thickness of wall = $B + H$) by using the conventional solid bricks of size $L \times B \times H$, where L, B and H are length, width and thickness of brick respectively ($L = 3H$ and $B = 1.5H$). Though considerable saving in the cost can be achieved by such techniques but their adoption in practice re-

quires thorough understanding about the response of such structures to lateral loads especially the earthquakes. The present study was conducted for assessing the performance of such low cost buildings and to improve their performance for resisting the earth- earthquake forces.

Brick masonry buildings respond to ground motion like all other structures and attract inertia forces depending on their stiffness, mass and damping characteristics [13]. Many investigators including Bruneau [3] investigated the performance of a number of unreinforced masonry buildings during earthquake in a large portion of North America which were constructed in the absence of mandatory earthquake design requirements, and unquestionably recognized the type of construction most vulnerable to earthquakes.

Tomezevic et al. [20] summarized the results of an experimental study that investigated the seismic behaviour of two and three-storey, plain and reinforced masonry building models with identical structural configuration. By reinforcing the masonry walls with vertical reinforcement and the border of the walls and horizontal reinforcement in mortar bed joints, the lateral resistance and energy dissipation capacity and global ductility of the building was significantly improved. The mechanism of the behaviour of the tested models changed from the storey mechanism that prevailed in the case of plain masonry model to coupled shear wall mechanism in the case of reinforced masonry building model, with floor slabs and bands contributing to the seismic resistance of the model in the latter case.

Yan et al. [21] developed a comprehensive analytical model and studied the response of unreinforced masonry under in-plane dynamic loads, including earthquake loads. Mostaghel et al. [14–15] presented a mathematical model for the response of sliding structures to harmonic motion which was first proposed by Qamaruddin et al. [17] for solving problem of single degree of freedom structures supported on sliding substructure and subjected to harmonic and also earthquake support motions. It was observed that for structures with time period less than 1.8 s the maximum sliding and residual displacements were of order of 1.25 times the peak ground displacements.

Lin et al. [12] proposed base isolation of masonry buildings, using two sets of mutually orthogonal free rolling rods under the basement of the structure. The result indicated that the super structure response decreases with the decrease in the rolling friction coefficients. Derham et al. [4] demonstrated that a building on rubber bearings will be protected simultaneously from unwanted vibration and from earthquake attack. The rubber bearings are suitable for masonry buildings as these are rigid. Qamaruddin et al. [16] studied the behaviour of unreinforced and partially reinforced masonry house models subjected to earthquake like loads and a new masonry building system with sliding substructure was also presented to obtain the advantage of seismic isolation. The results of analysis showed that the sliding system scheme was a practical and economical seismic isolation technique to achieve less damage as well as non collapsible masonry buildings requiring only the usual skills of construction locally available. Experimental tests by Arya et al. [1–2] reported the performance of a half size single storey brick masonry buildings subjected to shock loading in a railway

wagon impact facility. Several types of building models were tested, including both isolated and un-isolated, and it was concluded that a building with sliding joints at plinth level performed better than a conventional building.

Though the idea of cost-effective masonry wall construction has been propagated by some investigators [11, 18–19] but it lacks experimental support to demonstrate their performance under different loading conditions especially the earthquake. The present study focuses on the investigation of some of the prevalent cost effective masonry buildings under lateral loads. The introduction of sliding type base isolation system in conventional as well as the cost-effective building models has also been investigated for their performance under dynamic loads.

2. Experimental program

2.1. Materials used

Half size hand moulded burnt clay traditional solid bricks have been used in the present study. The average size of half size bricks was 114×57×38 mm having frog of 85×30×4 mm on one bed face only. The shape of frog was rectangular with rounded corners. These bricks were moulded manually in the laboratory from the brick-earth and were burnt properly in brick-kiln. Samples of bricks were tested for crushing strength and moisture absorption [5, 9]. The test results obtained are as follows:

- weight of brick = 0.44 kg,
- crushing strength on bed and on edge = 8.40 and 6.60 MPa,
- efflorescence: Nil,
- water absorption after 24 h immersion in cold water = 12.60%.

Ordinary Portland cement was used in the preparation of brick masonry walls of building models. The cement was tested for the normal consistency, compressive strength (28 days), initial and final setting time [8] and the values obtained were 30%, 29.7 MPa, 40 min and 8 h, respectively. The total quantity of cement required was procured in one instalment so as to ensure uniformity.

Locally available river sand was used. The grading of sand conforms to zone IV of BIS [10]. The fineness modulus of sand was 1.98. Throughout the experiment the same sand has been used for making the building models so as to achieve uniformity in cement-sand mortar as far as possible.

2.2. Masonry mortar

The brick masonry walls of building models were made in 1:6 cement-sand mortar. Different values of water-cement (w/c ratios) were tried to obtain the mortar of desired workability that was more of a qualitative judgment than a quantitative one, however its value was approximately 0.8. The compressive strength of mortar was determined using 70.6 mm cubes [7], whereas the tensile strength of mortar was determined using

briquettes. The bond strength of mortar on horizontal bed has been determined by detaching two bricks bonded together with the help of mortar. The bricks were at right angles to each other with equal projection on either side and the frog of both of the bricks was upward.

The same mason prepared all of the building models so as to achieve uniform workmanship. The thickness of mortar was kept one-sixth of the thickness of brick i.e. 6 mm. The compressive and tensile strength of mortar were 7.11 and 0.78 MPa respectively, whereas the bond strength was 0.14 MPa.

2.3. Types of brick masonry

Three different types of brick masonry were considered for the construction of walls viz. (i) type A – conventional one-brick thick solid masonry wall with bricks on bed in Flemish bond; (ii) type B (Low cost option-1) – solid masonry wall of reduced thickness and (ii) type D (Low cost option-2) – one brick thick cavity wall with bricks on edge in Flemish bond. It may be noted here that all the three types of brick masonry are produced using same solid bricks.

The arrangement of bricks in different courses of brick masonry in the construction of walls and its junctions for the two types of low cost brick masonry are shown schematically in Figures 1 and 2.

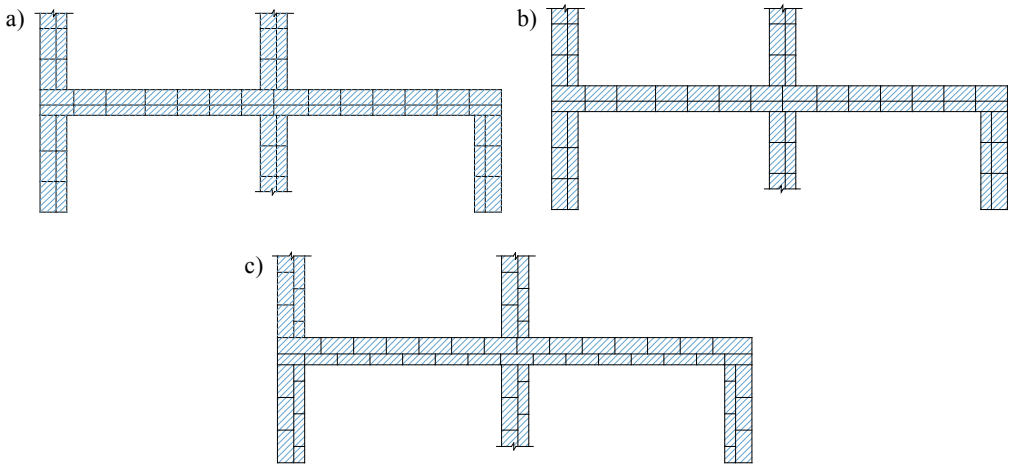

Fig. 1. Wall with masonry type B: a) I-I Course, b) II-I/II Course, c) III-II Course

In Figure 1, two course numbers are specified (viz. I-I, II-I/II, III-II), first one is for bricks on bed, whereas the second course number is for bricks on edge. It is to be noted that in the second course of bricks on bed, there are two courses for bricks on edge (half from each course) due to which it is written as: II-I/II Course. The saving in the cost and merits of such low cost masonry are:

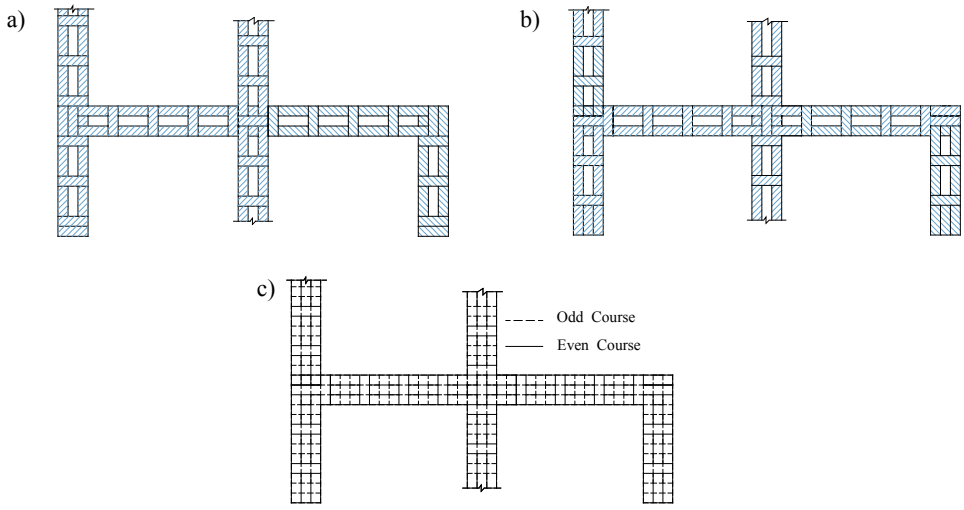

Fig. 2. Wall with masonry type D: a) Odd Course. All bricks on edge with alternate header/stretche, b) Even Course. All bricks on edge with alternate header/stretcher, c) Odd/Even Course. Two courses shown together

I) Use of one-brick thick cavity wall and solid wall of reduced thickness results in a 25% and 16% saving of bricks respectively.

II) Reduction in the number of bricks reduces the quantity of mortar and results in the reduction of dead load of the superstructure, thus reducing the cost of foundation.

III) Wall surface becomes smooth and gives better appearance; hence plastering may not be required.

IV) The cost of brick masonry walls is about 35% and that of the plastering is about 10% of the total cost of building, thus the saving in the cost of building due to the saving in the number of bricks, masonry mortar and plastering as well as due to reduced cost of foundation may be approximately 20–25%. Though there will be some increase in the cost of labour because of the specialized construction but the mason has to handle less number of bricks, therefore, the net increase in the cost of labour is almost negligible which has also been observed in practice [19].

V) Cavities in one brick thick cavity walls act as an insulator and reduce the chiselling work done for electrification purposes.

2.4. Masonry building models

The building models of single room were constructed with half-size model bricks (114 × 57 × 38 mm), three each for the three types of masonry (i.e. types A, B and D), using 1:6 cement-sand mortar with w/c ratio of 0.80.

Two models of each masonry type were having fixed base, whereas the third model had base isolation. For base isolation, Teflon sheet (PTFE) was provided at the plinth

level covering the entire length and thickness of the walls. One building model of each masonry type with fixed base was tested under static lateral load and the remaining two models of each masonry type were tested for dynamic loads using shake table. During construction, sides of the walls were checked for verticality. Length, width and height of the building models were 1070, 990 and 660 mm respectively. Thickness of cast-in-situ reinforced concrete (RC) slab was 40 mm reinforced with ϕ5@ 200 mm c/c both ways. A double leaf wooden door (210×340 mm) was fitted in the middle of one of the longer walls and a double leaf glass window (200 × 120 mm) with wooden panel was used in the other longer wall. The direction of load/vibration was parallel to the longer walls. The constructed building models were kept under wet gunny bags for 24 h and thereafter cured for 10 days [6]. These building models were constructed on 1100 × 1000 mm rectangular frames of rolled steel channel section ISJC 100@5.8 kg/m.

Door and windows were fitted in the equal angle (25.4 × 1.5 mm) section frame. Window fame was anchored in the walls by 50 mm extension of angle at all the four corners and door frames were anchored only at the top corners.

Experimental setup for testing under lateral static loads: The models prepared for studying the performance of brick masonry buildings under lateral static load, were named as HM-1, HM-2 and HM-3 for the three types of masonry i.e. Types A, B and D respectively. The lateral static load was applied at the roof level with the help of a hydraulic jack at an increment of 0.5 kN. The measurements of lateral deflections were taken with the help of dial gauges, whereas the diagonal compression and tension was measured with the help of the Demac gauges. The cracks developed on different walls during loading were marked. The testing was continued till the failure of building.

Experimental setup for shake table testing: The shake table supporting the building models was subjected to uniaxial sinusoidal vibrations with speeds varying from 300 to 3000 rpm in steps of 300 rpm. Linear variable displacement transducers (LVDTs) were used to record displacements with a precision of 0.01 mm and piezoelectric accelerometers were used to record acceleration. The direction of motion of shake table was parallel to the longer walls. Two accelerometers, one each at top and middle of a short wall of building models and one at the shake table were used to record the acceleration. Two LVDTs, one each at the top and base of the short wall of building models were used to record the displacement of building models. Both the LVDTs and accelerometers lie in the same vertical line passing through the mid length of the short wall.

3. Lateral static response of building models

3.1. Crack pattern

The cracks observed in different walls of various building models are shown in Figures 3 to 5. The crack Identification marks viz. C1, C2 and C3 are used for cracks developed at increasing magnitude of lateral load. The crack identification marks are

written on the walls of the building models and are shown in Figures 3 to 5. The propagation of cracks in different walls of the building models at increasing magnitude of lateral load, are given in Table 1. The cracks developed in the models are mainly diagonal, whereas, some of the cracks are horizontal and close to the slab. All the cracks observed in different building models are along the mortar joints.

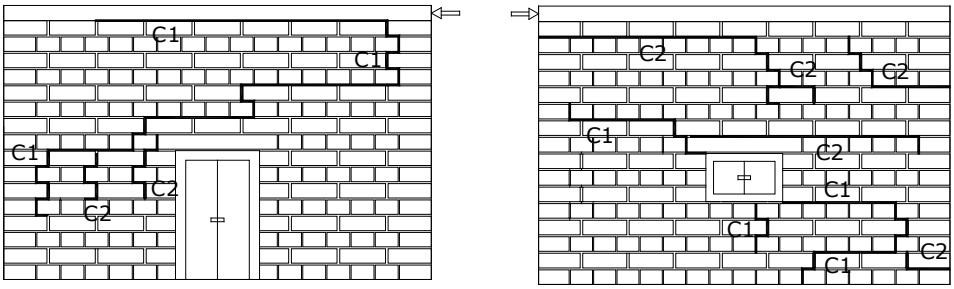

Fig. 3. Model of masonry type A (HM-1) after testing under static load

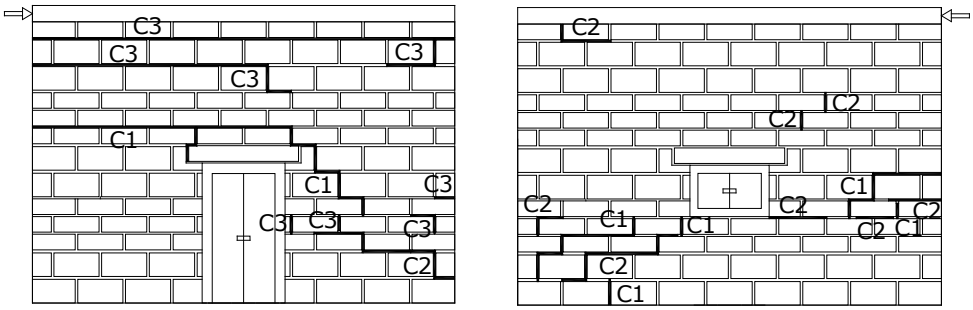

Fig. 4. Model of masonry type B (HM-2) after testing under static load

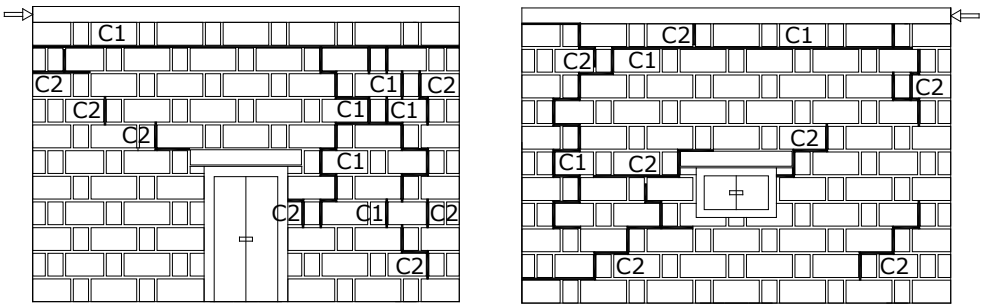

Fig. 5. Model of masonry type D (HM-3) after testing under static load

The observed pattern of diagonal cracks in the shear walls are due to the combined effect of elongation of far-diagonal, contraction of near-diagonal, fixity at

the base and brittleness of the masonry. Whereas, the cracks near the edges may be due to some invisible eccentricity and stress concentration. The pattern of dominant horizontal cracks in the cross walls are due to combined effect of lateral deflection of building in the direction of load and brittleness of brick masonry which reduces the shear strength of brick masonry. The different types of crack patterns observed on different faces of building models provide strengthening criteria of such buildings against destructive forces that are likely to act on buildings during service conditions.

Table 1. Crack propagation observed in different building models tested under static lateral load

Lateral load (kN)	Crack propagation*				Remark
	Wall F1	Wall F3	Wall F2	Wall F4	
Model HM-1 (Masonry type A)					
2.00	C1	C1	C1	–	
2.50	C2	C2	C2	C1	Ultimate load
Model HM-2 (Masonry type B)					
1.00	C1	–	C1	–	
1.50	C2	C1	C2	–	
2.00	C3	C2	C3	C1	Ultimate load
Model HM-3 (Masonry type D)					
1.00	C1	C1	C1	C1	
1.50	C2	C2	C2	C2	Ultimate load

* F1 and F3 are long walls having door and window respectively; F2 is the wall on which static lateral load is applied at the top

3.2. Shear strength of building models

The variation of mean elongation and contraction of the diagonals on long walls with lateral load is plotted in Figures 6 and 7.

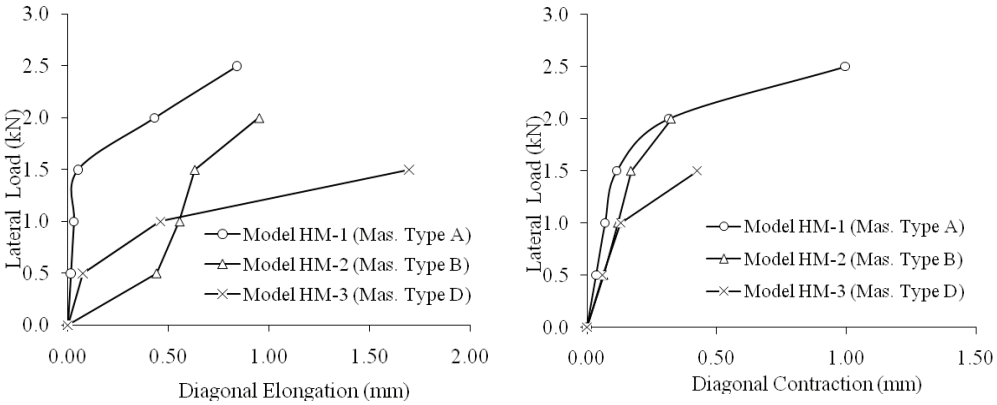

Fig. 6. Deformation of diagonal for door side wall (static test)

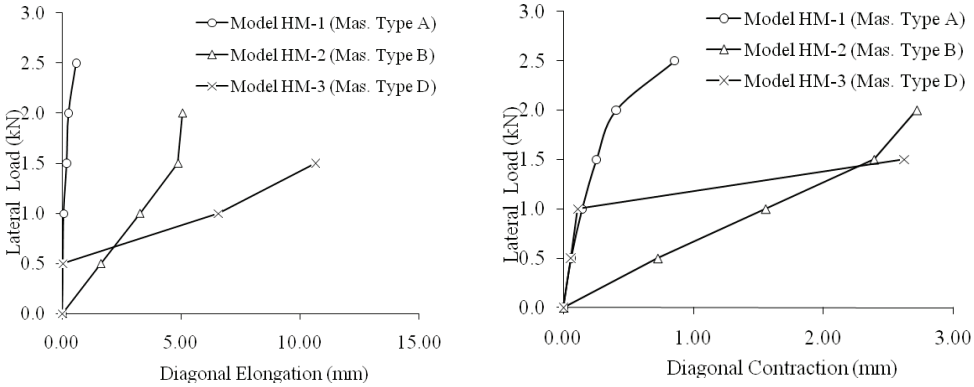

Fig. 7. Deformation of diagonal for window side wall (static test)

The magnitude of elongation is more than the contraction of diagonal which is due to the fact that the tensile strength of brick masonry is less than its compressive strength. The deflection of the base of the building model recorded by the dial gauges placed on the short wall opposite to the loaded face wall is zero for all the building models which shows that the base remained fixed during the application of load. The maximum deflection at the top of different building models recorded by dial gauge is given in Table 2.

Table 2. Maximum lateral load and corresponding deformation in building models

Type of models	Type of walls	Ultimate lateral load (kN)	Max. average deformation of diagonal (mm)		Maximum deflection at top (mm)
			Elongation	Contraction	
HM-1 (Masonry type A)	Wall F1 Wall F3	2.5	0.840 0.595	0.995 0.855	15.85
HM-2 (Masonry type B)	Wall F1 Wall F3	2.0	0.950 5.075	0.325 2.720	8.52
HM-3 (Masonry Type D)	Wall F1 Wall F3	1.5	1.695 10.650	0.425 2.620	22.15

The variation of deflection at top with lateral load is shown in Figure 8. The observations made from these figures and table are:

I) The static lateral load carrying capacity of building models HM-2 (Masonry type B) and HM-3 (Masonry type D) are 80% and 60% respectively of building model HM-1 (Masonry type A). The peak lateral deflection of building model HM-3 is maximal, whereas its value for building models HM-1 and HM-2 is 28% and 61% less than HM-3 respectively.

II) Out of the two low cost brick masonry building models, building model HM-2 is found to be 33% stronger than HM-3 in carrying the lateral load and the peak lateral deflection of the top of building model HM-3 is 160% more than building model HM-2.

III) The experimental observations of deflection on wall F4 of different building models show that the deflection at the two corners at the top are not the same which may be due to small rotation of building resulting from the unsymmetrical building configuration.

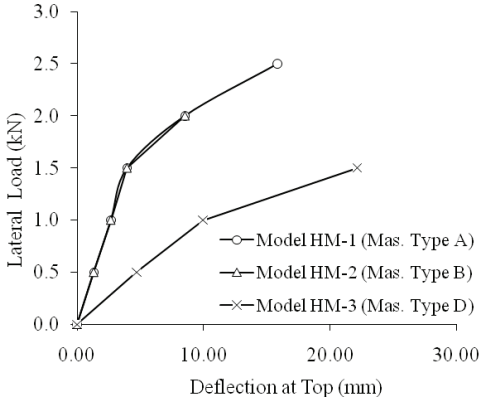

Fig. 8. Load v/s deflection at top (Static test)

4. Mathematical analysis for dynamic response of buildings

A single-storey building model as shown in Figure 9a represents the concept of single storey structure with base sliding. It is assumed that a layer of suitable material with known coefficient of friction is laid at plinth level. The superstructure is allowed to slide freely after overcoming the friction. The sliding type of building is idealized as a discrete mass model with two degrees of freedom for computing the earthquake response as shown in Figure 9b.

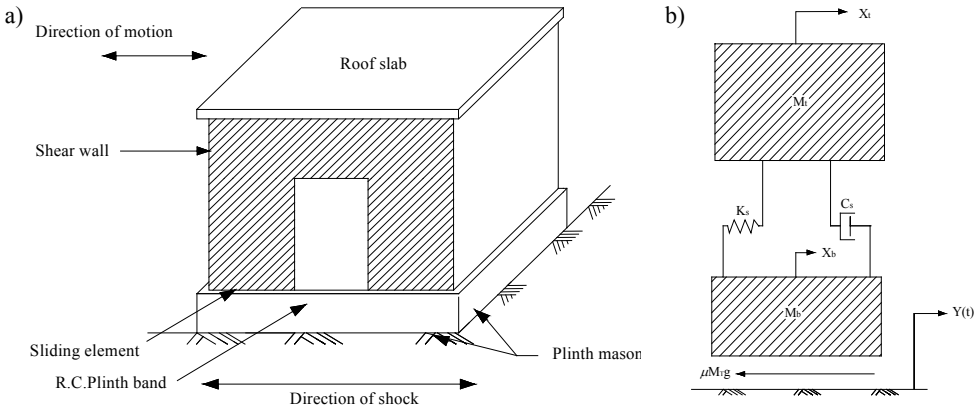

Fig. 9. Idealized sliding type single storey structure and mathematical model:
a) Building, b) Mathematical model

The spring action in the system is assumed to be provided by the shear walls, which resist shear force parallel to the direction of earthquake shock. Internal damping is represented by a dashpot that is in parallel with the spring. The mass of roof slab and one-half of the wall is lumped at the top (= M_t) and the lower mass, M_b, is assumed to rest on a plane with dry friction damping. Further assumptions made in the analysis of the sliding system are as follows:

I) The coefficient of friction between the sliding surfaces is assumed to be constant throughout the motion of the system.

II) The materials used for the building construction are linearly elastic within the limit of proportionality, thus the idealized spring is linear elastic.

III) The sliding displacement can occur at the contact surface without overturning or tilting.

IV) The building is assumed to be subjected to only one horizontal component of ground motion at a time. The effect of vertical ground motion is not considered.

There are three different phases in the complete motion history of the base sliding system due to the frictional resistance at its base. The equations of motion for the three phases are given in the following:

4.1. Phase I

Initially, so long as the acceleration of the sliding system does not overcome the frictional resistance, bottom mass, M_b, moves with the base since there is no sliding and the system behaves as a single degree of freedom system. Therefore, the equation of motion is:

$$M_t \ddot{X}_t + C_s\left(\dot{Z}_t - \dot{Z}_b\right) + K_s\left(Z_t - Z_b\right) = 0, \tag{1}$$

$$\ddot{Z}_t + 2\omega\xi\left(\dot{Z}_t - \dot{Z}_b\right) + \omega^2\left(Z_t - Z_b\right) = -\ddot{y}(t), \tag{2}$$

where:

C_s is coefficient of viscous damping,

K_s is spring constant,

M_b and M_t are masses lumped at base and roof level,

$\ddot{X}_t, \ddot{Z}_t$ are absolute and relative accelerations of the top mass respectively,

$\ddot{y}(t)$ is ground acceleration at time t,

Z_b, Z_t are lateral relative displacements of masses M_b & M_t respectively,

$\dot{Z}_b, \dot{Z}_t$ are relative velocities of masses M_b and M_t respectively,

natural circular frequency of the system, ω, and fraction of critical damping, ξ, are given by $\omega = \sqrt{\dfrac{K_s}{M_t}}$ and $\xi = \dfrac{C_s}{2\omega M_t}$.

4.2. Phase II

The sliding of bottom mass begins when the force which causes sliding overcomes the frictional resistance at the plinth level. The force to cause sliding S_f is given by:

$$S_f = C_s\left(\dot{Z}_t - \dot{Z}_b\right) + K_s\left(Z_t - Z_b\right) - M_b\ddot{X}_b. \tag{3}$$

Sliding of mass occurs if $\left|S_f\right| \rangle \mu M_T g,$ where, g is the acceleration due to gravity, $M_t = M_b + M_t$ and μ is the coefficient of friction. The system now acts as a two degrees of freedom system for which the equation of motion can be written in simplified form as:

$$\ddot{Z}_b + 2\omega\xi\theta\left(\dot{Z}_t - \dot{Z}_b\right) + \omega^2\theta\left(Z_t - Z_b\right) + F = -\ddot{y}(t), \tag{4}$$

$$\ddot{Z}_t + 2\omega\xi\left(\dot{Z}_t - \dot{Z}_b\right) + \omega^2\left(Z_t - Z_b\right) = -\ddot{y}(t), \tag{5}$$

where:

$$F = \mu g\left(1+\theta\right)\mathrm{sgn}\left(\dot{Z}_b\right) \tag{6}$$

$\ddot{X}_b, \ddot{Z}_b$ – absolute and relative accelerations of bottom mass, M_b,

$\theta = \dfrac{M_t}{M_b}$ – mass ratio,

sgn ($\dot{Z}_b$) = +1, if $\dot{Z}_b$ is positive; = –1, if $\dot{Z}_b$ is negative.

4.3. Phase III

At any time during the motion of the system, if

$$\left|S_f\right| \le \mu M_T g, \tag{7}$$

then the sliding of the bottom mass is stopped but the top mass continues to vibrate and the system again converts to a single degree of freedom system as considered in Phase I. Throughout the history of ground shaking, the bottom mass of the system either stops or continues to slide according to the conditions enumerated above.

5. Dynamic response of building models

The identification mark inscribed on the building models are such that the first character is the masonry type and the second and third characters tell about the type of

base ("R" stands for rigid base and "BI" stands for base isolation). The building models were tested different speed of motor, which was increased from 300 to 3000 rpm in steps of 300 rpm. The displacement, acceleration and crack pattern observed from experimental testing have been discussed in the subsequent subsections. The nomenclature of walls used in subsequent discussion is such that F1 and F3 are long walls having door and window respectively, whereas F2 is the short wall on which displacement was recorded and F4 is the remaining short wall.

5.1. Crack pattern

Building model AR (Figure 10): In this model, no crack was observed up to 1800 rpm. Whereas, three horizontal cracks were observed in wall F1 at 2100 rpm. One crack was two courses below the roof level, running throughout the length of the wall. The other two cracks were located at the top and bottom level of the door on the same side of the door. In the wall F3, three horizontal cracks were observed at a speed of 2100 rpm. Out of these three cracks, one crack was located two courses below the roof level covering the whole length of the wall, second crack was at the lintel level of the window and third crack was at the bottom level of the window only on one side of the window. On the wall F2, two horizontal cracks were observed two courses below the roof level running throughout the length of the wall. One horizontal crack was also observed five courses above the base of the wall only on half length of the wall. On the wall F4, one horizontal crack was observed two courses below the roof level running throughout the length of the wall. Some small horizontal cracks were also observed at the base of the wall.

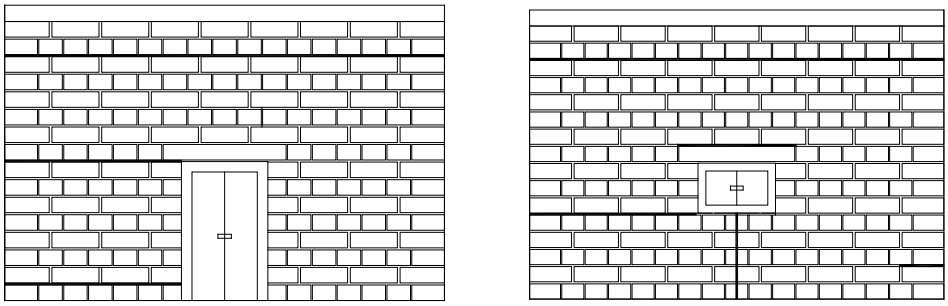

Fig. 10. Model of masonry type A with rigid base after shake table testing

At a speed of 2700 rpm, one vertical crack below the window passing from the mid length of the window was observed and some small horizontal cracks were also observed at the base of wall F3. With further increase in the speed no additional cracks were observed on any of the walls of building model. Only the cracks, already formed, widened in their width.

Building model ABI (Figure 11): In this model no crack was observed up to a speed of 2400 rpm. At 2700 rpm, three horizontal cracks and one vertical crack were observed on the wall F1. One horizontal crack was located just below the roof starting from the corner and running up to two-brick length; second horizontal crack was one course below the roof level starting from the corner and the crack became vertical at the door level and came down up to the top corner of the door. The third horizontal crack was just below the second horizontal crack only for one brick length near the corner. In the wall F3, three horizontal cracks were observed. The first crack was located just below the roof level starting from the corner and running up to the middle of the wall. The other two cracks were only one brick length long. One crack near the opposite corner, one course below the roof level and the other crack was near the top corner of the window and below the previous small crack.

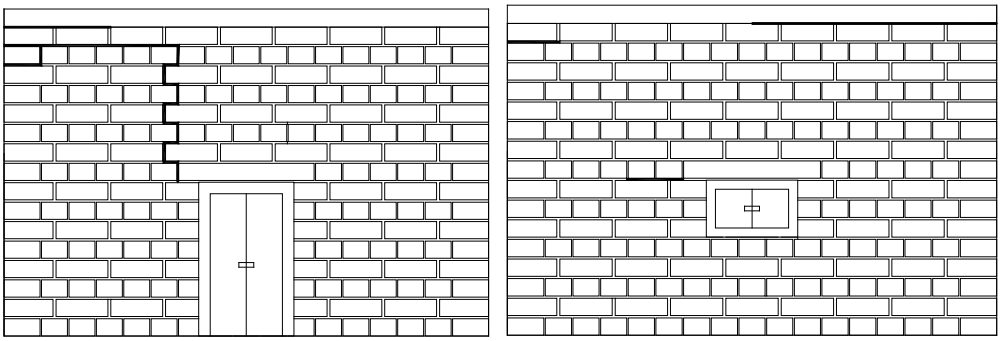

Fig. 11. Model of masonry type A with base isolation after shake table testing

At 3000 rpm, three horizontal cracks were observed in the wall F4. The first crack is just below the roof level covering the whole length of the wall and the other two cracks are only one brick length long located near the opposite corners and one course below the first crack. No crack was observed on the wall F2.

Building model BR (Figure 12): In this model no crack was observed up to a speed of 2100 rpm. At 2400 rpm, cracks appeared on all the walls except the wall F3. In the wall F1, one horizontal crack was observed at one of the bottom corners which was one brick long just one course above the base of the wall then it became vertical passing through the vertical mortar joint for one brick thickness reaching to the bottom of the wall then again the crack became horizontal and extended up to the bottom of the door. At 2700 rpm, new cracks were not formed, only cracks already formed, widened.

At 3000 rpm, two bricks laid on edge in the second course from bottom of the wall F4 near one corner got detached from the wall. One brick got detached from the wall F2 at 2400 rpm at the corner from the bottom course, whereas one more brick came out at 3000 rpm from the opposite corner from the same course. The bricks that get detached were the bricks on edge and these bricks were located near the corners of the walls.

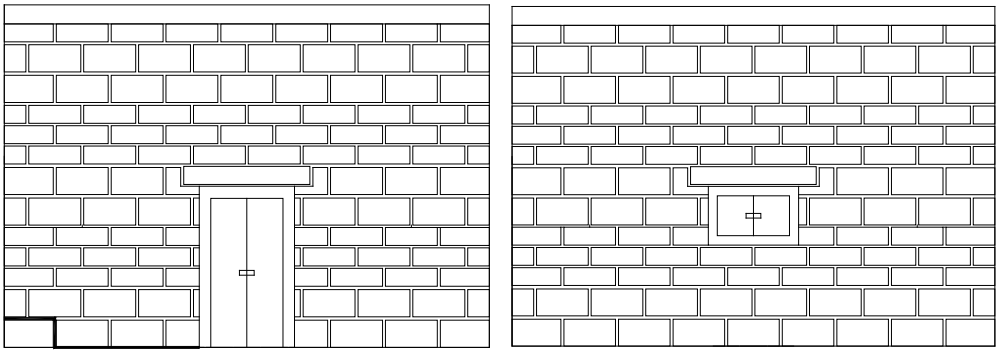

Fig. 12. Model of masonry type B with rigid base after shake table testing

Building model BBI (Figure 13): In this model, no crack was observed in different walls up to 2700 rpm but at 3000 rpm there was some sign of sliding of the slab due to the development of horizontal cracks throughout the perimeter of the model at the roof level. No other crack was observed in model.

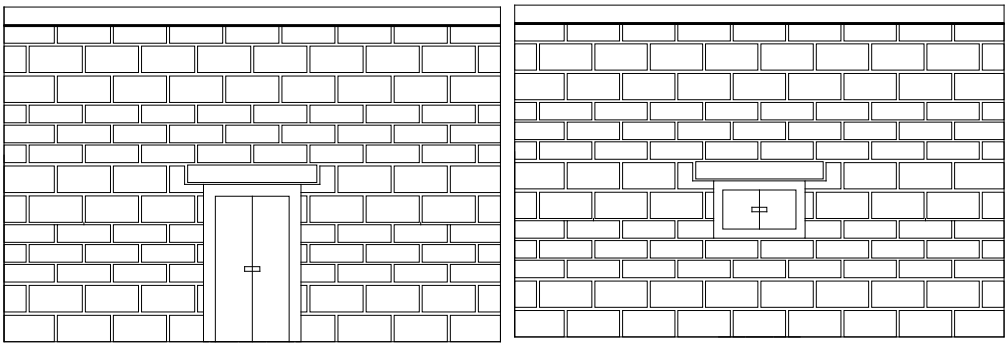

Fig. 13. Model of masonry type B with base isolation after shake table testing

Building model DR (Figure 14): In this model, no crack was observed in the walls up to 2100 rpm. At 2400 rpm, one horizontal crack developed at two courses above the base of the wall F1 starting from one corner and running up to the door then from the opposite end of the door for one brick length which remained horizontal and thereafter it became vertical through the vertical mortar joint and again it became horizontal reaching up to the other corner of the wall. In the wall F3, one horizontal crack located one course below the roof level and running along the length of the wall was observed.

At 2700 rpm, one diagonal crack appeared starting from one of the corners of the door and covering two courses in wall F1. Bricks got detached from the two corners, one and two courses above the base of the wall. In the wall F2, two horizontal cracks were observed, one crack was running along the length of the wall and located three

courses from the base and the other crack was just one course below the roof level and started from one corner running only half length of the wall. At 3000 rpm, the brick on edge got detached because of the lateral inertial force on the brick being greater than the sum of the bond strength of vertical face of brick with mortar and the shear strength of horizontal mortar bed.

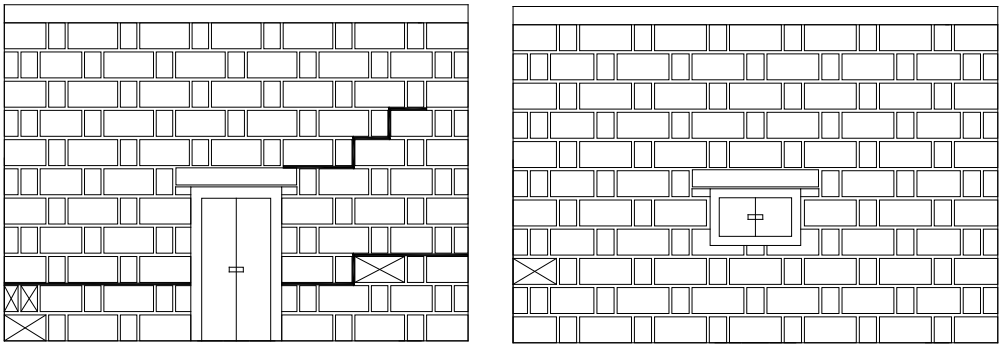

Fig. 14. Model of masonry type D with rigid base after shake table testing
(Note: Detached bricks are crossed)

Building model DBI (Figure 15): In this model no crack was observed up to 2400 rpm but at 2700 rpm few minor horizontal cracks at the roof level appeared in the walls of the model. At this speed one small diagonal crack was also observed at one corner of the door covering two courses in the wall F1. At the maximum speed of 3000 rpm, some of the bricks got detached from the top course of all the walls.

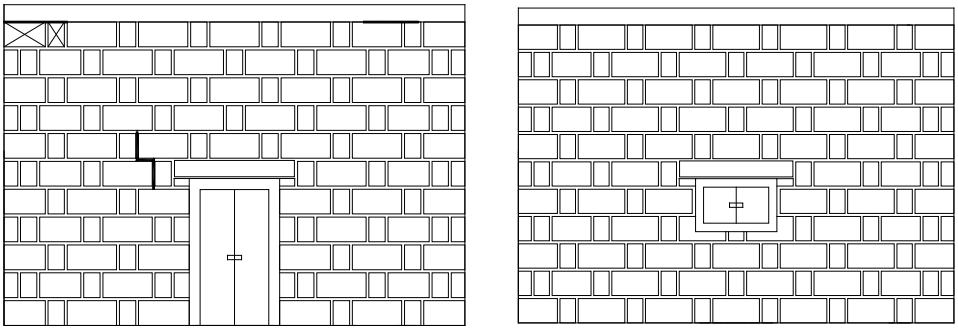

Fig. 15. Model of masonry type D with base isolation after shake table testing
(Note: Detached bricks are crossed)

5.2. Acceleration response

The brick masonry building models were subjected to gradually increasing shake table accelerations. The variation of acceleration at top of building models with shake

table accelerations (base accelerations) have been plotted in Figures 16 to 18. The theoretical values of acceleration obtained from the analysis presented in Section 4 are also plotted in these figures. It is seen from the figures that the theoretical values are in good agreement with the experimental values with the percentage error for all the cases less than 10%. The variation is almost linear for all types of building models with and without base isolation.

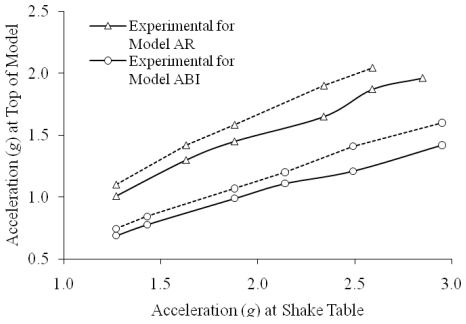

Fig. 16. Base vs. top acceleration for type A

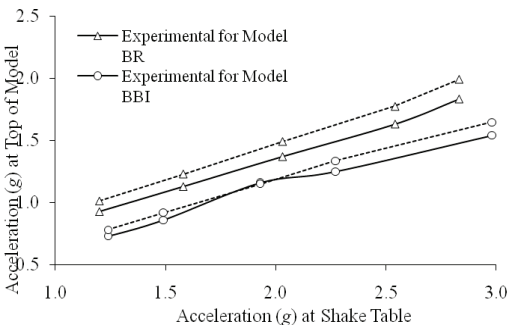

Fig. 17. Base vs. top acceleration for type B

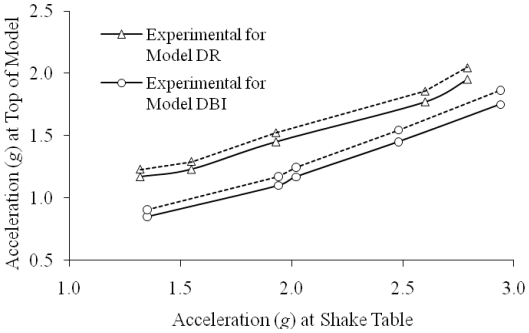

Fig. 18. Base vs. top acceleration for type D

Masonry type – A: The percentage reduction in the acceleration at top of model AR with respect to shake table acceleration varies from 20% to 31% whereas for model ABI this reduction varies from 37% to 51%. In building model ABI sliding started at an acceleration of 1.27 g, the sliding recorded at this acceleration was 19 mm which is 8.3% of the thickness of wall. With further increase in shake table acceleration, the magnitude of sliding had increased. The maximum sliding of 51 mm (22.4% of the thickness of wall) was recorded at shake table acceleration of 2.95 g.

Masonry type – B: The percentage reduction in the acceleration at top of model BR with respect to shake table acceleration varies from 23% to 36% whereas for model BBI this reduction is from 40% to 48%. In building model BBI, sliding started at an

acceleration of 1.24 g, the sliding recorded at this acceleration was 23 mm which is 12.1% of the thickness of wall. With further increase in shake table acceleration, the magnitude of sliding had increased. The maximum sliding of 55 mm (29.0% of the thickness of wall) was recorded at shake table acceleration of 2.98 g.

Masonry type – D: The percentage reduction in the acceleration at top of model DR with respect to shake table acceleration varies from 11% to 32% whereas for model DBI this reduction varies from 37% to 43%. In building model DBI sliding started at an acceleration of 1.35 g, the sliding recorded at this acceleration was 30 mm which is 13.2% of the thickness of wall. With further increase in shake table acceleration, the magnitude of sliding had increased. The maximum sliding of 58 mm (25.4% of the thickness of wall) was recorded at shake table acceleration of 2.94 g.

In view of the above data, obtained for different building models by shake table testing, following conclusions may be drawn:

I) With the increase in shake table acceleration, the acceleration at top of all building models also increases. This is due to increase of dynamic force to which models are subjected.

II) In the building models ABI, BBI and DBI higher reduction in the acceleration was observed as compared to building models AR, BR and DR, this is due to the provision of base isolation in models ABI, BBI and DBI. This observation indicated that the base isolation resulting from sliding had an appreciable influence and that the input energy at the base was dissipated to some extent in the sliding of the model.

III) For building model of masonry type D, the reduction in contact area at the base and hence the reduction in the friction force is more as compared to the reduction in weight of the building. It is due to this reason that building model of masonry type D suffered maximum sliding as compared to the building models of masonry types A and B.

5.3. Displacement response

The displacement recorded by two LVDTs, one each at top and base of a short wall (Wall-F2) of different building models, are given in Table 3 and discussed in the sub-sequent sections.

Table 3. Maximum displacement of building models observed in shake table testing

Building model	Maximum displacement (mm)	
	At the top	At the base
AR	10.45	8.43
ABI	12.39	10.07
BR	12.96	10.88
BBI	13.85	12.02
DR	13.96	12.24
DBI	16.86	14.32

Masonry type – A: The maximum displacement recorded for model AR at the top is 24.0% more than the displacement recorded at the base, whereas, for building model ABI this increase is 23.0%. The displacement recoded at the top and the base for building model ABI is 18.6% and 19.5% more than the building model AR, re respectively.

Masonry type – B: The maximum displacement recorded for model BR at the top is 19.1% more than the displacement recorded at the base, whereas, for building model BBI this increase is. 15.2%. The displacement recoded at the top and the base for building model ABI is 6.9% and 10.5% more than the building model BR, respectively.

Masonry type – D: The maximum displacement recorded for model DR at the top is 14.1% more than the displacement recorded at base, whereas, for building model DBI this increase is. 17.7%. The displacement recoded at the top and the base for building model DBI is 20.8% and 17.0% more than the building model DR, respectively.

6. Conclusions

There is considerable reduction in the static shear strength of the two cost effective options (types B and D) of masonry buildings. The static lateral load carrying capacity of building models HM-2 (Masonry type B) and HM-3 (Masonry type D) is 80% and 60% respectively of building model HM-1 (Masonry type A). The reduction in strength is more than the saving in the material, which is due to the increase in the vertical mortar joints in both masonry types. The shake table testing also shows more damage to masonry type B and D and especially the detachment of bricks which was though at high speed.

All cracks observed in different building models are along the mortar joints. Though the vertical mortar joints are more important in both types of low cost brick masonry construction (type B, D) because of the use of bricks on edge but these are especially more important for brick masonry type B where mixed arrangement of bricks is there.

The study confirmed that the performance of building models with base isolation using Teflon sheet at the plinth level is much better as compared to building models without base isolation. Thus the sliding arrangement shows great promise for adoption in actual building construction as a measure of earthquake safety.

Acknowledgement

The authors are grateful to All Council for Technical Education (AICTE), New Delhi, India for financial support under TAPTAC scheme.

References

[1] Arya A.S., Chandra B., Qamaruddin M.: *A new concept for resistance of masonry buildings in severe earthquake shocks*, Journal of the Institution of Engineers India, Vol. 61, 1981, pp. 302–308.

[2] Arya A.S.: *Sliding concept for mitigation of earthquake disaster to masonry buildings*, In: Proceedings 8th World Conference on Earthquake Engineering, San Francisco, Vol. 5, 1984, pp. 951–958.
[3] Bruneau M.: *State-of-the-Art report on seismic performance of unreinforced masonry building*, Journal of Structural Engineering, Vol. 120, 1994, pp. 925–945.
[4] Derham C.J., Kelly J.M., Thomas A.G.: *Non-linear natural rubber bearings for seismic isolation*, Journal of Earthquake Eng. & Structural Dynamics, Vol. 84, 1985, pp. 417–428.
[5] IS 1077, *Specification for commonly burnt clay building bricks*, Bureau of Indian Standards (BIS), India, 1976.
[6] IS 2212, *Code of practice for brickwork*, BIS, India, 1962.
[7] IS 2250, *Code of practice for preparation and use of masonry mortar*, BIS, India, 1981.
[8] IS 269, *Specification for ordinary and low heat Portland cement*, BIS, India, 1976.
[9] IS 3495, *Methods of tests of burnt clay building bricks*, BIS, India, 1976.
[10] IS 383, *Specification for coarse and fine aggregates from Natural Resources*, BIS, India, 1970.
[11] Keswani K.: *The contribution of building centres to low-cost housing in India*, Building Research & Information, Vol. 25, 1997, pp. 50–64.
[12] Lin B.C. et al.: *Response of base isolated buildings to random excitation described by C-P spectral model*, Journal of Earthquake Engineering & Structural Dynamics, Vol. 18, 1989, pp. 49–62.
[13] Majid S.A., Qadeer A., Farrukh A.: *Dynamic behaviour of multistoreyed brick building models*, In: Proceedings of 10th Symposium on Earthquake Engineering, University of Roorkee, India, Vol. 2, 1994, pp. 983–988.
[14] Mostaghel N., Hejazi M., Tanbakuchi J.: *Response of sliding structures to harmonic motion*, Journal of Earthquake Eng. & Structural Dynamics, Vol. 11, 1983, pp. 355–366.
[15] Mostaghel N., Khodaverdian M.: *Dynamics of resilient friction base isolator (R-FBI)*, Journal of Earthquake Engineering & Structural Dynamics, Vol. 116, 1987, pp. 839–854.
[16] Qamaruddin M., Rasheeduzzafur, Arya A.S., Chandra B.: *Seismic response of masonry buildings with sliding substructure*, Journal of Structural Engineering, Vol. 112, 1986, pp. 2001–2011.
[17] Qamaruddin M.: *Development of brick building systems for improved earthquake performance*, Ph. D. Thesis, University of Roorkee, Roorkee, India, 1978.
[18] Raman P.G.: *Structural masonry and architectural expression*, Construction and Building Materials, Vol. 18, 2004, pp. 133–139.
[19] Sengupta N.: *Use of cost-effective construction technologies in India to mitigate climate change*, General Articles, current science, Vol. 94, 2008.
[20] Tomazevic M., Weiss P.: *Seismic behaviour of plain and reinforced masonry build building*, Journal of Structural Engineering, Vol. 120, 1994, pp. 323–337.
[21] Yan Z., David T., John C.: *Nonlinear dynamic analysis of unreinforced masonry*, Journal of Structural Engineering, Vol. 125, 1998, pp. 270–277.

Statyczna i dynamiczna odpowiedź efektywnych ekonomicznie budynków murowanych o niezbrojonych, ceglanych ścianach

W uzupełnieniu do konwencjonalnych budynków o murowanej konstrukcji ścian z cegły w pracy zaprezentowano dwa typy budynków charakteryzujące się ekonomicznie efektywną konstrukcją ścian, uzyskaną poprzez: zmniejszenie ich grubości oraz zastosowanie pustki powietrznej. Jedno piętrowe modele budynków poddano analizie w zakresie statycznym pod względem odporności na obciążenie boczne oraz testowano ze względu na dynamiczne wymuszenia za pomocą stołu wzbudzającego. Wyniki badań wskazują, że istnieje znacząca redukcja w wytrzymałości na ścinanie budynków o zaproponowanej ekonomicznej konstrukcji murowanych ścian i jest ona bardziej znacząca niż oszczędności materiałowe, które wynikają ze wzrostu spoin pionowych w obu rozpatrywanych typach murów. Efektywność systemu izolacji podłoża przy pomocy przekładki teflonowej wskazuje na duże możliwości zaadoptowania go w budynkach tradycyjnych, jak i tych o ekonomicznej konstrukcji ścian, jako środek ich bezpieczeństwa w trzęsieniach ziemi.

ARCHIVES OF CIVIL AND MECHANICAL ENGINEERING

Vol. XI 2011 No. 4

Numerical analysis of hydrodynamic forces due to flow instability at lift gate

S.W. KOSTECKI
Wrocław University of Technology, Wybrzeże Wyspiańskiego 25, 50-370 Wrocław, Poland.

A numerical method, being a combination of the vortex method and the boundary element method, is used here to predict the two-dimensional flow field in the vicinity of an underflow vertical lift gate. In practice, tunnel-type flat-bottomed lift gates experience strong hydrodynamic loading, due to vortex detachment from the gate bottom edge, and near-wake velocity fluctuations. This paper presents a stream function, and velocity and vorticity distributions for two gate gaps. The vortex detachment mechanism is described and the vortex shedding frequency, expressed as a Strouhal number, is presented. The predicted velocity and vorticity fields are then used to calculate the pressure distribution on the gate surface by the boundary element method. The time histories of the lift and drag coefficients are presented. The proposed numerical method has been validated by the measurements of the downpull coefficient for the flow around the lift gate.

Keywords: *vorticity, vortex method, flow instability, vertical lift gate, boundary element method, hydrodynamic force*

1. Introduction

The calculation of hydrodynamic forces on hydraulic gates is a major problem which designers involved in hydroengineering face. When the flow around the gate is unstable, a changeable hydrodynamic load arises, which may result in vibrations of the gate, influencing its operational reliability and safety. This unfavourable phenomenon occurs predominantly at the high head gates of dams and hydropower plants. The most widely used high head gates are vertical lift gates or radial gates, working as regulating (partially opened) gates or as emergency and guard gates during opening and closing. In this paper the case of a lift gate with a submerged and pressurized underflow space is investigated.

The instability of the stream flowing under the gate depends mainly on the shape of the gate lip from which the shear layer is separated. The mechanism of this instability stems from the changeability of the layer separation point and from the fact that the shear layer impinges on the protruding gate elements.

When the stream flowing under the gate is unstable, the resulting pressure fluctuations cause the hydrodynamic force to fluctuate too. The latter's downpull component has been the subject of numerous researches and experiments by among others: Simmons [18] who conducted tests (based on the air model) on the flow around the gate,

Colgate [5] who carried out downpull pattern tests and natural measurements, and also Sagar [17] who suggested various lift gate designs. The fluctuations in the hydrodynamic force are the cause of flow-induced vibrations. Many studies have been undertaken to determine this mechanism and the optimum lower edge shape minimizing flow-induced vibrations (e.g. Campbell [4], Naudascher [14], Hardwick [9], Kolkman [10] and Thang [19]). In the case of gate underflow, the most common cause of vibration is the instability of the single layer separating from the gate lip (the instability induced excitation mechanism), see: e.g. Naudascher [16] and Naudascher & Rockwell [15]. Experimental research into this mechanism for a rectangular plate with two degrees of freedom was done by Billeter [1, 2] who found that the vibrations were caused by two phenomena: the streamline impinging-leading-edge-vortex (SILEV) mechanism and the instability of the shear layer (ISL) in the tail water. The phenomena result in the pulsation of the pressure acting on the gate's bottom and rear edges. Typically the unstable flow is determined numerically or analytically and the hydrodynamic forces are calculated by integrating the pressure distribution over the gate area.

This paper presents a numerical method for analyzing the aforementioned phenomena by interpreting the velocity, vorticity and pressure fields.

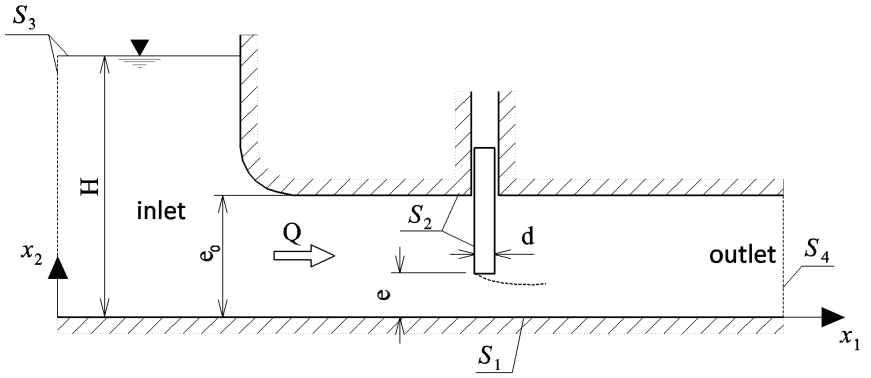

Fig. 1. Channel and gate parameters

It is very difficult to model the velocity field because of the strong turbulence generated at the gate. Moreover, as vortical structures separate from the boundary layer a recirculation zone forms behind the gate. This paper describes how to use the vortex method to analyze fluid motion instability under the lift gate and the boundary element method (BEM) to calculate the pressure. A scheme of the gate is shown in Figure 1.

2. Mathematical basis

A flat incompressible viscous flow is described by the Navier–Stokes (N–S) equation which through rotation can be transformed into the Helmholtz equation. As a result,

the pressure gradient and the force of inertia are eliminated from the N–S equation, which assumes this form:

$$\frac{\partial \omega}{\partial t} + \mathbf{u} \cdot \nabla \omega - \nu \nabla^2 \omega = 0, \quad \mathbf{x} = (x_1, x_2) \in D, \quad t > 0, \tag{1}$$

where $\mathbf{u}(\mathbf{x},t) = \left[u_1(\mathbf{x},t), u_2(\mathbf{x},t)\right]$ is the velocity vector, $\omega = \partial u_2 / \partial x_1 - \partial u_1 / \partial x_2$ – the vorticity, ν – the coefficient of kinematic viscosity and D – the flow area. Equation (1) should be completed with the equation of mass conservation

$$\nabla \cdot \mathbf{u} = \frac{\partial u_1}{\partial x_1} + \frac{\partial u_2}{\partial x_2} = 0, \tag{2}$$

and the initial condition

$$\omega\big|_{t=0} = \omega_0 \tag{3}$$

and the *no-through-flow* and *no-slip-flow* boundary conditions on the solid walls. Moreover, it is assumed that the stream function in the particular segments of the boundary satisfies the following conditions (Figure 1):

$$\begin{aligned} &\psi = 0\big|_{S1}, \\ &\psi = Q\big|_{S2}, \\ &\psi = \left.\frac{Q x_2}{e_0}\right|_{S3}, \\ &\frac{\partial \psi}{\partial x_1} = \left.0\right|_{S4}, \end{aligned} \tag{4}$$

where Q is the flow rate, S is the boundary and $S = S1 \cup S2 \cup S3 \cup S4$.

3. Random vortex method algorithm

The vortex method was developed for the analysis of unsteady and vortical flows in a wide range of engineering applications. Its simple algorithm is based on flow physics and enables completely grid free Lagrangian calculations without the use of any RANS type turbulent models. A detailed description of the method and proofs of its convergence can be found in the extensive literature on the subject, e.g. Cottet & Koumoutsakos [6], Hald [8], Majda [13].

In the vortex method, vorticity field ω is approximated using a set of N regularized vortex particles:

$$\omega(\mathbf{x},t)=\sum_{j=1}^{N} f_\varepsilon\left(\mathbf{x}-\mathbf{X}\left(\boldsymbol{\alpha}_j,t\right)\right)\boldsymbol{\Gamma}_j, \tag{5}$$

where $\mathbf{X}(\boldsymbol{\alpha}_j,t)$ is the trajectory of a vortex particle, originating from $\boldsymbol{\alpha}_j=\left(\alpha_1^j,\alpha_2^j\right)$, $\boldsymbol{\Gamma}_j$ is the vortex particle strength and $f_\varepsilon(\mathbf{x}),\ \varepsilon>0$ is the standard mollifying function with the Cauchy function as its base.

The solution of vorticity transport Equation (1) by the random vortex method (RVM) consists in its decomposition into two stages: advection and diffusion. The advection stage is formulated in the Lagrangian frame for vortex particle trajectories:

$$\frac{\mathrm{d}\,\omega\left(\mathbf{X}(\boldsymbol{\alpha},t),t\right)}{\mathrm{d}\,t}=0. \tag{6}$$

According to relation (6), vorticity is preserved along the trajectory of each particle $\omega\left(\mathbf{X}(\boldsymbol{\alpha},t),t\right)=\omega_0(\boldsymbol{\alpha}),\ t>0$.

In the case of diffusion, vorticity is required to satisfy the standard diffusion relation

$$\frac{\partial\omega(\mathbf{x},t)}{\partial t}-\nu\nabla^2\omega(\mathbf{x},t)=0. \tag{7}$$

Since Equation (7) can be interpreted as a description of the Brownian movement of the particles, it will be solved by the random walk method. This means that the particles are subjected to random displacement $\boldsymbol{\eta}\left(\alpha_j,t\right)=\left(\eta_1\left(\alpha_j,t\right),\eta_2\left(\alpha_j,t\right)\right)$, which is a normal (Gaussian) random distribution with the expected value equal to zero and variance $2t\nu$ [12].

According to the RVM calculation algorithm, the vortex field (approximated by the set of vortex particles) is determined in successive time steps. Passing from time step t to step $t+\Delta t$ requires the following calculations:

1. First, velocity field $\mathbf{u}_\omega(\mathbf{x},t)$ corresponding to the vorticity field is determined using the Biot–Savart formula:

$$\mathbf{u}_\omega(\mathbf{x},t)=\sum_j \mathbf{K}_\varepsilon\left(\mathbf{x}-\mathbf{X}\left(\boldsymbol{\alpha}_j,t\right)\right)\boldsymbol{\Gamma}_j,\quad \mathbf{K}_\varepsilon=\mathbf{K}*f_\varepsilon,\quad \mathbf{K}(\mathbf{x})=\frac{(-x_2,x_1)}{2\pi|\mathbf{x}|^2}, \tag{8}$$

where vector function $\mathbf{K}_\varepsilon$ is a mollification of kernel $\mathbf{K}$, "*" means convolution and $\mathbf{X}(\boldsymbol{\alpha}_j, t)$ is the position of the j-th vortex particle in time t.

2. To satisfy the *no-through-flow* boundary condition, $\mathbf{u}_\omega(\mathbf{x},t)$ is modified by adding potential velocity field $\mathbf{u}_p(\mathbf{x},t)$ such that normal component $(\mathbf{u}_p + \mathbf{u}_\omega)\cdot\mathbf{n} = 0$ on the solid boundary. Potential velocity field $\mathbf{u}_p$ is sought as a gradient of potential stream function ψ_p which satisfies the Laplace equation

$$\nabla^2\psi_p = 0, \qquad t \geq 0, \quad \text{in } D \tag{9}$$

with the boundary conditions given in (4) for stream function $\psi_p + \psi_\omega$, where ψ_ω is a stream function corresponding to $\mathbf{u}_\omega$, which can be approximated as follows:

$$\psi_\omega(\mathbf{x}, t+\Delta t) = \sum_j G_\varepsilon\left(\mathbf{x} - \mathbf{X}(\boldsymbol{\alpha}_j, t+\Delta t)\right)\boldsymbol{\Gamma}_j, \quad G_\varepsilon = G * f_\varepsilon, \quad G(\mathbf{x}) = -(2\pi)^{-1}\ln|\mathbf{x}| \tag{10}$$

The potential flow problem described by Equation (9) is solved here by the boundary element method. In this way an approximation to complete velocity field $\mathbf{u} = \mathbf{u}_\omega + \mathbf{u}_p$ is obtained.

3. The friction forces between the liquid and the solid boundary produce the *no-slip-flow* effect. Thus, the fluid velocity in direction $\hat{\mathbf{t}}$ tangent to the boundary is equal to zero, which can be expressed by relation $\mathbf{u}(\mathbf{x},t)\cdot\hat{\mathbf{t}} = 0$ on the solid boundary.

Since friction produces torque on the liquid particles adhering to the boundary, vorticity is generated on the latter. In the present calculations this phenomenon is modelled by nascent vortex sheet $\gamma(\mathbf{x},t)$ on the solid boundary. The intensity of the vortex sheet can be determined by solving the 2nd kind Fredholm integral equation derived by the author in [11]:

$$\pm\gamma(\boldsymbol{\xi}) = -2(\mathbf{u}_\omega + \mathbf{u}_p)(\boldsymbol{\xi})\cdot\hat{\mathbf{t}}(\boldsymbol{\xi}) + \frac{1}{\pi}\int_S \gamma(\mathbf{x})\frac{\partial\ln|\mathbf{x}-\boldsymbol{\xi}|}{\partial\hat{\mathbf{n}}(\boldsymbol{\xi})}dS(\mathbf{x}), \quad \mathbf{x},\boldsymbol{\xi}\in S \tag{11}$$

where unit vectors $\hat{\mathbf{n}}(\boldsymbol{\xi})$ and $\hat{\mathbf{t}}(\boldsymbol{\xi})$ are respectively normal and tangent to the boundary at point $\boldsymbol{\xi}$. The sign on the equation's left side is positive when the normal to boundary vector $\hat{\mathbf{n}}$ is directed outwards the flow region.

After its generation the vortex sheet is discretized to vortex particles whose strength is given by:

$$\mathbf{\Gamma}_i = -\int_{ds_i} \gamma(\mathbf{x}) \cdot dS, \qquad \mathbf{x} \in S \tag{12}$$

where ds_i stands for the elementary segments into which the solid boundary is divided. As a result, in each time step "new" vortex particles are generated in the centres of the segments, compensating the tangent velocity component on the solid boundary.

4. In this time step the displacements of the "old" vortex particles are determined:

$$\mathbf{X}^*\left(\boldsymbol{\alpha}_j, t+\Delta t\right) = \mathbf{X}\left(\boldsymbol{\alpha}_j, t\right) + \Delta t\, \mathbf{u}_j(t), \quad \mathbf{u}_j(t) = \mathbf{u}\left(\mathbf{X}\left(\boldsymbol{\alpha}_j, t\right), t\right). \tag{13}$$

5. Now all the ("new" and "old") vortex particles are displaced in the process of vorticity diffusion, according to this equation:

$$\mathbf{X}(\boldsymbol{\alpha}_j, t+\Delta t) = \mathbf{X}^*\left(\boldsymbol{\alpha}_j, t+\Delta t\right) + \boldsymbol{\eta}\left(\alpha_j, t\right). \tag{14}$$

6. In the final step of the algorithm the vortex particles which cross the flow area boundary as a result of the advective and diffusive displacement are eliminated.

One should note that in each time step one can derive a vorticity field from Equation (5) and a velocity field from Equations (8) and (9) to determine the pressure and the hydrodynamic force, which will be presented in the next section.

4. Pressure and hydrodynamic force

From the point of view of engineering practice, pressure field distribution is one of the most important characteristics of the flow. The RVM method allows one to determine the velocity and vortex field distributions from which the pressure in the flow can be calculated. There are two approaches commonly used for this purpose. One approach is to integrate the N-S equations to determine the pressure gradient. But then unavoidable numerical errors appear in the solution. The other approach consists in solving the Poisson equation for pressure by applying divergence to the N-S equations:

$$-\nabla^2 P = div\mathbf{B} \quad \text{in } D \tag{15}$$

with the Neumann boundary condition

$$\frac{\partial P}{\partial n} = -\mathbf{B} \cdot \hat{\mathbf{n}} \quad \text{on } S \tag{16}$$

where $P = p/\rho$ is kinematic pressure, $\mathbf{B} = \dfrac{\partial \mathbf{u}}{\partial t} + (\mathbf{u}\nabla\mathbf{u}) - \nu\nabla^2\mathbf{u}$, $\hat{\mathbf{n}}$ is a vector normal to boundary S and directed outwards bounded area D in which the flow is considered.

The boundary element method (BEM), which allows one to write relation (15) in the integral form, was used to solve the Poisson problem. After appropriate transformations the equation assumed the form which made it possible to determine pressure at any point ξ on the boundary.

$$c(\xi)P(\xi) + \int_S P\frac{\partial P^*(\mathbf{x},\xi)}{\partial \hat{\mathbf{n}}}dS(\mathbf{x}) = -\int_D \mathbf{B}\cdot\nabla P^*(\mathbf{x},\xi)d\mathbf{x}, \tag{17}$$

where $P^*(\mathbf{x},\xi) = -1/2\pi\ln|\mathbf{x}|$ [7] and $c(\xi) = 1 - \alpha/2\pi$ where α is an exterior angle formed in point ξ by the tangents to the boundary. The advantage of this approach is that the right side of the equation depends on the value of vector **B** only inside area D, and not on the boundary where **B** could be singular.

Solution (17) requires that vector function **B** be integrated over whole area D. Having in mind the effectiveness and accuracy of the numerical calculations, the integrals were transformed to forms containing expressions with only first-order derivatives:

$$\begin{aligned}\int_D \mathbf{B}\cdot\nabla P^*(\mathbf{x},\xi)d\mathbf{x} &= \int_S P^*(\mathbf{x},\xi)\frac{\partial \mathbf{u}}{\partial t}\cdot\hat{\mathbf{n}}dS(\mathbf{x}) + \int_D \nabla\left(\frac{\mathbf{u}^2}{2}\right)\cdot\nabla_{\mathbf{x}}P^*(\mathbf{x},\xi)d\mathbf{x} + \\ &\int_D \omega\left(\mathbf{u}\times\nabla_{\mathbf{x}}P^*(\mathbf{x},\xi)\right)d\mathbf{x} - \nu\int_D(\nabla\times\boldsymbol{\omega})\cdot\nabla_{\mathbf{x}}P^*(\mathbf{x},\xi)d\mathbf{x}.\end{aligned} \tag{18}$$

The velocity $\mathbf{u}(\mathbf{x},t)$ functions and the vorticity functions $\omega(\mathbf{x},t)$ in Equation (18) are previously determined by RVM; $\nabla_{\mathbf{x}}$ stands for a gradient relative to variable **x**.

Flow area D was divided into triangular elements and integration over the area was replaced by the sum of the integrals over the elements. The integrals were calculated approximately using numerical quadrature. For a detailed description of the above transformations and the solution (see [11]).

Having the pressure distribution one can determine the variable hydrodynamic load, which from the engineering practice point of view is the main aim of the calculations. Although the hydrodynamic force is the result of not only the pressure, but also of the viscous friction acting on the structure around which the stream flows, in cases with a high Reynolds number the friction force caused by viscous friction is very weak in comparison with the force resulting from the pressure, and so it can be neglected. Here the hydrodynamic force was determined as an integral from the pressure along boundary S:

$$\mathbf{F} = -\int_S p\hat{\mathbf{n}}dS. \tag{19}$$

5. Numerical simulation of flow under lift gate

In this section the capabilities of RVM for calculating the flow instability under the lift gate are demonstrated. Figure 2 shows a vertical lift gate placed in a 2.8 m high, 2.3 m wide and 25 m long outlet duct. The gate is 0.4 m wide and its bottom edge profile is rectangular. This shape of the gate was chosen since sharp corners give rise to strong pressure fluctuations on the gate (see Thang [19], Billeter [2]).

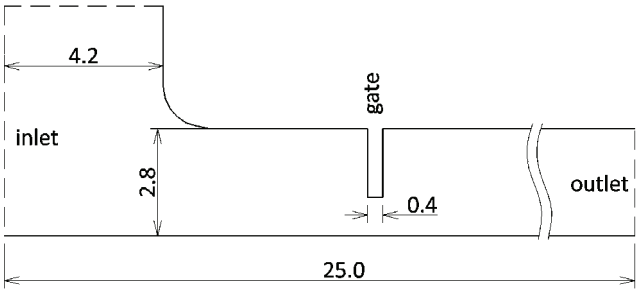

Fig. 2. Scheme of vertical lift gate

Figure 3 shows four gaps of 0.5 m, 1.0 m, 1.5 m, and 2.0 m considered in cases A, B, C and D, respectively.

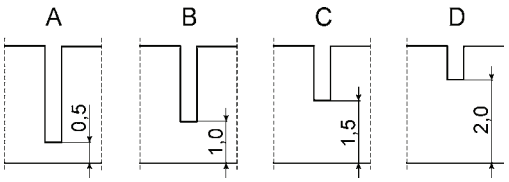

Fig. 3. Four cases of gate opening

The assumed water elevations H at inlet (Figure 1) was 18 m. Conventional hydraulic calculations were done to determine the water discharge through the conduit, including minor and major head losses. The results of the calculations for the four cases of gate opening are as follows: Q_A = 13.52 m^3/s, Q_B = 26.84 m^3/s, Q_C = 39.97 m^3/s, Q_D = 52.92 m^3/s.

The flow was modelled in the non-dimensional system. This means that all the distances were divided by hydraulic radius R_h corresponding to the size of the gate cross section and the velocities were divided by mean horizontal velocity u_0 of the flow through the gate cross section. The Reynolds number was

$$Re = \frac{u_0 R_h}{\nu}, \tag{20}$$

where R_h is the hydraulic radius and $\nu = 10^{-6}$ m^2/s is the kinematic viscosity of water at 18°C. The velocities and the Reynolds numbers for the four cases of gate lifting were respectively: u_{0A} =11.76 m/s, u_{0B} = 11.67 m/s, u_{0C} = 11.59 m/s, u_{0D} =11.50 m/s, $Re_A = 2.41 \cdot 10^6$, $Re_B = 4.07 \cdot 10^6$, $Re_C = 5.26 \cdot 10^6$ and $Re_D = 6.15 \cdot 10^6$.

Vortex method simulations of the flow were run for the following non-dimensional parameters:

– $ds = 0.1$ – the length of the border segment on which the vorticity layer is transformed into a vorticity particle,

– $dt = 0.1$ – the time step,

– $kt = 1200$ – the number of time steps in each simulation.

Figure 4 shows the stream function and the velocity and vorticity fields for Case B after time $t = 100$ (non-dimensional).

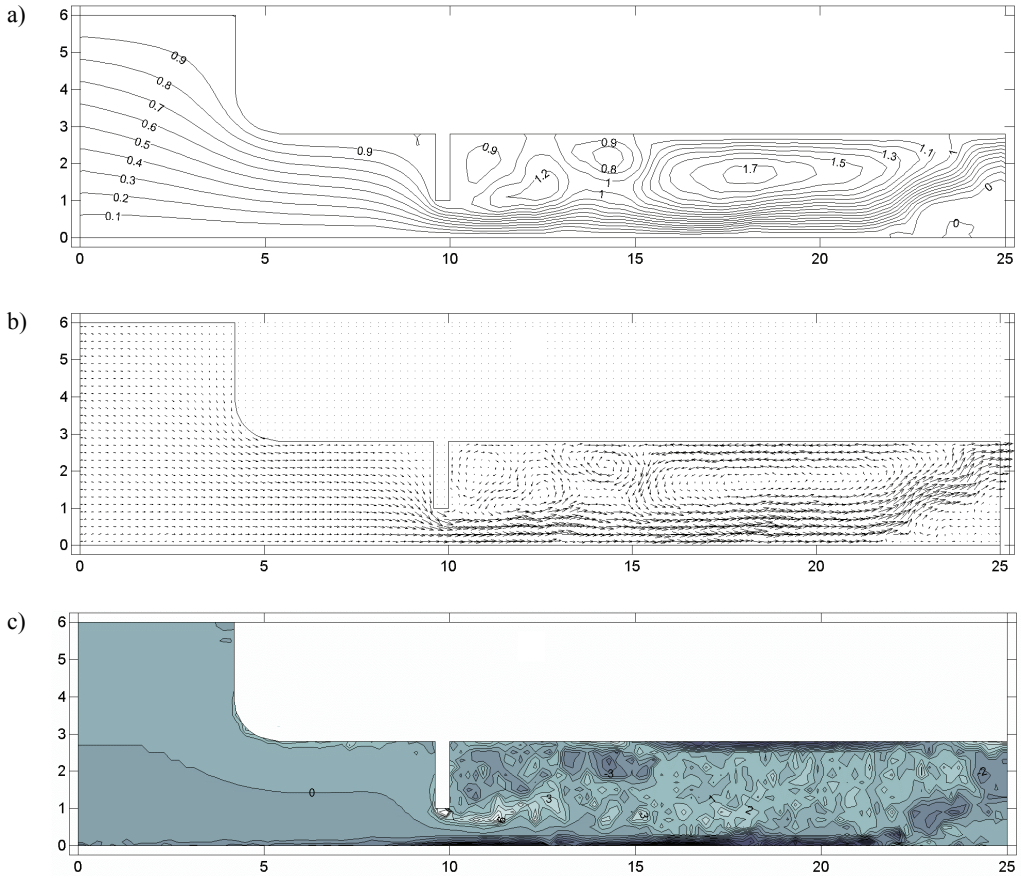

Fig. 4. Simulation results for case B – R_h = 4070000, kt = 1000, Δt = 0.1 and N = 17376: a) streamlines; b) velocity field; c) vorticity contours

There is a recirculation zone behind the gate, which can be observed in Figure 4a along the closed stream lines and in Figure 4b in the form of a vortex defined by the velocity field vectors. The vorticity isolines in Figure 4c reach their extreme positive non-dimensional values in the cross section below the gate while their extreme negative values occur along the conduit bed behind the gate. The extremes result from the intense generation of vorticity.

Figure 5 shows the position of vortex particles for time step 1000 (N – the number of vorticity particles). A flow velocity vector is attached to each particle to demonstrate the vorticity dynamics. The vorticity particles detached from the gate edge simulate the creation and evolution of the shear layer.

The results of the numerical simulation for time step kt = 1000 in Case D are presented in Figure 6.

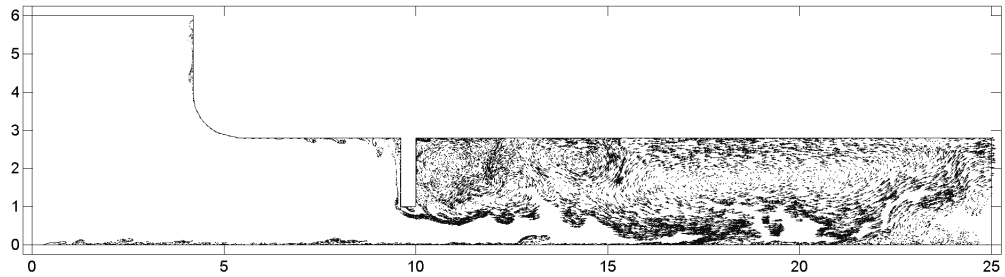

Fig. 5. Distribution of vortex particles in case B: Re = 4070000, kt = 1000, Δt = 0.1 and N = 17376

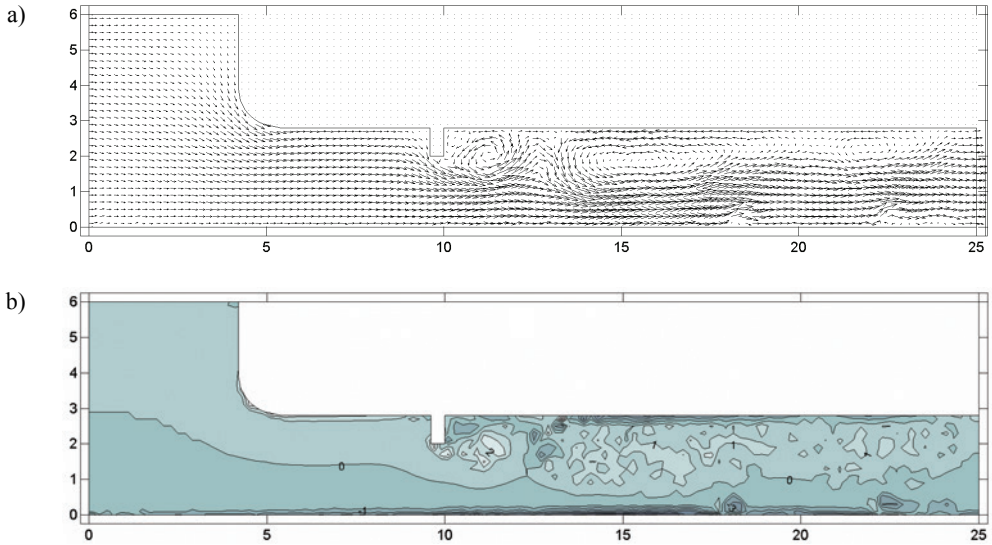

Fig. 6a, b. Simulation results in case D – Re = 6150000 at kt = 1000 for Δt = 0.1 and N = 11987: a) velocity field; b) vorticity contours;

c)

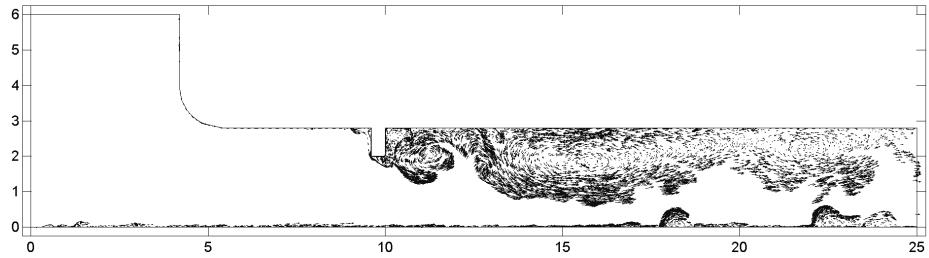

Fig. 6c. Simulation results in case D – Re = 6150000 at kt = 1000 for Δt = 0.1 and N = 11987: c) vortex particle distribution

According to Figures 4, 5 and 6, the recirculation zone decreases as the gate opening increases. The vorticity reaches considerably lower values than in the case of the 1.0 m opening.

Figure 7 shows some details of the boundary layer at the gate edges.

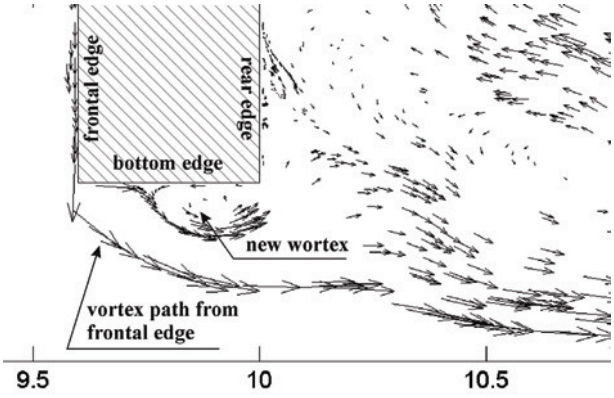

Fig. 7. Generation of new vortex at lift gate bottom edge – case B

The vortex particles flowing along the leading edge detach from the corner, creating a constant vortex path under the gate. A vortex arises at the gate's bottom and after some time it detaches from the bottom edge causing quasi-periodical changes in pressure on the edge. This constitutes the SILEV mechanism. The detached vortex joins the layer which flows off the rear trailing edge of the gate, forming larger coherent vortical structures interacting with the vortex path detached from the front edge. The vortical structures are then advected towards the outlet. The movement of the vortical structures affects the velocity field and the pressure distribution at the rear edge and in consequence, the ISL mechanism of flow-induced vibrations arises. Downstream from the gate the diameter of the vortical structures grows due to vorticity diffusion and boundary generated vorticity. Figure 8 shows vortex detachment from the gate and the subsequent downstream drift of the vortex structures.

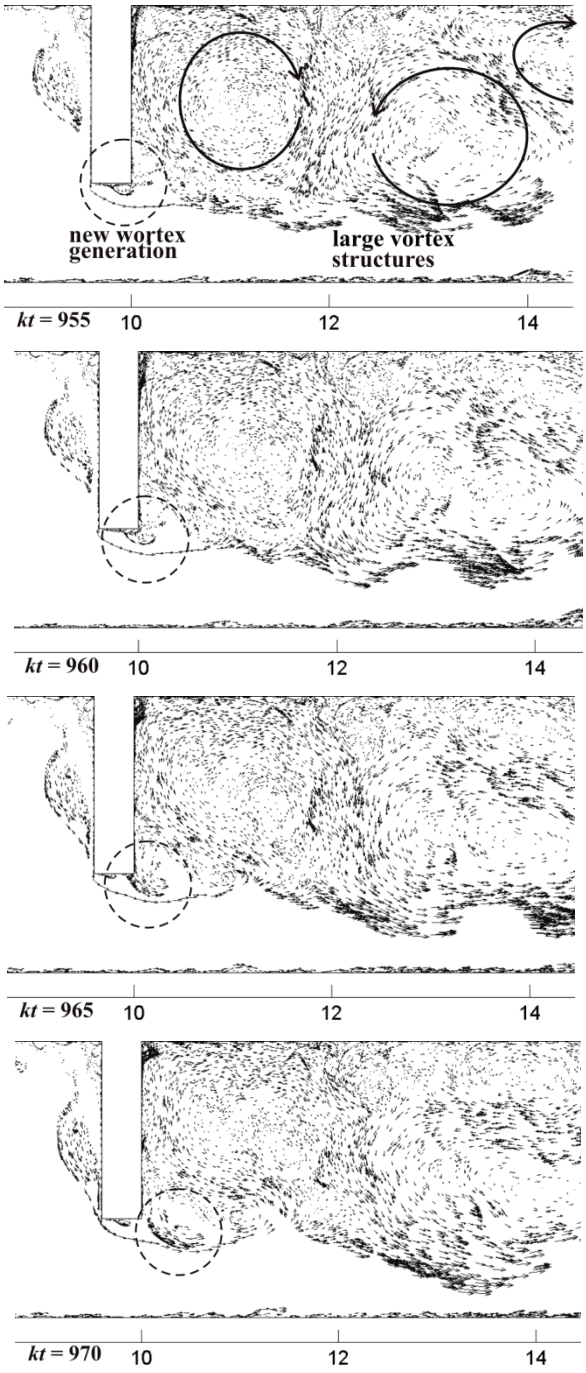

Fig. 8. Evolution of new vortical structure behind gate (case B) for time steps: 955, 960, 965 and 970

SILEV causes vertical vibrations of the gate because of the pressure changes at the bottom edge whereas ISL causes pressure changes at the rear wall, resulting in horizontal vibrations of the gate. The frequency of SILEV is characterized by the non-dimensional Strouhal number:

$$Sh_{\mathrm{SILEV}} = \frac{nd}{u_0}, \tag{21}$$

where n is the frequency of the vortex shedding from the lower edge of the gate (obtained by applying FFT to the velocity signal in the time interval from the 500th to the 1000th time step) and d is the gate width. In case B, Sh_{SILEV} = 0.205, which is very close to the value of 0.2 obtained by Thang [19] and Billeter [2].

Figure 9 shows the instantaneous reduced vorticity circulation at a point beneath the bottom edge of the gate in case B. The mean value of the circulation is 3.4 and its standard deviation amounts to 2.7

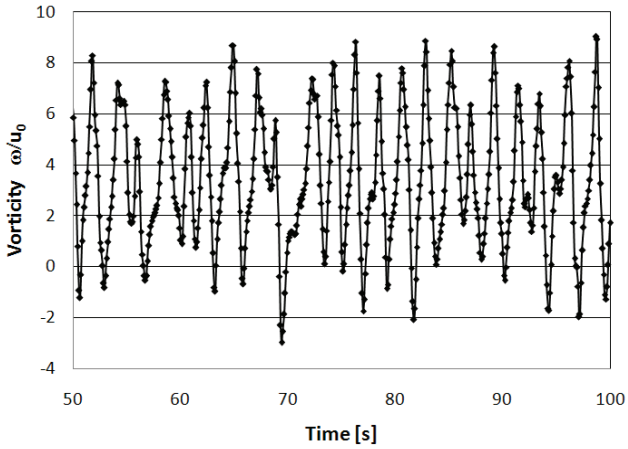

Fig. 9. Time history of vorticity at gate bottom edge: case A

As the relative gap increases, the strength of detached vortices decreases. The mean value of the reduced circulation is 2.7 and 2.6 in respectively case C and D, at the same standard deviation of 1.6. As a result, the amplitudes of the vertical and horizontal hydrodynamic force components will be smaller as well.

In cases C and D, Sh_{SILEV} = 0.22 and 0.16, respectively. The calculated Strouhal number for SILEV is similar for all the simulations. However, Sh_{ISL} is much more difficult to estimate because of the interactions between the vortex detaching from the gate and the downstream vortical structures (Figure 8). A sensible approach is to calculate the frequency of the horizontal force fluctuations determined by integrating the pressure distributions on the gate's front and rear faces. This will be demonstrated in the next section.

6. Pressure and hydrodynamic force calculations

The pressure in the flow under the gate was calculated by BEM in accordance with the principles presented in section 4 (Equations (17) and (18)). The pressure distribution on the boundary was determined (in non-dimensional terms) in the form of pressure coefficient $C_p = \dfrac{p - p_0}{\rho u_0^2/2}$, p_0 – the pressure in the cross section of the contracted flow behind the gate. Figure 10 shows the mesh of triangular elements used for the calculation of the surface integrals in Equation (18). Figure 10 shows the distribution of coefficient C_p on the front, bottom and rear edge of the gate in case B for selected three instants at which the values of C_p are significantly different.

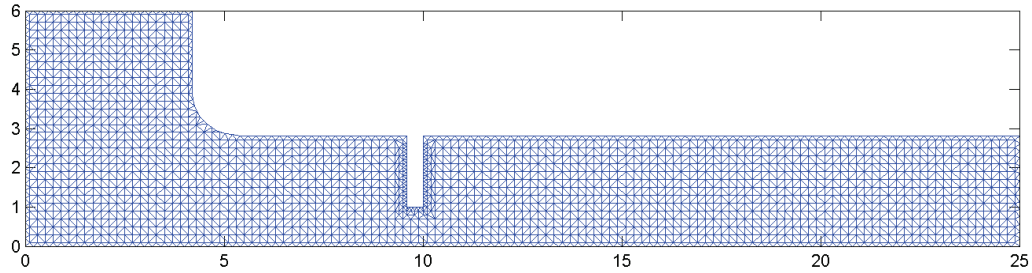

Fig. 10. Flow area discretization by $M = 4593$ triangles: case B

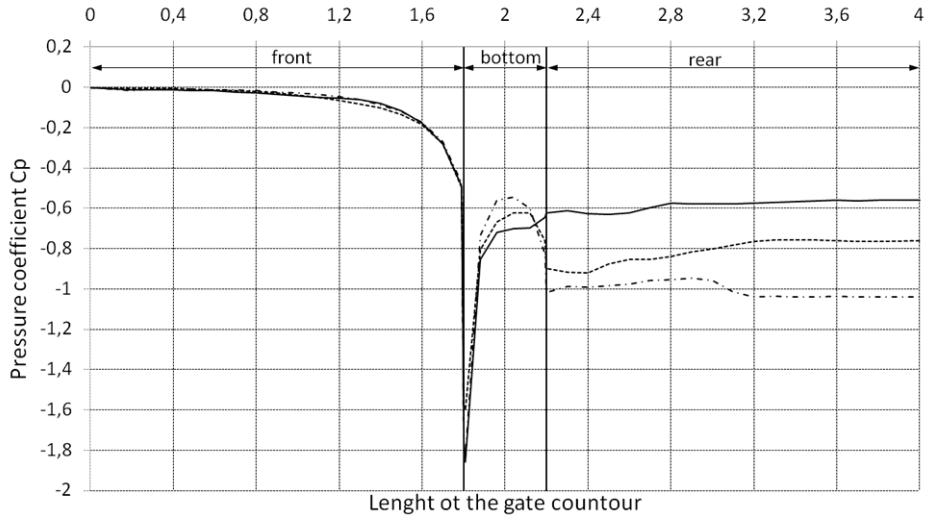

Fig. 11. Distribution of C_p along gate edge in case B: (—)kt = 1060,(− −) kt = 1070, (− · −) kt = 1095

The distribution of pressure on the front wall is approximately constant over time. Due to the formation of a vortex path, the pressure varies significantly, resulting in a strong ISL mechanism.

By integrating, in accordance with Equation (19), the distribution of pressure coefficient C_p for the front, rear and bottom edge, the hydrodynamic force coefficient components: horizontal C_{FH} and vertical C_{FV} were obtained. The components in case B for the time steps from the 700th to the 1000th are shown in Figure 13.

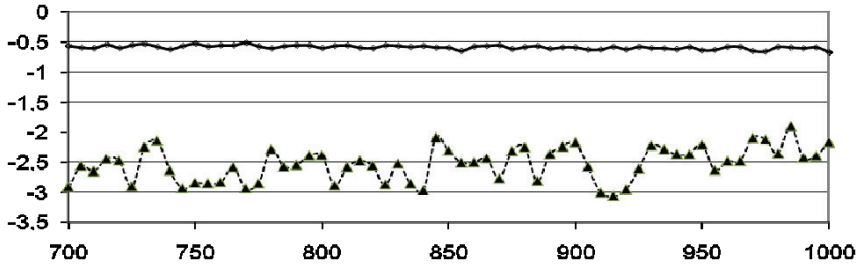

Fig. 12. Coefficient of horizontal C_{FH} and vertical C_{FV} hydrodynamic force. Case A: (—) C_{FV}, (− −) C_{FH}

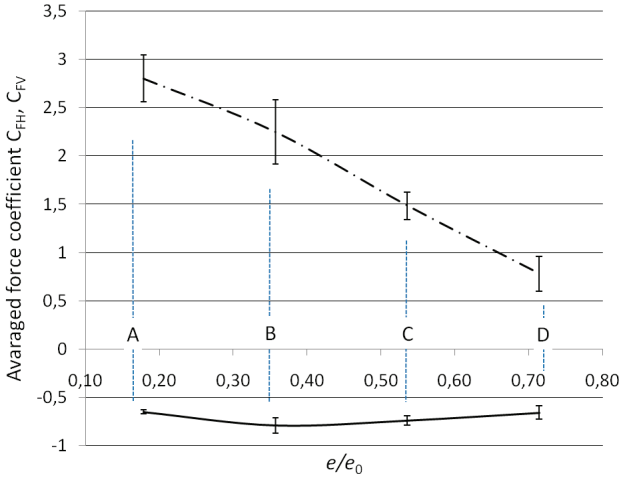

Fig. 13. Averaged coefficients of horizontal C_{FH} and vertical C_{FV} hydrodynamic force and standard deviations for case A, B, C and D

In case B, horizontal component C_{FH} acting on the rear wall has a predominantly negative value. The component shows an irregular frequency and amplitude, due to the simultaneous action of several large vortex structures on the rear wall of the gate. The horizontal hydrodynamic force coefficient component acting on the front wall is approximately constant. Its slight fluctuations are caused by the flow off of fine vortex

structures (forming along the curved upper part of the channel) along the front edge. Horizontal component C_{FH} results from the difference between the components acting on respectively the front and rear edge of the gate.

In comparison with the horizontal component, vertical component C_{FV} is small, since it acts on the narrow bottom edge however the unit values are pretty the same. It is periodic and its frequency is consistent with the changes in the vorticity field under the gate, shown in Figure 9.

At the larger gate openings (cases C and D), the vertical and horizontal components of the hydrodynamic force are clearly smaller and less regular, which agrees with the observations that the greatest excitation of vibrations occurs when the ratio of the gap under the gate to the latter's thickness is $0.5 < e/d < 1.0$ (Thang [19], Naudascher [16]). Figure 13 shows the averaged values and standard deviations of C_{FH} and C_{FV} for the four cases.

7. Verification of method

Because of the lack of accurate pressure measurements for the flat gate the proposed numerical method, being a combination of the vortex method and the boundary element method, for determining the pressure and the hydrodynamic force at high Reynolds numbers is verified below for the downpull coefficient of the flat gate.

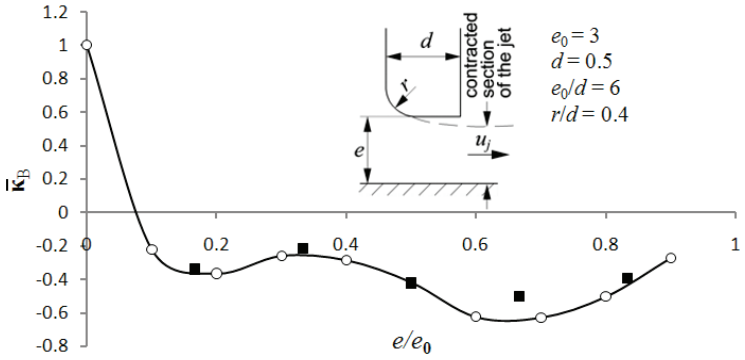

Fig. 14. Variation in $\bar{\kappa}_B$ with relative gate opening e/e_0 at $Re = 1.65 \cdot 10^6$: (■) RVM+BEM; (—○—) Naudascher 0

This coefficient is described by the following relation:

$$\bar{\kappa}_B = \frac{1}{d}\int_0^d \frac{2\left(h_i - h_j\right)}{\rho g u_j^2} = \frac{1}{d}\int_0^d \frac{2\left(p_i - p_j\right)}{\rho u_j^2} = \frac{1}{d}\int_0^d C_p, \tag{22}$$

where p_i is the pressure calculated in points lying along the gate's bottom edge, u_j, h_j, p_j are respectively the averaged horizontal velocity component, the piezometric head and the pressure in the contracted jet flow below the gate.

The downpull coefficient was calculated for a flat-bottom gate with a rounded leading edge (Figure 14) for five relative gaps e/e_0 = 0.167, 0.333, 0.5, 0.667 and 0.833. The location of the flow contraction was determined from the averaged stream function for each gate position. The calculation results were compared with the measurements for $Re = 2u_0 d/\nu = 1.65 \times 10^5$ presented in (Naudascher [16], Chapter 3.3.3). The calculations were done for four gate positions and the calculated pressure values were averaged over time t = 40 (non-dimensional). The results are presented in Figure 14.

Satisfactory consistency was obtained for all the relative openings e/e_0. One should note that the distribution of pressure strongly depends on the gate geometry, but also on the shape of the channel and the initial turbulence, which is probably the cause of the slight differences in the values of $\overline{\kappa}_B$.

8. Conclusions

Numerical experiments were performed to compute the flow under a vertical lift gate with a submerged outlet and a flat bottom edge at high Reynolds numbers in order to determine flow instability and hydrodynamic load fluctuations. Flow instability was simulated by the random vortex method (RVM), which uses a very simple algorithm (presented in this paper) based on flow physics and enables completely grid free Lagrangian calculations without any RANS type turbulent models. The RVM simulations run for several gate openings confirmed that (as the experimental data show) the flow instability is caused by the cyclic rise of a large vortex at the gate's bottom and its detachment, resulting in quasi-periodical changes in pressure. This constitutes a vertical vibration inducing mechanism, called SILEV. By analyzing the vorticity time histories for the four gaps by the FFT method, the vortex shedding frequency was determined. In Case B, the calculated Strouhal number was 0.205 which is very similar to value of 0.2 determined experimentally by Thang [19] and Billeter [2].

Changes in the velocity field in the recirculation zone, resulting from the interactions between the vortex path detached from the front edge and the coherent vortical structures forming behind the gate, cause fluctuations in the pressure acting on the gate's rear edge. These are referred to as ISL-type flow-induced horizontal vibrations. In order to investigate the ISL parameters, the pressure fluctuations on the gate were calculated using a numerical method based on BEM. In this method the pressure is determined from the velocity and vorticity field values within the flow area, previously calculated by RVM. The calculation results, in the form of curves of hydrodynamic force coefficient C_{FH}, show that the force strongly depends on the degree of gate opening: the larger the opening, the lower the mean value and amplitude of the force. Averaged over time C_{FH} is in a range of 0.8–2.8 for the relative gate opening of

e/e_0 = 0.18, 0.36, 0.54, 0.71. The frequency of the horizontal component is irregular. In case B, the dominant Strouhal number determined from the FFT analysis was also 0.2.

In order to verify the proposed method, downpull coefficient $\overline{\kappa}_B$ for a gate with rounded leading bottom edge for several gate gaps was calculated and compared with the results for a similar case, published by Naudascher [16]. Satisfactory agreement between the respective results was obtained. The slight differences can be due to the fact that the downpull coefficient depends not only on the shape of the gate, but also on the turbulence of the stream flowing to the gate. Because of the lack of sufficient data the two factors could not be accurately modelled.

The calculation results indicate that the vortex method can capture the dynamics of the flow around a lift gate and determine the significant fractions of turbulence and large coherent structures. The proposed method, being a combination of RVM and BEM, allows one to calculate, with a high degree of accuracy, the pressure, and in consequence the hydrodynamic forces.

References

[1] Billeter P.: *Flow-inducted multiple-mode vibrations of gates with submerged discharge*, Journal of Fluids and Structures, Vol. 14, 2000, pp. 323–338.
[2] Billeter P.: *Properties of single shear layer instabilities and vortex-inducted excitation mechanisms of thick plates*, Journal of Fluids and Structures, Vol. 19, 2004, pp. 335–348.
[3] Braza M., Chassaing P., Ha Minh H.: *Numerical study and physical analysis of the pressure and velocity fields in the near wake of a circular cylinder*, J. Fluid Mech., Vol. 165, 1986, pp. 79–130.
[4] Campbell F.B.: *Vibration problems in hydraulic structures*, J. Hydr. Div., Vol. 2, 1961, pp. 61–77.
[5] Colgate D.: *Hydraulic downpull forces on high head gates*, J. Hydr. Div., Vol. 11, 1959, pp. 39–52.
[6] Cottet G-H., Koumoutsakos P.D.: *Vortex methods: theory and practice*, Cambridge University Press, 2000.
[7] Gaul L., Kögl M., Wagner M., *Boundary Element Methods for Engineers and Scientists, An Introductory Course with Advanced Topics*, Springer-Verlag, Berlin Heidelberg, 2003.
[8] Hald O.H.: *Convergence of vortex methods for Euler's equations II*, SIAM J. Numer. Anal., Vol. 16, 1979, pp. 726–755.
[9] Hardwick J.D.: *Flow induced vibration of vertical – lift gate*, Proc. ASCE, J. Hydr. Div. Vol. 5, 1974.
[10] Kolkman P.A.: *Gate vibration. Developments in hydraulic engineering* – 2, Ed. by P. Novak, Elsevier, 1984.
[11] Kostecki S.: *Numerical determination of the hydrodynamic pressure acting on a hydraulic gate*, Polish J. of Environ. Stud., Vol. 16, No. 6B, 2007, pp. 39–45.
[12] Lewis R.I., *Vortex Element Methods for Fluid Dynamic Analysis of Engineering Systems*, Cambridge University Press, London, 2005.

[13] Majda A.J., Bertozzi A.L.: *Vorticity and incompressible flow*, Cambridge University Press, Cambridge, 2002.
[14] Naudascher E.: *Vibration of gate during overflow and underflow*, J. Hydr. Div., Vol. 5, 1961 pp. 63–86.
[15] Naudascher E., Rockwell, D.: *Flow-induced vibrations*, An Engineering Guide, A.A. Balkema, 1994.
[16] Naudascher E.: *Hydrodynamic forces*, A.A. Balkema, 1991.
[17] Sagar B.T.A., ASCE Hydrogates Task Committee Design Guidelines for High-Head Gates, IAHR J. Hydraul. Eng., Vol. 121, No. 12, 1995, pp. 845–852.
[18] Simmons W.P.: *Air model studies of hydraulic downpull on large gates*, J. Hydr. Div., Vol. 1, 1959, pp. 41–59.
[19] Thang N.D.: *Gate vibrations due to unstable flow separation*, J. Hydr. Eng. Vol. 116, No. 3, 1984, pp. 342–361.

Numeryczna analiza sił hydrodynamicznych wywołanych niestabilnością przepływu, działających na zamknięcie zasuwowe

W pracy przedstawiono numeryczną metodę wynikającą z połączenia metody wirów i metody elementów brzegowych do określenia dwuwymiarowego pola prędkości pod zamknięciem zasuwowym. W praktyce, zamknięcia w spustach dennych, pracujące jako ciśnieniowe są poddane silnym obciążeniom dynamicznym, wynikającym z odrywania się wirów od dolnej krawędzi zamknięcia i fluktuacji pola prędkości w strumieniu za zamknięciem. W artykule przedstawiono funkcję prądu, pole prędkości i wirowości dla dwóch poziomów otwarcia zasuwy. Przedstawiono mechanizm odrywania wirów i podano częstość tego zjawiska, wyrażoną za pomocą liczby Strouhala. Obliczone pola prędkości i wirowości zostały następnie wykorzystane do obliczenia rozkładu ciśnienia na powierzchni zamknięcia metodą elementów brzegowych. Zaprezentowano również przykładowe przebiegi czasowe współczynnika siły unoszenia i oporu. Wyniki symulacji numerycznych zweryfikowano na podstawie cytowanych w literaturze pomiarów współczynnika siły ssania działającej na zamknięcie zasuwowe.

ARCHIVES OF CIVIL AND MECHANICAL ENGINEERING

Vol. XI 2011 No. 4

Load capacity of damaged RC slab spans of railway-bridges

M. MAKSYMOWICZ
Gifford LLP, Carlton House, Ringwood Road, Woodlands, SO40 7HT Southampton, United Kingdom.

P.J.S. CRUZ
University of Minho, Campus de Azurém, 4800-058 Guimarães, Portugal.

J. BIEŃ
Wrocław University of Technology, Wybrzeże Wyspiańskiego 27, 50-370 Wrocław, Poland.

European railway bridges are relatively old and degradation processes cause defects diminishing their load capacity. This paper presents computer-based DAGA system supporting the load capacity assessment of damaged railway slab spans made of reinforced concrete (RC). Construction of the analysed bridge spans and types of considered defects (mainly material losses and strength reduction) are based on a study of the railway infrastructure in Poland and Portugal as well as on results of the international research projects focused on railway bridges. Presented system is equipped with an advanced graphical editor which enables precise and fast creation of a three-dimensional model of the damaged bridge span and offers graphical presentation of the results of the load capacity analysis. Effective algorithm of static and strength analysis allows simultaneous modelling of various defects with non-limited intensity, extent and location.

Keywords: load capacity, defect, RC slab span, railway bridge, visualization

1. Introduction

During bridge service life, degradation mechanisms occur resulting in various defects reducing its overall condition. In order to keep the infrastructure serviceable, its assessing is a crucial issue. Bridges need to be assessed to give their administration a basis for rational decisions on their further service. Repair, traffic load reduction, closing track or even bridge replacement are common problems to face, especially if financial restrictions are imposed. A structural assessment demands from an engineer much more as compared to a new structure design, usually considered as undamaged with clear geometry and constructed of sound materials. The analysis of damaged structures requires computer tools with user-friendly interface for easy input of the inspection data, graphical modelling of damaged structures and quick data processing with a graphical output. Currently, the market offers a great number of software provided with the Finite Element Methods interface (LUSAS, ROBOT, COSMOS, SAP, etc.) for designing new structures. Unfortunately, they do not cover simple facilities to deal with

defects. Therefore, a need for a suitable tool for assessment of damaged structures seems to be a current issue.

European railway infrastructure stock research [1, 8–9, 12, 19, 21, 26] showed single span bridges as the majority (54%) with those carrying single tracks prevailing (89%). The railway bridge structures are old and only 11% of them are aged less than 20 years, 22% are 20 to 50 years old, 35% are 50 to 100 years old and 35% – over 100 years. Reinforced concrete (RC) was used for about 25% of the whole population of about 250 000 railway bridges located along almost 220 000 km of railway lines. Considering also various degradation mechanisms, the existing bridge infrastructure is an important problem for railway administration.

These statistics and lack of suitable software led to a conception of a computer system called "Damage Assessment Graphic Analysis – DAGA" for assessing load capacity of damaged RC railway slab spans [21–24]. The system is addressed to the administration responsible for bridge maintenance and operation management as well as to design and consulting offices involved in bridge condition assessment. Presented system is equipped with an advanced graphical editor which enables precise and fast creation of a 3D model of a damaged span, ensures effective static-strength analysis and offers clear graphical presentation of results.

Degradation processes of reinforced concrete are very complex (e.g. [2, 5, 7, 9], [20, 23, 27]) and a large group of testing methods have been developed for detection and identification of defects, e.g. [2, 14–16, 23, 25]. In the taxonomy of RC bridge defects, six main types can be distinguished [2, 4–5, 11, 13, 28]: contamination, deformation, deterioration, discontinuity, displacement and loss of material. Deterioration of concrete and loss of material have the most influence on load capacity. Deterioration usually manifests itself in the strength reduction (of concrete and steel). Loss of material should be considered both for reinforcement and concrete. The analysis of load capacity in the DAGA system is to be carried out for any combination of the defects considered, with no limits regarding their parameters, i.e. location, intensity and extent.

2. Procedure of load capacity assessment

In Figure 1, the assessment procedure implemented in the DAGA system is presented. Having created a record with a bridge structure, the user provides the system with all the information regarding the geometry and defects. In order for the data to be transformed, models of material as well as loads need also to be specified.

The transformed data is used to build a model of a damaged structure, then static and strength analyses are to be carried out to produce envelopes of internal forces and cross-section capacity. Comparison of these two envelopes enables assessment of the load capacity of the damaged slab span. The information based on a three-dimensional model of the damaged bridge span and effective algorithm of static and strength analysis offer a basis for making rational decisions in structure operation and maintenance management.

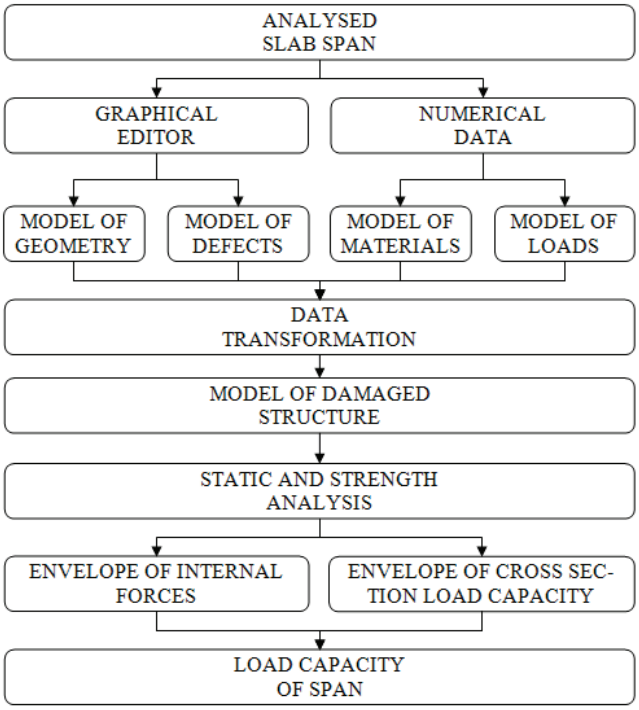

Fig. 1. Functional scheme of DAGA system

3. Modelling of damaged structure geometry

Models of geometry applied in the bridge engineering can be classified in terms of the dimension (e^i) of elements used in a bridge model, with possible application of non-dimensional (e^0), one- (e^1), two- (e^2), or three-dimensional elements (e^3) and space dimension (s^j) in which the bridge model is created – from a non-dimensional space (s^0) to a real 3D space (s^3) [2], [17]. Combinations of the parameters (e^i) and (s^j) give ten basic classes of the considered models of bridge geometry denoted as (e^i, s^j), where i is the dimensionality of elements, and j is the dimensionality of space (Table 1). For example, a model consisting of two-dimensional (e^2) elements formed in a 3D (s^3) space belongs to class (e^2, s^3).

Table 1. Classification of geometry models of bridge structures [2–3]

Element dimension	Space dimension			
	(s^0)	(s^1)	(s^2)	(s^3)
(e^0)	(e^0, s^0)	(e^0, s^1)	(e^0, s^2)	(e^0, s^3)
(e^1)	x	(e^1, s^1)	(e^1, s^2)	(e^1, s^3)
(e^2)	x	x	(e^2, s^2)	(e^2, s^3)
(e^3)	x	x	x	(e^3, s^3)

Models based on the non-dimensional elements (e^0) are usually used in the computer-based Bridge Management Systems [3] and all other classes of geometry models can be applied in bridge structure analysis.

The DAGA generates a 3D model of a bridge span, i.e. a class (e^3, s^3). However, the fully 3D model is saved in the data base for graphical presentation purposes. In the analysis, some simplifications take place and the assessment is to be performed by means of the mixed model of geometry. The structural assessment requires the location of a damaged cross-section to determine whether the maximal allowed effort of a cross-section is exceeded. The static analysis is based on the simply supported beam class (e^1, s^3), but in the strength analysis, the vertical location of the reinforcement and concrete needs to be considered referring to the class (e^2, s^3). Table 2 presents model classes implemented in the DAGA system.

Table 2. Geometry models applied in the DAGA system

Defect	Data base	Strength analysis	Static analysis
Loss of concrete	(e^3, s^3)	(e^2, s^3)	(e^1, s^3)
Loss of reinforcement			
Modification of concrete strength		(e^1, s^3)	
Modification of reinforcement strength			

4. Analysed slab span

The idea of the DAGA system is to deal with a bridge structure as a database containing all the information usable to create its structural model. The program has been written mainly in VB.NET, but all operations with database are conducted by means of the SQL language. Dimensions of an analysed slab span (Figure 2), defined by the system operator, are used for creation of a 3D model of the bridge, including abutments and track components (Figure 3).

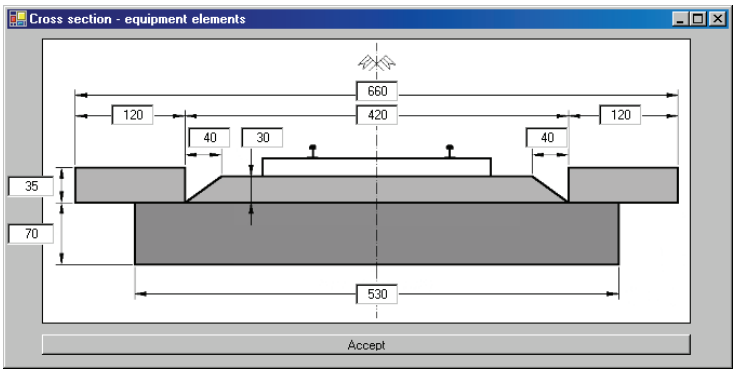

Fig. 2. Modelling of cross section geometry of railway slab span

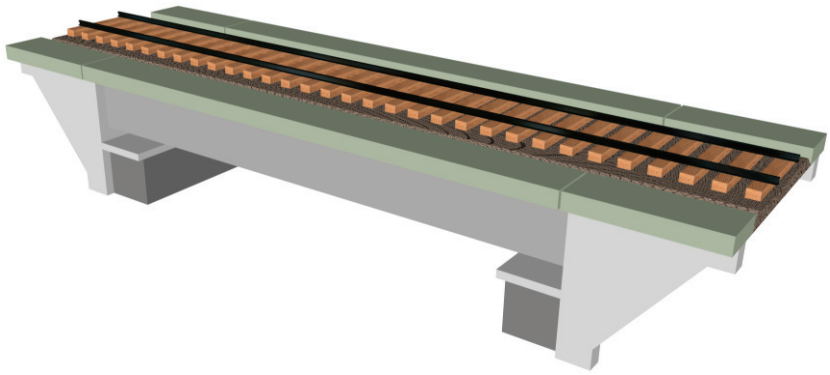

Fig. 3. Three-dimensional model of bridge span generated by the DAGA system

Geometrical data on location, diameter and number of longitudinal reinforcing bars (Figure 4a) and stirrups (Figure 4b) form the basis for creation of a three-dimensional model of span reinforcement. In the model of reinforcement network location and diameters of all steel bars are represented (Figure 4c).

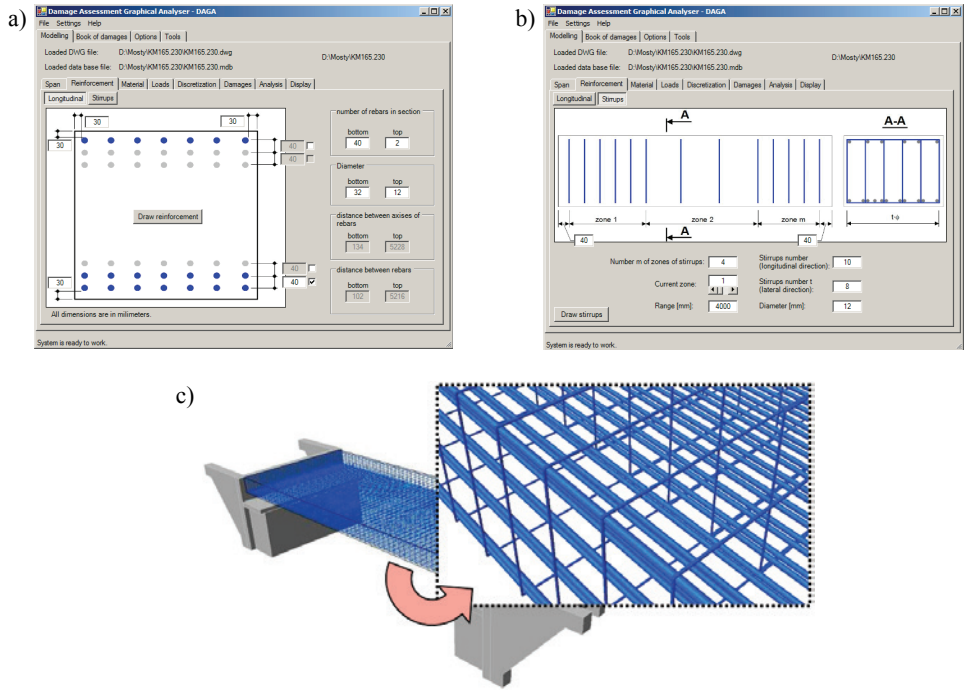

Fig. 4. Reinforcement: a) longitudinal bars data, b) stirrups data,
c) model of reinforcement generated by the DAGA system

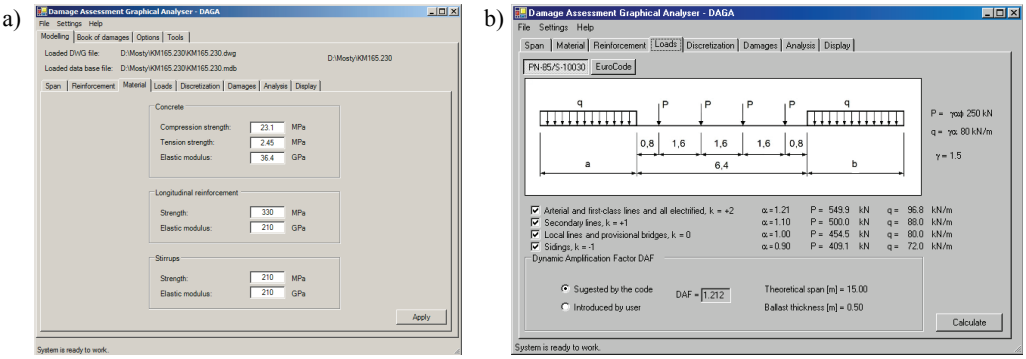

Fig. 5. Modelling of: a) material properties, b) loads according to the design code

After the span geometry is defined, the material parameters of the slab can be set, i.e. compressive and tensile strengths of concrete, strength of reinforcement and elastic modulus of concrete and reinforcement (Figure 5a). These parameters are saved in the database to be processed according to a selected code. The considered load consists of the dead and live part. The user can consider one or more load classes (Figure 5b) taking into account various load standards.

5. Structure defects

5.1. Graphical editor

Defects and especially their irregular forms make the modelling more difficult as compared to structures being designed. To represent defect parameters with required accuracy, the bridge model discretization is necessary. Development of computer technologies enables precise and effective 3D modelling of the bridge structures, e.g. [3], [6], [10], [18]. In the presented DAGA system [21] the slab is initially divided into 640 (20 × 8 × 4) elements. Moreover, each of them can be divided into the 1000 (10 × 10 × 10) elements and once again in the same way. In the case of construction of a common bridge with a 14.0 m span, the system allows modelling loss of concrete exact to 5–7 mm, which seems to be acceptable. The discretization of longitudinal reinforcement is carried out at the moment of its creation and causes creation of 20 elements along their axes. Each of them can be divided once again into the 10 new smaller elements. Moreover, to increase the accuracy, each of them can be further divided in this way. Structure defects can be modelled by means of a graphic editor. The user specifies the intensity of reinforcement loss and selects rebars to model the defect. The intensity is linked to a colour as a corrosion indicator from blue (sound material) through green (40–60%) and red (70–80%) to brown (90%). Defect intensity of 100% means a fracture of the rebar. Intensity and location of defect is visually presented as change of rebar diameter (Figure 6).

a) b)

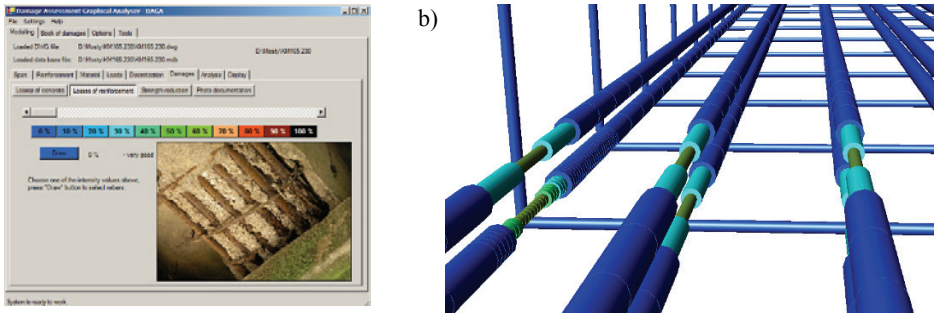

Fig. 6. Modelling of reinforcement losses: a) defining of defect parameters, b) visualisation of damaged bars in DAGA system

Regarding losses of concrete, the idea is to select elementary concrete volumes to be removed from the model. In reality, they are moved to a hidden layer, but in the analyses they are ignored to represent a loss. An example of defect visualisation with the discretization methodology applied is presented in Figure 7.

a)

b)

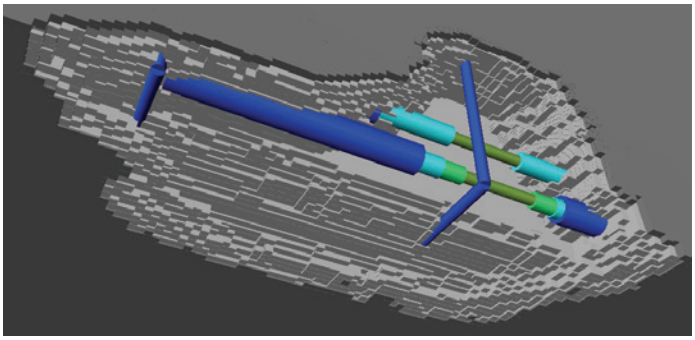

Fig. 7. Modelling of concrete losses: a) documentation of bridge inspection, b) combination of concrete and reinforcement losses visualised by means of DAGA system

Visualisation of defects gives a general impression of a current condition of a structure. However, it is also useful to see a graph with a defect distribution along the span axis (Figure 8). In the case presented here, the distribution of the reinforcement ratio ρ varies between 1.87% (designed condition) and 1.52 (current condition). The compressive strength of concrete σ_c varies between 40 MPa (designed condition) and 30 MPa (current condition). The strength of reinforcement σ_s is equal to 270 MPa (designed condition) and in the worst cross-section it is equal to 256 MPa (current condition).

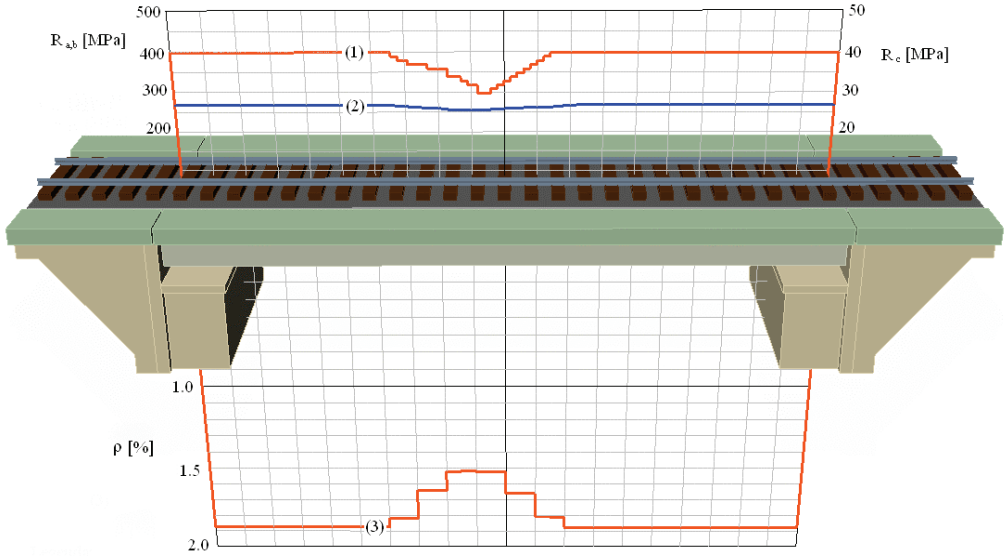

Fig. 8. Representation of the bridge span defects after transformation to class (e^1, s^1) geometry model: (1) compressive strength of concrete R_c (right axis), (2) strength of steel in the bottom layer $R_{a,b}$ (left axis), (3) decrease of reinforcement ratio ρ [%]

5.2. Defect modelling based on photos

The modelling of damaged structures in computer systems requires an engine of high precision. Usually, defects are characterized by irregular forms making this process difficult. Non-adequate defect representation in the model may cause severe consequences regarding results. The simplest way is to describe the defect taking into account results of direct measurements, but very often the structure is inaccessible.

In order to simplify this problem, an additional tool has been introduced to the DAGA system. Instead of the direct measurement, a photographical documentation collected during bridge inspections can be used. The pictures of damaged parts of a structure are to be stored in the database and then the photos are geometrically transformed to be applied in DAGA program [21].

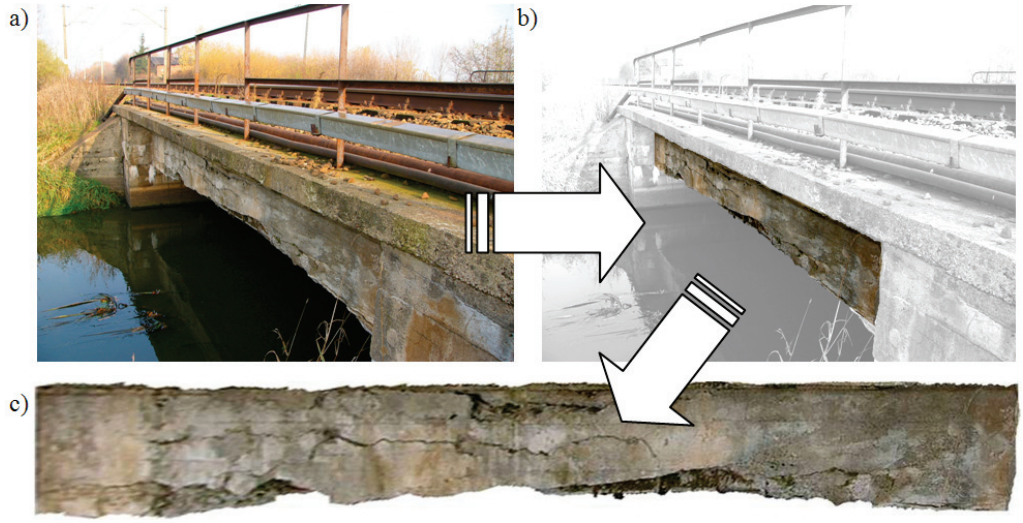

Fig. 9. Acquisition of the slab surface image procedure: a) the analysed bridge construction (photograph courtesy of Jerzy Cząstkiewicz, PKP), b) the extracted surface image, c) the geometrically transformed image applicable in the DAGA system

In order to geometrically transform the picture, the common programs for image editing (i.e. ACD FotoCanvas, Corel, Photoshop etc.) can be applied. In Figure 9, the procedure of slab surface image acquisition and transformation is presented. After the picture of the considered bridge span (Figure 9a) is taken, the area of the considered span surface (Figure 9b) has to be extracted. The final result (Figure 9c) can be applied in the analysis.

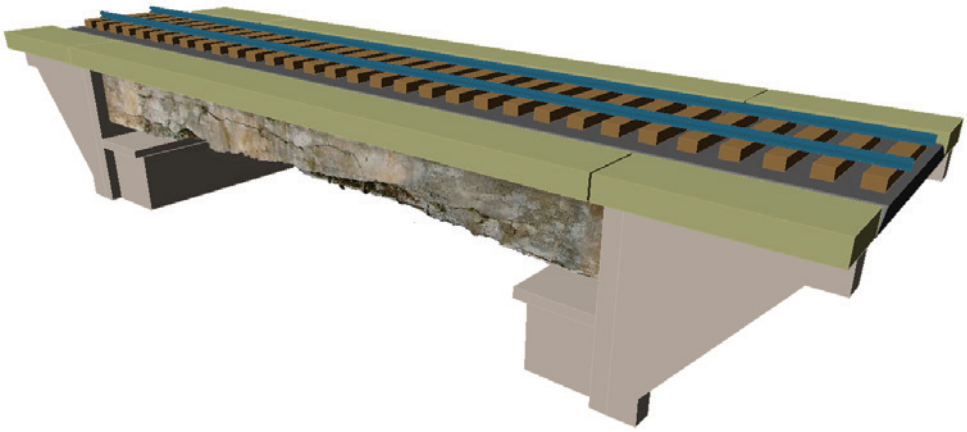

Fig. 10. Application of the photo documentation in 3D model of the damaged structure

Particular pictures are automatically attributed to the surfaces of the bridge span model and are ready to be displayed. The user selects the date of the visual inspection and pictures inserted in that time allow the proper defect representation and load capacity assessment. An example of application of this facility is presented in Figure 10. Severe losses of material are visible and easy to represent in the model. Another advantage of this solution is a possibility of monitoring of the bridge degradation progress based on visual inspections every reasonable period of time. The superposition of collected results allows reconstruction of degradation progress during bridge operation and prediction of its future condition.

6. Static and strength analysis

In the DAGA system, only bending as a dominant influence on load capacity has been considered. Shear force in the RC slab structures is of less importance. An influence of torsion and punching at considered moving load (centrically situated) type can be also omitted. General scheme of the load capacity assessment is presented in Figure 1.

Procedure of discretization of an analysed structure is presented in Figure 11. Each distinguished cross section has an identification $i = 1, 2, ..., n$ and each layer of cross section is represented as $j = 1, 2, ..., m$.

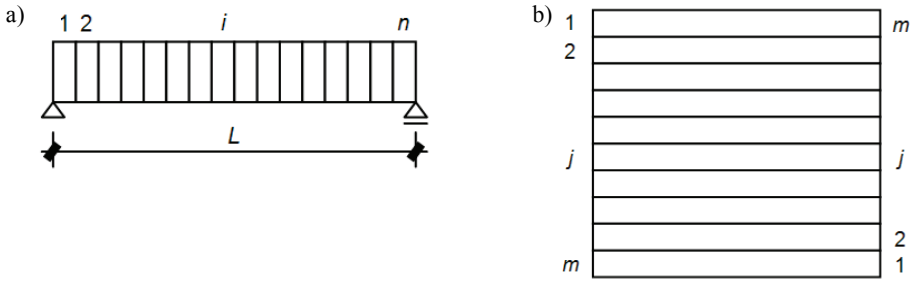

Fig. 11. Discretization of the analysed structure: a) along the span, b) in the cross section

The following symbols describe strains, stresses, and internal forces:

F_{ij}^{c} – force in concrete at layer "j" of cross section "i";

F_{ij}^{s} – force in reinforcement at layer "j" of cross section "i";

ε_{ij} – strain at layer "j" of cross section "i";

σ_{ji}^{c} – stress in concrete at layer "j" of cross section "i";

σ_{ji}^{s} – stress in reinforcement at layer "j" of cross section "i".

The index "max" means the maximal acceptable value of strain/stress according to the considered code. Applied algorithm of the load capacity is an iteration process based on

the incremental modification of internal forces in each cross section (Figure 12). Details of the algorithm are presented in Figure 13.

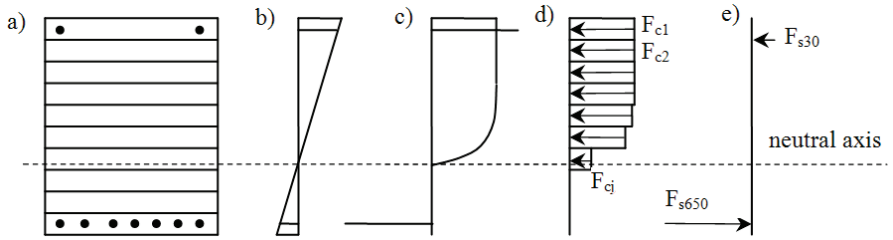

Fig. 12. Distribution of internal forces: a) layers of the cross section, b) strain distribution, c) stress distribution, d) internal forces in concrete layers, e) internal forces in reinforcement [21]

The $\Delta\varepsilon_{im}$ controls the program flow. The $\varepsilon_{\text{eff}}^{s,\max}$ (introduced in preliminary strain distribution) is a strain in the bottom concrete layer, while the bottom layer of reinforcement has the maximal acceptable strain. The cover of reinforcement is subjected to a higher strain and for this reason this parameter is enriched by the "eff" (effective) index. A schema of cross section discretization and internal forces distribution is presented in Figure 12.

At the beginning of the analysis, the top layer of cross section is subjected to strain causing maximum effort of concrete $\varepsilon_{i1} = \varepsilon^{c,\max}$. The strain in the bottom layer of cross section ε_{im} is equal to zero. At this moment, the cross section is not at equilibrium of forces. In order to find this equilibrium, the iteration loop is started. The stress at the bottom layer is increased. From strain distribution it is possible to pass to the stress distribution (using the relations $\sigma = f(\varepsilon)$) and then to the internal forces distribution. The equilibrium of forces is checked. Increasing of strain is performed until the sum of forces is equal to zero. While the equilibrium of forces is reached, the location of neutral axis can be found.

The next step is strain or stress verification of whether the maximal values in particular layers are not exceeded. If strains or stresses exceed the limits, then the initial conditions have to be inverted. It means the bottom layer of cross section is subjected to strain $\varepsilon_{\text{eff}}^{s,\max}$ causing maximum effort of bottom reinforcement and strain at the top layer is equal to zero. The next steps are similar.

When the equilibrium of forces is reached, then the load capacity of cross section can be evaluated according to the following formula:

$$M_R = \sum_{i=1}^{ns} \left(F_{si} \cdot r_{si}\right) + \sum_{i=1}^{nc} \left(F_{ci} \cdot r_{ci}\right), \tag{1}$$

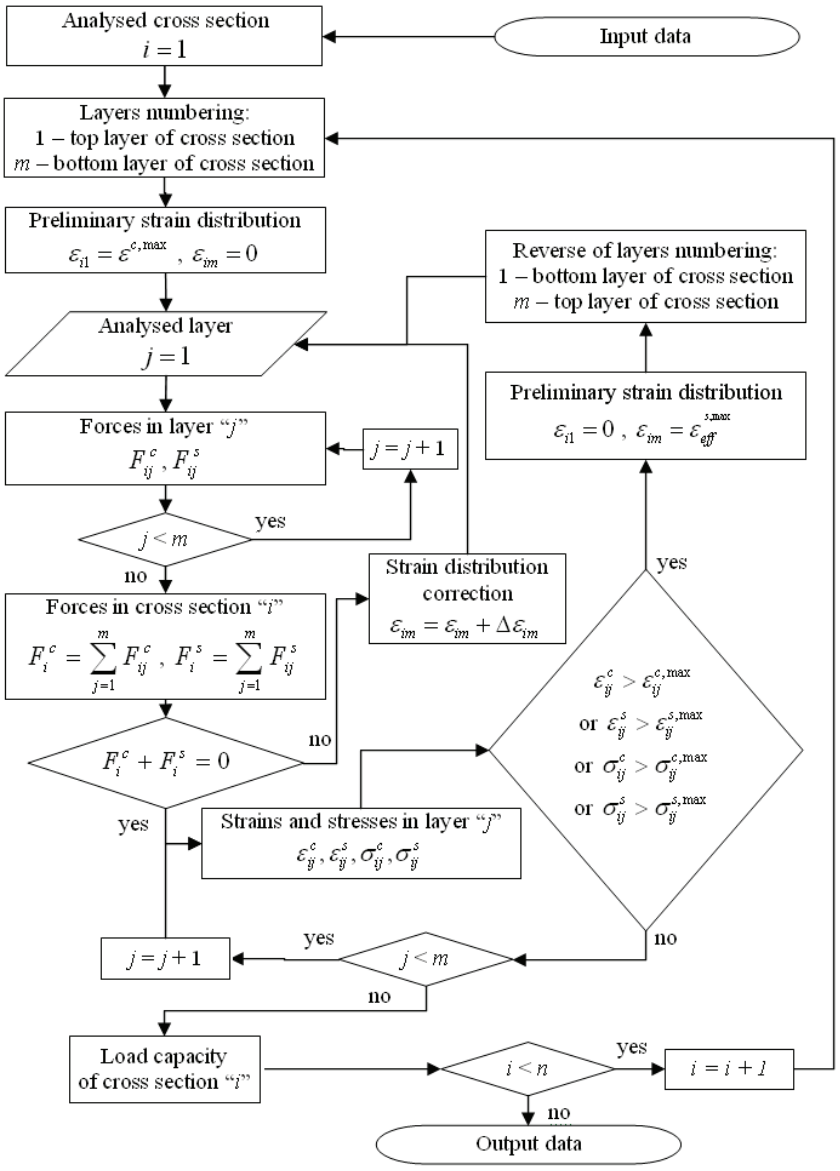

Fig. 13. Algorithm of load capacity calculation

where:

M_R – load capacity of analysed cross section;

F_{si} – value of the force in the current layer of the reinforcement;

r_{si} – location of current rebar layer against the neutral axis of the cross section;

n_s – total number of reinforcement layers;

F_{ci} – value of the force in the current layer of the concrete;
r_{ci} – location of current concrete layer against the neutral axis of cross section;
n_c – total number of concrete layers.

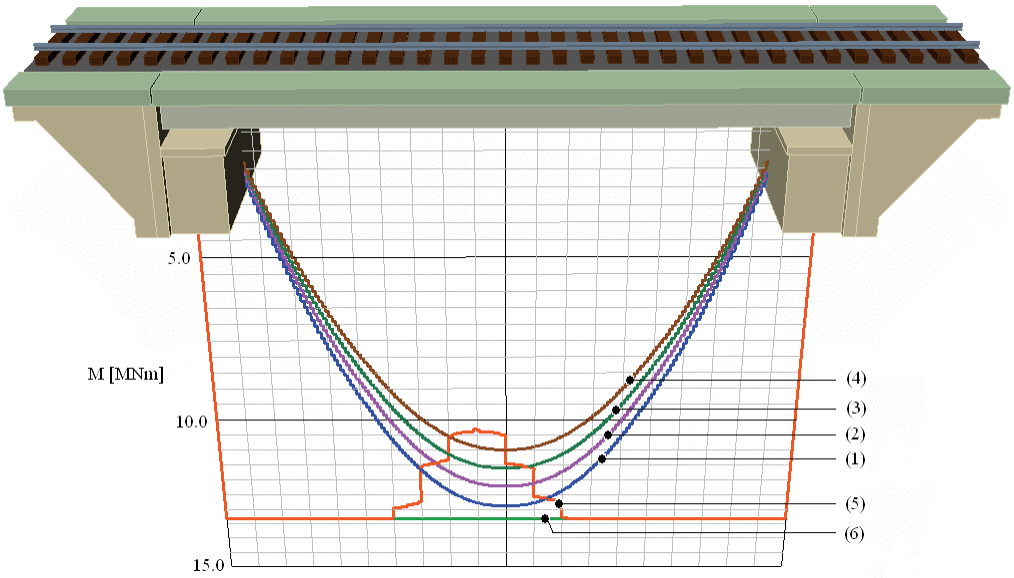

Fig. 14. Envelopes of bending moment for: (1) arterial lines, (2) secondary lines, (3) local lines, (4) sidings and envelopes of the cross section load capacity: (5) with defects defined in Figure 8, (6) without defects

Results of the static-strength analysis are to be presented in the form of envelopes of internal forces against the envelope of cross section load capacity as shown in Figure 14 for span with defects defined in Figure 8. This enables detection of the "critical zones" at which values of the internal forces exceed the cross section capacity.

7. Conclusions

Presented computer system "Damage Assessment Graphic Analysis – DAGA" enables easy modelling and analysis of RC slab bridge spans taking into account the most frequent defects of the structures: loss of material (concrete and reinforcement) as well as changes of material properties. The main advantages of the DAGA can be listed as follows:

- user-friendly three-dimensional modelling of damaged structure by means of graphical editor,

- simultaneous modelling of all identified defects with non-limited intensity, extent and location,
- visualisation of the modelling results for better control of the created model,
- non-limited density of structure discretization in accordance with required precision of modelling,
- effective procedures of static and strength analysis of a damaged bridge span,
- easy assessment of structure load capacity and immediate identification of span critical zones thanks to visualisation of the analysis results.

The DAGA system can be used as an easy and precise tool of condition evaluation of each individual railway slab bridge with defects. The system can be also applied for parametric analysis of the structure sensitivity to various types of defects. Selected results of such analysis are presented in [22], [24].

The DAGA system can be operated by civil engineers familiar with basics of computer graphics and the Finite Element Method because it does not require advanced knowledge and special training. The system can be used as an independent system or can be implemented as a module of the Bridge Management System.

References

[1] Bell B.: *How the project priorities were established*. In: "Sustainable Bridges – Assessment for Future traffic Demands and Longer Lives" (Eds.: J. Bień, L. Elfgren, J. Olofsson), Wrocław, 2007, pp. 53–64.

[2] Bień J.: *Defects and diagnostics of bridge structures* (in Polish), Wydawnictwa Komunikacji i Łączności, Warsaw, 2010.

[3] Bień J.: *Modelling of structure geometry in Bridge Management Systems*, Archives of Civil and Mechanical Engineering, Vol. 11, No. 3, 2011, pp. 512–532.

[4] Bień J., Cruz P.J.S., Maksymowicz M.: *Unified classification of damages of railway concrete bridges (in Polish)*, Proc. of the 5th Conf. "Problems in design, construction and maintenance of short- and medium-span bridges", Wrocław, 2004, p. 31–40.

[5] Bień J., Jakubowski K., Kamiński T., Kmita J., Rawa P., Cruz P., Maksymowicz M.: *Railway bridge defects and degradation mechanisms*, In: "Sustainable Bridges – Assessment for Future traffic Demands and Longer Lives" (Eds.: J. Bień, L. Elfgren, J. Olofsson), Wrocław, 2007, pp. 105–116.

[6] Bień J., Kużawa M., Bień B.: *To see is to know: Visualization in bridge inspection and management,* Proc. of the 5th Int. Conference "Bridge maintenance, safety, management and life-cycle optimization", IABMAS, Philadelphia, USA, 2010, pp. 267–574.

[7] Błaszczyński T.: *The influence of crude oil products on RC structure destruction,* Journal of Civil Engineering and Management, Vol. 7, No. 1, 2011, pp. 146–156.

[8] *Bridge Management in Europe – BRIME*, Research Project, 4th Framework Programme, www.trl.co.uk/brime/index.htm

[9] *Corrosion of steel in reinforced concrete structures – COST 521. Final report* (Eds.: R. Cigna, C. Andrade, U. Nürnberger, R. Polder, R. Weydert, E. Seitz), European Commission, Directorate-General for Research, 2003.

[10] Diehl, S.: *Software visualization*, Springer, 2007.
[11] Enright M.P., Frangopol D.M.: *Survey and evaluation of damaged concrete bridges*, Journal of Bridge Engineering, Vol. 5, No. 1, 2000, pp. 31–38.
[12] *Guideline for structural health monitoring*, Final report, Research project "Structural assessment monitoring and control – SAMCO", 2006, www.samco.org.
[13] *Guideline for inspection and condition assessment of railway bridges,* 2007, www.sustainable bridges.net
[14] Hoła J., Książek M.: *Research on suitability of sulphur polymer composite for corrosion protection of reinforcing steel in concrete*, Archives of Civil and Mechanical Engineering, Vol. 9, No. 1, 2009, pp. 47–60.
[15] Hoła J., Schabowicz K.: *State-of-the-art nondestructive methods for diagnostic testing of building structures - anticipated development trends*, Archives of Civil and Mechanical Engineering, Vol. X, No. 3, 2010, pp. 5–18.
[16] Kamaitis Z.: *Modelling of corrosion protection as standby system for coated reinforced concrete structures*, Journal of Civil Engineering and Management, Vol. 15, No. 4, 2009, pp. 387–394.
[17] Kmita J., Bień J., Machelski Cz.: *Computer-aided design of bridges* (in Polish), Wydawnictwa Komunikacji i Łączności, Warsaw, 1989.
[18] Luebke D. et al.: *Level of detail for 3D graphics*, Elsevier Science, 2003.
[19] *Panorama of transport*. European Commission, Luxemburg Office for Official Publications of the European Community, 2007.
[20] Mačiulaitisa R., Vaičienea M., Žurauskienea R.: *The effect of concrete composition and aggregates properties on performance of concrete*, Journal of Civil Engineering and Management, Vol. 15, No. 3, 2009, pp. 317–324.
[21] Maksymowicz M.: *Evaluation of load capacity of concrete railway slab spans with defects,* PhD Thesis, University of Minho, Guimarães, Portugal, 2008.
[22] Maksymowicz M., Bień J., Cruz P.J.S.: *Assessment of load capacity of railway RC slab spans with reinforcement losses*, Proc. of the 2nd International Congress of Federation Internationale du Beton, Naples, Italy, 2006, pp. 632–633.
[23] Maksymowicz M., Cruz P., Bień J., Helmerich R.: *Concrete railway bridges – taxonomy of degradation mechanisms identified by NDT methods*, Proc. of the 3rd International Conference on Bridge Maintenance, Safety and Management, Porto, Portugal, 2006, pp. 943–944.
[24] Maksymowicz M., Bień J., Cruz P.J.S.: *Evaluation of load capacity of railway slab spans with damages* (in Polish), Seminar „Technological aspects in design and construction of concrete bridges", Wrocław, 2006, pp. 199–208.
[25] Malhorta V.M., Carino N.J.: *CRC Handbook on nondestructive testing of concrete*, CRC Press, 2003.
[26] Olofsson J. et al.: *Assessment of european railway bridges for future traffic demands and longer lives – EC project "Sustainable bridges"*, Journal of Structure and Infrastructure Engineering, Vol. 1, No. 2, 2005, pp. 93–100.
[27] Šelih J.: *Performance of concrete exposed to freezing and thawing in different saline environments*, Journal of Civil Engineering and Management, Vol. 16, No. 2, 2010, pp. 306–311.
[28] UIC Code 778-4 R. *Defects in railway bridges and procedures for maintenance*, 2009.
[29] Wenzel H.: *Health Monitoring of Bridges*, J. Wiley & Sons Ltd., 2009.

Nośność uszkodzonych żelbetowych przęseł płytowych mostów kolejowych

Europejskie mosty kolejowe są stosunkowo stare, a procesy degradacji powodują uszkodzenia obniżające ich nośność. W niniejszej pracy przedstawiono system komputerowy DAGA wspomagający ocenę nośności żelbetowych przęseł płytowych mostów kolejowych z uwzględnieniem ich uszkodzeń. Rozwiązania konstrukcyjne oraz typy uszkodzeń analizowanych przęseł określono na podstawie analiz stanu infrastruktury kolejowej w Polsce i w Portugalii, z wykorzystaniem rezultatów międzynarodowych projektów badawczych dotyczących mostów kolejowych. Prezentowany system jest wyposażony w zaawansowany edytor graficzny umożliwiający precyzyjne i szybkie tworzenie trójwymiarowego modelu uszkodzonego przęsła oraz prezentację wyników analizy. Efektywny algorytm analizy statyczno-wytrzymałościowej pozwala na równoczesne uwzględnianie różnych typów uszkodzeń o dowolnej intensywności, rozległości i usytuowaniu.

ARCHIVES OF CIVIL AND MECHANICAL ENGINEERING

Vol. XI 2011 No. 4

Influence of material properties on the interaction between residual stress and springback in the case of in plane sheets forming

N. NANU, G. BRABIE
University of Bacau, 157 Marasesti Street, 5500 Bacau, Romania.

In the case of cold forming of sheets metal, the springback phenomenon leads to undesired effects on the geometry and dimensions of the formed parts. One of the main causes that lead and influence the intensity of this instability phenomenon is the state of stresses generated by the forming process in the deformed material. To establish an interaction between springback and distribution of stresses it must be known the law of variation of their parameters, their factors of influence and their causes. If the determination of springback parameters can be performed without difficulty, the determination of stresses variation in the case of out of plane sheet metal forming is a difficult problem because of the complexity of process, tools and part geometry. A solution of the problem can be the determination of stresses and of their interaction with springback in the case of in plane forming, the obtained model of interaction following to be extended for the case of out of plane forming of metal sheets. The present paper performs an analysis of the influence of materials on the interaction between the state of stresses generated by tensile loading and springback in the case of in plane forming by applying the principles of the three bars method.

Keywords: *residual stresses, springback, interaction, three bars method*

1. Introduction

The most frequent defects in the case of parts made by cold plastic forming are their deviations from their theoretical profile that are determined by the springback phenomenon. The main effects of springback are as follows: the alteration of the part form and dimensions after the tools removing and also the change of the state of stresses and strain in the deformed material. [1], [9]. The models used in the calculation of spring-back parameters were constructed by assimilating the springback with a bending process [2], based on the assumption that the springback is the effect of a contact force and of a heterogeneous redistribution of efforts on the sheet thickness [5] etc. All the elaborated models were generally constructed for simple configurations of parts (especially for U-bent parts) and their extension for complex parts presents many difficulties. Hence, the determination, elimination or avoidance of the defects generated by springback requires the analysis and knowledge of springback specific causes and of its interaction with different factors of influence.

One of the main causes that generate the springback and its effects is considered to be the distribution of the stresses in the sheet thickness. [1], [6]. But, a relationship between springback and stresses is difficult to be established in the case of drawn parts especially because of difficulty to determine the stresses distribution and also because of the parts and process complexity. A model for description of the interaction between stresses state and springback was performed by using the Prandtl and Reuss plasticity equations associated with a kinematic hardening model developed by Lemaître and Chaboche [7]. But the determined models were constructed especially for the particular case of sheets bending and hence their application cannot be extended for complex drawn parts. A solution of the problem can be the determination of interaction between springback and stresses in the case of in plane forming, by using the "three bars method" and on the basis of obtained results the extension of the model for complex parts. Such model was constructed based on the Swift law of material behaviour for an aluminium alloy sheet [4].

The present paper analyses the results of an investigation by experiment concerning the influence of the material on the interaction between residual stresses and springback in the case of in plane forming of thin sheets (made from aluminium alloy and alloyed steel). Based on this analysis a description of the models concerning the above mentioned influence was established by using the Swift and Hollomon material constitutive equations.

2. Methodology of experimental investigation

The analysis of the stresses distribution and springback parameter was performed by using an experimental device whose construction was made by applying the principles of the three bars method and the model described in [4]. The device is composed by two grips, one fix and the other mobile, that maintain three samples, two of them having the same length – l_1 and the third having a different length – l_3 (Figure 1).

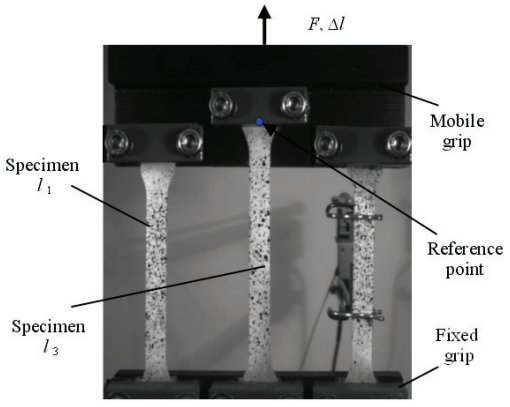

Fig. 1. Testing device

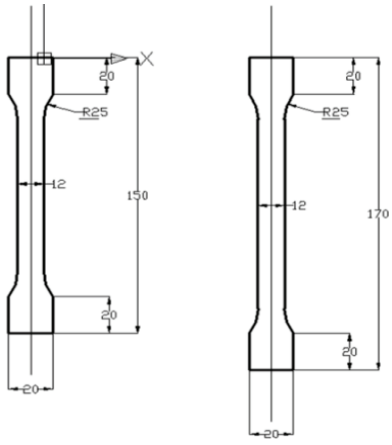

Fig. 2. Samples geometry

The device was installed on a tensile testing machine – Lloyd EZ 50 that performs the needed forming force and the displacement of the mobile grip so that all three samples to be displaced up on the same distance Δl. After unloading the external force will be equal to zero, all three samples being displaced down with $\Delta l'$, that represent the springback parameter and due to the difference of the samples lengths, the residual stresses will be induced in all samples.

The experimental determination of springback and residual stresses in the case of in plane deformations by using the three bars method was performed by using specimens made from steel and aluminium alloy and the above presented device. The dimensions of the samples are shown in Figure 2, the chemical composition of the selected materials is given in Table 1 and the materials mechanical properties are presented in Table 2.

Table 1. Chemical composition of the selected materials

Aluminium alloy	Al	Cr	Cu	Fe	Mg	Mn	Si	Ti	Zn	Other elements		
	95.8–98.6	0.04–0.35	0.15–0.4	<= 0.70	0.8–1.2	0.15	0.4–0.8	<= 0.15	<= 0.25	<= 0.15		
Steel	C	Si	Mn	P	S	Cr	Ni	N2	Cu	Al	Mo	As
	0.03	0.02	0.23	0.009	0.006	0.02	0.01	0.004	0.02	0.035	0.001	0.001

Table 2. Mechanical properties of materials

Sheet material	Young modulus	Yield stress	Uniform elongation	Total elongation	Strength coefficient	Anisotropy coefficient	Hardening exponent
	[MPa]	[MPa]	%	%	[MPa]	–	–
Aluminium alloy	57926	204	15.68	18.61	478	0.910	0.1859
Steel	140097	168	25.97	45.89	452	1.074	0.2

Generally, in the case of alloyed steels, the Young modulus decreases to the increase of plastic strain [3], [7] and [8]. In the case of steel used in the present experiment, the variation of the Young modulus in relation with plastic strain is shown in Figure 3. The values of Young modulus corresponding to the chosen level of strains imposed in the experiments are also presented in Table 2.

The thickness of aluminium alloy sheet was equal to 1 mm and that of the steel sheet was equal to 0.75 mm. The rolling direction of the used sheets was equal to 0°, the imposed displacement – Δl was equal to 8 mm and the applied strain rate was equal to $7.5 \cdot 10^{-4}$ s^{-1}. The experimental determination of springback was made by using two methods: based on extensometer and based on image analysis. The determination of stresses generated in the samples before springback was made by using the material stress-strain curve. The residual stresses were determined as follows: on the basis of experimental determined displacements and also by using the hole drilling method. In the case of last method the distribution of stresses was determined in the sheet thickness.

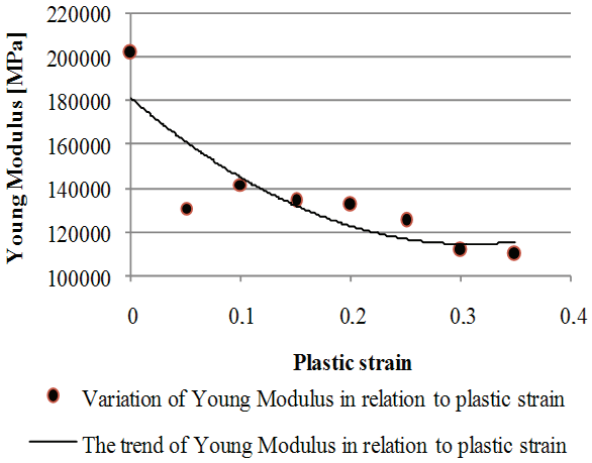

Fig. 3. Variation of Young Modulus in relation with plastic strain for alloyed steel

The stresses determination was made in the following two cases: for the unloaded specimen and for the loaded specimen (mounted in the testing device and loaded). The procedure used to determine the stresses was applied in the following steps: the testing device was mounted on a hydraulic press (Figure 4a), the mobile grip being mounted on the press mobile head and the fixed ones on the press fixed table; after loading, the samples were blocked by using a special blocking system; the device was removed from the press and the hole drilling equipment was used in order to determine the stresses before springback (Figure 4b).

a) b)

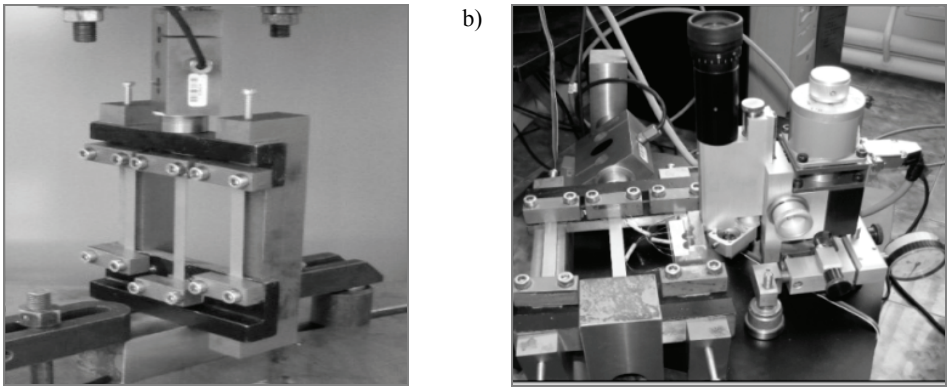

Fig. 4. Experimental system used for experimental determination of residual stresses:
a) device mounted on the hydraulic press, b) hole drilling equipment

The stresses were determined in the central and lateral samples in two locations for steel (in the middle of the sample and at a distance of ¼ from the sample length) and

one location for aluminium alloy (in the middle of sample). In order to determine the residual stresses the same procedure was used but other blocking element having a high assembly clearance were used. In this case the residual stresses were determined in a single location for steel and aluminium alloy (in the middle of samples).

3. Analysis of experimental results

3.1. Springback parameters and stresses determined by using the extensometer and image analysis techniques

In order to determine the springback parameter and stress, the extensometer was mounted on the central and lateral samples. During loading the extensometer measures the deformation of the reference length and after unloading the extensometer measures the deformation of the sample corresponding to springback parameter. The determination of springback for the sample was made in assumption that the deformation was constant on the sample length. The experimental results obtained by using the extensometer are presented in Table 3.

Table 3. Experimental results – by using extensometer

Sheet material	Springback parameter $\Delta l'$	Lateral samples		Central sample	
		Stress before springback	Residual stresses	Stress before springback	Residual stresses
	[mm]	[MPa]	[MPa]	[MPa]	[MPa]
Aluminium alloy	0.619	292.42	–7.95	284.35	27.50
Steel	0.245	268.55	–10.51	260.17	21.54

In the case of image analysis application a reference point on the superior extremity of central sample was chosen and the history of displacement was registered by a high resolution video camera. The value of the springback was directly determined. The results obtained by using the image analysis are presented in Table 4. The variations of the springback parameters and residual stresses, experimentally determined before springback by using extensometer and image analysis, are presented in Figure 5.

By analysing the values of stresses and springback parameter in the case of in plane forming of metal sheet by using the three bars method the following aspects can be remarked:

- the differences between springback parameter values obtained by using extensometer and image analysis are small, the values obtained by using image analysis being smaller than those obtained by using extensometer; the difference resulted between the values obtained by using extensometer and calculation is due to the fact that the use of extensometer implies the assumption that the deformations are constant on the sample length, while the use of the image analysis gives directly the springback parameter;

- the extensometer measures the springback parameter of the calibrated zone and the springback of the sample is determined in assumption that the deformations are constant over the sample length;
- the values of springback parameters are higher in the case of aluminium alloy than in the case of steel;
- the value of springback parameter depends on the level of stresses from samples before springback; thus, the high values of springback parameters correspond to high values of stresses, in the both case of aluminium alloy and steel sheets.

Table 4. Experimental results – by using image analysis

Sheet material	Springback parameter $\Delta l'$	Lateral samples		Central sample	
		Stress before springback	Residual stresses	Stress before springback	Residual stresses
	[mm]	[MPa]	[MPa]	[MPa]	[MPa]
Aluminium alloy	0.6184	292.42	–7.70	284.35	27.72
Steel	0.2440	268.55	–9.44	260.17	22.46

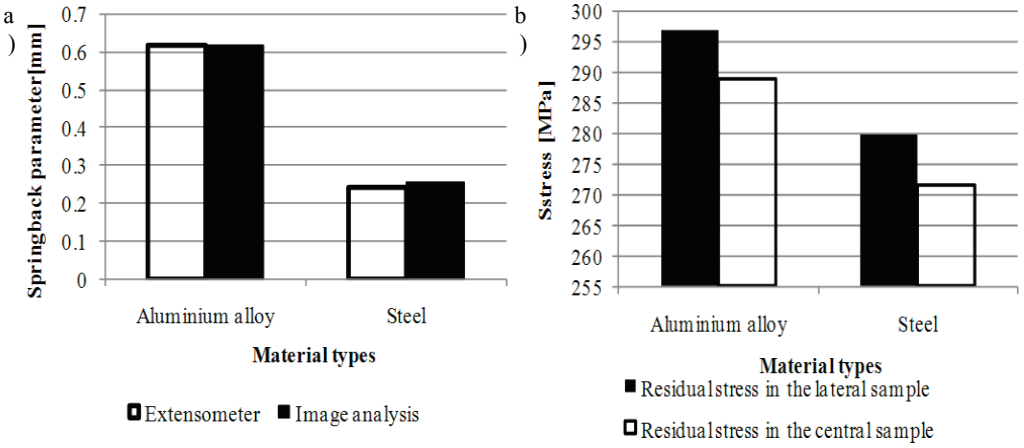

Fig. 5. Variation of springback parameters and residual stresses before springback: a) springback parameter variation, b) residual stresses variation

3.2. Stresses determined by using the hole drilling method

The variations of stresses obtained by applying the hole drilling method are presented in Figure 6.

The analysis of experimental results obtained in the case of aluminium alloy leads to following conclusions:

- the stresses are not constant on the sheet thickness and varies between positive and negative values;
- the stress values are not equal on the inner and outer faces of sheet;

- in the areas located nearby the inner and outer faces of sheet the stresses are negative;
- in the areas located nearby the middle axis, the stresses are positive and the highest values are generated along this axis;
- the distribution of stresses determined in the loaded central and lateral samples depends on the initial state of stress in the unloaded samples.

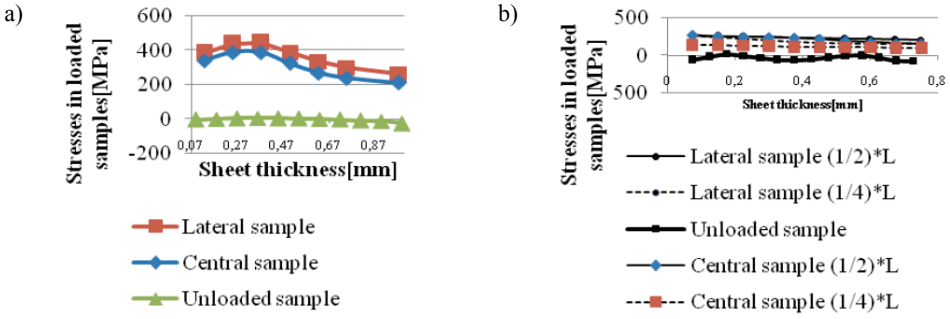

Fig. 6. Residual stresses variation determined by using the hole drilling method: a) aluminium alloy, b) steel

The analysis of experimental results obtained in the case of steel sheets leads to following conclusions:

- the residual are not constant on the sheet thickness, the minimum values being obtained on the inner and outer faces and nearby the middle axis of the sample, in this area the stresses having negative values;
- the maximum values of the stresses are located at a distance of about ¼ from the sheet thickness, in this case the stresses having positive values;
- the stresses on inner and outer faces of sheet are not equals;
- the stresses determined in the middle of central and lateral samples have smaller values than the stresses determined at a distance of about ¼ from the sample length due to the fact as the deformations are not constant on the sample length;
- the stresses determined after springback are not constant on the sheet thickness, their distribution depending on stresses distribution on the non-deformed samples.

4. Mathematical modelling of interaction between residual stress and springback as a function of sheets material

4.1. General aspects

According to the model described in [4], in the case of three bars methods after unloading the external force becomes equal to zero and the generated residual stresses in the samples satisfy the following equation of equilibrium:

$$2\sigma_1' S_1' + \sigma_3' S_3' = 0, \tag{1}$$

where:

σ_1' is the residual stress in the lateral samples,

S_1' is the cross section area of the lateral sample after springback,

σ_3' is the residual stress in the central sample,

S_3' is the cross section area of the central sample after springback.

By applying the equation of equilibrium, the following expression is obtained:

$$\frac{\sigma_3'}{\sigma_1'} = -2 \cdot \frac{S_1'}{S_3'}. \tag{2}$$

If the samples have the same initial cross section area, and applying the hypothesis of volume constancy the following expression is obtained:

$$\frac{\sigma_3'}{\sigma_1'} = -2 \cdot \frac{l_1(l_3 + \Delta l)}{l_3(l_1 + \Delta l)}. \tag{3}$$

4.2. Modelling of interaction between residual stresses and springback parameter in the case of aluminium alloy

According to [7], in the case of aluminium alloy sheets the plastic behaviour of material is better described by the Swift linear equation that has the following expression:

$$\sigma = \sigma_0 + K\varepsilon. \tag{4}$$

The residual stresses in central and lateral samples will be as follows:

$$\sigma_1' = \sigma_1 - \frac{E \cdot \Delta l'}{l_1 + \Delta l}, \qquad \sigma_3' = \sigma_3 - \frac{E \cdot \Delta l'}{l_3 + \Delta l}, \tag{5}$$

where $\Delta l'$ is the springback parameter. By replacing Equation (4) into Equations (5), the residual stresses and springback parameter will be obtained in the form of equations:

$$\Delta l' = \frac{3 \cdot \sigma_0 \cdot l_1 \cdot l_3 + \sigma_0 \cdot l_3 \cdot \Delta l + 2 \cdot \sigma_0 \cdot l_1 \cdot \Delta l}{E \cdot (l_1 + 2 \cdot l_3 + 3 \cdot \Delta l)} + \frac{K \cdot \Delta l}{E}, \tag{6}$$

$$\sigma_1' = \sigma_0 - \frac{3 \cdot \sigma_0 \cdot l_1 \cdot l_3 + \sigma_0 \cdot l_3 \cdot \Delta l + 2 \cdot \sigma_0 \cdot l_1 \cdot \Delta l}{l_1 \cdot (l_1 + 2 \cdot l_3 + 3 \cdot \Delta l)}, \tag{7}$$

$$\sigma_3' = \sigma_0 - \frac{3 \cdot \sigma_0 \cdot l_1 \cdot l_3 + \sigma_0 \cdot l_3 \cdot \Delta l + 2 \cdot \sigma_0 \cdot l_1 \cdot \Delta l}{l_3 \cdot (l_1 + 2 \cdot l_3 + 3 \cdot \Delta l)}, \tag{8}$$

The material parameters in the case of aluminium alloy are as follows: yield stress σ_0 = 204.54 MPa and strength coefficient K = 1081 MPa. The results obtained by applying the Swift law in the case of aluminium alloy are given in Table 5.

Table 5. Springback and residual stresses resulted from calculation

Springback parameter $\Delta l'$	Lateral samples		Central sample	
	Stress before springback	Residual stresses	Stress before springback	Residual stresses
[mm]	[MPa]	[MPa]	[MPa]	[MPa]
0.626	280.4308	–11.13	269.09	22.04

4.3. Modelling of interaction between residual stresses and springback parameter in the case of steel sheets

In the case of steel sheets the plastic behaviour of material is better described by the Hollomon nonlinear equation that has the following expression:

$$\sigma = K \varepsilon^n, \tag{9}$$

where:

K – the strength coefficient,

ε – the plastic strain,

n – the strain hardening exponent.

The stresses before springback will be given by the following equations:

$$\sigma_1 = K \cdot \left[\ln\left(1 + \frac{\Delta l}{l_1}\right) \right]^n, \qquad \sigma_3 = K \cdot \left[\ln\left(1 + \frac{\Delta l}{l_3}\right) \right]^n \tag{10}$$

and after springback by the following equations:

$$\sigma_1' = K \cdot \left[\ln\left(1 + \frac{\Delta l}{l_1}\right) \right]^n - \frac{E \cdot \Delta l'}{l_1 + \Delta l}, \qquad \sigma_3' = K \cdot \left[\ln\left(1 + \frac{\Delta l}{l_3}\right) \right]^n - \frac{E \cdot \Delta l'}{l_3 + \Delta l}. \tag{11}$$

By replacing the Equations (11) into Equation (3) the expressions for the springback parameters and residual stresses are as follows:

$$\Delta l' = \frac{2Kl_1\left[\ln\left(1+\frac{\Delta l}{l_1}\right)\right]^n\left(l_3+\Delta l\right)+l_3\left[\ln\left(1+\frac{\Delta l}{l_3}\right)\right]^n\left(l_1+\Delta l\right)}{E\left(l_1+2l_3+3\Delta l\right)}, \tag{12}$$

$$\begin{aligned}\sigma_1' &= K\left[\ln\left(1+\frac{\Delta l}{l_1}\right)\right]^n - \frac{2Kl_1\left[\ln\left(1+\frac{\Delta l}{l_1}\right)\right]^n\left(l_3+\Delta l\right)+\left[\ln\left(1+\frac{\Delta l}{l_3}\right)\right]^n\left(l_1+\Delta l\right)}{\left(l_1+\Delta l\right)\left(l_1+2l_3+3\Delta l\right)},\\ \sigma_3' &= K\left[\ln\left(1+\frac{\Delta l}{l_3}\right)\right]^n - \frac{2Kl_1\left[\ln\left(1+\frac{\Delta l}{l_1}\right)\right]^n\left(l_3+\Delta l\right)+l_3\left[\ln\left(1+\frac{\Delta l}{l_3}\right)\right]^n\left(l_1+\Delta l\right)}{\left(l_3+\Delta l\right)\left(l_1+2l_3+3\Delta l\right)}.\end{aligned} \tag{13}$$

The material parameters in the case of steel are as follows: yield stress σ_0 = 168 MPa, strength coefficient K = 452 MPa and hardening exponent n = 0.2. The residual stresses and springback parameter obtained by applying the Hollomon law are presented in Table 6.

Table 6. Springback and residual stresses resulted from calculation

Springback parameter $\Delta l'$	Lateral samples		Central sample	
	Stress before springback	Residual stresses	Stress before springback	Residual stresses
[mm]	[MPa]	[MPa]	[MPa]	[MPa]
0.217	265.71	–11.48	257.25	22.71

5. Conclusions

The variations of the springback parameters and residual stresses obtained for both materials by applying all experimental methods and the specific model of calculation are presented in Table 7 and Figure 7, respectively.

Analysing the influence of the material on the interaction between residual stress and springback in the case of in plane deformations of different metal sheets, the followings aspects can be remarked:

- in the case of the both used materials the intensity of springback depends on the level and distribution of residual stresses generated in samples by in plane forming before springback; thus, if the residual stresses have had high values the springback parameters have also had high values;

- the values of springback parameters and residual stresses are also dependent on the initial state of residual stresses which exist in the non-deformed samples;
- the mathematical modelling of the interaction between residual stresses and springback parameters must take into account the law of the material plastic behaviour;
- between the values of stresses determined by applying the image analysis, extensometer or mathematical model and those obtained by using the hole drilling method some differences resulted; such differences are caused by the fact that in the case of application of the methods based on extensometer/image analysis and mathematical model, the residual stresses are assumed to be constant, but in the case of hole drilling method, it was observed that residual stresses are not constant on the sample length and sheet thickness.

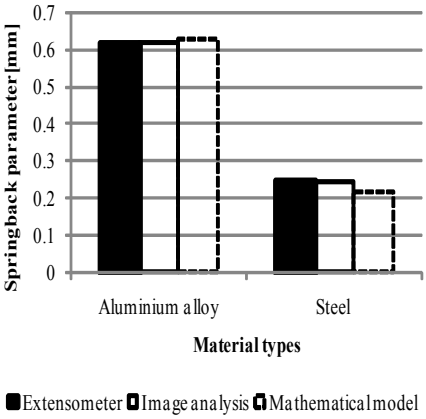

Springback parameters

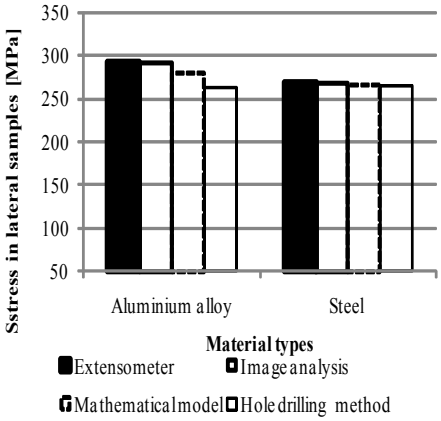

Stresses in lateral samples

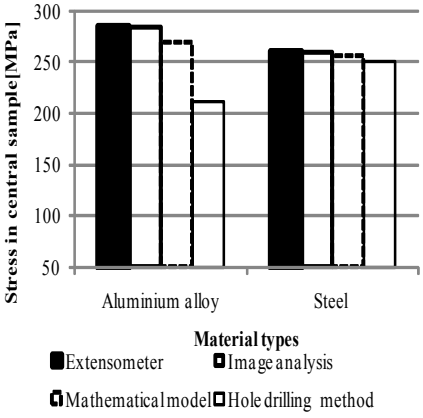

Stresses in the central sample

Fig. 7. Variation of springback parameters and residual stresses before springback obtained by applying different methods of determination

Table 7. Values of residual stresses obtained by applying different methods of determination

Sample material	Method of determination	Lateral samples		Central sample	
		Stress before springback	Residual stresses	Stress before springback	Residual stresses
		[MPa]	[MPa]	[MPa]	[MPa]
aluminium alloy	calculated	280.4308	–11.13785	269.09649	22.04335
	image analysis	292.42	–7.70	284.35	27.72
	extensometer	292.42	–7.95	284.35	27.50
	hole drilling	263	–12.46	211	–28.14
steel	calculated	265.71	–11.48	257.25	22.71
	image analysis	268.55	–9.44	260.17	22.46
	extensometer	268.55	–10.51	260.17	21.54
	hole drilling	264	–13.52	251	24.89

Between the values of springback parameters and residual stresses determined from experiment and by calculation based on the mathematical models some differences resulted. Such differences are caused by the fact that the mathematical model supposes that the values of the stresses in the case of non-deformed materials are equal to zero.

Acknowledgments

The present research was performed with the financial support from the Romanian Ministry of Education and Research – CNCSIS.

References

[1] Brabie G.: *Cold forming of metal sheets. Instability phenomena* (in Romanian), Ed. Junimea, Iaşi, 2005.
[2] Eglin J.C., Gouty O., Joanna D.: *Shape and process parameters optimization for the accurate control of springback in sheets metal forming*, Sheet Metal, Vol. 2, Univ. of Twente, 1996, pp. 3–14.
[3] Hai Y.Y.: *Variation of elastic modulus during plastic deformation and its influence on springback*, Materials and Design, Vol. 30, No. 3, 2009, pp. 846–850.
[4] Incandela O.M.: *Définition de protocoles rationnels d'identification des lois de comportement élastoplastiques: Application à la simulation éléments finis d'opérations industrielles d'emboutissage*, PhD thesis, Annecy, France, 2006.
[5] Joannic D.: *Modelisation mecanique et simulation du retour elastique en emboutissage des toles minces et optimisation parametrique*, Ph. D. Thesis, Université de Franche-Compté, Besançon, 1998.
[6] Marciniak Z., Duncan J.L.: *Mechanics of sheet metal forming*, Edward Arnold, London, 1992.
[7] Morestin F., Boivin M., Silva C.: *Elastic plastic formulation using a kinematic hardening model for springback analysis in sheet metal forming*, Journal of Materials Processing Technology, Vol. 56, 1996, pp. 619–630.

[8] Ninshu M.: *Springback prediction by Yoshida-Uemori model and compensation of tool surface using Jstamp*. Proceedings of Numisheet, 2008, pp. 473–478.
[9] Samuel M.: *Experimental and numerical prediction of springback and side wall curl in U-bending of anisotropic sheet metals*, Journal of Materials Processing Technology, Vol. 105, 2000, pp. 382–393.

Wpływ właściwości materiału na interakcję pomiędzy naprężeniami własnymi i sprężynowaniem podczas kształtowaniu blach

W kształtowaniu blach na zimno, zjawisko sprężynowania prowadzi do niepożądanych zmian geometrii i wymiarów wyrobu. Jedną z najważniejszych tego przyczyn jest stan naprężeń generowany przez proces deformacji blachy. Aby ustalić interakcję pomiędzy sprężynowaniem a rozkładem naprężeń znane muszą być parametry, czynniki oraz ich przyczyny. O ile parametry sprężynowania mogą zostać ustalone bez problemu to określenie zmian naprężeń w blachach nastręcza dużo problemu. W pracy przedstawiono analizę wpływu materiału na relację pomiędzy interakcję pomiędzy naprężeniami własnymi i sprężynowaniem na drodze eksperymentalnej.

ARCHIVES OF CIVIL AND MECHANICAL ENGINEERING

Vol. XI 2011 No. 4

Critical loads calculations of annular three-layered plates with soft elastic or viscoelastic core

D. PAWLUS
University of Bielsko-Biała, ul. Willowa 2, 43-309 Bielsko-Biała, Poland.

This paper presents the computational results of annular three-layered plates loaded in the plane of their facings. The calculations are carried out by means of finite element method using the ABAQUS system. The critical and supercritical behaviours of plates with connected analysis of static and dynamic loss of their stability have been observed. The both examples of the axially-symmetrical form of plate buckling and circumferentially wavy form of its critical deformation are the subject of the investigations. The wavy form is particularly observed for plates compressed on the outer perimeter. The way of modelling of three-layered plate with the soft core made of the foam with elastic and viscoelastic properties is highlighted and discussed in the work.

Keywords: *sandwich annular plate, static dynamic stability, elasticity, viscosity, finite element method, ABAQUS*

1. Introduction

The calculations of the critical, static loads of plates precede the proper analysis of their dynamic behaviours in the field of the critical and supercritical loads. The load acting in the plane of the analysed plate structure is the cause of loss of its stability, which buckling form depends on the various parameters of the examined annular plate. The critical deformation form corresponding to the minimal value of the plate critical load could be regular, axially-symmetrical or wavy in circumferential and radial plate directions.

The investigations of the stability problem of the annular plate with the laminar structure are still undertaken. However, the field of the analysis is often limited to the axially-symmetrical problems, see for example works by [1–2], [11–12]. The presented computational results of exemplary, three-layered plates with elastic and viscoelastic core complement the results of investigations, which have been done recently and they are also a certain generalization of the plate stability problem in wide range of static and dynamic analysis.

Presented in this paper mesh model of examined plate was used in calculations carried out by means of finite element method in ABAQUS system.

The application of the finite element method supports the basic analysis of the plate critical loads by means of the additional evaluation of the general critical stress state of plates.

2. Computational plate model

The three-layered, annular plate loaded in the plane of its facings is the subject of the consideration. The cross-section structure of the examined plate is symmetric, composed of thin, steel facings and soft, foam core. The scheme of plate with slidably clamped edges is presented in Figure 1.

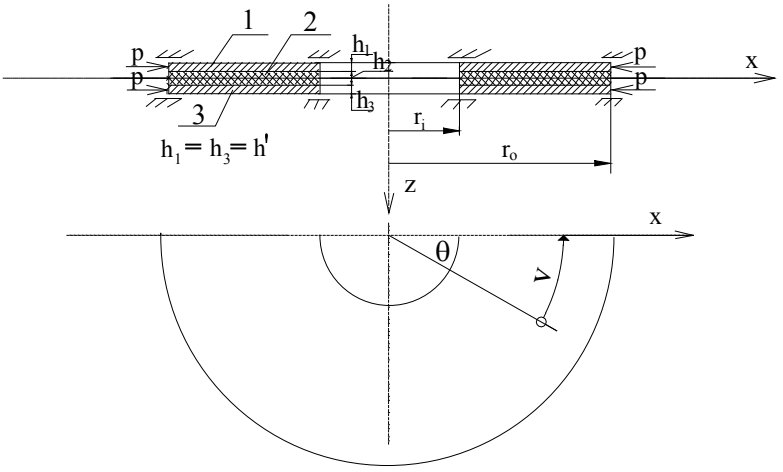

Fig. 1. The scheme of analysed plate

The main goal of the investigations of static and dynamic plate stability is the determination of minimal values of critical loads and corresponding to them buckling forms of the example plate cases. Considering the problem of the dynamic analysis, the plate was subjected to the linear, rapidly increasing in time loading, expressed by the formula:

$$p = st, \tag{1}$$

where p is compressive stress, s is rate of plate loading growth, t is time.

The critical time, load and deflection have been evaluated in plate dynamic stability analysis.

In the building of mesh model the classical in sandwich plate theory participation of the plate layers in carrying the basic stresses: normal by the facings and shear by the core has been used. The shell and solid elements were applied in creating of facings and core mesh of the plate. The proposal of such selection of elements in sandwich mesh structure has been presented in work [4]. Using the surface contact interaction the surfaces of facings mesh elements have been tied with the surfaces of the core elements. The model of full plate annulus is presented in Figure 2.

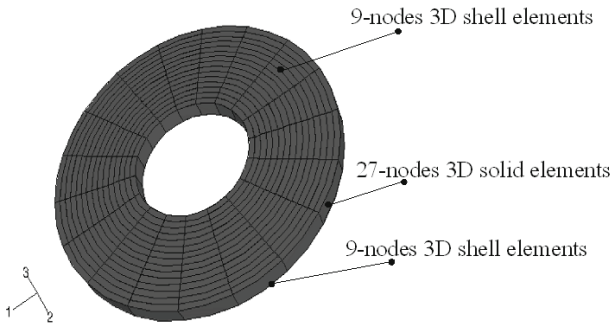

Fig. 2. Full annulus plate model

The example numerical calculations were carried out for plates with the following geometric parameters:

– inner plate radius $r_i = 0.2$ m,
– outer plate radius $r_o = 0.5$ m,
– thickness of plate facing $h' = 0.001$ m,
– thickness of plate core $h_2 = 0.005$ m and 0.02 m.

The material parameters of plate layers are as follows:

– steel facing: Young's modulus $E = 2.1 \cdot 10^5$ MPa, Poisson's ratio $\nu = 0.3$, mass density $\mu = 7.85 \cdot 10^3$ kg/m^3,

– two kinds of polyurethane foam of core material with the following elastic parameters: Kirchhoff's modulus $G_2 = 5$ MPa, mass density $\mu_2 = 64$ kg/m^3 [5]; Kirchhoff's modulus $G_2 = 15.82$ MPa, mass density $\mu_2 = 93.6$ kg/m^3 [9], Poisson's ratio $\nu = 0.3$ [10].

Young's moduli of foams material were calculated treating the material as isotropic. They are equal to: $E_2 = 13.0$ MPa, $E_2 = 41.13$ MPa, respectively.

The rheological properties of polyurethane foam have been described by the accepted formulas of the standard model of the viscoelastic medium. The scheme of standard model is presented in Figure. 3.

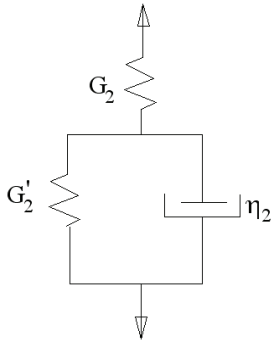

Fig. 3. Standard model

The elastic and viscous constants of the foam core materials are as follows:

– $G'_2 = 69.59$ MPa, $\eta_2 = 7.93 \cdot 10^4$ MPa·s [9],

– $G'_2 = 3.13$ MPa, $\eta_2 = 212.92 \cdot 10^4$ MPa·s, calculated using the creep function $\varphi = 0.845(e^{-0.36t} - e^{-0.036t})$, presented in work [5], after its approximation to the function of the standard model.

The viscoelastic properties of the core material have been described by the single term of Prony's series for the shear relaxation modules [3]:

$$G_R(t) = G_o\left(1 - q_1^p\left(1 - e^{-t/\tau_1^G}\right)\right), \tag{2}$$

where:

q_1^p, τ_1^G – material constants,

G_o – instantaneous shear modulus corresponding to the elastic values of core Kirchhoff's modulus.

Comparing the suitable members of the Equation (2) with the relaxation function of standard model, the material constants q_1^p, τ_1^G have been expressed:

$$q_1^p = \frac{G_2}{G_2 + G_2'}, \qquad \tau_1^G = \frac{\eta_2}{G_2 + G_2'}. \tag{3}$$

The values of parameters q_1^p and τ_1^G for the elastic and viscous foam parameters are as follows:

– $q_1^p = 0.615$, $\tau_1^G = 26.19 \cdot 10^4$ s for the foam with $G_2 = 5$ MPa,

– $q_1^p = 0.185$, $\tau_1^G = 928.46$ s for the foam with $G_2 = 15.82$ MPa.

The calculations were carried out at the Academic Computer Center Cyfronet-Cracow using the ABAQUS system – the number of computational grant (KBN/SGI_ ORIGIN_2000/PŁódzka/030/1999).

3. Results of calculations

The numerical calculations were carried out for plates compressed on inner or outer perimeter of their facings. The schemes of the facing loading are showed in Figure 4.

The loss of plate stability evaluated in dynamic analysis has been determined using the criterion presented by Wolmir in work [13]. According to this criterion the loss of

plate stability occurs at the moment of time when the speed of the point of maximum deflection reaches the first maximum value.

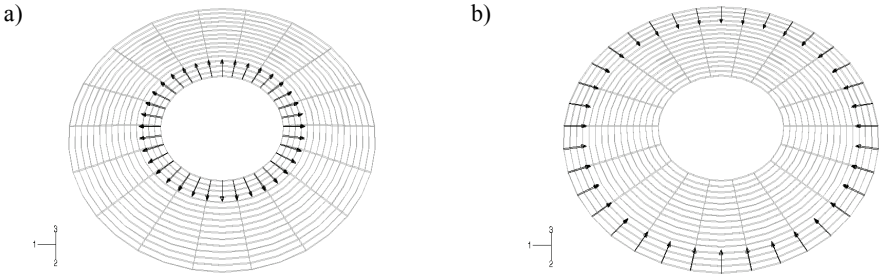

Fig. 4. Forms of plate loading: a) on inner edge, b) on outer edge

3.1. Critical static loads

The critical form of plate deformation corresponding to the minimal value of critical load is important in a plate stability problem. The calculations show that the plate with both slidably clamped edges compressed on the inner edge loses stability in the axially-symmetrical, regular form (Figure 5) but the plate compressed on outer perimeter loses stability in some wavy forms (Figure 6). The number (described by m) of the circumferential waves strongly depends on the plate material and geometrical parameters.

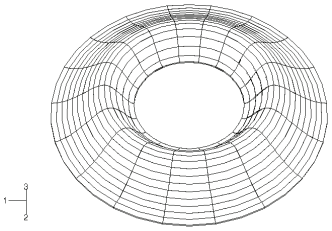

Fig. 5. Regular, axially-symmetrical form of plate buckling

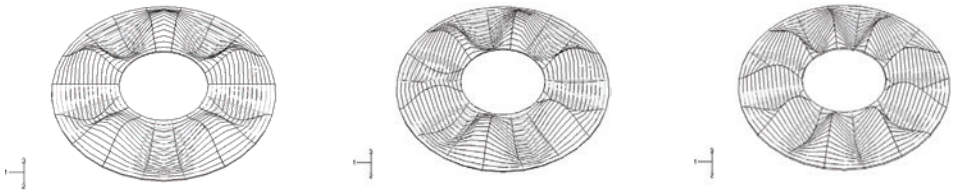

Fig. 6. Wavy forms of plate buckling

The example values of critical, static loads with the forms of critical deformations of plates loaded on an outer perimeter have been presented in Table 1.

Table 1. Critical static loads p_{cr} and forms of buckling for plates loaded on an outer edge

h_2/G_2 [m/MPa]					
0.005/5		0.005/15.82		0.02/5	
p_{cr} [MPa]	m	p_{cr} [MPa]	m	p_{cr} [MPa]	m
16.48	5	35.04	6	43.71	7
16.75	6	35.46	5	43.80	6
17.02	4	35.57	7	44.61	8
17.68	7	36.94	8	45.09	5
18.65	3	37.19	4	46.25	9
19.25	8	38.98	9	48.02	10
21.49	9	40.87	3	49.62	3
21.52	2	42.48	10	53.26	11

With the increase in the stiffness of plate structure (the core thickness or/and value of core Kirchhoff's modulus) both the value of critical, static load p_{cr} and the number m of buckling waves, which corresponds to this minimal value of load, increase.

Table 2. Critical static loads p_{cr} and forms of buckling for plates loaded on inner edge

h_2/G_2 [m/MPa]					
0.005/5		0.005/15.82		0.02/5	
p_{cr} [MPa]	m (n)	p_{cr} [MPa]	m (n)	p_{cr} [MPa]	m (n)
64.08	0	120.30	0	143.76	0
75.75	1	136.10	1	161.05	1
107.04	0 (1)	178.04	0 (1)	203.99	2
109.89	2	178.90	2	205.25	0 (1)
113.95	1 (1)	188.18	1 (1)	216.48	1 (1)
141.35	2 (1)	222.86	2 (1)	251.97	2 (1)

n – number of waves in radial direction

Analysing the plates loaded on the inner perimeter their form of buckling is regular, axially-symmetrical independently of their geometric and material parameters. The results are presented in Table 2.

3.2. Critical dynamic loads

The investigations of plates subjected to the time-dependent load require the determination of the form and the rate of a plate preliminary deflection. The assumed form of pre-deflection is expressed by the following equation:

$$\zeta_o(\rho,\theta) = \xi\eta(\rho)\cos(m\theta), \tag{4}$$

where:

$\zeta_o = \dfrac{w_o}{h}$, $\rho = \dfrac{r}{r_o}$ – dimensionless preliminary deflection and plate radius, respectively,

w_o – preliminary plate deflection,

$h = h_1 + h_2 + h_3$ – total thickness of plate,

ξ – calibrating number,

$\eta(\rho) = \rho^4 + A_1\rho^2 + A_2\rho^2\ln\rho + A_3\ln\rho + A_4$,

A_i – quantities fulfilling the conditions of clamped edges by the function $\eta(\rho)$, $I = 1, 2, 3, 4$.

The critical buckling form, which is the response to the assumed loading, could not correspond with the form of plate imperfection.

The plate compressed on the inner edge loses its dynamic stability in the same regular, axially-symmetrical form as it is accepted for plate preliminary deflection. Table 3 shows the results of critical dynamic loads and maximum deflections of plates loaded with the equal value of the rate of loading growth equal to: s = 4346 MPa/s (1).

Table 3. Values of critical dynamic loads p_{crdyn} and critical maximum deflection w_{cr}

h_2/G_2 [m/MPa]	p_{crdyn} [MPa]	w_{cr} [m]
0.005/5	86.92	$4.15\cdot10^{-3}$
0.005/15.82	136.90	$3.54\cdot10^{-3}$
0.02/5	149.94	$3.06\cdot10^{-3}$

The distribution of plate deflections for the axially-symmetrical form of its critical buckling is presented in Figure 7. The results are for plate with parameters: h_2 = 0.005 m and G_2 = 5 MPa. The example results of stresses state are showed in Figures 8, 9. Figure 8 presents the distribution of von Misses equivalent stresses in plate facings. Figure 9 shows the core shearing stresses in the *xz* plane.

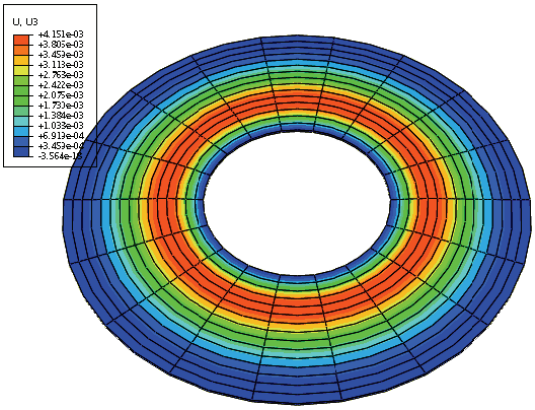

Fig. 7. Distribution of plate deflections

In the buckling area of plate deformation the equivalent stress is about 200 MPa. The maximum value is significant. The critical, maximum core shearing stress is equal to 0.59 MPa. The time histories of maximum deflection and velocity of deflection for this plate are showed in Figure 10.

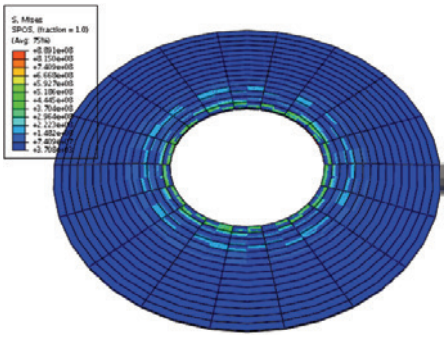

Fig. 8. Distribution of von Misses equivalent stresses

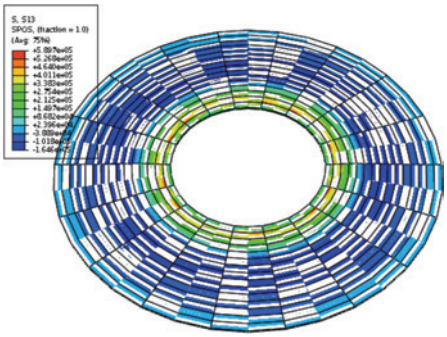

Fig. 9. Distribution of core shearing stresses

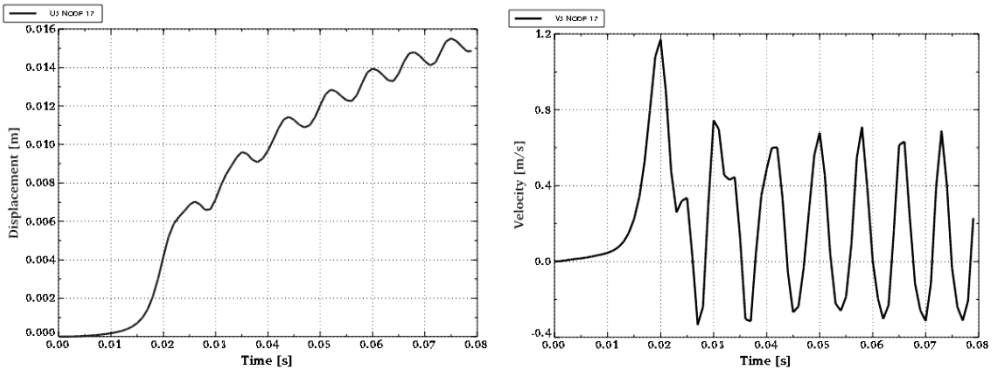

Fig. 10. Time histories of deflection and velocity of deflection of plate loaded on an inner edge

The plates compressed on an outer perimeter lose their dynamic stability in the form corresponding to the plate imperfection form. The change of the critical buckling form is observed for plates with the low number m of circumferential waves determining the form of plate preliminary deflection. It is number m equal to 0, 1, 2. Then the "jump" in the form of critical deformations to the higher number of waves could be observed. Table 4 presents the example results of critical dynamic loads and maximum deflections of plates with parameters $h_2 = 0.005$ m and $G_2 = 5$ MPa compressed on the outer edge with the rate of loading growth equal to: $s = 410.4$ MPa/s.

Table 4. Values of critical dynamic loads p_{crdyn}, deflections w_{cr} and number m of buckling waves

p_{crdyn} [MPa]	19.70	16.62	16.01	16.01	17.24	19.08
w_{cr} [m]	$1.45\cdot10^{-3}$	$0.96\cdot10^{-3}$	$0.84\cdot10^{-3}$	$0.74\cdot10^{-3}$	$0.74\cdot10^{-3}$	$0.75\cdot10^{-3}$
m	3	4	5	6	7	8

The minimal critical values of dynamic loads are for plates with number of buckling waves m equal to 5, 6. These forms could be considered as qualitatively comparable. Figure 11 shows the time histories of maximum deflection and velocity of deflection for the plate with number $m = 6$ of circumferential waves.

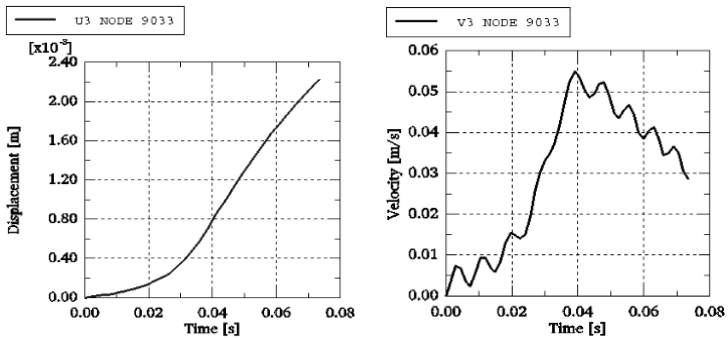

Fig. 11. Time histories of deflection and velocity of deflection of plate loaded on an outer edge

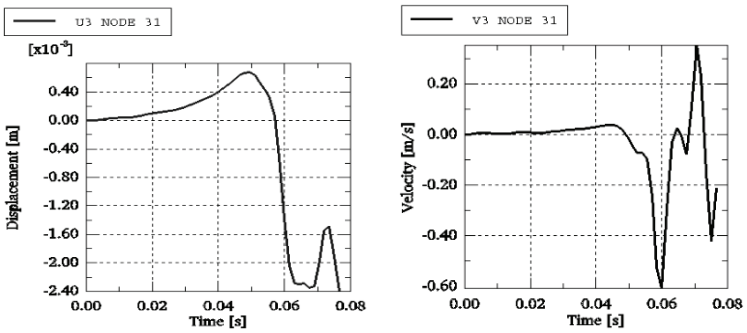

Fig. 12. Time histories of deflection and its velocity of plate with two waves of preliminary deflection

The change of the form of buckling for the same plate but with the $m = 2$ waves describing the form of plate preliminary deflection is presented in Figures 12 and 13.

Figure 12 shows the time histories of deflection and its velocity, but Figure 13 shows the forms of deformations at the time $t = 0.042$ s and $t = 0.06$ s.

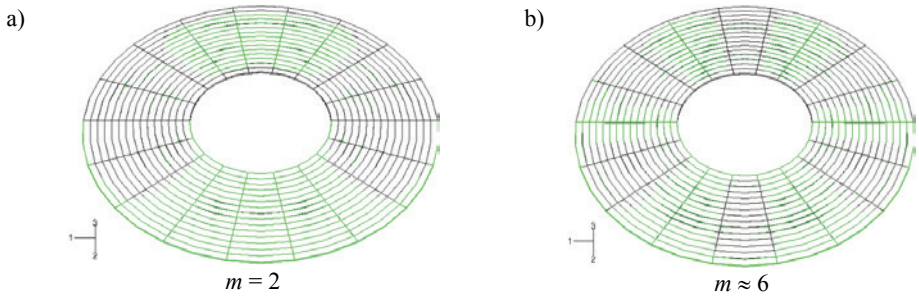

Fig. 13. The forms of plate buckling at the time: a) $t = 0.042$ s, b) $t = 0.06$ s

3.3. Computational results of plate with viscoelastic core

The case of plate loaded on the inner edge, which loses its dynamic stability in regular, axially-symmetrical form for the minimal critical loads, enables the use of the axisymmeric elements in the building of the model of plate structure. Figure 14 shows the mesh of such plate model built of shell and solid elements, too.

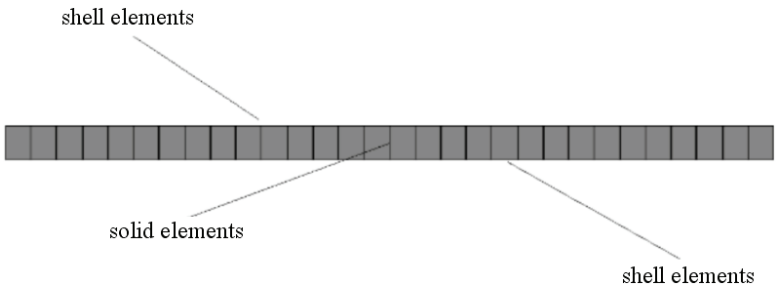

Fig. 14. Plate model built of axisymmetric elements

This model was used in calculations of plates with viscoelastic core for evaluation of the influence of the rheological core properties on the critical plate behaviour. The example results are presented in Table 5.

Table 5. Values of critical dynamic loads p_{crdyn} and critical maximum deflection w_{cr}

h_2/G_2 [m/MPa]	p_{crdyn} [MPa]	w_{cr} [m]
0.005/5	86.80	$3.27 \cdot 10^{-3}$
0.005/15.82	138.88	$3.67 \cdot 10^{-3}$
0.02/5	151.90	$3.44 \cdot 10^{-3}$

The calculations were carried out for the value of the rate of loading growth equal to: $s = 4346$ MPa/s.

The time histories of maximum deflection and velocity of deflection and the distributions of von Misses equivalent stresses and core shearing stresses for plate with parameters: $h_2 = 0.005$ m, $G_2 = 5$ MPa, $G'_2 = 3.13$ MPa, $\eta_2 = 212.92 \cdot 10^4$ MPa·s, are showed in Figures 15, 16, 17, respectively.

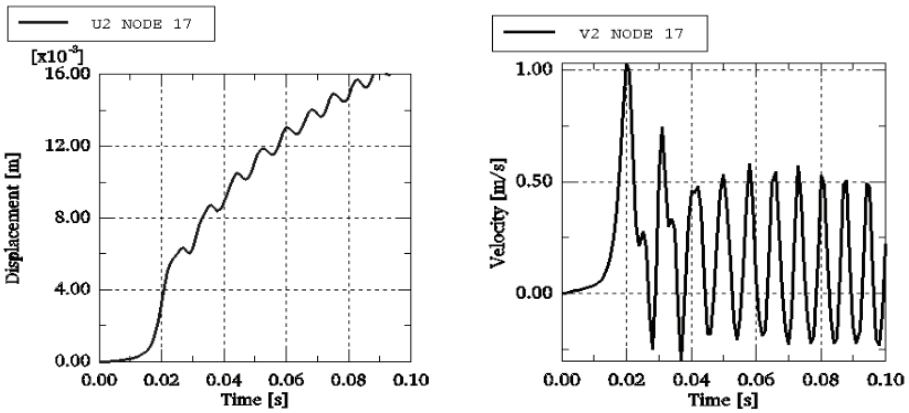

Fig. 15. Time histories of deflection and velocity of deflection for plate model built of axisymmetric elements

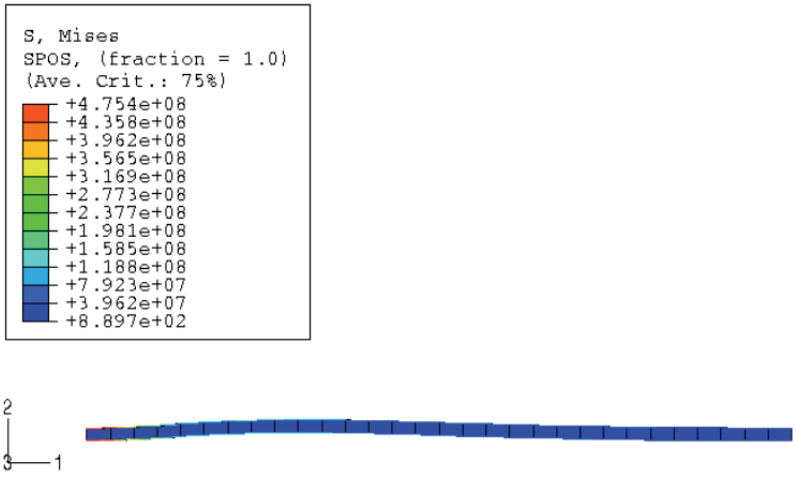

Fig. 16. Distribution of von Misses equivalent stresses for plate model built of axisymmetric elements

Comparing these critical results with the results obtained for the plate modelled in the form of full annulus, with elastic core (Figure 10, Table 3) one can observe their good consistency.

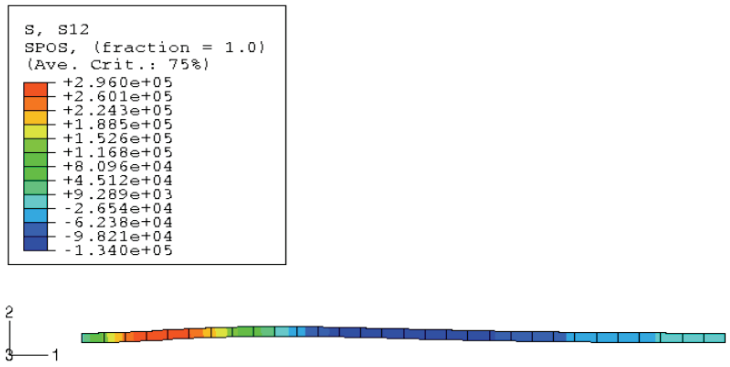

Fig. 17. Distribution of core shearing stresses for plate model built of axisymmetric elements

The influence of the rheological properties of analysed foam core materials on the final results is insignificant in such dynamic problem of rapidly loaded plates. The influence of values of viscous constant η_2 on values of critical, dynamic loads is presented in Figure 18.

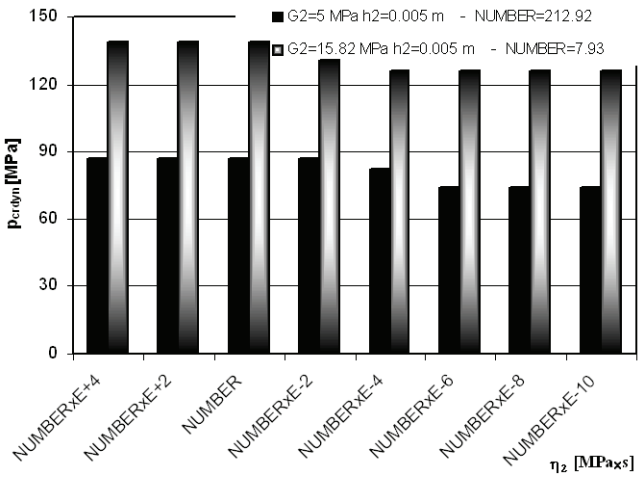

Fig. 18. Critical loads distribution depending on the values of core viscous constant

The results are obtained for two kinds of foam core materials:

– $G_2 = 15.82$ MPa, $G_2' = 69.59$ MPa, $\eta_2 = 7.93 \cdot 10^4$ MPa·s,
– $G_2 = 5$ MPa, $G_2' = 3.13$ MPa, $\eta_2 = 212.92 \cdot 10^4$ MPa·s.

Some differences in the values of plate critical parameters are observed for the significantly decrease (about 8 times) in values of viscous constant of core foam material. Then, the values of critical, dynamic loads are lower and the time to loss of plate stability becomes shorter.

3.4. Evaluation of computational results

The additional plate models composed of various number of solid elements layers building the mesh of core layer have been used in evaluation of computational results of plate static and dynamic critical loads. The calculations were carried out for plate model built of axisymmetric elements (Figure 14). The computational results of plate loaded on the inner edge, which core mesh layer was modelled by one, two and four layers of solid elements were compared.

The Figure 19 shows plate models with two (Figure 19a) and four (Figure 19b) layers of solid elements in core mesh.

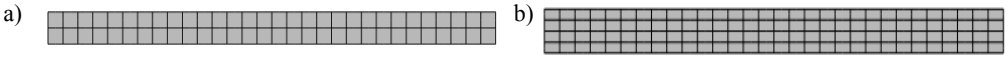

Fig. 19. Plate models built of axisymmetric elements with:
a) two, b) four layers of solid elements in core mesh

The values of static critical loads of examined three plate models built of axisymmetric elements are presented in Table 6. The axisymmetric form of plate buckling is shown in Figure 20.

Table 6. Values of critical static loads p_{cr} corresponding to axisymmetric buckling ($m = 0$) of plate models with various number of solid elements layers in core mesh

	p_{cr} [MPa]		
	plate models built of axisymmetric elements		
h_2/G_2 [m/MPa]	single layer of solid elements in core mesh	double layer of solid elements in core mesh	quaternary layer of solid elements in core mesh
0.005/5	64.00	64.00	64.00
0.005/15.82	119.92	119.91	119.91
0.02/5	143.20	143.14	143.13

The obtained values of static critical loads p_{cr} of plate models built of axisymmetric elements are consistent and they correspond to values of loads p_{cr} calculated for full annulus of plate model (see the first line of Table 2).

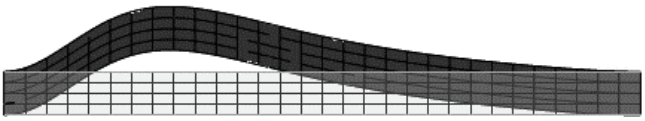

Fig. 20. Axisymmetric form of plate buckling

The values of dynamic, critical loads and critical, maximum deflections of plate models built of axisymmetric elements are presented in Table 7. The calculations were carried out for elastic material of core loading the plate with the growth rate s, equal to: $s = 4346$ MPa/s.

Table 7. Values of critical dynamic loads p_{crdyn} and critical maximum deflection w_{cr} of plate models loaded on inner plate edge

	p_{crdyn} [MPa] w_{cr} [m]		
	plate models built of axisymmetric elements		
h_2/G_2 [m/MPa]	single layer of solid elements in core mesh	double layer of solid elements in core mesh	quaternary layer of solid elements in core mesh
0.005/5	86.92 $3.27 \cdot 10^{-3}$	86.92 $3.27 \cdot 10^{-3}$	86.92 $3.27 \cdot 10^{-3}$
0.005/15.82	139.07 $3.67 \cdot 10^{-3}$	139.07 $3.67 \cdot 10^{-3}$	139.07 $3.67 \cdot 10^{-3}$
0.02/5	147.76 $2.94 \cdot 10^{-3}$	147.76 $2.95 \cdot 10^{-3}$	147.76 $2.96 \cdot 10^{-3}$

The obtained values of critical, dynamic loads are consistent. Insignificant differences are only observed for values of critical deflections. The consistency of values p_{crdyn}, w_{cr} occurs for two analysed, qualitatively different plate models: simplistic, built of axisymmetric elements and in the form of full annulus (see, Tables 7 and 3).

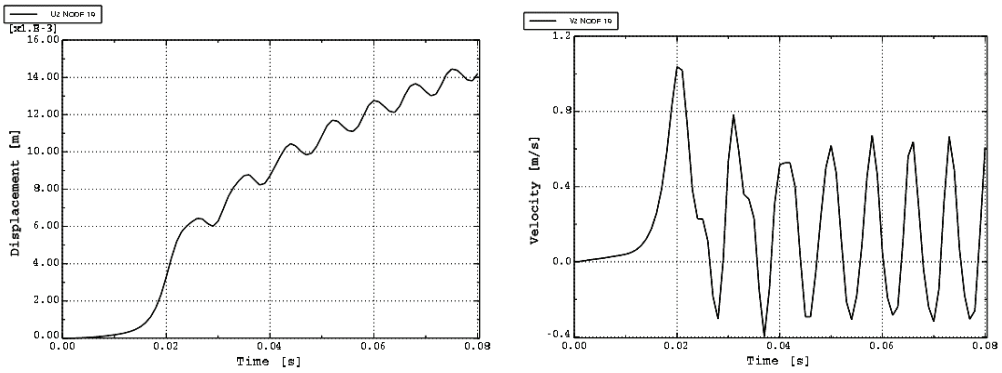

Fig. 21. Time histories of deflection and velocity of deflection of plate loaded on an inner edge, modelled by four layers of solid elements in core mesh

The exemplary time histories of maximum deflection and velocity of deflection with distribution of plate deflections for plate ($G_2 = 5$ MPa, $h_2 = 0.005$ m) model with four layers of solid elements in core mesh, are shown in Figures 21, 22 respectively.

The results are comparable with the results presented in Figures 7 and 10.

Presented calculation analysis of examined plate models shows the modest influence of mesh model structure (the core layer structure) on the values of plate critical loads. The consistency of values of critical loads of full annulus plate model with the values obtained for simple plate model built of axisymmetric elements is the good verification of correctness of conducted calculations.

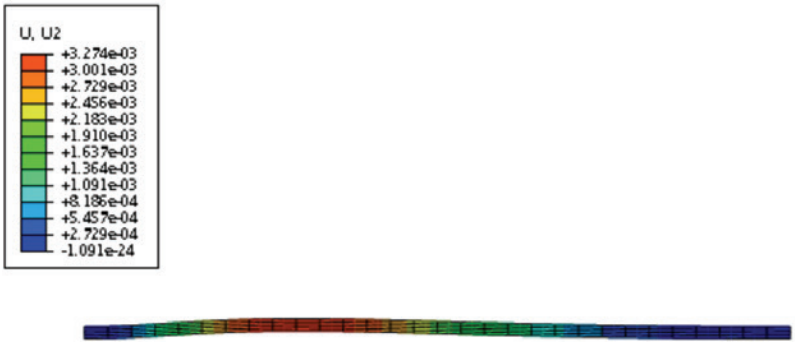

Fig. 22. Distribution of deflections for plate model with four layers of elements in core mesh

The results presented in Table 4 for the instance of plate with geometrical and material parameters: $G_2 = 5$ MPa, $h_2 = 0.005$ m, compressed on the outer edge with the rate of loading growth $s = 410.4$ MPa/s have been confirmed carrying out the calculations for alternative mesh structure. The full annulus plate model is built of two times more 4-nodes shell and 8-nodes solid elements in circumferential plate direction. In Table 8 the computational results of selected plate instances with number m, equal to: $m = 4, 6, 8$ buckling waves are presented. The Figure 23 shows the exemplary distribution of critical deflections for plate with $m = 6$ buckling waves.

Table 8. Values of critical dynamic loads p_{crdyn} and critical maximum deflection w_{cr} of plate loaded on outer edge

p_{crdyn} MPa]	16.83	16.01	20.52
w_{cr} [m]	$0.99 \cdot 10^{-3}$	$0.68 \cdot 10^{-3}$	$0.72 \cdot 10^{-3}$
m	4	6	8

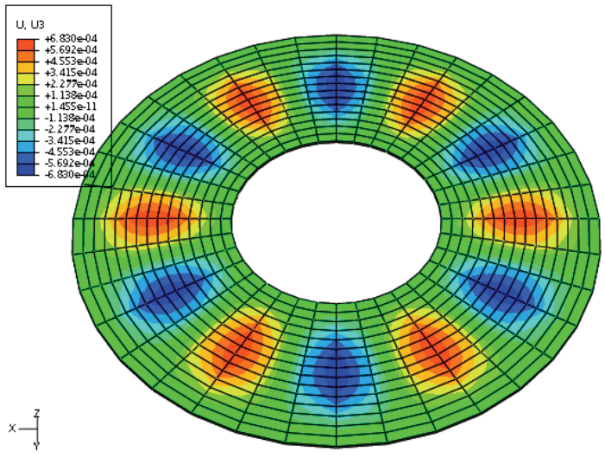

Fig. 23. Critical deflections distribution of plate with $m = 6$ buckling waves

The obtained values of critical, dynamic loads p_{crdyn} and maximum plate deflection w_{cr} denoted at the moment of the loss of plate stability and the observations of plate behaviours agree with computational results for the main plate model presented in this paper (see, Figure 2).

4. Conclusions

The work contains the general evaluation of the critical loads of three-layered, annular plates showing the influence of some plate parameters on its critical behaviour and presents the way of plate model building in finite element method.
The main observations are as follows:

- in the case of loading of the inner plate perimeter, the minimal values of compressive static and dynamic loads are found for regular, axially-symmetrical form of loss of plate stability,
- in the case of loading of the outer plate perimeter, the minimal values of compressive static and dynamic loads and numbers of buckling waves depend on the geometrical and material parameters. With the increase in the plate stiffness the critical static loads and numbers of circumferential buckling waves increase,
- deformation response of plates compressed on outer edge with the axially-symmetrical form of predeflection or with one or two waves could not correspond with the form of plate imperfection and the plate could take the circumferential wavy form with the larger number m, e.g. equal to 6,
- the influence of the rheological properties of foam material are insignificant for analysed plates compressed with rapidly increasing load,
- the evaluation of the complete stress state of the plate at the moment of its loss of stability is an important element of analysis. The observed values of critical stresses could be significant,
- there is the small sensitivity of FEM plate model on the mesh structure of plate core layer (the layer number of solid elements) for plates with the core thickness h_2 in the range of values: from $h_2 = 0.005$ m to $h_2 = 0.02$ m.

Presented computational results obtained using the finite element method are comparable with the results of plates, which have been determined using the finite difference method in the solution to the static and dynamic stability problems. Exemplary comparisons of results are presented, e.g. in works [6–8].

References

[1] Chen Y.R., Chen L.W., Wang C.C.: *Axisymmetric dynamic instability of rotating polar orthotropic sandwich annular plates with a constrained damping layer*, Composite Structures, Vol. 73, No. 2, 2006, pp. 290–302.

[2] Dumir P.C., Joshi S., Dube G.P.: *Geometrically nonlinear axisymmetric analysis of thick laminated annular plate using FSDT*, Composites: Part B, Vol. 32, 2001, pp. 1–10.
[3] Hibbitt, Karlsson and Sorensen, Inc.: *ABAQUS/Standard. User's Manual*, Ver. 6.1, 2000.
[4] Kluesener M.F., Drake M.L.: *Mathematical modelling. Damped structure design using finite element analysis*, Shock and Vibration Bulletin, Vol. 52, 1982, pp. 1–12.
[5] Majewski, S., Maćkowski, R.: *Creep of foamed plastics used as the core of sandwich plate* (in Polish), Engineering and Building Industry, Vol. 3 (Inżynieria i Budownictwo), 1975, pp. 127–131.
[6] Pawlus D.: *Dynamic stability problem of three-layered annular plate under lateral time-dependent load*, Journal of Theoretical and Applied Mechanics, Vol. 43, No. 2, 2005, pp. 385–403.
[7] Pawlus D.: *Solution to the static stability problem of three-layered annular plates with a soft core*, Journal of Theoretical and Applied Mechanics, Vol. 44, No. 2, 2006, pp. 299–322.
[8] Pawlus D.: *Dynamic stability of three-layered annular plates with viscoelastic core*, The Archive of Mechanical Engineering, Vol. LV, No. 1, 2008, pp. 27–55.
[9] Romanów, F.: *Strength of sandwich constructions* (in Polish), WSI in Zielona Góra, Poland, 1995.
[10] Standard, PN-84/B-03230 *Lightweight curtain walls and roofs of sandwich and rib panels. Static calculation and design* (in Polish), Standardization Publishers "Alfa", Warszawa, 1985.
[11] Wang H.J., Chen L.W.: *Axisymmetric dynamic stability of sandwich circular plates*, Composite Structures, Vol. 59, 2003, pp. 99–107.
[12] Wang H.J., Chen L.W.: *Axisymmetric dynamic stability of rotating sandwich circular plate*, Journal of Vibration and Acoustics, Vol. 126, 2004, pp. 407–415.
[13] Wolmir A.S.: *Nonlinear dynamic of plates and shells* (in Russian), Science, Moskow, 1972.

Obliczenia krytycznych obciążeń trójwarstwowych płyt pierścieniowych z rdzeniem sprężystym i lepkosprężystym

Praca przedstawia wyniki obliczeń płyt pierścieniowych o trójwarstwowej strukturze, poddanych obciążeniom ściskającym w płaszczyźnie ich okładzin. Obliczenia prowadzono wykorzystując metodę elementów skończonych. Zastosowano program ABAQUS. Obserwacji poddano krytyczne i pokrytyczne zachowania płyt oceniając statyczną i dynamiczną utratę ich stateczności. Badaniom poddano zarówno przypadki osiowosymetrycznych postaci utraty ich stateczności, jak i występujące szczególnie dla płyt ściskanych na brzegu zewnętrznym pofalowane obwodowo postacie wyboczenia. W pracy zwrócono uwagę na sposób budowy modelu obliczeniowego warstwowej płyty z miękkim, piankowym rdzeniem o własnościach sprężystych i lepkosprężystych.

ARCHIVES OF CIVIL AND MECHANICAL ENGINEERING

Vol. XI 2011 No. 4

Influence of heat treatment on resistance to electrochemical corrosion of the strain-hardened strips made of the Ni_3Al phase based alloys

M. PODREZ-RADZISZEWSKA
Institute of Materials Science and Applied Mechanics, Wrocław University of Technology, Smoluchowskiego 25, 50-372 Wrocław, Poland.

P. JÓŹWIK
Department of the Advanced Materials and Technologies, Military University of Technology, Kaliskiego 2, 00-908 Warszawa, Poland.

The paper presents results of the electrochemical corrosion resistance tests of the fine-crystalline strips made of the Ni_3Al intermetallic phase base alloys with the chemical composition in % at.: Ni – 22.13Al – 0.26Zr – 0.1B. Subject of the analysis was a material in the state of strain hardening to 50% deformation, as well as after one-hour annealing in the 600, 700, 800 and 1100 °C temperatures. An influence of the heat treatment temperature at the obtained electrochemical parameter values and correlation of the changes with recovery and recrystallisation processes observed in the material have been found.

Keywords: *electrochemical corrosion resistance, Ni_3Al intermetallic phase base alloys, strain hardening*

1. Introduction

Nickel in the protective coating has been widely applied in the engineering of construction materials [3–4]. Also, it is one of the basic elements in the alloy austenitic steels. Alloys based on nickel have been applied mainly as the heat-resisting and high-temperature creep-resisting materials. However, they have also been used for parts, which should show resistance to the aggressive water media. Its equilibrium potential is –0.25 V, and the stationary potential in 0.5 n NaCl is –0.02 V [3, 14].

Recently, wide interest in the alloys based on intermetallic phase, frequently referred to as intermetals, has been observed [1–6, 8–10, 12]. This is a group of materials, in which a basic structural component is one of the intermetallic phases [3–4]. Alloys based on the Ni_3Al intermetallic phase show much better fatigue strength, higher strength in higher temperature at the high strain rate, relatively low density, structural stability and high resistance to the high-temperature corrosion, in comparison to the commonly used high-temperature creep-resisting alloys based on nickel (superalloys) [3–4].

So far, the materials were applied in the automotive, machine and aircraft industries. They are mainly destined for turbo-compressor parts, valves, valve-seats and cylinder sleeves in combustion engines (among others from: AP Cummins Engine Company, PCC Airfoils), stamping dies, accessories of furnace for heat-and-chemical treatment (among others from: General Motors, Oak Ridge National Laboratory), as well as for directed crystallisation, for turbine blades in jet engines (among others from: General Electric, Beijing Institute of Aeronautical Materials) [4–6]. Besides the above applications, research works have been conducted in parallel to find application of the alloys in other areas, such as micro-components and structures of high surface integration. In the subject literature there is only a few elaborations concerning the electrochemical corrosion resistance of alloys based on the intermetallic phases. Research in that direction would enable potential increase in application of the studied alloys.

The aim of the performed study was evaluation of the influence of heat treatment temperature on the electrochemical corrosion resistance of the fine-crystalline strain-straightened strips made of an alloy based on the Ni_3Al intermetallic phases.

2. Material and test methodology

The study material was an alloy based on the Ni_3Al intermetallic phase, with chemical composition % at.: Ni – 22.13Al – 0.26Zr – 0.1B. An initial study state – strips of fine-crystalline microstructure of the base (γ' phase) (state W), was achieved as a result of plastic and heat treatment, while keeping up to precisely defined parameters for the processes [1–2, 6] (Figure 1). The material achieved in that way was subjected to 50% cold strain hardening (state U) and, in the next stage, to annealing in temperature 600, 700, 800 and 1100 °C, within one hour time (correspondingly the U600, U700, U800 and U1100 states). Depending on the material state, markings according to Table 1, have been adopted in the paper.

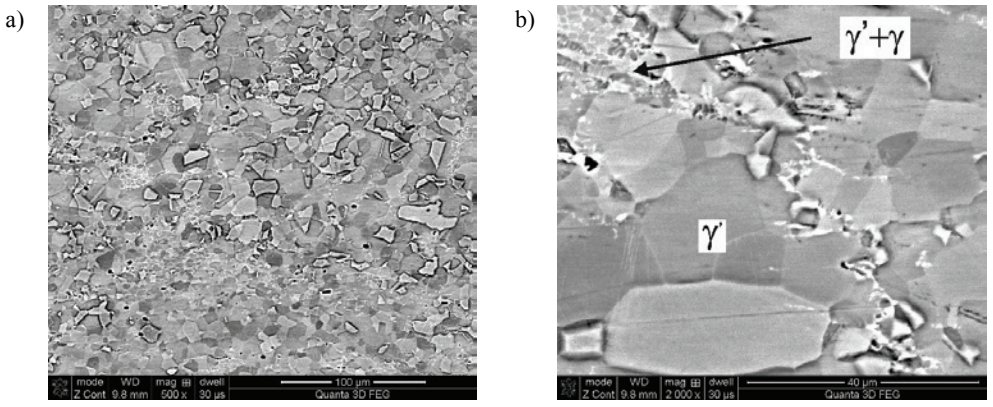

Fig. 1. a) fine-crystalline microstructure of strips made of alloy based at the Ni_3Al intermetallic phase, b) magnified fragment of picture from Figure 1a. SEM SE

Table 1. Marking of the tested samples

Marking	Material state
W	fine-crystalline material in the initial state (before strain hardening)
U	after strain hardening to 50% reduction (without heat treatment)
U 600	after strain hardening to 50% reduction and annealing in temperature of 600 ^{o}C/1h
U 700	after strain hardening to 50% reduction and annealing in temperature of 700 ^{o}C/1h
U 800	after strain hardening to 50% reduction and annealing in temperature of 800 ^{o}C/1h
U 1100	after strain hardening to 50% reduction and annealing in temperature of 1100 ^{o}C/1h

Samples for metallographic tests were prepared by cutting them in the electrical discharge machine, and then grinded and polished mechanically. Microstructure details have been revealed by etching with the Marble chemical. In addition, hardness tests using the Vickers method at 5 kG (49.05 N) load within 10 s time, performing 10 measurements for each state were made. Microstructure observations and hardness tests were performed at the Chair of Advanced Materials and Technologies of the Military University of Technology, using the FEI Quanta 3D FEG analysing scanning electron microscope.

Electrochemical direct-current measurements aimed at evaluating the corrosion resistance were performed at the Institute of Materials Science and Applied Mechanics of the Wrocław University of Technology, using methods involving measurement of open circuit potential and recording the $i = f(E)$ relationship during polarisation tests in the three-electrode measuring system. The fully automated measurement system consisted of a measurement cell, Atlas 0531 Elektrochemical Unit & Impedance Analyser potentiostat and a computer controller. The auxiliary electrode was made of austenitic steel, and as the reference electrode the saturated Ag/AgCl electrode was used. Samples for corrosion tests were grinded and then mechanically polished. Surface area of the test electrode was 0.785 cm^2. Before the measurements each sample was exposed to 5% NaCl solution for 20 minutes at room temperature for their stabilizing, and next subjected to polarization in the anode direction with the rate of $\mathrm{d}E/\mathrm{d}t = 1$ mV/s, in the same solution. The initial value of the potential was determined basing at the stabilized value of the open circuit potential E_o, assuming the value lover by some 200 mV. Density of corrosion current I_{corr}, corrosion potential E_{corr} as well as the polarisation resistance R_p were determined by Stern method for the anodic and cathodic parts of the $i = f(E)$ curve within the range of ±20 mV from the measured cathodic-anodic transition potential at the potential increase rate of 1 mV/s.

Microscopic observations performed after the corrosion tests were aimed at determining the character of changes appearing on the tested materials surface. The tests were made in the Institute of Materials Science and Applied Mechanics of the Wrocław University of Technology using the scanning electron microscopy methods and the JEOL 5800 LV microscope.

3. Test results

3.1. Microstructure tests

The tested material in the initial state (state W) was characterised with dual phase microstructure. Base of the alloy was the ordered secondary solid solution of the Ni_3Al intermetallic phase – the γ' phase of the average grain size determined by the equivalent diameter of about 7 μm. Size of the crystallite was determined by equivalent diameter, which was defined as the diameter of a circle with the same area as the measured object. The measurements were performed by using the analysing software (NIS AR Element Nikon Company) on the SEM image. The second structural component was a mixture of γ′ and γ phase – unordered solid solution of aluminium in the lattice of nickel (Figure 1) [1–2, 6]. The material was subjected to 50% cold strain hardening (state U), and next annealing in the temperature of 600, 700, 800 and 1100 °C, in one hour (Figure 2).

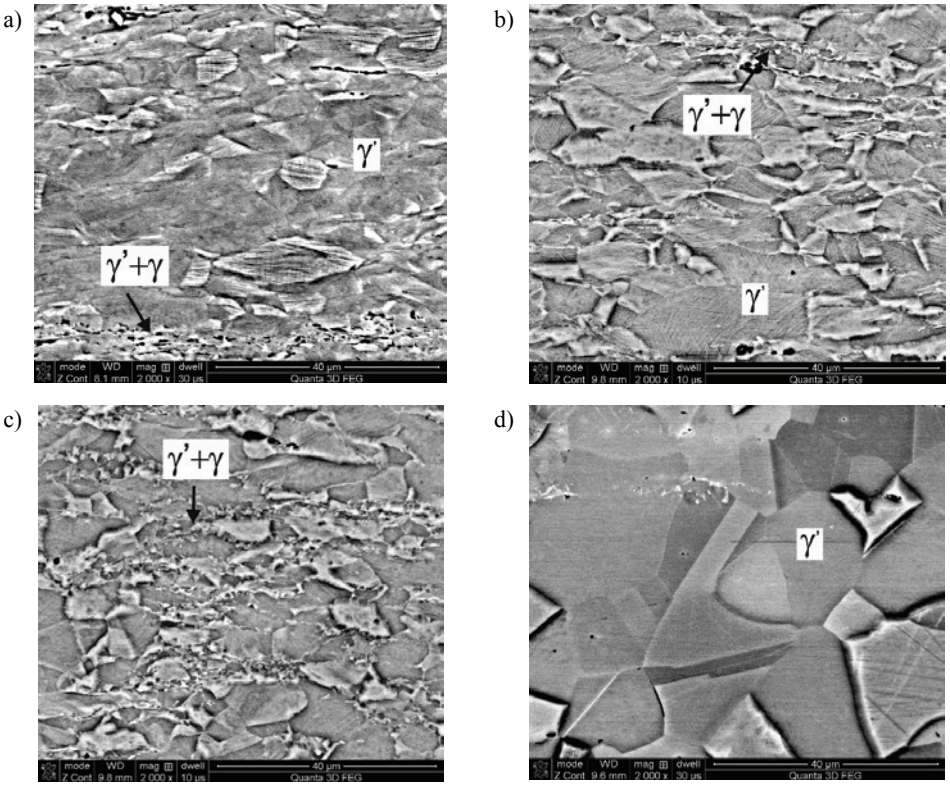

Fig. 2. Exemplary microstructure of fine crystalline strips of alloy based at the Ni_3Al intermetallic phase in the states of: a) after strain hardening (without heat treatment) – state U, b) after strain hardening and annealing in temperature of 600 °C/1h – state U600, c) after strain hardening and annealing in temperature of 800 °C/1h – state U800, d) after strain hardening and annealing in temperature of 1100 °C/1h – state U1100. SEM SE

Microstructure of the material hardening by cold work (state U) was characterised by fibrous microstructure, directed in accordance with the plastic deformation applied, with numerous slip bands (Figure 2a). Microscopic tests and hardness measurements performed for each particular state after the heat treatment have shown that distinct hardness drop and changes in microstructure (observable in the scanning electron microscope image), indicating initiation of the alloy recrystallization process, appear in samples after annealing above temperature of 800 °C (Figure 2c). However, this requires confirmation by tests with the use of transmission electron microscopy.

Insignificant drop in hardness was observed for a sample after annealing in temperature of 600 °C, which suggests initiation of the material recovery (Figures 2b, 3). Previous investigation exhibited that the 1-hour annealing below 1000 °C did not change essentially the phase composition [6]. After heat treatment conducted in the temperature of 1100 °C, a selective grain growth (secondary recrystallization) was observed, which led to a hardness drop below that obtained for the state W. Research performed has also shown that applying higher annealing temperatures causes significant drop in diphase areas participation ($\gamma' + \gamma$), Figure 2d [6]. Probably, the amount of γ phase was dramatically decreased by gradual homogenising and ordering into the ordered γ' phase. Results of hardness tests made for particular states have been collected in the form of graph on Figure 3.

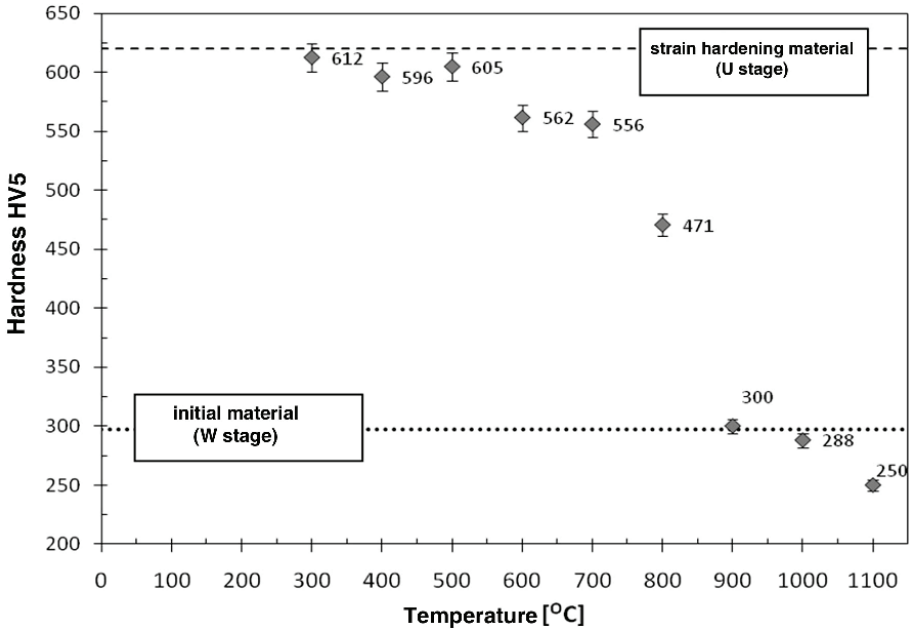

Fig. 3. Hardness change as a function of annealing temperature of fine-crystalline strips made of alloy based on Ni_3Al intermetallic phase after 50% strain hardening

3.2. Electrochemical tests

Based on the electrochemical tests performed, the stationary potential E_o, density of corrosion current I_{corr}, corrosion potential E_{corr}, and the polarisation resistance R_p have been determined. Their results have been collected in Table 2. For all the tested states the material was characterised by similar polarisation curve course (Figure 4), however, in case of the material not subjected to strain hardening (state W), the highest current densities in the anodic part of the curves were observed at high values of overvoltage. The lowest values have been achieved for the U1100 state.

Table 2. Electrochemical parameters obtained for individual samples

Material state	Average value			
	E_o [mV]	E_{corr} [mV]	I_{corr} [A/cm^2]	R_p [Ω·cm^2]
W	–239	–252	5.95E07	1.46E+05
U	–197	–235	9.05E-07	5.28E+04
U 600	–180	–207	5.41E-07	8.46E+04
U 700	–197	–225	7.65E-07	8.57E+04
U 800	–227	–253	8.18E-07	9.27E+04
U 1100	–237	–258	5.72E-07	1.07E+05

The conducted research indicates the rise in the open circuit (stationary) potential value E_o for the U state in relation to the initial state of the material (state W). Annealing of the samples in temperature of 600 °C leads to further increase in its value (for the sample U600 the highest value of E_o has been obtained). Application of higher temperatures causes gradual drop in the potential and return to the value achieved for the initial state. A drop in the stationary potential value observed from annealing temperature of 700 °C, has to be related to the heat-activated processes observed in the microstructure, which finds confirmation in the strengthening change for the analysed material states. Microstructure analysis using SEM has not shown significant changes for strengthened strips annealed at the temperature of 700 °C (lack of recrystallization process effects, among others). A change in the E_o potential value may indicate initiation of the recovery processes, or the recovery and beginning the recrystallization (nucleation). For the univocal determination of the processes, further structural analyses using TEM are considered.

The E_o value achieved for the individual states remains closely correlated with the value of corrosion potential E_{corr}. In each individual sample insignificant changes in the E_{corr} potential value were found. While observing the value of both E_{corr}, and E_o, it can be noticed that their values are the lowest and comparable to the initial material value (state W) and the state U1100. Insignificant changes appearing in the potential values have to be related to the fact that performed heat treatments do not lead to precipitation of new phases in the tested material, and exclusively to reducing the share of diphase areas ($\gamma' + \gamma$) above the temperature of 1000 °C [6].

Based on the potential-dynamic relationships recorded within the ±0.20 V range in relation to the measured corrosion potential the current density and polarisation resistance R_p values have also been determined. It has been found that the sample subjected to cold work without heat treatment (state U) was characterised with the highest value of corrosion current density I_{corr}. For the samples W, U600 and U1100, the lowest and close to the corrosion current values I_{corr} were obtained. The observed tendency for insignificant rise in the corrosion current density within the temperature range from 700–800 °C, could be related to the incomplete progress of the heat-activated processes beginning in places of highest concentration of stresses and, in consequence, creating the local electrochemical micro-cells. On annealing in the temperature of 1100 °C, a distinct drop in the I_{corr}, value occurs again and reaches the level close to the initial state.

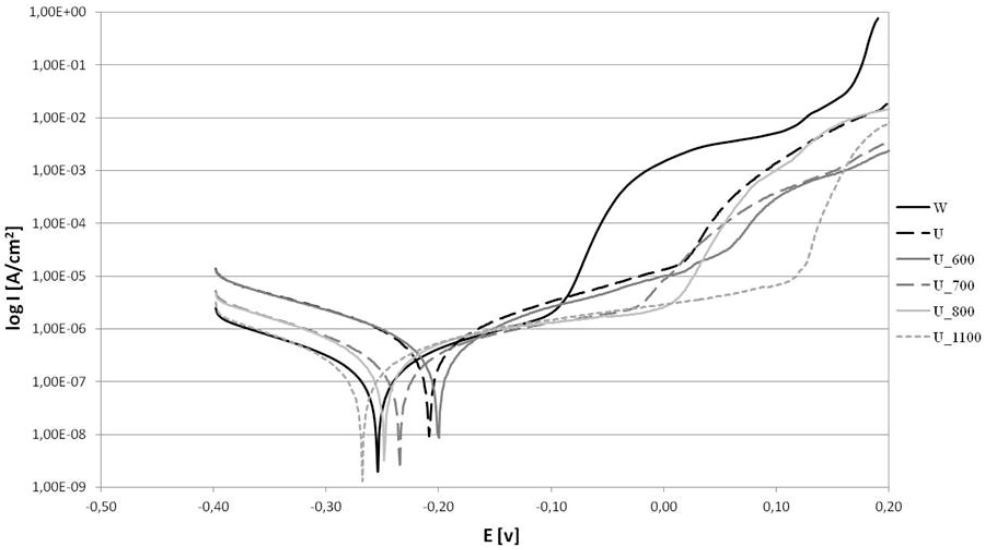

Fig. 4. Exemplary potential-dynamic curves for material in various heat treatment states

Polarisation resistance R_p, responsible for a corrosion rate reaches the highest value for the equilibrium states, i.e. the initial one W, and the completely recrystallised one, U1100. The lowest value has been achieved for the sample subjected to strain hardening (state U). Lowering the resistance for corrosion after cold work has been typical for metallic materials and is related to a drop in their thermodynamic durability after plastic deformation, as well as upsetting the tightness of the passive layers created at their surface [12, 14]. Along with the rise in the sample annealing temperature of strain hardening samples, a gradual increase in the R_p resistance takes place, related to the rate of corrosion processes. The results are convergent with the obtained values of corrosion current densities I_{corr}, and they have to be connected with the heat-activated processes, such as recovery and recrystallization.

3.2. Microscopy of surfaces after corrosion tests

Microscopy, performed after the electrochemical tests, has shown that the proceeding corrosion is uniform in character and reveals microstructure of the tested materials. The oxides layer created at their surface, loosely bound with substrate, has not been found. In case of alloys subjected to plastic working, local pitting has been observed at the surfaces of samples, probably initiating the corrosive destruction (Figures 6–7). Also, a selective dissolving of one of the phases present in the material microstructure has not been observed, which proves close electrochemical properties of the γ and γ' phases. Exemplary microscopic pictures of the sample surfaces after electrochemical tests have been shown in Figures 5–7.

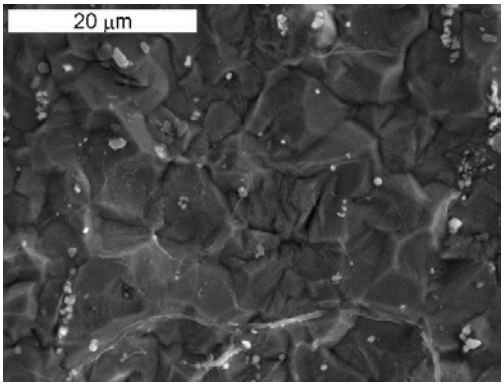

Fig. 5. Surface of the initial material – fine-crystalline band of Ni_3Al without strain hardening (state W) and electrochemical tests performed. Revealed fine-grain microstructure of the tested material. SEM SE

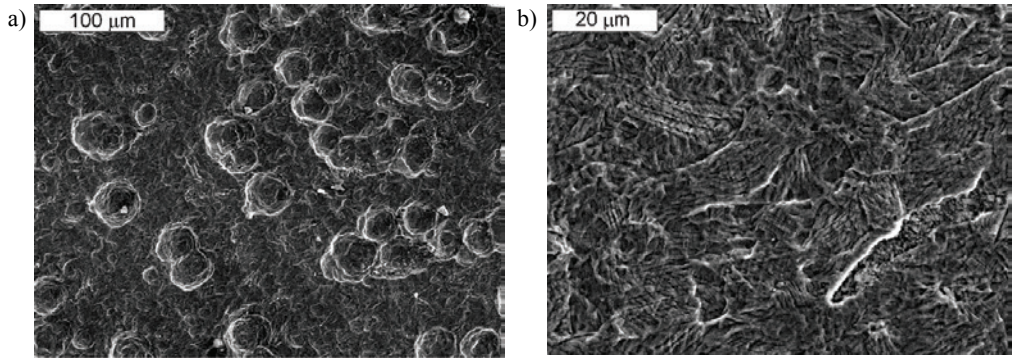

Fig. 6. a) Sample surface after strain hardening (state U) and electrochemical tests performed. Visible uniform dissolving of metallic base with creating local corrosive pitting at the sample surface. b) Magnified fragment of image from Figure 6a. Revealed, strongly plastically deformed microstructure of the studied material. SEM SE

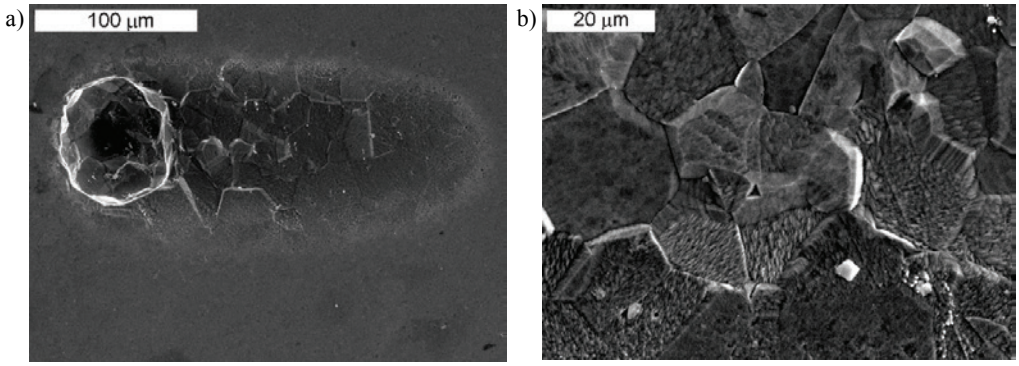

Fig. 7. Sample surface after strain hardening, annealing in temperature of 1100 °C (state U1100) and electrochemical tests. a) Visible pit created at the sample surface and local dissolving of the studied material. b) Magnified fragment of image from Figure 7a. Revealed microstructure of the tested material with clearly drawn grain boundaries. SEM SE

4. Conclusions

As a result of the conducted studies, it has been found that the applied annealing temperature influences electrochemical corrosion resistance in the alloy based at the Ni_3Al intermetallic phase with the chemical composition in % at.: Ni – 22,13Al – 0,26Zr – 0,1B, after the strain hardening to 50% reduction. For all the tested states the material was characterised by close course of polarisation curves, although differences in the obtained values of corrosion current density I_{corr} and polarisation resistance R_p. have been demonstrated. Changes in their values show close correlation with the processes of recovery and recrystallization proceeding in the material.

Insignificant changes in the stationary E_o, and corrosive E_{corr} potential values within the range of about ±50 mV have been found. The changes have to be related mainly to disturbance in the thermodynamic equilibrium of the material after strain hardening, because as shown in work [6], the heat treatment did not lead to creation of new phases in the alloy. It is known, that the zone of the defects such as dislocations and grain boundaries has higher value of the free energy. In work [11] Miyamoto et al. explained it as a reason for having the lower half-cell electrode potential whereas the areas without defects having relatively low energy are characterised by higher half-cell electrode potential. Recovery is based on regrouping and annihilation of dislocations, whereas recrystallisation on nucleation and the growth of new crystallites. These processes lead to reduced value of free energy and improved corrosion resistance of the material. The influence of grain size on the corrosion resistance of nickel was observed in work [7]. Authors found that the grain refinement was a reason for worse corrosion resistance of nickel. They suggested that the reason was higher reactivity of the grain boundary.

At the same time, a selective dissolving of one of the phases present in the material microstructure has not been observed, which testifies close electrochemical properties

of phases γ and γ′ in the 5% water solution of NaCl. Therefore, the change in diphase area share ratio of (γ′ + γ) to the base γ′, observed after applying higher annealing temperatures [6], has insignificant influence on the E_o and E_{corr} potential values for the material in the various heat treatment states.

Acknowledgements

The Authors sincerely thank for financial support in years 2008–2010 from the Ministry of Science and Higher Education (OR00004905).

References

[1] Bojar Z., Jóźwik P.: *Sposób kształtowania parametrów wytrzymałościowych taśm ze stopów na osnowie fazy międzymetalicznej Ni_3Al o wysokiej wytrzymałości*, Patent P-376267.21. 07.2005.

[2] Bojar Z., Jóźwik P.: *Sposób wytwarzania mikrokrystalicznych, plastycznych w temperaturze pokojowej taśm z jedno i dwufazowych stopów na osnowie fazy międzymetalicznej Ni_3Al (Method of manufacturing microcrystallite, plastic in the room temperature strips made of the one- and dual phase alloys based on Ni_3Al intermetallic phase)* (in Polish), Patent P-375804, 16.06.2005.

[3] Bojar Z., Przetakiewicz W.: *Metal materials containing intermetallic phases*, BEL Studio, Warszawa, 2006.

[4] Deevi S.C., Sikka V.K.: *Nickel and iron aluminides: an overview on properties, processing and applications*, Intermetallics, Vol. 4, No. 5, 1996, pp. 357–375.

[5] Hufenbach W., Jaschinski J., Gottwald R.: *Investigations on the applicability of chemically deposited Ni-shell tools for deep-drawing processes*, Archives of Civil and Mechanical Engineering, Vol. 9, No. 1, 2009, pp. 61–68.

[6] Jóźwik P., Zasada D., Bojar Z.: *Influence of heat treatment on structure and mechanical properties of Ni3Al (Zr, B) intermetallic alloy*, Archives of Foundry, Vol. 6, No. 18, 2006, pp. 249–254.

[7] Krajewski C., Sitek R., Ura-Bińczyk E., Pachla W., Matysiak H., Garbacz H., Kurzydłowski K.J.: *Effect of grain refinement on the corrosion resistance of Nickel 200* (in Polish), Ochrona przed Korozją, Vol. 6, 2011, pp. 298–300.

[8] Lachowicz M.: *Microstructural changes in padding welds made from the 713C alloy after heat treatment*, Archives of Foundry Engineering, Vol. 10, No. 3, 2010, pp. 11–16.

[9] Lachowicz M., Dudziński W., Haimann K., Podrez-Radziszewska M.: *Microstructure transformations and cracking in the matrix of gamma-gamma' superalloy Inconel 713C melted with electron beam*, Materials Science and Engineering A, Structural Materials: Properties, Microstructure and Processing, Vol. 479, No. 1–2, 2008, pp. 269–276.

[10] Lachowicz M., Dudziński W., Podrez-Radziszewska M.: *TEM observation of the heat-affected zone in electron beam welded superalloy Inconel 713C*, Materials Characterization, Vol. 59, No. 5, 2008, pp. 560–566.

[11] Miyamoto H., Harada K., Mimaki T., Vinogradov A., Hashimoto S.: *Corrosion of ultra-fine grained copper fabricated by equal-channel angular pressing*, Corrosion Science, Vol. 50, 2008, pp. 1215–1220.

[12] Rutkowska-Gorczyca M., Podrez-Radziszewska M., Kajtoch J.: *Corrosion resistance and microstructure of steel AISI 316L after cold plastic deformation*, Metallurgy of Foundry Engineering, No. 1, Vol. 35, 2009, pp. 35–43.
[13] Sikka V.K., Deevi S.C., Viswanathan S., Swindeman R.W., Santella M.L.: *Advances in processing of Ni_3Al-based intermetallics and applications*, Intermetallics, Vol. 8, No. 9–11, 2000, pp. 1329–1337.
[14] Tomashov N.D.: *Theory of corrosion and protection of metals*, PWN, Warsaw, 1982.

Wpływ obróbki cieplnej na odporność na korozję elektrochemiczną taśm ze stopu na osnowie fazy Ni_3Al umocnionych odkształceniowo

W pracy przedstawiono wyniki badań odporności na korozję elektrochemiczną drobnokrystalicznych taśm ze stopu na osnowie fazy międzymetalicznej Ni_3Al o składzie chemicznym % at.: Ni – 22,13Al – 0,26Zr – 0,1B. Analizowano materiał w stanie po odkształceniu na zimno do zgniotu 50%, a także po jednogodzinnym wygrzewaniu w temperaturze 600, 700, 800 i 1100 °C. Stwierdzono wpływ temperatury wygrzewania na wartości uzyskiwanych parametrów elektrochemicznych oraz korelację tych zmian z obserwowanymi w materiale procesami zdrowienia i rekrystalizacji.

ARCHIVES OF CIVIL AND MECHANICAL ENGINEERING

Vol. XI 2011 No. 4

Effects of recycled concrete aggregate on the fresh properties of self-consolidating concrete

M.D. SAFIUDDIN
Department of Civil and Environmental Engineering, Faculty of Engineering,
University of Waterloo, 200 University Avenue West, Waterloo, Ontario, Canada N2L 3G1.

M.A. SALAM, M.Z. JUMAAT
Department of Civil Engineering, Faculty of Engineering, University of Malaya,
50603 Kuala Lumpur, Malaysia.

Concrete wastes are generally delivered to the landfill sites for disposal. Due to increasing charges of landfill and scarcity of natural coarse aggregate (NCA), recycled concrete aggregate (RCA) derived from concrete wastes is growing interest in construction industry. In the present study, RCA was used as partial and full replacements of NCA to produce self-consolidating concrete (SCC). Different SCC mixes were produced with RCA substituting 0%, 30%, 50%, 70% and 100% NCA by weight. The water to cement (W/C) ratio and high-range water reducer (HRWR) dosage were kept the same for all concretes. The effects of RCA on the key fresh properties such as filling ability, passing ability and segregation resistance of SCC were investigated. The test results revealed that the filling ability and passing ability of SCC were improved for 30% and 50% RCA. The SCC mixes with 30% and 50% RCA also possessed adequate segregation resistance. In addition, strong correlations were observed for filling ability, passing ability and segregation resistance. The overall test results suggest that RCA can be used to produce SCC substituting up to 50% NCA without affecting the key fresh properties of concrete.

Keywords: *filling ability, passing ability, recycled concrete aggregate, segregation resistance, self-consolidating concrete*

1. Introduction

Self-consolidating concrete (SSC) is a highly flowing concrete that spreads through congested reinforcement, fills every corner of the formwork, and gets consolidated under self-weight [11]. The concept of SCC was proposed in 1986 by Professor Okamura [18], and the first prototype was developed in Japan in 1988 by Professor Ozawa [19]. However, the development of SCC was first reported in 1989 [17]. By the early 1990's, Japan started to produce and use SCC commercially. Since its inception, SCC has been widely used in large construction in Japan [18]. Globally, the use of SCC in civil engineering structures has been remarkably increased over the last two decades.

The basic ingredients of SCC are similar to those of normal concrete. The traditional concrete aggregates such as gravel or crushed stone, and river or mining sand are also used in SCC. Generally, the aggregates occupy 55–60% of the SCC volume

[18] and play a substantial role in determining the workability, strength, dimensional stability, and durability of concrete. The aggregates also have a significant effect on the cost of SCC. Therefore, less expensive aggregates are desirable for use in SCC. In addition, there is a critical shortage of natural aggregates in many regions of the world due to construction boom in developing countries and re-construction in developed countries [28]. Consequently, there is a growing interest in using alternative aggregates in construction. In the recent decade, the recycled concrete aggregate (RCA) obtained from concrete wastes has been used in the production of new concrete. The scarcity of natural coarse aggregate (NCA) and the increasing charges for landfill have encouraged the use of RCA in concrete [10]. In addition, the increased distance between the sources of natural aggregates and construction sites has constrained the contractors to consider RCA as an alternative of NCA [8].

A large quantity of concrete wastes often generates from demolished old structures, tested concrete, and excess or returned concrete. The removal and disposal of these wastes cause significant environmental problems. In this context, the recycling of concrete wastes as RCA is important because it can minimize the environmental pollution and reduce the huge consumption of natural aggregates in construction. Many researchers have shown that RCA can be a reliable alternative of NCA in construction, particularly for non-structural application [23]. Levy and Helene [15] as well as Poon et al. [21] have graded RCA as potentially good for use in new concrete. Properly processed RCA can be used to produce new concrete for pavements, shoulders, barriers, embankments, sidewalks, curbs, gutters, and bridge foundations. It can also be used in structural grade concrete, bituminous concrete, and soil-cement pavement bases [22]. Moreover, RCA has been used to produce durable and sustainable concretes [9, 26]. In comparison, limited studies have been conducted to use RCA in SCC. Recently, et al. [27], Kou and Poon [14], and Grdic et al. [8] have produced SCC using RCA as partial and full replacements of NCA. However, these studies gave more emphasis on the hardened properties and no comprehensive study investigated the effects of RCA on the key fresh properties of SCC. Also, no studies were carried out to produce SCC using RCA derived from tested and excess or returned concretes.

In the present study, the RCA derived from tested concrete was used to produce SCC substituting 0–100% NCA by weight. The effects of RCA on the key fresh properties such as filling ability, passing ability and segregation resistance of SCC were observed. The research outcome shows that SCC possessing good filling and passing abilities and adequate segregation resistance can be produced using RCA up to 50% replacement of NCA.

2. Research significance

Demolished old structures, tested concrete, and excess or returned concrete create a huge amount of concrete wastes, thus causing a substantial disposal problem. Since such disposal problem is becoming more and more difficult particularly in many densely

populated countries, a proper waste management needs to be practised. Indeed the shortage of land and the increasing charges for landfill require recycling of concrete wastes to produce RCA as a means of the waste management process. Moreover, there is a critical shortage of natural aggregates in many regions of the world. The use of RCA in SCC will contribute not only to find a solution for the disposal problem caused by the concrete wastes but also to reduce the demand for natural aggregates. In addition, the use of RCA in SCC will reduce the environmental impact due to the harvesting and processing of virgin aggregates from natural resources.

3. Materials and methods

3.1. Materials

Three types of aggregates such as NCA, RCA and mining sand were used. NCA and RCA acted as the coarse aggregate (CA), whereas mining sand performed as the fine aggregate (FA). The NCA used was crushed granite stone. RCA was derived from the tested 50-MPa concrete cubes (water to cement (W/C) ratio: 0.40; age: 6 months) that contained well-graded crushed granite stone (maximum size: 20 mm), and had a density of 2270 kg/m^3 and a porosity of 11%. The concrete cubes were crushed to the specified size and gradation of NCA using a hammer. The nominal maximum size of NCA and RCA was 20 mm, and that of FA was 5 mm. NCA, RCA and FA were sieved to meet the ASTM specifications [1].

Table 1. Basic physical properties of fine and coarse aggregates

Physical property	RCA	NCA	FA
Saturated surface-dry based specific gravity	2.51	2.62	2.69
Oven-dry based specific gravity	2.46	2.53	–
Absorption (wt. %)	1.91	0.60	1.32
Moisture content (wt. %)	1.32	0.17	0.31
Compacted bulk density (kg/m^3)	1366.2	1513	1618.5
Angularity number	9.47	7.45	–
Fines (< 4.75 mm) from aggregates* (wt. %)	7.75	–	–

*after 1-min mixing with an equal amount of fine aggregate

The basic physical properties of the aggregates are shown in Table 1. The gradation curves of the aggregates are presented in Figure 1. The size distributions of FA, NCA and RCA were within the ASTM limits, as shown in Figure 1. RCA was more angular than NCA and therefore possessed a higher angularity number (Table 1). In addition, RCA had porous surfaces consisting of reclaimed mortar and thus possessed a higher absorption value than NCA (see Table 1). The surface roughness of RCA was also greater than that of NCA. The visual inspection of aggregates revealed the greater angularity, surface roughness, and surface porosity of RCA (Figure 2). Also, the surface hardness of RCA was less than that of NCA due to porous reclaimed mortar.

Hence, RCA contributed to increase the fines content because of abrasive mixing action. In the present study, it was found that 7.75% fines finer than no. 4 sieve were generated from RCA when it was mixed for 1-min with an equal amount of mining sand. This mixing time was used since the aggregates were initially mixed for 1 min before adding the cement and water during preparation of SCC mixes.

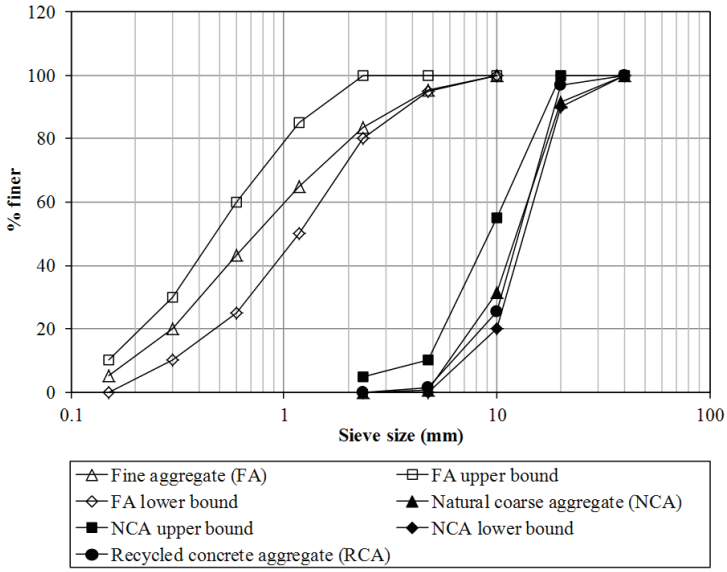

Fig. 1. Size distributions of FA, NCA and RCA

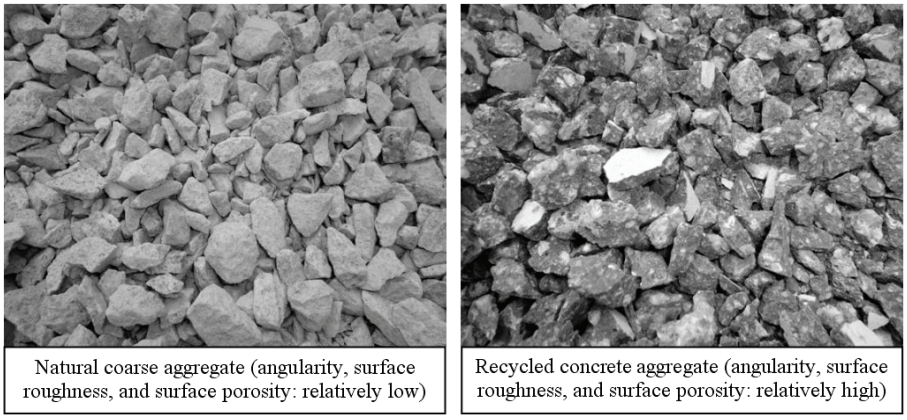

Fig. 2. Visual appearances of natural and recycled concrete aggregates

The aggregates were bound together by means of paste, which contained cement and water. ASTM type I portland cement (C) was used as the binder. The mix water

(W) used was normal tap water. Also, a polycarboxylate-based high-range water reducer (HRWR) was used with an adequate dosage to obtain the required filling ability and passing ability of SCC without any segregation. The specific gravity of cement was 3.12 and that of HRWR was 1.06. The solid content of HRWR was 13.5%, which aided to calculate its water contribution to concrete mix.

3.2. Concrete mix proportions

Nine trial concrete mixes using NCA were prepared with different W/C ratios (0.50, 0.60, and 0.65) and HRWR dosages. The basic mix proportions (without HRWR dosage) of these concretes were determined based on the British DoE mix design method [5]. From the trial concrete mixes, a suitable control mix satisfying the workability (filling ability, passing ability, and segregation resistance) requirements of SCC was decided. The W/C ratio and HRWR dosage of the selected control mix was 0.60 and 1.5% of cement by weight, respectively. Using the same W/C ratio and HRWR dosage, four different concretes were produced with RCA substituting 30%, 50%, 70% and 100% NCA by weight. The basic mix proportions of these concretes were calculated based on the absolute volume of constituent materials and 2% entrapped air content. The W/C ratio and HRWR dosage of these concretes were kept the same as used in the control mix (0% RCA) to observe the effects of RCA. The mix proportions of control and RCA concretes are shown in Table 2.

Table 2. Mix proportions of different SCC mixes (volume of concrete: 1 m^3)

Mix	RCA (%)	W/C ratio	FA/TA † ratio	HRWR (% C)	W (kg)	C (kg)	FA (kg)	NCA (kg)	RCA (kg)
CR0	0	0.60	0.50	1.50	205	342	914	914	0
CR30	30	0.60	0.50	1.50	205	342	873.4	611.7	262.1
CR50	50	0.60	0.50	1.50	205	342	870	435	435
CR70	70	0.60	0.50	1.50	205	342	866.2	259.9	606.3
CR100	100	0.60	0.50	1.50	205	342	860.5	0	860.5

* CA = NCA + RCA; †TA = FA + CA

The concretes were designated based on the RCA content. For example, the CR50 designation was used for a concrete including 50% RCA content.

3.3. Preparation of concretes

Air-dry fine and coarse aggregates were used in preparing the concretes. These aggregates absorbed some water at the time of mixing. In contrast, the liquid HRWR contributed some water during mixing. Therefore, the proportions of aggregates and mix water were corrected before mixing the constituent materials of concrete.

The mixing sequence and duration are very important in the production of SCC, as they influence the workability of concrete. In the present study, the coarse and fine aggregates were first charged into a revolving pan-type concrete mixer and mixed with

one-third of the mix water for 60 s. Then the mixer was stopped for 60 s to increase the wetness of aggregates. After this first rest period, the cement was added followed by the second one-third of the mix water and the mixing action was continued for 120 s. The mixer was stopped thereafter and allowed for a second rest period of 180 s. During the first and second rest periods, the mixer was covered with a piece of wet burlap to minimize the evaporation of water. Finally, the remaining one-third of the mix water blended with the HRWR dosage was added and the mixing operation was continued for 180 s to produce the fresh concretes.

3.4. Test methods and procedures

The filling ability, passing ability, and segregation resistance are the key fresh properties of SCC. Immediately after the completion of mixing, the freshly mixed SCC mixes were tested to determine these three fresh properties.

3.4.1. Filling ability tests

The filling ability is defined as the ability of SCC to flow in unconfined condition and fill every corner of the formwork under self-weight. In the present study, the filling ability was measured with respect to slump flow, T_{50} slump flow time and V-funnel flow time. The slump flow was determined according to the test method given in ASTM C 1611/C 1611M [3]. The slump flow test assesses the horizontal free flow of SCC in the absence of obstructions. This test also judges the capability of concrete to flow under its self-weight [7].

The T_{50} slump flow time was determined according to the test method given in EFNARC guidelines and specifications [6]. In this test, the time that a concrete sample requires for a spread of 50 cm diameter is determined. This time is well-known as T_{50}, which gives an indication for the relative viscosity of SCC mix. The rate of concrete spreading is inversely proportional to its viscosity. Thus, the T_{50} slump flow time provides a relative assessment of the unconfined flow rate of concrete.

The V-funnel flow time (T_V) was determined following the procedure given in EFNARC specifications and guidelines [6]. In this test, the time that a concrete sample needs for flowing out of a V-shaped box is determined to measure the filling ability of SCC. The shorter the flow time, the greater is the filling ability. This test also provides a qualitative assessment of the relative viscosity of SCC and indicates the blocking effect caused by segregation [25]. A shorter flow time suggests a lower viscosity, whereas a prolonged flow time indicates the blocking susceptibility of the mix [6].

3.4.2. Passing ability test

The passing ability is defined as the ability of SCC to flow in confined condition and completely fill all spaces within the formwork under self-weight and without any vibration. In the present study, the passing ability was determined with respect to

J-ring flow (JF) following the test method depicted in EFNARC specifications and guidelines [6]. In addition, the blocking index (BI: difference between slump flow and J-ring flow, SF-JF) was determined to assess blocking resistance as well as passing ability. A lower blocking index suggests a greater blocking resistance and a higher passing ability.

3.4.3. Segregation tests

Segregation resistance plays an important role in SCC. Poor segregation resistance would cause less flowing ability and blockage around congested reinforcement [11]. SCC must have good segregation resistance for application in structural members. In the present study, the Japanese sieve stability and column segregation tests were carried out to determine the segregation resistance of SCC mixes. The Japanese sieve stability test was conducted according to the procedure given by Nagataki and Fujiwara [16]. In this test, the mortar mass passing through a no. 4 sieve was expressed as the percentage of the total mortar content of original concrete sample to quantify the segregation resistance of SCC with respect to segregation index (SI).

The column segregation test was conducted following the procedure given in ASTM C 1610/C 1610M [2]. In this test, the saturated surface-dry based mass difference of coarse aggregates collected from the top and bottom sections of a column apparatus was expressed as the percentage of the average aggregate content of concrete for both sections to measure the segregation resistance of SCC with regard to segregation ratio (SR).

4. Results and discussion

The test results for the filling ability (slump flow, T_{50} slump flow time, and V-funnel flow time), passing ability (J-ring flow and blocking index), and segregation resistance (segregation index and segregation ratio) of various SCC mixes are given in Table 3. It is obvious from Table 3 that the presence of RCA significantly influenced the filling ability, passing ability, and segregation resistance of SCC. The mix parameters that influenced these three properties of SCC are shown in Table 4.

Table 3. Fresh properties of various SCC mixes

Concrete	Filling ability			Passing ability		Segregation resistance	
	Slump flow, SF (mm)	T_{50} slump flow time (s)	V-funnel flow time, T_V (s)	J-ring flow, JF (mm)	Blocking index, BI (mm)	Segregation index, SI (%)	Segregation ratio, SR (%)
CR0	620	3.1	7.3	580	40	9.8	11.7
CR30	640	2.9	7.1	610	30	10.9	15.0
CR50	650	2.6	6.8	615	35	11.2	14.8
CR70	610	3.4	10.2	560	50	9.5	20.1
CR100	550	4.5	18.6	505	45	8.3	24.2

Table 4. Mix parameters for various SCC mixes

Concrete	Initial FA (kg/m^3)	Post-mixing FA* (kg/m^3)	Initial CA (kg/m^3)	Post-mixing CA† (kg/m^3)	Paste volume‡ (m^3)	Mortar volume‡ (m^3)	Mortar density (kg/m^3)
CR0	914	914	914	914	0.320	0.661	2218
CR30	873.8	894.1	873.8	853.5	0.320	0.654	2213
CR50	870	903.1	870	836.3	0.320	0.657	2215
CR70	866.2	913.2	866.2	819.2	0.320	0.661	2218
CR100	860.5	926.9	860.2	793.5	0.320	0.666	2221

* Includes the fines generated from RCA; †excludes the fines generated from RCA; ‡per unit volume of concrete

4.1. Filling ability

4.1.1. Slump flow

The slump flow results achieved for the concrete mixes with different RCA contents are given in Table 3. The slump flow varied in the range of 550–650 mm. A minimum slump flow of 600 mm is generally recommended for SCC to ensure adequate self-consolidation capacity [12]. Therefore, the SCC mix with 100% RCA did not fulfil the requirement for slump flow. The absorption of RCA and the dosage of HRWR had no effect on the slump flow of SCC. This is because the water correction was done for the absorption of RCA and considered during concrete mixing. Also, the amount of HRWR was the same for all SCC mixes.

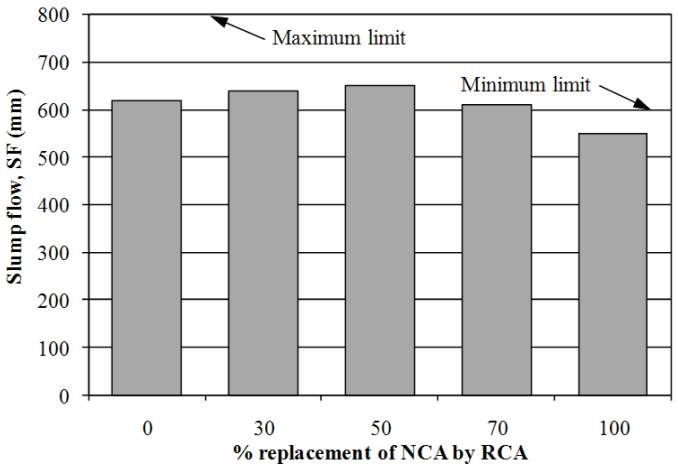

Fig. 3. Effect of RCA on the slump flow of concrete

The effect of RCA on the slump flow of SCC is evident from Figure 3, which shows that the slump flow increased for 30% and 50% RCA. This is mainly attributed to the

reduced content of coarse aggregate. Also, the post-mixing fine aggregate content was slightly lower at 30% and 50% RCA (see Table 4). At the reduced fine and coarse aggregate contents, more free water was available to improve the filling ability. In addition, the paste volume was the same in all concrete mixes (refer to Table 4). Consequently, the paste volume per unit aggregate content became higher, thus reducing the friction between aggregate particles. As a result, the dispersion of the aggregates increased leading to a greater slump flow.

The slump flow decreased for 70% and 100% RCA. In particular, the significant reduction in slump flow occurred for 100% RCA. This is in contrast with the slump flow results obtained for 30% and 50% RCA. The substantial decrease in slump flow at 100% RCA is mostly due to the increased amount of fine aggregate that caused to decrease the free water content in SCC mix. The paste volume, mortar content and mortar density had no effect in the reduction of slump flow, since these parameters were more or less similar for all SCC mixes (see Table 4). But the post-mixing fine aggregate content became significantly higher for 100% RCA, as some fines (passing no. 4 sieve) were generated from RCA during abrasive mixing action (refer to Table 4). As a result, the demand for water increased for a given slump flow. Since the water content was the same for all concretes, the SCC mix with 100% RCA provided relatively a low slump flow. A similar effect was not observed in the cases of 30% and 50% RCA, because the total fine aggregate content including the fines generated from RCA was still lower than that of control concrete (0% RCA). In the case of 70% RCA, the post-mixing fine aggregate content was almost equal to that of the control concrete with 0% RCA. Yet, a slight reduction in slump flow occurred owing to the adverse physical characteristics (angularity, surface roughness, surface porosity, etc.) of RCA.

The RCA used in the present study was more angular than NCA (see Table 1 and Figure 2). The high absorption capacity of RCA also indirectly suggests that it was more porous and much rougher than NCA due to reclaimed mortar. The rough-textured RCA particles increase the harshness of SCC mix, and thus can decrease its slump flow at a greater RCA content. The loss of cement paste into the surface pores of RCA can also decrease the slump flow of concrete [24]. However, these effects were not predominant due to the reduction in post-mixing coarse aggregate content with a subsequent increase in the amount of fine aggregate (refer to Table 4).

4.1.2. T_{50} slump flow time

The T_{50} slump flow time results of the concretes with different RCA contents are given in Table 3. The T_{50} slump flow time varied in the range of 2.6–4.5 s. According to EFNARC specifications and guidelines [6], the T_{50} slump flow time of SCC generally ranges from 2 s to 5 s. Hence, the T_{50} slump flow times were within the acceptable range. The effect of RCA on the T_{50} slump flow time of SCC is evident from Figure 4.

The T_{50} slump flow time decreased for 30% and 50% RCA. This is mostly due to the reduced content of coarse aggregate (see Table 4). However, the role of reduced

coarse aggregate content in reducing T_{50} slump flow time was not predominant at 70% and 100% RCA due to the similar reasons as discussed in section 4.1.1.

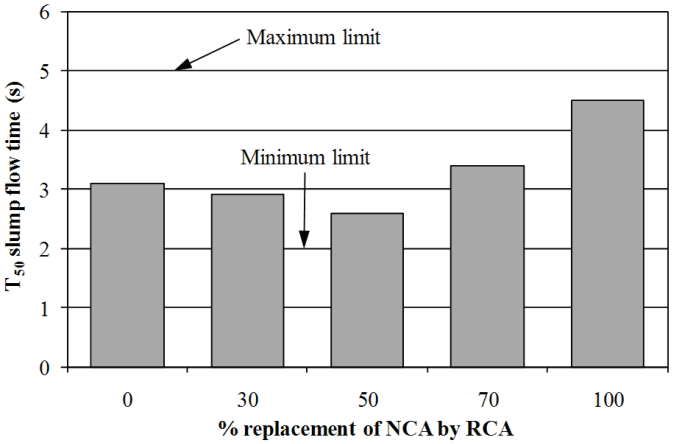

Fig. 4. Effect of RCA on the T_{50} slump flow time of concrete

The fine aggregate confines some mix water, thus decreasing the free water content in the concrete mix. In addition, the greater surface roughness and angularity of RCA increase the friction between coarse aggregates. These two effects were more dominant for 70% and 100% RCA. As a result, the SCC mixes with 70% and 100% RCA became more viscous and provided a higher T_{50} slump flow time.

4.1.3. V-funnel flow time

The V-funnel flow time results of the SCC mixes with various RCA contents are given in Table 3. The V-funnel flow time varied in the range of 6.8–18.6 s. According to EFNARC specifications and guidelines [6], the V-funnel flow time of SCC shall be in the range of 6–12 s. Therefore, the V-funnel flow times were within the acceptable limits except for 100% RCA. In the case of 100% RCA, the flow became intermittent with a longer flow time of concrete. A high flow time can be caused by either a low flowing ability or a blockage of the flow [11]. The lack of cohesiveness can cause accumulation of coarse aggregates in the tapered outlet of a V-funnel. This can lead to arching of coarse aggregates leading to the blockage of concrete flow. However, the good cohesiveness of CR100, as indicated by the T_{50} slump flow time, suggests that the blockage due to coarse aggregate arching was unlikely for this concrete. No significant blockage was also observed in the J-ring flow test; the blocking index of CR100 was less than the maximum limit of 50 mm (refer to Table 3). Therefore, the high V-funnel flow time of CR100 SCC mix was mostly due to its low flowing ability, as perceived from the results of slump flow test.

The variation in V-funnel flow time followed a similar trend as observed in the case of T_{50} slump flow time. The effect of RCA on the V-funnel flow time of SCC is evident from Figure 5. The flow time decreased for 30% and 50% RCA but significantly increased for 70% and 100% RCA. The reasons are the same as discussed in the case of T_{50} slump flow time (section 4.1.2). The shorter flow time indicates the greater flowing ability [6]. However, a very small flow time does not necessarily give an indication of good flowing ability. In fact, the SCC mixes with a very low V-funnel flow time show excessive bleeding and/or segregation, thus causing blockage leading to intermittent concrete flow. Also, the SCC mixes with a very high V-funnel flow time are greatly viscous and therefore may exhibit intermittent concrete flow with a reduced flowing ability. For instance, the SCC with 100% RCA (CR100) provided a high V-funnel flow time of 18.6 s in the present study. This high flow time was linked with an excessive viscosity that interrupted the continuous flow of concrete through the lower opening of V-funnel.

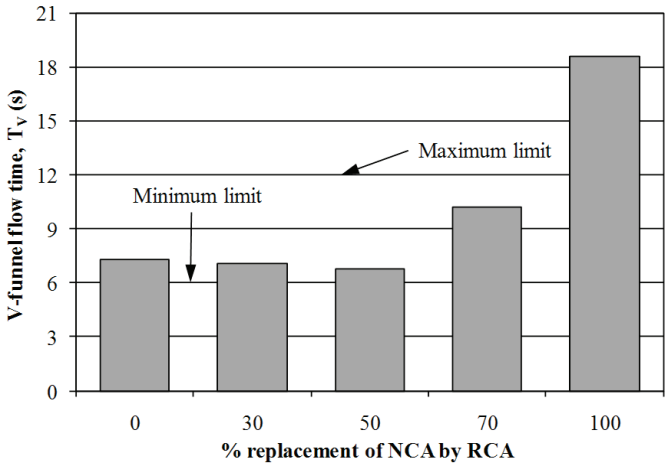

Fig. 5. Effect of RCA on the V-funnel flow time of concrete

4.2. Passing ability

4.2.1. J-ring flow

The results of J-ring flow are given in Table 3. The maximum reduction in slump flow in the presence of J-ring was not greater than 50 mm. According to Brameshuber and Uebachs [4], the difference between slump flow and J-ring flow (blocking index, SF–JF) should be ≤50 mm for SCC to ensure good passing ability without significant blockage. Hence, all SCC mixes produced in the present study possessed reasonably good passing ability.

The effect of RCA on the J-ring flow is obvious from Figure 6. This figure reveals that the passing ability was improved for 30% and 50% RCA, since the J-ring flow

increased. In contrast, the J-ring flow decreased at 70% and 100% RCA, thus indicating a lower passing ability. The reasons are the same as discussed in the case of slump flow (section 4.1.1). The higher replacement of NCA by RCA made the concrete harsh and increased the blocking tendency of SCC mix. At a higher content, the rough surface texture and angularity of RCA also became predominant to reduce the passing ability of SCC due to increased friction.

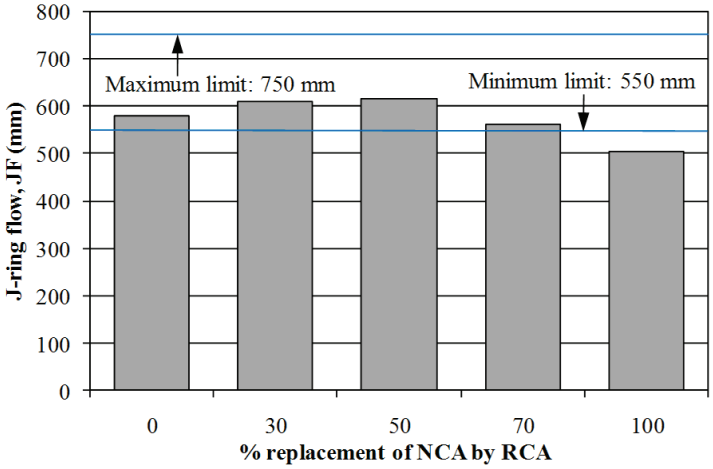

Fig. 6. Effect of RCA on the J-ring flow of concrete
(limits shown are based on slump flow limits and maximum blocking index)

However, no significant blockage was observed for 70% and 100% RCA although their filling ability was relatively low. It can be seen from Table 3 that the blocking index for the SCC mixes with 70% and 100% RCA was ≤50 mm (maximum limit). This is mainly credited to the reduced content of post-mixing coarse aggregate (see Table 4). The reduction in coarse aggregate content with a subsequent increase in fine aggregate quantity contributed to avoid any substantial blockage.

4.3. Segregation resistance

4.3.1. Segregation index

The segregation indices of various SCC mixes are given in Table 3. The recommended maximum limit for segregation index is 18% [20]. In the present study, the segregation index varied in the range of 8.3–11.2%. Hence, all SCC mixes had reasonably good segregation resistance according to the results of the Japanese sieve stability test.

The effect of RCA on the segregation index is apparent from Figure 7. The SCC mixes with 30% and 50% RCA provided a higher segregation index than the control concrete (CR0). The segregation index of control concrete was 9.8% whereas that of the SCC mixes with 30% and 50% RCA was 10.9% and 11.2%, respectively. Hence, these

two SCC mixes had relatively low segregation resistance. This is due to the less cohesive nature of these two RCA concretes at lower aggregate content (refer to Table 4).

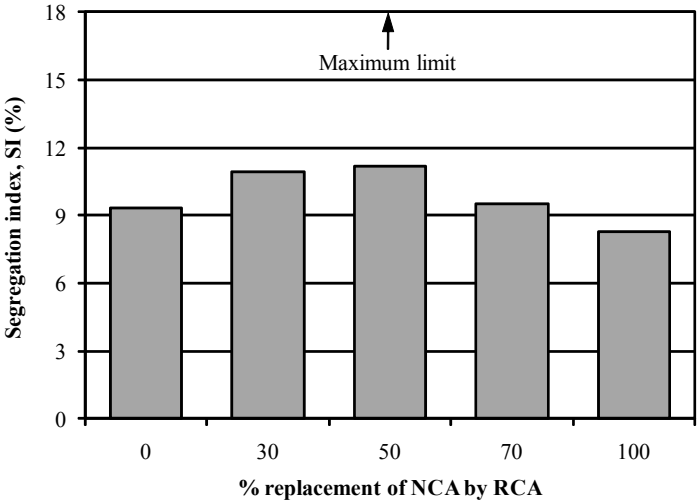

Fig. 7. Effect of RCA on the segregation index of concrete

The slump flow, T_{50} slump flow time, and V-funnel flow time results suggest that the SCC mixes with 30% and 50% RCA possessed a lower cohesiveness than the control concrete. A less cohesive concrete mix gives a higher slump flow but a lower flow time. A decrease in the cohesiveness increases the separation of mortar, thus resulting in a higher value of segregation index. However, the segregation index was reduced at 70% and 100% RCA. This is because the greater fine aggregate content (see Table 4) increased the cohesiveness of SCC mix at lower free water content. In addition, the increased angularity and surface roughness at a higher RCA content contributed to increase the cohesiveness, thus leading to a reduced segregation index.

4.3.2. Segregation ratio

The segregation ratios of various SCC mixes are given in Table 3. The segregation ratio varied in the range of 11.7–24.2%. The recommended maximum limit for segregation ratio is 15% [13]. Thus, the SCC mixes with 70% and 100% RCA did not exhibit an acceptable segregation resistance, which is in contrast with the segregation index results.

The effect of RCA on the segregation ratio is clear from Figure 8. A reasonably good segregation resistance was noticed for the SCC mixes with 0%, 30% and 50% RCA, which provided a segregation ratio ≤15%. In contrast, the SCC mixes with 70% and 100% RCA gave a segregation ratio significantly higher than 15%. These two concrete mixes had relatively low fluidity (see Table 3) and reduced coarse aggregate content (refer to Table 4), which generally contribute to decrease the degree of segregation in SCC. How-

ever, the uniform distribution of coarse aggregates along the height of column apparatus can be hindered due to aggregate collisions and adverse physical characteristics of RCA when the fluidity is significantly low. As a result, the heterogeneity along the depth of concrete might occur during placement, thus leading to a higher value of segregation ratio.

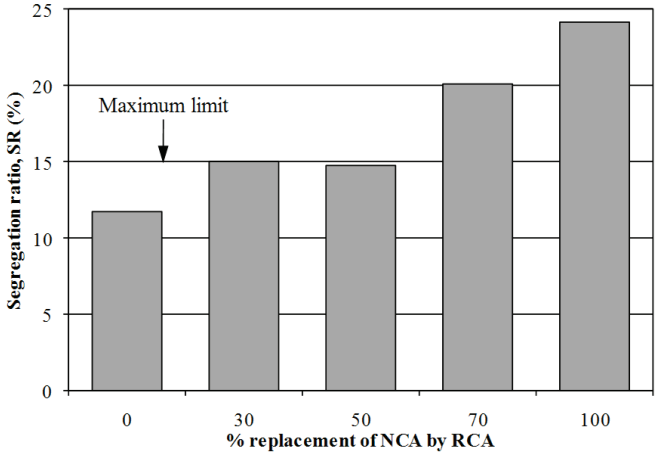

Fig. 8. Effect of RCA on the segregation ratio of concrete

4.4. Correlation between J-ring flow and slump flow

The slump flow and J-ring flow were determined as a measure of filling ability and passing ability, respectively. The relationship between the slump flow and J-ring flow results of concrete is shown in Figure 9.

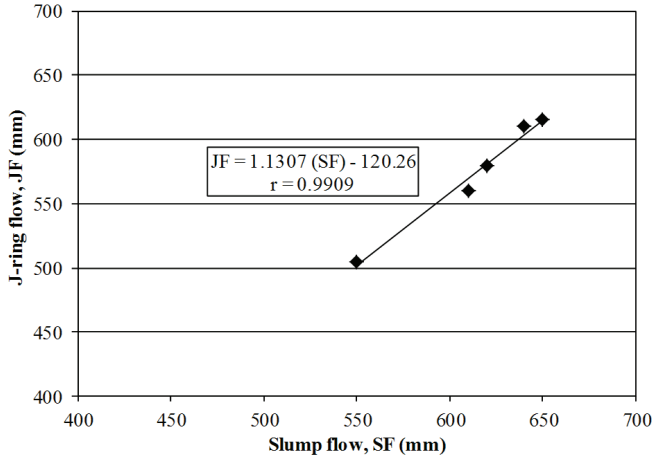

Fig. 9. Correlation between J-ring flow and slump flow of concrete

It is evident from Figure 9 that the J-ring flow and slump flow of the SCC mixes were strongly correlated with a linear relationship. The correlation coefficient is 0.9909, which points to a strong relationship. The strong correlation was observed since both slump flow and J-ring flow varied similarly with the RCA content. It was also understood from such strong correlation that the filling ability and passing ability of SCC are interrelated. Therefore, it is possible to predict the passing ability of SCC based on the result of a filling ability test.

4.5. Correlation between V-funnel flow time and T_{50} slump flow time

The relationship between T_{50} slump flow time and V-funnel flow time results is shown in Figure 10. It is obvious from Figure 10 that the V-funnel flow time and T_{50} slump flow time of the SCC mixes were strongly correlated with a linear relationship.

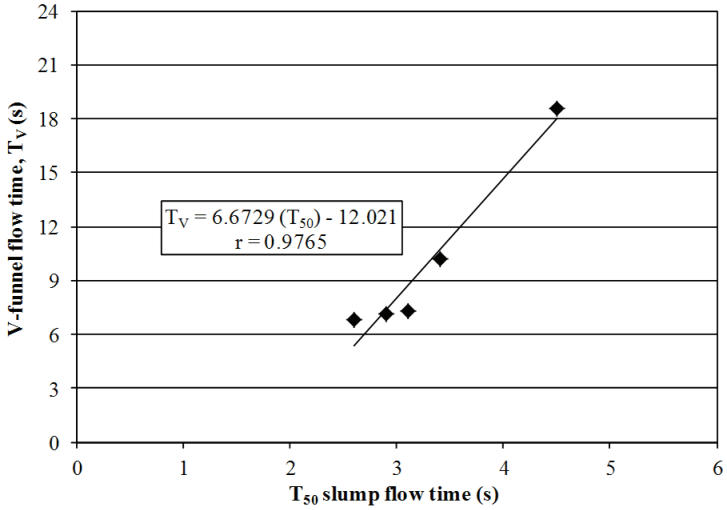

Fig. 10. Correlation between V-funnel flow time and T_{50} slump flow time of concrete

The correlation coefficient was 0.9765, which suggests a strong relationship. The strong correlation was noticed because both T_{50} slump flow time and V-funnel flow time varied with the RCA content in a similar way. Such strong correlation implies that either T_{50} slump flow or V-funnel flow test is adequate to assess the relative viscosity and cohesiveness of SCC.

4.6. Correlation between segregation index and slump flow

The relationship between slump flow and segregation index is shown in Figure 11. It is clear from Figure 11 that the segregation index and slump flow of the SCC mixes were strongly correlated with a linear relationship.

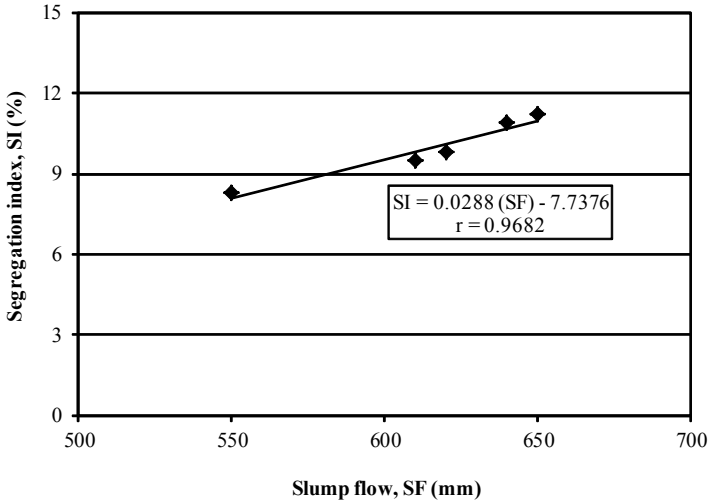

Fig. 11. Correlation between segregation index and slump flow of concrete

The correlation coefficient was 0.9682, which indicates a strong relationship. The strong correlation was obtained since both slump flow and segregation index varied identically with the RCA content. Such strong correlation also suggests that slump flow can give an indication for the segregation resistance of SCC.

5. Conclusions

The following salient conclusions can be drawn based on findings of the present study:

1) The filling ability of SCC was improved at 30% and 50% RCA mainly due to reduced coarse aggregate content and relatively high paste volume per unit aggregate content. In contrast, the filling ability was reduced at a RCA content higher than 50%. Particularly, a significant reduction in filling ability was observed for 100% RCA because of the increased amount of post-mixing fine aggregate.

2) The passing ability was satisfactory for all SCC mixes. A slight increase in passing ability occurred at 30% and 50% RCA due to lower coarse aggregate content. The passing ability at 70% and 100% RCA was within the recommended maximum limit although the filling ability was relatively low. This is credited to the reduction in coarse aggregate content with a subsequent increase in the quantity of fine aggregate.

3) The SCC mixes with a RCA content higher than 50% were more viscous as indicated by the T_{50} slump flow time and V-funnel flow time results. In particular, the high viscous nature of the SCC mix with 100% RCA was not conducive to obtain a continuous concrete flow during the V-funnel flow test. The flow was intermittent and therefore the concrete mix required a relatively long time to flow out of the V-funnel.

4) All SCC mixes had good segregation resistance, as noticed from the results of the Japanese sieve stability test. The segregation indices of concretes obtained

from this test were significantly below the recommended maximum limit (18%). However, this finding was not in agreement with all segregation ratios obtained from the column segregation test. In particular, the segregation ratios of the SCC mixes with 70% and 100% RCA were significantly higher than the recommended maximum limit (15%) although they provided the lowest level of segregation index. The high values of segregation ratio at 70% and 100% RCA were obtained due to the significant non-uniform distribution of coarse aggregates that occurred during concrete placement mostly because of aggregate collisions at relatively low fluidity.

5) The physical characteristics of RCA such as surface roughness, angularity, and surface porosity were not conducive to improve the fresh properties of SCC. These physical properties can act adversely to decrease the filling ability and passing ability of SCC at a higher content of RCA. Also, these properties may contribute to cause non-uniform distribution of coarse aggregates, thus developing the heterogeneity leading to segregation in concrete, particularly at a higher RCA content.

6) Strong correlations were observed between J-ring flow and slump flow, V-funnel flow time and T_{50} slump flow time, and segregation index and slump flow due to their similar variations with the RCA content.

7) The overall test results showed that RCA can be used in SCC as a replacement of NCA up to 50% by weight without affecting the key fresh properties such as filling ability, passing ability and segregation resistance of concrete.

Acknowledgement

The authors gratefully acknowledge the financial support through the research grant (RG 050-09AET) from the University of Malaya, Kuala Lumpur, Malaysia.

References

[1] ASTM C 33: *Standard specification for concrete aggregates*, Annual Book of ASTM Standards, American Society for Testing and Materials, Philadelphia, USA, 2009.

[2] ASTM C 1610/C 1610M: *Standard test method for static segregation of self-consolidating concrete using column technique*, Annual Book of ASTM Standards, American Society for Testing and Materials, Philadelphia, USA, 2009.

[3] ASTM C 1611/C 1611M: *Standard test method for slump flow of self-consolidating concrete*, Annual Book of ASTM Standards, American Society for Testing and Materials, Philadelphia, USA, 2009.

[4] Brameshuber W., Uebachs S.: *Practical experience with the application of self-compacting concrete in Germany*, Proceedings of the Second International Symposium on Self-Compacting Concrete, COMS Engineering Corporation, Tokyo, Japan, 2001, pp. 687–695.

[5] DoE: *Design of normal concrete mixes*, Department of Environment (DOE), The Building Research and Establishment (BRE) Publication, Watford, UK, 1975.

[6] EFNARC: *Specifications and guidelines for self-consolidating concrete*, European Federation of Supplies of Specialist Construction Chemicals (EFNARC), Surrey, UK, 2002.
[7] Felekoglu B., Türkel S., Baradan B.: *Effect of water/cement ratio on the fresh and hardened properties of self-compacting concrete*, Building and Environment, Vol. 42, No. 4, 2007, pp. 1795–1802.
[8] Grdic Z.J., Toplicic-Curcic G.A., Despotovic I.M., Ristic N.S.: *Properties of self-compacting concrete prepared with coarse recycled concrete aggregate*, Construction and Building Materials, Vol. 24, No. 7, 2010, pp. 1129–1133.
[9] Hendriks C.F., Pieterson H.S.: *Concrete: durable but also sustainable*, Proceedings of the International Conference on the Use of Recycled Concrete Aggregates, Thomas Telford, London, UK, 1998, pp. 1–18.
[10] Katz A.: *Properties of concrete made with recycled aggregate from partially hydrated old concrete*, Cement and Concrete Research, Vol. 33, No. 5, 2003, pp. 703–711.
[11] Khayat K.H.: *Workability, testing, and performance of self-consolidating concrete*, ACI Materials Journal, Vol. 96, No. 3, 1999, pp. 346–353.
[12] Khayat K.H.: *Optimization and performance of air-entrained, self-consolidating concrete*, ACI Materials Journal, Vol. 97, No. 5, 2000, pp. 526–535.
[13] Koehler E.P., Fowler D.W.: *ICAR mixture proportioning procedure for self-consolidating concrete*, International Centre for Aggregates Research, University of Texas at Austin, Texas, USA, 2006.
[14] Kou S.C., Poon C.S.: *Properties of self-compacting concrete prepared with coarse and fine recycled concrete aggregates*, Cement and Concrete Composites, Vol. 31, No. 9, 2009, pp. 622–627.
[15] Levy S.M., Helene P.: *Durability of recycled aggregates concrete: a safe way to sustainable development*, Cement and Concrete Research, Vol. 34, No. 11, 2004, pp. 1975–1980.
[16] Nagataki S., Fujiwara H.: *Self-compacting property of highly flowable concrete*, Proceedings of the Second CANMET/ACI International Symposium on Advances in Concrete Technology, American Concrete Institute, Farmingham Hills, Michigan, USA, 1995, pp. 301–314.
[17] Okamura H., Ouchi M.: *Self-compacting concrete-development, present and future*, Proceedings of the First International RILEM symposium on Self-Compacting Concrete, RILEM Publications, Bagneux, France, 1999, pp. 3–14.
[18] Okamura H., Ouchi M.: *Self-compacting concrete*, Journal of Advanced Concrete Technology, Vol. 1, No. 1, 2003, pp. 5–15.
[19] Ozawa K., Mackawa K., Okamura H.: *High performance concrete based on the durability design of concrete structures*, Proceedings of the Second East Asia Pacific Conference on Structural Engineering and Construction, Chiang-Mai, Thailand, 1989, pp. 445–450.
[20] Parez N., Romero H., Hermida G., Cuellar G.: *Self-compacting concrete, on the search and finding of an optimized design*, Proceedings of the First North American Conference on the Design and Use of Self-Consolidating Concrete, Hanley-Wood, LLC, Illinois, USA, 2002, pp. 101–107.
[21] Poon C., Kou S., Lam L.: *Influence of recycled aggregate on slump and bleeding of fresh concrete*, Materials and Structures, Vol. 40, No. 9, 2007, pp. 981–988.
[22] Portland Cement Association: *Recycled aggregate*, Concrete Technology, Available from http://www.cement.org /tech/cct_aggregates_recycled.asp, Access in May 13, 2010.

[23] Sagoe-Crentsil K.K., Brown T., Taylor A.H.: *Performance of concrete made with commercially produced coarse recycled concrete aggregate*, Cement and Concrete Research, Vol. 31, No. 5, 2001, pp. 707–712.
[24] Su N., Wang B.L.: *Study on the engineering properties of recycled aggregate concrete and recovered aggregate from demolished concrete*, Journal of the Chinese Institute of Civil and Hydraulic Engineering, Vol. 12, No. 3, 2000, pp. 435–444.
[25] Tang L.: *Evaluation of methods for testing fresh self-compacting concrete*, Proceedings of the First International Symposium on Design, Performance and Use of Self-Consolidating Concrete, Changsha, Hunan, China., 2005, pp. 245–252.
[26] Tu T.-Y., Chen Y.-Y., Hwang C.-L.: *Properties of HPC with recycled aggregates*, Cement and Concrete Research, Vol. 36, No. 5, 2006, pp. 943–950.
[27] Tu T.-Y., Jann Y.-Y., Hwang C.-L.: *The application of recycled aggregates in SCC*, Proceedings of the First International Symposium on Design, Performance and Use of Self-Consolidating Concrete, Changsha, Hunan, China, 2005, pp. 145–152.
[28] Zakaria M., Cabrera J.G.: *Performance and durability of concrete made with demolition waste and artificial fly ash-clay aggregates*, Waste Management, Vol. 16, No. 1–3, 1996, pp. 151–158.

Wpływ kruszywa uzyskanego z recyklingu betonu na właściwości świeżego betonu samozagęszczalnego

Odpady betonowa są dostarczane zazwyczaj na składowiska odpadów w celu utylizacji. Ze względu na rosnące koszty składowania, a zarazem niedostatek naturalnego kruszywa grubego (NCA), kruszywowa uzyskane z recyklingu betonu (RCA) i pochodzące z odpadów betonowych zyskuje coraz większe zainteresowanie w branży budowlanej. W niniejszej pracy analizowane jest wykorzystanie RCA w postaci częściowego jaki i pełnego zastąpienie kruszywa NCA do produkcji betonu samozagęszczalnego (SCC). W pracy przeanalizowano wpływ RCA na kluczowe właściwości świeżego betonu SCC. Ogólne wyniki badań wskazują, że RCA może być użyty do produkcji SCC przy zastąpieniu przez niego do 50% NCA bez wpływu na kluczowe właściwości świeżego betonu.

ARCHIVES OF CIVIL AND MECHANICAL ENGINEERING

Vol. XI 2011 No. 4

Analytic bending solutions of rectangular cantilever thin plates

B. TIAN
Department of Science and Technology, China Road and Bridge Corporation, Beijing 100011, PR China.

Y. ZHONG, R. LI
Faculty of Infrastructure Engineering, Dalian University of Technology,
Dalian 116024, Liaoning Province, PR China.

Analytic bending solutions of rectangular cantilever thin plates subjected to arbitrary loads are derived using the double finite integral transform method. Since only the basic governing equations of the plates are used and there are no predetermined functions, the present method overcomes the deficiency of the conventional semi-inverse methods thus serves as a completely rational model in solving plate bending problems. The method can be extended to more boundary value problems of plates such as buckling and vibration.

Keywords: *rectangular cantilever thin plate, bending solution, analytic solution*

1. Introduction

Rectangular thin plate is an important structural component used in various engineering applications such as bridge decks, rigid pavements of highways, traffic zones of airports and houses' decks. Therefore, bending analysis of rectangular thin plates has been one of important issues in theory and engineering. However, exact solutions for some of these problems are difficult to be obtained, such as for rectangular cantilever plates. One of the most commonly adopted numerical methods is the finite element method [13], which is actually an approximate solution method. As for analytical solution methods, the superposition method, firstly employed by Timoshenko and Woinowsky-Krieger [9], has yielded some exact series solutions such as for clamped plates. Using the superposition method involving generalized simply supported edge, Chang [1–3] gave the series solutions for the bending of both uniformly loaded and concentrated loaded rectangular cantilever thin plates, where complex calculation has to be performed and a new procedure be executed for every new loading case. It should be pointed out that the superposition method is semi-inverse which requires preselection of the deflection functions. In recent years, Zhong and Yao [11], Lim et al. [5], Yao et al. [10], Zhong et al. [12], Liu and Li [6] derived some solutions of plates by the symplectic geometry method, which, however, has not been directly applied to the problems with complex boundary conditions such as cantilever plate problem.

Integral transform is an important approach to obtain the explicit solutions to some partial differential Equations [7]. The method has been often adopted to analyze some structural engineering problems [8]. However, to the authors' knowledge, there have been no reports on the analysis for a rectangular cantilever thin plate using the finite integral transform.

In this paper, the double finite integral transform method is adopted to acquire exact bending solutions of rectangular cantilever thin plates under arbitrary loading, which is known as one of the most difficult problems in theory of elasticity for its complexity in both the governing equations and boundary conditions. The analysis is conducted rationally without any trial functions, which demonstrates the advantage of the present method over others.

2. The governing equation of a rectangular thin plate and the finite integral transform method

The governing equation for bending of a rectangular thin plate is

$$D\nabla^4 W(x,y) = q, \tag{1}$$

where: $\nabla^2 = \partial^2/\partial x^2 + \partial^2/\partial y^2$, $D = Eh^3/12(1-\nu^2)$ is the flexural rigidity, E, h, ν, are the elastic modulus, plate thickness and Poisson's ratio, respectively, $q(x, y)$ is the distributed transverse load acting on the surface of the plate, $W(x, y)$ is the transverse deflection.

The internal forces of the plate are

$$M_x = -D\left(\frac{\partial^2 W}{\partial x^2} + \nu\frac{\partial^2 W}{\partial y^2}\right);\ M_y = -D\left(\frac{\partial^2 W}{\partial y^2} + \nu\frac{\partial^2 W}{\partial x^2}\right);\ M_{xy} = -D(1-\nu)\frac{\partial^2 W}{\partial x \partial y}, \tag{2}$$

$$Q_x = -D\frac{\partial(\nabla^2 W)}{\partial x};\ Q_y = -D\frac{\partial(\nabla^2 W)}{\partial y}, \tag{3}$$

$$V_x = Q_x + \frac{\partial M_{xy}}{\partial y};\ V_y = Q_y + \frac{\partial M_{xy}}{\partial x}, \tag{4}$$

where:

D is the flexural rigidity,
M_x and M_y are the bending moments,
M_{xy} is the torsional moment,
Q_x and Q_y are the shear forces,
V_x and V_y are the effective shear forces.

The coordinate system of a rectangular cantilever plate is illustrated in Figure 1.

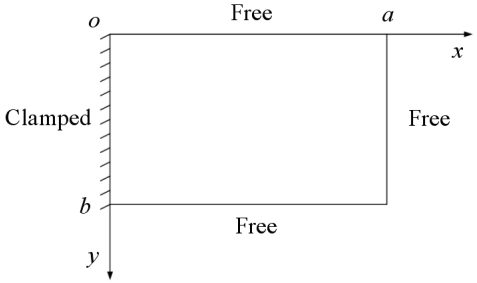

Fig. 1. Rectangular cantilever thin plate

The boundary conditions of the plate can be expressed as

$$W\big|_{x=0}=0; \quad \left.\frac{\partial W}{\partial x}\right|_{x=0}=0, \tag{5}$$

$$M_x\big|_{x=a}=-D\left(\frac{\partial^2 W}{\partial x^2}+\nu\frac{\partial^2 W}{\partial y^2}\right)\Bigg|_{x=a}=0; \quad M_y\big|_{y=0,b}=-D\left(\frac{\partial^2 W}{\partial y^2}+\nu\frac{\partial^2 W}{\partial x^2}\right)\Bigg|_{y=0,b}=0, \tag{6}$$

$$\begin{aligned} V_x\big|_{x=a}&=-D\frac{\partial}{\partial x}\left[\frac{\partial^2 W}{\partial x^2}+(2-\nu)\frac{\partial^2 W}{\partial y^2}\right]\Bigg|_{x=a}=0,\\ V_y\big|_{y=0,b}&=-D\frac{\partial}{\partial y}\left[\frac{\partial^2 W}{\partial y^2}+(2-\nu)\frac{\partial^2 W}{\partial x^2}\right]\Bigg|_{y=0,b}=0, \end{aligned} \tag{7}$$

$$M_{xy}\Big|_{\substack{x=a,y=0\\x=a,y=b}}=-2D(1-\nu)\left.\frac{\partial^2 W}{\partial x\partial y}\right|_{\substack{x=a,y=0\\x=a,y=b}}=0. \tag{8}$$

Based on the properties of the finite integral transforms and the boundary conditions of the cantilever plate, we define a double finite integral transform [7]

$$W_{mn}=\int_0^a\int_0^b W(x,y)\sin\frac{\alpha_m}{2}x\cos\beta_n y\,dxdy \quad (m=1,3,...;\ n=0,1,2,...). \tag{9}$$

The inverse transform can be represented as

$$W(x,y)=\frac{2}{ab}\sum_{m=1,3\cdots}^{\infty}W_{m0}\sin\frac{\alpha_m}{2}x+\frac{4}{ab}\sum_{m=1,3\cdots}^{\infty}\sum_{n=1,2\cdots}^{\infty}W_{mn}\sin\frac{\alpha_m}{2}x\cos\beta_n y, \tag{10}$$

where $\alpha_m = m\pi/a$, $\beta_n = n\pi/b$, a and b denote the length and width of the plate respectively.

The double integral transforms of higher-order partial derivatives of W used in this paper are derived as follows:

$$\int_0^a\int_0^b \frac{\partial^4 W}{\partial x^4}\sin\frac{\alpha_m}{2}x\cos\beta_n y dxdy = \int_0^b\left[(-1)^{\frac{m-1}{2}}\frac{\partial^3 W}{\partial x^3}\bigg|_{x=a} + \frac{\alpha_m}{2}\frac{\partial^2 W}{\partial x^2}\bigg|_{x=0} - (-1)^{\frac{m-1}{2}}\frac{\alpha_m^2}{4}\frac{\partial W}{\partial x}\bigg|_{x=a} - \frac{\alpha_m^3}{8}W\big|_{x=0}\right]\cos\beta_n y dy + \frac{\alpha_m^4}{16}W_{mn}, \tag{11}$$

$$\int_0^a\int_0^b \frac{\partial^4 W}{\partial y^4}\sin\frac{\alpha_m}{2}x\sin\beta_n y dxdy = \int_0^a\left[(-1)^n\frac{\partial^3 W}{\partial y^3}\bigg|_{y=b} - \frac{\partial^3 W}{\partial y^3}\bigg|_{y=0} - (-1)^n\beta_n^2\frac{\partial W}{\partial y}\bigg|_{y=b} + \beta_n^2\frac{\partial W}{\partial y}\bigg|_{y=0}\right]\sin\frac{\alpha_m}{2}x dx + \beta_n^4 W_{mn}, \tag{12}$$

$$\int_0^a\int_0^b \frac{\partial^4 W}{\partial x^2\partial y^2}\sin\frac{\alpha_m}{2}x\cos\beta_n y dxdy = \int_0^a\left[\frac{\alpha_m^2}{4}\frac{\partial W}{\partial y}\bigg|_{y=0} - (-1)^n\frac{\alpha_m^2}{4}\frac{\partial W}{\partial y}\bigg|_{y=b}\right]\sin\frac{\alpha_m}{2}x dx - \int_0^b\left[(-1)^{\frac{m-1}{2}}\beta_n^2\frac{\partial W}{\partial x}\bigg|_{x=a} + \frac{\alpha_m}{2}\beta_n^2 W\big|_{x=0}\right]\cos\beta_n y dy + \frac{\alpha_m^2}{4}\beta_n^2 W_{mn} + (-1)^{\frac{m-1}{2}+n}\frac{\partial^2 W}{\partial x\partial y}\bigg|_{x=a,y=b} - (-1)^{\frac{m-1}{2}}\frac{\partial^2 W}{\partial x\partial y}\bigg|_{x=a,y=0} + (-1)^n\frac{\alpha_m}{2}\frac{\partial W}{\partial y}\bigg|_{x=0,y=b} - \frac{\alpha_m}{2}\frac{\partial W}{\partial y}\bigg|_{x=0,y=0}. \tag{13}$$

By performing over Equation (1) the double finite integral transform and the substitution of Equations (11–13), we have

$$\int_0^b\left[(-1)^{\frac{m-1}{2}}\frac{\partial^3 W}{\partial x^3}\bigg|_{x=a} + \frac{\alpha_m}{2}\frac{\partial^2 W}{\partial x^2}\bigg|_{x=0} - (-1)^{\frac{m-1}{2}}\left(\frac{\alpha_m^2}{4}+2\beta_n^2\right)\frac{\partial W}{\partial x}\bigg|_{x=a} - \left(\frac{\alpha_m^3}{8}+\alpha_m\beta_n^2\right)W\big|_{x=0}\right]\cos\beta_n y dy + \int_0^a\left[(-1)^n\frac{\partial^3 W}{\partial y^3}\bigg|_{y=b} - \frac{\partial^3 W}{\partial y^3}\bigg|_{y=0} - (-1)^n\left(\frac{\alpha_m^2}{2}+\beta_n^2\right)\frac{\partial W}{\partial y}\bigg|_{y=b} + \left(\frac{\alpha_m^2}{2}+\beta_n^2\right)\frac{\partial W}{\partial y}\bigg|_{y=0}\right]\sin\frac{\alpha_m}{2}x dx + 2(-1)^{\frac{m-1}{2}+n}\frac{\partial^2 W}{\partial x\partial y}\bigg|_{x=a,y=b} - 2(-1)^{\frac{m-1}{2}}\frac{\partial^2 W}{\partial x\partial y}\bigg|_{x=a,y=0} + (-1)^n\alpha_m\frac{\partial W}{\partial y}\bigg|_{x=0,y=b} - \alpha_m\frac{\partial W}{\partial y}\bigg|_{x=0,y=0} + \left(\frac{\alpha_m^2}{4}+\beta_n^2\right)^2 W_{mn} = \frac{q_{mn}}{D}, \tag{14}$$

where $q_{mn}=\int_0^a\int_0^b q(x,y)\sin\frac{\alpha_m}{2}x\cos\beta_n y dxdy$ represents the double integral transform of the load function $q(x, y)$.

After the single finite cosine and sine transforms over two formulas in Equation (7) respectively, we obtain

$$\left.\frac{\partial^3 W}{\partial x^3}\right|_{x=a}=(2-\nu)\beta_n^2\left.\frac{\partial W}{\partial x}\right|_{x=a};\quad \left.\frac{\partial^3 W}{\partial y^3}\right|_{\substack{y=0\\y=b}}=(2-\nu)\frac{\alpha_m^2}{4}\left.\frac{\partial W}{\partial y}\right|_{\substack{y=0\\y=b}}. \tag{15}$$

Substituting Equations (8), (15) and the first formula of Equation (5) into Equation (14) gives

$$\begin{aligned}&\left(\frac{\alpha_m^2}{4}+\beta_n^2\right)^2 W_{mn}-\int_0^b\left[(-1)^{\frac{m-1}{2}}\left(\frac{\alpha_m^2}{4}+\nu\beta_n^2\right)\left.\frac{\partial W}{\partial x}\right|_{x=a}-\frac{\alpha_m}{2}\left.\frac{\partial^2 W}{\partial x^2}\right|_{x=0}\right]\cos\beta_n y dy-\\&-\left(\nu\frac{\alpha_m^2}{4}+\beta_n^2\right)\int_0^a\left[(-1)^n\left.\frac{\partial W}{\partial y}\right|_{y=b}-\left.\frac{\partial W}{\partial y}\right|_{y=0}\right]\sin\frac{\alpha_m}{2}x dx=\frac{q_{mn}}{D}.\end{aligned} \tag{16}$$

Let

$$\begin{aligned}&I_m=\int_0^a\left.\frac{\partial W}{\partial y}\right|_{y=b}\sin\frac{\alpha_m}{2}x dx;\ J_m=\int_0^a\left.\frac{\partial W}{\partial y}\right|_{y=0}\sin\frac{\alpha_m}{2}x dx;\\&K_n=\int_0^b\left.\frac{\partial W}{\partial x}\right|_{x=a}\cos\beta_n y dy;\ L_n=\int_0^b\left.\frac{\partial^2 W}{\partial x^2}\right|_{x=0}\cos\beta_n y dy.\end{aligned} \tag{17}$$

Accordingly Equation (16) is expressed in terms of unknown constants I_m, J_m, K_n, and L_n as

$$W_{mn}=C_{mn}\left[\frac{q_{mn}}{D}+(-1)^n R_{mn}I_m-R_{mn}J_m+(-1)^{\frac{m-1}{2}}T_{mn}K_n-\frac{\alpha_m}{2}L_n\right], \tag{18}$$

where $C_{mn}=1\Big/\left(\alpha_m^2/4+\beta_n^2\right)^2$, $R_{mn}=\nu\frac{\alpha_m^2}{4}+\beta_n^2$ and $T_{mn}=\frac{\alpha_m^2}{4}+\nu\beta_n^2$.

Substitution of Equation (18) in Equation (10) gives the expression of W in terms of I_m, J_m, K_n, and L_n for $m = 1, 3,\ldots$ and $n = 0, 1, 2,\ldots$, i.e.

$$W(x,y)=\frac{2}{ab}\sum_{m=1,3\cdots}^{\infty}C_{m0}\left[\frac{q_{m0}}{D}+R_{m0}I_m-R_{m0}J_m+(-1)^{\frac{m-1}{2}}T_{m0}K_0-\frac{\alpha_m}{2}L_0\right]\sin\frac{\alpha_m}{2}x+$$
$$+\frac{4}{ab}\sum_{m=1,3\cdots}^{\infty}\sum_{n=1,2\cdots}^{\infty}C_{mn}\left\{\frac{q_{mn}}{D}+(-1)^n R_{mn}I_m-R_{mn}J_m+(-1)^{\frac{m-1}{2}}T_{mn}K_n-\frac{\alpha_m}{2}L_n\right\} \tag{19}$$
$$\sin\frac{\alpha_m}{2}x\cos\beta_n y.$$

When M and N terms are taken for m and n, we have $2[M/2]+2(N+1)$ undetermined coefficients where $[M/2]$ denotes the integer part of $M/2$.

As mentioned above, Equation (19) can meet the boundary conditions described by Equations (7), (8) and the first formula of Equation (5).

It can be seen that I_m, J_m and K_n in Equation (17) are the coefficients of the series describing the slopes of the free edges. Observing

$$\int_0^b\left.\frac{\partial^2 W}{\partial y^2}\right|_{x=0}\cos\beta_n y dy=$$
$$\left(\left.\frac{\partial W}{\partial y}\right|_{x=0}\cos\beta_n y\right)\Bigg|_0^b+\beta_n\left[\left(W|_{x=0}\sin\beta_n y\right)\Big|_0^a-\beta_n\int_0^a W|_{x=0}\cos\beta_n y dy\right]=0, \tag{20}$$

the 4th formula of Equation (17) is rewritten as $L_n=\int_0^b\left.\left(\frac{\partial^2 W}{\partial x^2}+\nu\frac{\partial^2 W}{\partial y^2}\right)\right|_{x=0}\cos\beta_n y dy$.

It is obvious that $-DL_n$ is the coefficient of the series describing the bending moment of the clamped edge. Therefore, the slopes of the free edges and the bending moment of the clamped edge are represented as

$$\left.\frac{\partial W}{\partial y}\right|_{y=b}=\frac{2}{a}\sum_{m=1,3\cdots}^{\infty}I_m\sin\frac{\alpha_m}{2}x;\qquad\left.\frac{\partial W}{\partial y}\right|_{y=0}=\frac{2}{a}\sum_{m=1,3\cdots}^{\infty}J_m\sin\frac{\alpha_m}{2}x$$
$$\left.\frac{\partial W}{\partial x}\right|_{x=a}=\frac{1}{b}K_0+\frac{2}{b}\sum_{n=1}^{\infty}K_n\cos\beta_n y;\quad M_x|_{x=0}=-D\left(\frac{1}{b}L_0+\frac{2}{b}\sum_{n=1}^{\infty}L_n\cos\beta_n y\right). \tag{21}$$

In quest of the solutions of I_m, J_m, K_n, and L_n substituting Equation (10) into the remaining boundary conditions represented by Equation (6) and the second formula of Equation (5), considering the differentiation procedure of trigonometric series [4], we obtain

$$
\begin{aligned}
&\sum_{m=1,3}^{\infty} \alpha_m W_{mn} = 0 \quad (n = 0, 1, 2\cdots),\\
&\sum_{m=1,3}^{\infty} (-1)^{\frac{m-1}{2}} \left\{ \nu (-1)^n I_m - \nu J_m + (-1)^{\frac{m-1}{2}} K_n - T_{mn} W_{mn} \right\} = 0 \quad (n = 0, 1, 2\cdots),\\
&I_m - J_m + (-1)^{\frac{m-1}{2}} \nu K_0 - R_{m0} W_{m0} +\\
&+2 \sum_{n=1,2}^{\infty} \left\{ (-1)^n I_m - J_m + (-1)^{\frac{m-1}{2}} \nu K_n - R_{mn} W_{mn} \right\} = 0 \quad (m = 1, 3\cdots),\\
&I_m - J_m + (-1)^{\frac{m-1}{2}} \nu K_0 - R_{m0} W_{m0} +\\
&+2 \sum_{n=1,2}^{\infty} (-1)^n \left[(-1)^n I_m - J_m + (-1)^{\frac{m-1}{2}} \nu K_n - R_{mn} W_{mn} \right] = 0 \quad (m = 1, 3\cdots).
\end{aligned}
\tag{22}
$$

Substituting Equation (18) into Equation (22), we finally obtain

$$
\begin{aligned}
&\sum_{m=1,3}^{\infty} (-1)^n \alpha_m C_{mn} R_{mn} I_m - \sum_{m=1,3}^{\infty} \alpha_m C_{mn} R_{mn} J_m + \sum_{m=1,3}^{\infty} (-1)^{\frac{m-1}{2}} \alpha_m C_{mn} T_{mn} K_n -\\
&-\frac{1}{2} \sum_{m=1,3}^{\infty} \alpha_m^2 C_{mn} L_n = -\frac{1}{D} \sum_{m=1,3}^{\infty} \alpha_m C_{mn} q_{mn} \quad (n = 0, 1, 2\cdots),
\end{aligned}
\tag{23}
$$

$$
\begin{aligned}
&\sum_{m=1,3}^{\infty} (-1)^{n+\frac{m-1}{2}} (\nu - C_{mn} R_{mn} T_{mn}) I_m - \sum_{m=1,3}^{\infty} (-1)^{\frac{m-1}{2}} (\nu - C_{mn} R_{mn} T_{mn}) J_m +\\
&+ \sum_{m=1,3}^{\infty} (-1)^{m-1} (1 - C_{mn} T_{mn}^2) K_n + \frac{1}{2} \sum_{m=1,3}^{\infty} (-1)^{\frac{m-1}{2}} \alpha_m C_{mn} T_{mn} L_n =\\
&= \frac{1}{D} \sum_{m=1,3}^{\infty} (-1)^{\frac{m-1}{2}} C_{mn} T_{mn}\, q_{mn} \quad (n = 0, 1, 2\cdots),
\end{aligned}
\tag{24}
$$

$$
\begin{aligned}
&\left[1 - \nu^2 + 2 \sum_{n=1}^{\infty} (-1)^n (1 - C_{mn} R_{mn}^2) \right] I_m - \left[1 - \nu^2 + 2 \sum_{n=1}^{\infty} (1 - C_{mn} R_{mn}^2) \right] J_m +\\
&+2 \sum_{n=1}^{\infty} (-1)^{\frac{m-1}{2}} (\nu - C_{mn} R_{mn} T_{mn}) K_n + \frac{2\nu}{\alpha_m} L_0 + \sum_{n=1}^{\infty} \alpha_m C_{mn} R_{mn} L_n =\\
&= \frac{4\nu}{D\alpha_m^2} q_{m0} + \frac{2}{D} \sum_{n=1}^{\infty} C_{mn} R_{mn}\, q_{mn} \quad (m = 1, 3\cdots),
\end{aligned}
\tag{25}
$$

Equations (23–26) are four infinite systems of linear simultaneous equations with unknowns I_m, J_m, K_n, and L_n (m = 1, 3, ...; n = 0, 1, 2, ...). When the first M and N terms

are taken for m and n respectively, we have $2[M/2] + 2(N + 1)$ equations and unknowns, which can be readily solved. Substituting the resultant I_m, J_m, K_n, and L_n into Equation (19) gives exact bending solutions of a rectangular cantilever thin plate.

$$\left[1-\nu^2+2\sum_{n=1}^{\infty}\left(1-C_{mn}R_{mn}^2\right)\right]I_m-\left[1-\nu^2+2\sum_{n=1}^{\infty}(-1)^n\left(1-C_{mn}R_{mn}^2\right)\right]J_m+$$
$$+2\sum_{n=1}^{\infty}(-1)^{n+\frac{m-1}{2}}\left(\nu-C_{mn}R_{mn}T_{mn}\right)K_n+\frac{2\nu}{\alpha_m}L_0+\sum_{n=1}^{\infty}(-1)^n\alpha_m C_{mn}R_{mn}L_n= \tag{26}$$
$$=\frac{4\nu}{D\alpha_m^2}q_{m0}+\frac{2}{D}\sum_{n=1}^{\infty}(-1)^n C_{mn}R_{mn}q_{mn}\quad (m=1,3\cdots).$$

3. Numerical examples

In order to verify the validity of the results derived in the paper, we took some cases in References [1] and [3] as examples. The transverse deflections and bending moments at specific locations for a square cantilever thin plate under a uniform load or a concentrated load at (a, 0.75b) with $\nu = 0.3$ are obtained. The first 50 terms of I_m and J_m and the first 100 terms of K_n and L_n are taken to ensure sufficient accuracy. For simplicity three significant figures are retained for the data in the tables.

It can be seen from Tables 1–4 that the agreement between the present results and those from the literature is satisfactory. The method developed in this paper is suitable for the problems of rectangular cantilever thin plates under arbitrary loads.

Table 1. Deflections W (qa^4/D) of the free edges $y = 0$ and $y = b$ for a square plate under uniform loading

W	$x = 0$		$x = 0.25a$		$x = 0.5a$		$x = 0.75a$		$x = a$	
	Ref. [1]	Present	Ref. [1]	Present	Ref. [1]	Present	Ref. [1]	Present	Ref. [1]	Present
$y = 0$	0	0	0.0119	0.0117	0.0443	0.0433	0.0850	0.0841	0.129	0.127
$y = b$	0	0	0.0119	0.0117	0.0443	0.0433	0.0850	0.0841	0.129	0.127

Table 2. Deflections W (qa^4/D) of the free edge $x = a$ and bending moments M_x(qa^2) of the clamped edge $x = 0$ for a square plate under uniform loading

	$y = 0$		$y = 0.25b$		$y = 0.5b$		$y = 0.75b$		$y = b$	
	Ref. [1]	Present	Ref. [1]	Present	Ref. [1]	Present	Ref. [1]	Present	Ref. [1]	Present
W (a, y)	0.129	0.127	0.131	0.129	0.131	0.129	0.131	0.129	0.129	0.127
M_x (0, y)	0	0	χ0.534	χ0.530	χ0.536	χ0.531	χ0.534	χ0.530	0	0

Table 3. Deflections W (Pa^2/D) of the free edges $y = 0$ and $y = b$ for a square plate under a concentrated load at (a, 0.75b)

W	$x = 0$		$x = 0.25a$		$x = 0.5a$		$x = 0.75a$		$x = a$	
	Ref. [3]	Present	Ref. [3]	Present	Ref. [3]	Present	Ref. [3]	Present	Ref. [3]	Present
$y = 0$	0	0	0.0162	0.0157	0.075	0.0733	0.166	0.163	0.274	0.268
$y = b$	0	0	0.0319	0.0323	0.123	0.125	0.252	0.256	0.398	0.402

Table 4. Deflections W (Pa^2/D) of the free edge $x = a$ and bending moments $M_x(P)$ of the clamped edge $x = 0$ for a square plate under a concentrated load at (a, 0.75b)

	$y = 0$		$y = 0.25b$		$y = 0.5b$		$y = 0.75b$		$y = b$	
	Ref. [3]	Present	Ref. [3]	Present	Ref. [3]	Present	Ref. [3]	Present	Ref. [3]	Present
$W(a, y)$	0.274	0.268	0.309	0.305	0.348	0.346	0.385	0.386	0.398	0.402
$M_x(0, y)$	0	0	χ0.934	χ0.935	χ1.11	χ1.09	χ1.21	χ1.26	0	0

4. Conclusions

Analytic bending solutions of rectangular cantilever thin plates subjected to arbitrary loads are derived using the double finite integral transform method. The mathematical approach employed does not require the preselection of a deformation function, which can scarcely be avoided in the traditional semi-inverse approaches. Also, the present approach provides an efficient and unified procedure for accurate plate bending analysis. The method can be further extended to other boundary value problems in plate bending as well as buckling, vibration, etc.

Acknowledgments

This work was supported by the Fundamental Research Funds for the Central Universities of China (2010) and the Scholarship Award for Excellent Doctoral Student granted by the Ministry of Education of China (2010).

References

[1] Chang F.V.: *Bending of uniformly cantilever rectangular plates*, Applied Mathematics and Mechanics-English Edition, Vol. 1, 1980, pp. 371–383.
[2] Chang F.V.: *Bending of a cantilever rectangular plate loaded discontinuously*, Applied Mathematics and Mechanics-English Edition, Vol. 2, 1981, pp. 403–410.
[3] Chang F.V.: *Elastic thin plates (2nd edition)* (in Chinese), Beijing, Science Press, 1984.
[4] Khalili M.R., Malekzadeh K., Mittal R.K.: *A new approach to static and dynamic analysis of composite plates with different boundary conditions*, Composite Structures, Vol. 69, 2005, pp. 149–155.
[5] Lim C.W., Cui S., Yao W.A.: *On new symplectic elasticity approach for exact bending solutions of rectangular thin plates with two opposite sides simply supported*, International Journal of Solids and Structures, Vol. 44, 2007, pp. 5396–5411.
[6] Liu, Y., Li, R.: *Accurate bending analysis of rectangular plates with two adjacent edges free and the others clamped or simply supported based on new symplectic approach*, Applied Mathematical Modelling, Vol. 34, 2010, pp. 856–865.
[7] Sneddon I.N.: *The use of integral transforms*, New York, McGraw-Hill Book Company, 1972.
[8] Sneddon I.N.: *Application of integral transforms in the theory of elasticity*, New York, McGraw-Hill Book Company, 1975.
[9] Timoshenko S., Woinowsky-Krieger S.: *Theory of plates and shells*, Auckland, McGraw-Hill Book Company, 1959.

[10] Yao W., Zhong W., Lim C.W.: *Symplectic elasticity*, Singapore, World Scientific, 2008.
[11] Zhong W.X., Yao W.A.: *New solution system for plate bending*, Computational Mechanics in Structural Engineering, Vol. 31, 1999, pp. 17–30.
[12] Zhong Y., Li R., Liu Y., Tian B.: *On new symplectic approach for exact bending solutions of moderately thick rectangular plates with two opposite edges simply supported*, International Journal of Solids and Structures, Vol. 46, 2009, pp. 2506–2513.
[13] Zienkiewicz O.C., Cheung Y.K.: *The finite element method for analysis of elastic isotropic and orthotropic slabs*, Proceedings-Institution of Civil Engineers, Vol. 28, 1964, pp. 471–488.

Rozwiązania analityczne zginanych, wspornikowych cienkich płyt prostokątnych

W pracy sformułowano analityczne rozwiązania dotyczące zginania prostokątnych, wspornikowych płyt cienkich poddanych dowolnym obciążeniom przy zastosowaniu metody podwójnej, skończonej transformaty całkowej. Ponieważ zastosowano tylko podstawowe równania płyt, zaprezentowana metoda przezwycięża niedobór konwencjonalnych metod semi-odwrotnych i może służyć jako całkowicie wymierny model przy rozwiązywaniu problemów zginania płyt. Zaprezentowana metoda może być rozszerzona na dalszą klasę problemów brzegowych płyt w zakresie ich wyboczenia oraz drgań.

ARCHIVES OF CIVIL AND MECHANICAL ENGINEERING

Vol. XI 2011 No. 4

Electrochemical polishing of total hip prostheses

S. ZABORSKI, A. SUDZIK
Wrocław University of Technology, Faculty of Mechanical Engineering, Łukasiewicza 7, 50-371 Wrocław, Poland.

A. WOŁYNIEC
SP ZOZ District Hospital in Oława, Poland.

Discusses the materials used for replacement. Suggests ways treatment heads prostheses of titanium alloy Ti6Al4V. Preliminary Operations performed on the implementation of heads CNC lathe Gildemeister CTX 400. The following operations are grinding, polishing, mechanical and electrochemical polishing. After electrochemical polishing roughness obtained approximately Ra = 0.05–0.15 μm. An increase participation of the carrier surface after electrochemical polishing by 25–30% compared to the surface after grinding. Also received a higher gloss of about 20% compared to the surface after mechanical polishing.

Keywords*: endoprosthesis, titanium alloys, electrochemical polishing*

1. Introduction

The continuous increase in the contemporary people's living standard and accelerated development of medical sciences result in a prolonged lifespan. However, the human living machine hasn't been designed for so long operation. Our sinews, joints, "pumps" and "hinges" are subject to wear. Moreover, the vertical posture of mankind, which developed as a result of evolution of our quadruped ancestors, has as the result a modified distribution of pressures exerted on vertebra and joints and causes the entire spine to become slightly curved. One of the main causes of advanced-age ailments is this vertical posture, which paradoxically made possible the development of civilization.

Fig. 1. Hip joint and its total replacement [2]

As a result of a person's movement, a considerable tension is exerted on his joints and spine. With advancing age, wear of joints sets in due to diminished synovial supply and increased joint load produced by incessant gravity action. This results in inflammatory conditions and, frequent in elderly people, the necessity of surgical intervention in the form of total hip joint replacement [1]. The hip joint is one of the most strained joints in humans. Its injury, either due to a pathological change or mechanical damage, is difficult to treat and limits, or even makes impossible, the affected person's moving ability. Total hip joint prostheses are being employed in medicine starting from the first half of 20th century. Figure 1 shows a healthy hip joint and a total hip joint replacement.

2. Materials employed in total hip joint prostheses

The chemical composition of hip joint replacements is determined by biological tolerance issues. Although some elements appear in human body in merely trace concentrations, their excess or deficiency can cause disorders of some functions of the organism. Materials used in medicine should be characterized by high biological tolerance and resistance to corrosion. Their physical and chemical properties should resemble those of living tissue, they can't exert poisonous and allergic influence on the organism and should remain neutral to tissue with chemical and immunological respects. Chemical elements present in implants cannot diffuse into the organism, i.e. due to corrosion. Originally, implants were manufactured from platinum-based alloys. Their main drawback was an extremely high price. At present, the most important metallic biomaterials are titanium and its alloys (Ti-6Al-4V, Ti-Al-Nb), titanium-nickel alloys Ti-Ni (nitinol), cobalt-based alloys (Co-Cr-Mo) and stainless steels [12, 8, 3]. Gold- and palladium-based alloys are also employed, dentistry being their main field of application. Examples of titanium alloys and their properties are shown in Table 1.

Table 1. Properties of selected titanium alloys

Alloy	R_m [MPa]	R_t [MPa]	A [%]	Z [%]	E [GPa]
Ti, sort 1	240	170	24	30	102.7
Ti, sort 2	345	275	20	30	102.7
Ti, sort 3	450	380	18	30	103.4
Ti, sort 4	550	485	15	25	104.1
Ti6Al4VELI	860–965	795–875	10–15	25–47	101–110
Ti6Al4Va	895–930	825–869	6–10	20–25	110–114
Ti6Al7Nb	900–1050	880–950	8–15	25–45	114

Apart from metallic materials mentioned above, ceramics, metal-glass materials, hydroxyapatite, carbon- and composite-materials are also used for the production of hip joint replacements [6, 4, 11, 7]. The research presented in this paper was focused on machining the heads of hip joint prostheses made of austenitic steel 316L, 304L

and titanium alloy Ti6A14V. For the purpose of investigation, a series of prosthesis heads were made from the materials mentioned. For the machining of heads employed in the investigation, a numerically controlled (CNC) lathe Gildemeister CTX 400 has been used. Figure 2 shows the prosthesis head clamped in a triple-jaw lathe clamp during turning.

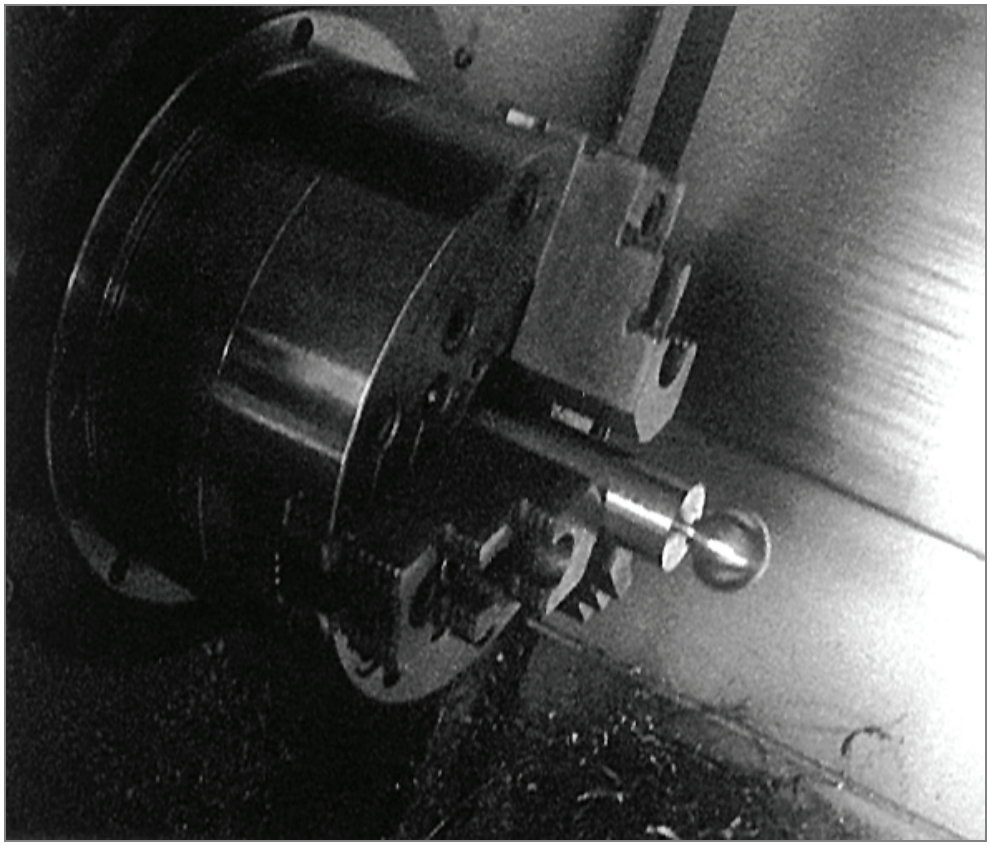

Fig. 2. Machining of hip joint prosthesis head

After turning, the work-piece was further processed by means of drilling and boring of the conical seat and grinding of its spherical surface. The prosthesis head thus processed is subjected to the finishing machining.

3. Finishing machining of the hip joint prosthesis head

After the completion of the machining phase of the spherical surface forming, the hip joint prosthesis heads are subjected to finishing grinding or to grinding and polishing.

A mesh of cracks remains after grinding that represents traces of abrasive machining. A few tens of peaks surpassing an average coarseness level by ca. 0.3 μm occurs on every 1 mm^2. Such a stereometric shaping of the surface influences unfavourably the carrying ratio and results in an increased friction coefficient at the head/bearing interface, causing accelerated wear of the prosthesis and thus extremely unfavourably affects its operating lifetime [5].

Machining of the spherical surface by means of grinding followed by polishing seems to be a more favourable solution for many reasons. Polishing the surface improves its corrosive resistance compared to surfaces subjected to grinding. Also coarseness parameters achieved as a result of polishing are much lower than those for grinding, which results in a decreased friction coefficient for interfacing surfaces. A surface subjected to polishing also reveals a higher carrying ratio compared to a surface that has been ground, which favourably affects the wear intensity of matching surfaces. In practice, two methods of polishing are employed – mechanical polishing and electrochemical polishing. Mechanical polishing does not require a complicated equipment, is however time- and labour-consuming. It consists in the application of a soft tool, e.g. felt disk and a polishing agent comprising abrasive micro-grains.

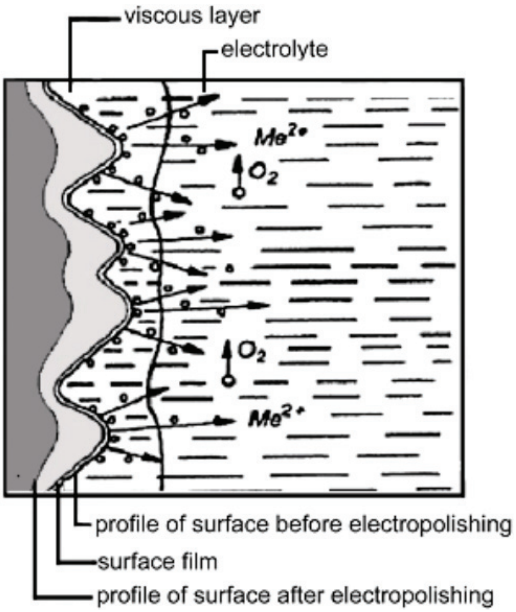

Fig. 3. Diagram of electrochemical polishing [9]

As a result of friction connected with the relative movement of the workpiece and tool, micro-cutting occurs accompanied by partial plastic deformation of micro-unevenness vertices. This is accompanied by emission of considerable quantities of heat

which can have an adverse effect on physical properties of the surface thus machined. Both cutting and emission of heat generate tensile stresses within the surface of the work-piece. Occasionally micro-cracks appear due to the stresses in the upper layer. Presence of stresses can result in decreased reliability during exploitation [9]. A properly polished metal surface exhibits increased corrosive resistance. Micro-cracks and increased stresses within the surface layer (SL) can constitute corrosion seeds or be the cause of e.g. stress corrosion.

Electrochemical polishing consists in the anodic dissolution of unevenness vertices due to electric current flow in a suitable electrolyte. The diagram of electrochemical polishing is shown in Figure 3 [14]. At the interface of work-piece surface and electrolyte, under the voltage applied, a viscous layer forms with electrical resistance considerably higher than that of electrolyte. This layer is the thinnest at the unevenness vertices and particularly at these places the most intensive dissolution of the material being polished occurs. This results in the smoothing of surface due to the reduction of the surface's coarseness. Electrochemical polishing is a technological process easy to automate and allowing simultaneously processing multiple work-pieces on the same workplace. Therefore, electrochemical polishing is preferred because of both economical reasons and properties of the surface obtained.

The process described herein allows obtaining minimal coarseness values and, additionally, does not introduce stresses which can generate micro-cracks, the latter being possible in mechanical polishing. Electrochemical polishing also diminishes stresses within the surface layer arising in the earlier process phases. For these reasons it is especially recommended for the machining of biological prostheses.

4. Investigation of electrochemical polishing process

Electrochemical polishing tests were carried out on an inhouse-designed workbench. A diagram of the workbench is shown in Figure 4. It is equipped with a controlled power supply capable of supplying voltage within the range of 0–100 V and current output up to 20 A. Additionally, the workbench can be equipped with a control module making it possible to obtain pulse currents with various characteristics. Parameters of electrical current characteristics and process duration are relied to the control module by means of a PC computer. Two graphite rods were used as auxiliary electrodes, located on both sides of the sphere being polished. Graphite electrodes don't dissolve in even the most aggressive electrolytes and therefore don't pollute the electrolyte with foreign substances.

Table 2. Samples composition of electrolyte for electrochemical polishing of steel

Pos.	H_2SO_4	H_3PO_4	Other
1	30%	65%	glycerine 5%
2	37%	60%	trietyloamine 3%
3	20–40%	44–80%	–

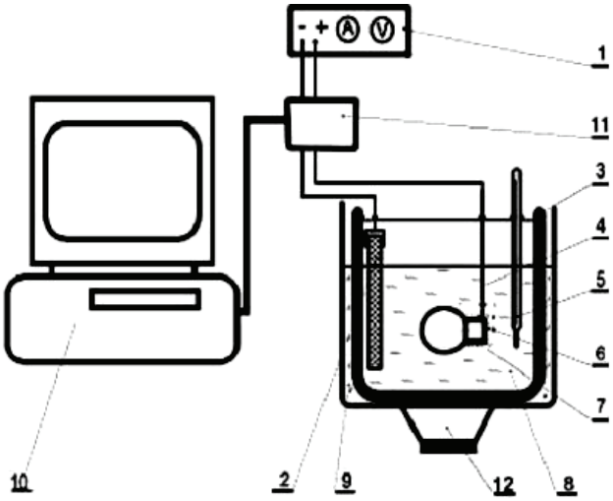

Fig. 4. Workbench for electrochemical polishing tests: 1 – power supply, 2 – cathode, 3 – electrolyte tank, 4 – conductor, 5 – thermometer; 6 – clamp, 7 – sample; 8 – electrolyte, 9 – water bath, 10 – PC computer, 11 – rely set, 12 – ultrasound generator [14]

Various electrolytes were tested for both the steel and titanium alloy. Samples of electrolyte composition are given in Tables 2 and 3.

Table 3. Samples composition of electrolyte for electrochemical polishing of titanium alloys

Pos.	HF	H_2SO_4	$HClO_4$	Other
1	10–18%	20–40%	–	CH_3COOH 42–62%
2	160 ml	–	–	CrO_3 500g, H_2O to 1 l
3	20–25%	60–65%	–	Glycerine 10–20%
4	30%	60%	–	Glycerine 10%
5	3–4%	–	–	Ethylene glycol to 100%

They were evaluated with respect to their effectiveness, simple process execution and problems related to the chemical composition. Electrolytes cited in the above tables using bold font were actually used in the polishing tests. In the case of electrolytes for the processing of stainless steels, no problems were encountered when performing the electrochemical polishing. Although electrolytes contain acids and troublesome chemical substances, they don't belong to the especially dangerous ones [10]. The majority of electrolytes for the polishing of titanium and titanium alloys contain however highly aggressive or toxic chemical compounds. These are, most commonly used in electrolytes, hydrofluoric acid, perchloric acid and chromium oxide (VI val.). Frequently the conditions required for the process to be carried out are difficult to obtain. Some of electrolytes require that the process is run at a negative temperature range or even at the temperature of dry ice, i.e. ca. –72 °C. Less troublesome electrolytes did not perform well in the tests.

5. Investigation results

Hip joint prosthesis heads, as they present themselves after the consecutive stages of machining, are shown in Figure 5, where: 1 – the head after turning, 2 – the head after grinding, 3 – the head after electrochemical polishing.

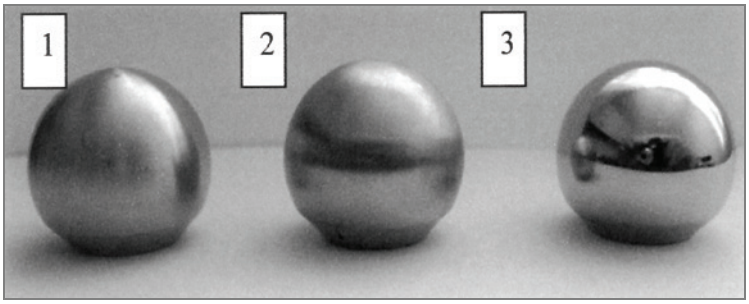

Fig. 5. Hip joint prosthesis heads after consecutive stages of machining

Investigation of the head polishing process did not include mechanical polishing because of its ubiquity, for the comparison purpose however measurements of a sample mechanically polished surface have been made. Figure 6 shows a microscopic image (mag. 100×) of Ti6Al4V titanium alloy surface polished mechanically using a felt disk and Cr_2O_3-based paste, while Figure 7 presents the profilograph of the surface.

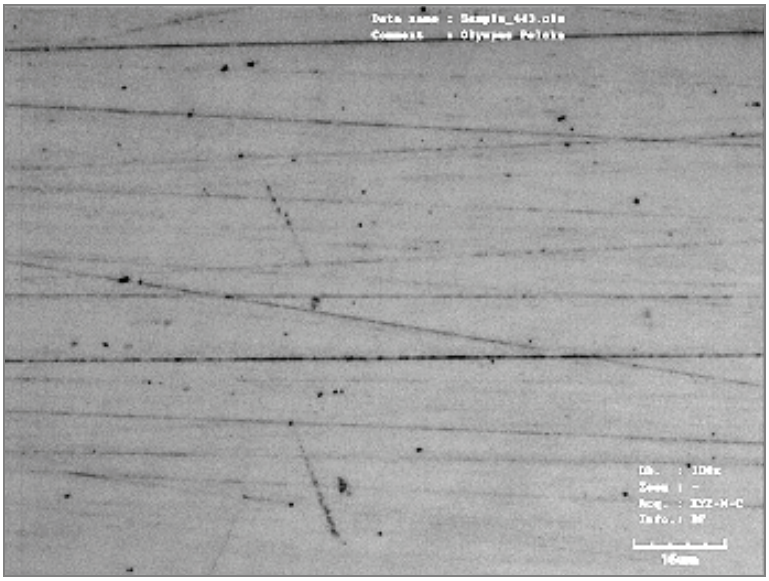

Fig. 6. Microscopic image of the surface of Ti6Al4V titanium alloy mechanically polished (mag. 100×)

The following Figures 8 and 9 depict the surface of the same alloy after electrochemical polishing [13]. Directional orientation of the surface structure can be clearly observed after mechanical polishing in the form of scratches consistent with the direction of machining. A similar structure can be observed on surfaces after finishing grinding, which is discussed in p. 3. On the other hand, the structure directional characteristic vanishes on surfaces subjected to electrochemical polishing. The distinguishable mesh reflects the crystalline structure of the material being processed.

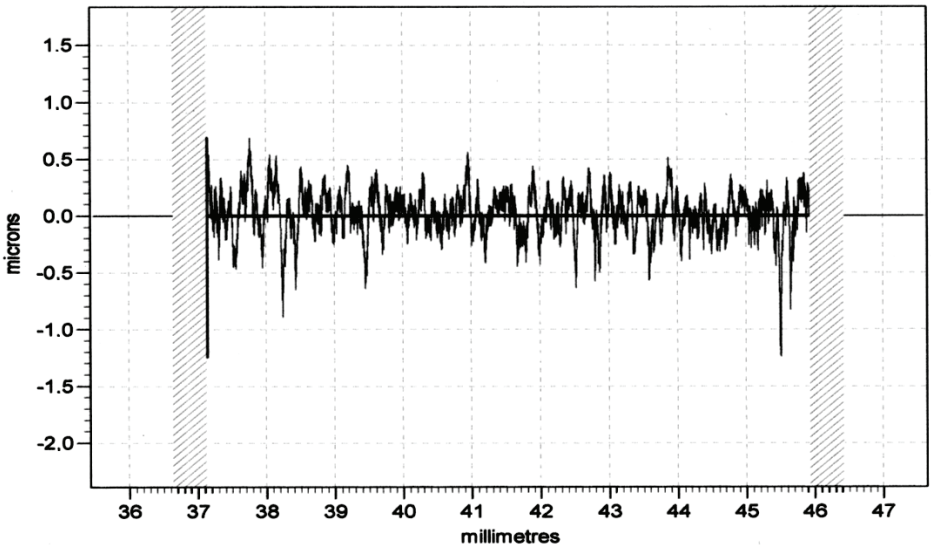

Fig. 7. Profilograph of mechanically polished Ti6Al4V titanium alloy surface, Ra = 0.116 μm

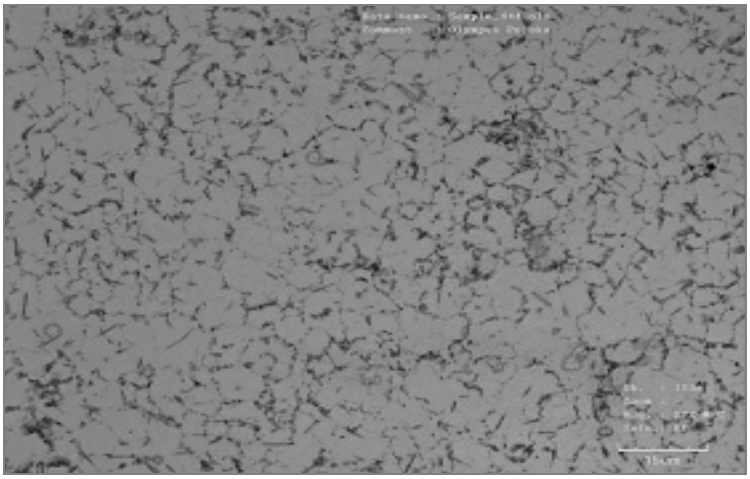

Fig. 8. Microscopic image of electrochemically polished Ti6Al4V titanium alloy surface (mag. 100×)

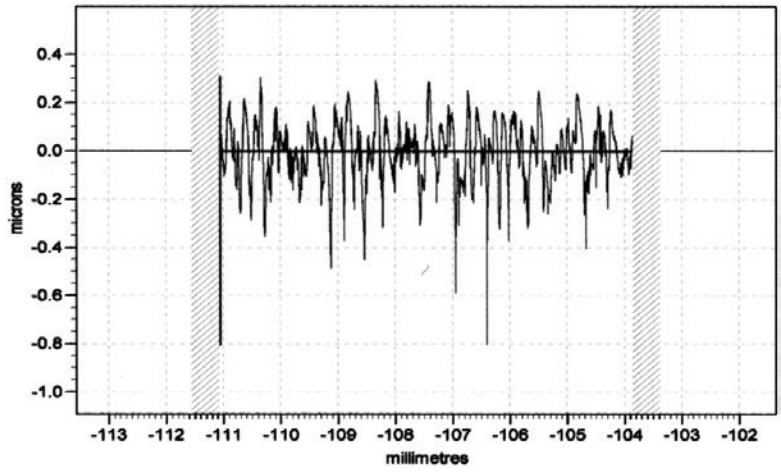

Fig. 9. Profilograph of electrochemically polished Ti6Al4V titanium alloy surface $Ra = 0.096$ μm

6. Summary

Electrochemical polishing made it possible to obtain ca. 0.05–0.15 μm coarseness for both steel and titanium alloy. Measurements taken by means of a profilograph device showed an increase in the carrying share for the electrochemically polished surface by 25–30% as compared to the surface machined by grinding. Electrochemical polishing entails the danger of the shape error build-up in the work-piece. In order to avoid it, two suitably formed and located electrodes were used. Also possible is the application of a pre-defined movement of the work-piece with respect to the electrodes during the process. Unfavourable effect of some electrolytes on the surface has been observed when the polishing was finished. For example, hydrofluoric acid contained in some electrolytes being tested caused local tarnishing of the surface when the work-piece was taken out of the electrolyte. This drawback was eliminated thanks to an appropriate procedure of polishing and quick termination of the electrolyte action. The lustre obtained on the investigated surfaces was by ca. 20% better than that obtained by mechanical polishing.

Due to high quality of the surface obtained by electrochemical polishing, high effectiveness of polishing and possibility of processing multiple work-pieces simultaneously, this method is highly recommended for the manufacture of hip joint prostheses.

References

[1] Będziński R.: *Biomechanika inżynierska: zagadnienia wybrane*, Oficyna Wydawnicza Politechniki Wrocławskiej, Wrocław, 1997.

[2] Bickels J., Meller I., Henshaw R., Malawer M.: *Proximal and total femur resection with endoprosthetic reconstruction*, 2001.

[3] Nałęcz M., *Biocybernetyka i inżynieria biomedyczna*, Tom 4, *Biomateriały*, Akademicka Oficyna Wydawnicza Exit, Warszawa, 2003.
[4] Chłopek J., Kmita G.: *Non-metallic composite materials for bone surgery*, Engineering Transaction, Vol. 2–3, 2003, pp. 307–323.
[5] Cwanek J.: *Wpływ obróbki ściernej na geometrię powierzchni głów endoprotez Wellera*, Podstawy i technika obróbki ściernej, Rzeszów, 2007.
[6] Jurczyk M., Jakubowicz J.: *Bionanomateriały*, Wydawictwo Politechniki Poznańskiej, Poznań, 2008.
[7] Lendelin A., Langer R.: *Biodegradable, elastic shape-memory polymers for potential biomedical applications*, Science, Vol. 296, 2002, pp. 1673–1676.
[8] Marciniak J.: *Biomateriały*, Wydawnictwo Politechniki Śląskiej, Gliwice, 2002.
[9] Nowicki B.: *Elektropolerowanie*, W: *Obróbka skrawaniem ścierna i erozyjna*, Praca zbiorowa pod redakcją Dąbrowskiego L., Marciniaka M., Nowickiego B., Oficyna Wydawnicza Politechniki Warszawskiej, Warszawa, 2001.
[10] Praca zbiorowa: Poradnik galwanotechnika, WNT, Warszawa, 2002.
[11] Ramakrishna S., Mayer J., Wintermantel E., Kam W.L.: *Biomedical applications of polymer--composite marerials: a reviev*, Comp. Scien. and Techn., Vol. 61, 2001, pp. 1189–1224.
[12] Stodolnik B.: *Badania materiałowe i biologiczne stopów kobaltowych o przeznaczeniu biomedycznym*, Mechanika w medycynie, Vol. 6, Rzeszów, 2002.
[13] Zaborski S., Sudzik A.: *Polerowanie mechaniczne i elektrochemiczne wyrobów z blachy nierdzewnej i stopu tytanu*, NSOŚ, 2006.
[14] Zaborski S., Sudzik A.: *Polerowania elektrochemiczne stopów tytanu stosowanych w biotechnologii*, Biocybernetyka i inżynieria biomedyczna, XV KKN, Wrocław, 2007.

Polerowanie elektrochemiczne główek endoprotez stawu biodrowego

Omówiono materiały stosowane na endoprotezy. Przedstawiono sposoby obróbki główek endoprotez ze stopu tytanu Ti6Al4V. Operacje wstępne wykonania główek wykonano na tokarce CNC Gildemaister CTX400. Następne operacje to szlifowanie, polerowanie mechaniczne i polerowanie elektrochemiczne. Po polerowaniu elektrochemicznym uzyskano chropowatość około Ra = 0,05–0,15 μm. Zaobserwowano wzrost udziału nośnego powierzchni po polerowaniu elektrochemicznym o 25–30% w stosunku do powierzchni po szlifowaniu. Otrzymano również wyższy połysk o około 20% w stosunku do powierzchni po polerowaniu mechanicznym.

ARCHIVES OF CIVIL AND MECHANICAL ENGINEERING

Vol. XI 2011 No. 4

Selection of construction enterprises management strategy based on the SWOT and multi-criteria analysis

E.K. ZAVADSKAS, Z. TURSKIS, J. TAMOSAITIENE
Vilnius Gediminas Technical University, Faculty of Civil Engineering, Department of Construction Technology and Management, Sauletekio av. 11, Vilnius, LT-10223, Lithuania.

The paper proposes a methodology for determining management strategies in construction enterprises. For this purpose, the SWOT (Strengths, Weaknesses, Opportunities and Threats) analysis as an instrument for formulating management strategies is recommended. The best practices for this reason are also analysed. The algorithm helps to select the most preferable strategies based on the AHP, expert judgment and permutation method of feasible alternatives. A perspective of construction enterprises management regarding the SWOT is carried out on a basis of selected description of the current state and the feasible future alternatives. Finally, the selected alternatives are ranked according to the permutation method of feasible alternatives. The case study shows the applicability of the proposed model to the real management problems solution.

Keywords: *management, strategy, enterprise, SWOT, AHP, expert judgment, permutation method, MCDM*

1. Introduction

Strategic management has the crucial importance of providing a company's long-term success. The task of strategic management can be broken down into strategic planning, implementation of strategies, and strategic control. Strategic planning is a systematic process which defines the way to guarantee the permanent accomplishment of the company's overriding goals and objectives. Strategies are long-term managerial guidelines guaranteeing the permanent accomplishment of the company's overriding goals and objectives. The strategies of a company define its future way of doing business [21].

Development of successful strategies is an essential and a complex task. Evaluation of strategies focuses mainly on existing success potentials or those to be built up within the planning period. The first approach to assessing strategic options deals with financial evaluation: calculating the net present value resulting from the investments complementing discounted cash-flow analysis.

However it fails in many cases due to the impossibility of making realistic forecasts of the long-term financial outcomes of specific strategic options. The prediction of the effects of investments to protect existing success potentials is often fraught with considerable uncertainty.

Evaluation of success potentials is possible with the help of substitute assessment criteria. These must fulfil the following two requirements [21]:

– On the one hand, it must be possible to obtain the data required for the assessment of success potentials using the substitute criteria.

– On the other hand, there should be a high probability that assessment of the success potentials using substitute criteria will in practice select the strategic option whose positive effect on long-term success is greatest. So there needs to be a well founded link between substitute criteria and company success.

A systemic approach to strategic planning is seen by many company leaders and management researchers as an essential requirement for long-term corporate success. Many companies today view strategic planning as a task of top management. Unfortunately, despite the best efforts of those responsible the results are often unsatisfactory.

It is the principal objective of this research to present an integrated system of analysis and assessment tools. One of the most important factors leading to the success of a construction is its strategy development scenario and successful application.

Many researchers investigated the problem of success and the importance of rational decision-making in constantly changing and risky environment [3, 8, 45, 58, 67, 71]. Gudonavicius et al. [23] state that enterprise strategy formulation can be improved significantly by applying strategy planning tools, by widening dimensions that describe the types of entrepreneur, and by integrating them into a particular system. A company's success depends on the successful selecting of a governance strategy. The SWOT (Strengths, Weaknesses, Opportunities and Threats) analysis as an instrument for forming management strategies is recommended. However, these instruments indicate the direction but their support is difficult to reach a final decision. There are a number of strategies (alternatives or actions) which can be ranked according to a number of criteria (criteria, aspects, or dimensions). Criteria can be cardinal or ordinal. It can be stated that the performance evaluation and optimal selection of strategy has multilevel and multi-criteria features, so it can be regarded as Multi-Criteria Decision Analysis. Multi-criteria decision analysis (MCDA), sometimes called multi-criteria decision making (MCDM), is a discipline of operations research aimed at supporting decision makers faced with making numerous and conflicting evaluations. MCDA aims at highlighting these conflicts and deriving a way to come to a compromise in a transparent process. Optimization models all so must be analyzed in the future [29, 51, 54, 64–65].

2. SWOT development and solving problem in construction

In many cases SWOT analysis is a strategic planning method and can be used in conjunction with other tools for audit and analysis of an involved venture [25]. It's originated from is "SOFT" (Satisfactory, Opportunity, Fault and Threat) and came from the research conducted during 1960–1970. The SOFT analysis was presented in a seminar at Zurich in 1964, Urick and Orr changed the F to a W and called it the

SWOT. Weihrich [75–76] modified SWOT (or TOWS) into the format of a matrix, matching the internal factors (i.e. the strengths and weaknesses) of an organisation with its external factors (i.e. the opportunities and threats) to systematically generate responses that ought to be undertaken by the organisation. Since this period SWOT has been applied in many fields and has undergone numerous researches, is given in review articles [12, 14, 32].

In the considered stage the data mined by SWOT analysis are applied as criteria values for MCDM. Shinno et al. [52] applied SWOT analysis aggregated with an Analytic Hierarchy Process (AHP). Problem solution on the basis of SWOT and uncertainty was developed. Kheirkhah et al. [31] proposed fuzzy SWOT analysis. Lee and Lin [34] analysed a fuzzy quantified SWOT procedure for environmental evaluation and etc.

SWOT was applied in many fields and has undergone numerous researches [12, 14, 32]. It has been widely used in all areas of business management and strategic management aspects. SWOT analysis has been successfully used for problem solving in construction areas: Lee et al. [35] analysed strategies choices for developing countries; Xu et al. [78] applied forms of collaboration and project delivery in Chinese construction markets; Maydl et al. [41] analysed applying of steel for building constructions.

Today's research focuses on multi-stage analysis including three elements: SWOT, MCDM, and fuzzy sets theory. Celik et al. [6] used the elements in the following way: he applied axiomatic design and TOPSIS methodologies under fuzzy environment for proposing competitive strategies; Zaerpour et al. [63] suggested an innovative hybrid methodology consisting of SWOT analysis and Fuzzy Analytic Hierarchy Process (FAHP).

3. Model of enterprise management based on the SWOT analysis

The strengths and weaknesses may either be identified be in the functional enterprises fields, or may be a consequence of abnormal interaction between different fields. Furthermore, the strengths and weaknesses of an aspect must be measured at different levels of the organization: at group level, individual enterprise level or product level. Success can only be achieved in this respect to the extent that one is familiar with the opportunities and threats resulting from the external environment. The recognition of internal strengths and weaknesses, as well as the external opportunities and threats, is based on of a SWOT analysis. To operate successfully the construction enterprise must concentrate its future objectives on its strengths, while averting tendencies related to its weaknesses. It is one of the methods finding wide application in economic activities, involving specifying the objective of the enterprise venture or project and identifying the internal and external factors that are favourable and unfavourable to achieve that objective. Responding to internal strengths and weaknesses is therefore an essential component of the strategic management process.

The management processes of the construction enterprises are complicated and resource consuming [18]. Wrong decision making is directly concerned (outcome) with heavy expenses. For this reason, the risk in construction is very high [67]. The enterprises success evaluation attributes are selected taking into consideration the interests and goals of the stakeholders as well as the factors that have influence on the construction process efficiency. Therefore, the SWOT analysis can be used for choosing the management strategy of enterprise.

The SWOT analysis was employed to develop a new model for management effectiveness in construction enterprises. It is presented in Figure 1.

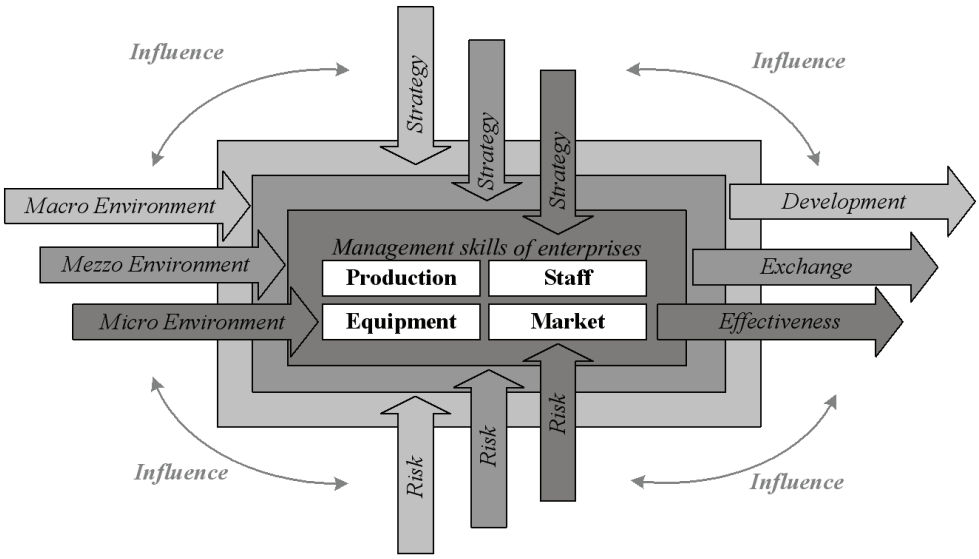

Fig. 1. The model of SWOT analysis for construction enterprise management

There are 4 general aspects of the developed model of SWOT analysis for effectiveness of management in construction enterprises:

1. Macro-, mezzo-, micro-environment analysis;
2. Determination strategy for the construction enterprise management;
3. Risk assessment;
4. Influence on the overall effectiveness, exchange and development.

Depending on the level strategy can be classified as: macro, mezzo and micro. Every enterprise is confronted with different internal and external environment which may compromise potential stimulants, or, on the other hand, can compromise potential limitations regarding the performances of the enterprises or the objectives the construction enterprises wish to achieve [16].

There are lot of SWOT analysis investigations which are applied in construction economics and management.

Ling et al. [38] presented a study where the SWOT of architectural, engineering and construction firms was investigated. The following researchers presented the SWOT analysis for the strategy in macro-level research: Chintoanu et al. [9] presented national strategy for production; Celik et al. [6] analysed competitive strategies; Ghazinoory and Kheirkhah [13] analysed strategic approach for decreasing accidents.

Lot of researches on SWOT analysis at micro- environment level is presented at last three years: Arslan and Er [2] presented successful bridge team organisation and safer operations; Ling and Gui [37], Ling et al. [38] applied SWOT for a consulting company; Celik and Peker [7] made benefit/cost analysis of production for diversification of income; Zhao et al. [74] assessed the performance and strategy of contractors in the international market; Lee [33] selected technology for changing markets; Ginevicius [19] analysed effectiveness of cooperation among industrial enterprises; Pleban-kiewicz [46] investigated prequalification of a construction contractor from Polish clients' perspective; Gudas [22] analysed management success. It is very important to assess all levels risk of environment. The SWOT analysis applying risk was presented by the following researchers: Andreica et al. [1] analysed the risk in project from managerial perspective, Bartel-Kratochvil et al. [4] analysed the success in local supply chains for products, etc.

The resolved problem influenced the effectiveness, exchange and development. Markovska et al. [39] used the SWOT analysis to investigate the sustainable development in energy sector. The results show that most identified factors determining innovation success in the market are attributed to the process of innovation creation and the knowledge-based framework. The SWOT analysis applying the above mentioned research aspects were presented by the following scientists: Diskiene et al. [10] presented a strategic management model for economic development; Dwivedi and Alavalapati [11] analysed stakeholders' perceptions in bioenergy development; Ghazinoory et al. [15] described the development of the national technology strategy; Markovska et al. [39] analysed the national energy sector for sustainable energy development; Pankratova et al. [43] proposed definition of indicators of sustainable development in the context of regional priorities. The selection of multiple criteria decision making model solve the problem under investigation is based on above presented overview. Plebankiewicz [46] investigated prequalification of a construction contractor from Polish clients' perspective; Gudas [22] analysed management success. It is very important to assess all levels risk of environment. The SWOT analysis applying risk was presented by the following researchers: Andreica et al. [1] analysed the risk in project from managerial perspective, Bartel-Kratochvil et al. [4] analysed the success in local supply chains for products, etc.

The resolved problem influenced the effectiveness, exchange and development. Markovska et al. [39] used the SWOT analysis to investigate the sustainable development in energy sector. The results show that most identified factors determining innovation success in the market are attributed to the process of innovation creation and the knowledge-based framework. The SWOT analysis applying the above mentioned research aspects were presented by the following scientists: Diskiene et al. [10] presented a strategic management model for economic development; Dwivedi and

Alavalapati [11] analysed stakeholders' perceptions in bioenergy development; Ghazinoory et al. [15] described the development of the national technology strategy; Markovska et al. [39] analysed the national energy sector for sustainable energy development; Pankratova et al. [43] proposed definition of indicators of sustainable development in the context of regional priorities.

4. Developing the model based on SWOT analysis and MCDM methods

Multiple criteria decision aid provides several powerful solution tools for confronting sorting problems [68]. For the solution of the problem considered in this paper three-stage different technique were to be developed and are presented below in Figure 2 [66]:

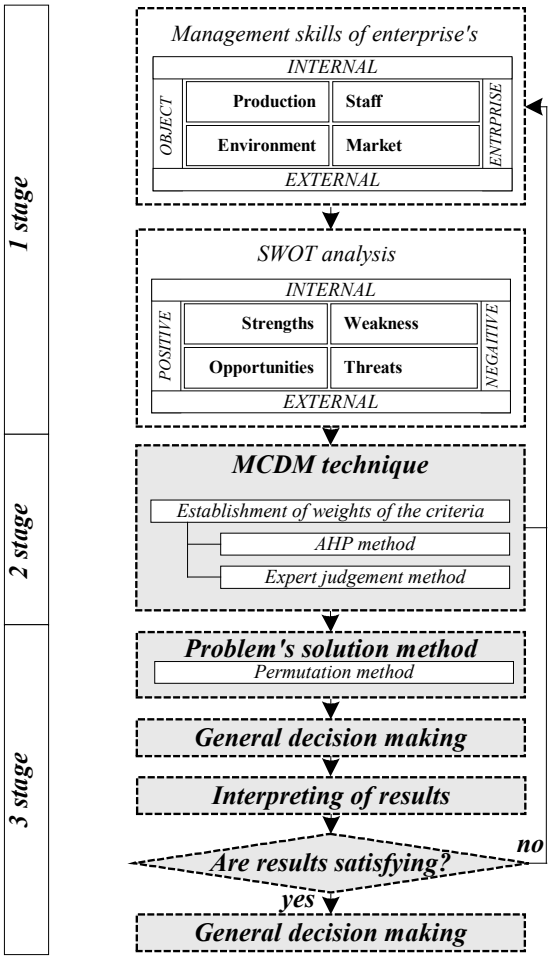

Fig. 2. The algorithm of SWOT analysis and MCDM for management effectiveness

Stage 1: Some of the key areas to consider when identifying and evaluating strengths, weaknesses, opportunities and threats are listed in the SWOT analysis;

Stage 2: Weight establishing methods, in the paper used as AHP, expert judgment techniques;

Stage 3: Problem solution method: in the paper used as permutation method.

For the development of the SWOT, the background information and the static knowledge was mostly obtained by study of different literature.

The key groups are the internal and external issues: strengths and weaknesses (internal factors), and opportunities and threats (external factors). Some of the key areas to consider when identifying and evaluating strengths, weaknesses, opportunities and threats are listed in the algorithm of SWOT and MCDM for management effectiveness.

4.1. Methodology for the weight establishment

The Analytic Hierarchy Process is a well-known method that is only able to rank different alternatives according to their AHP weights, accept/reject alternatives based on AHP weights. In that method, pairwise comparisons are performed by the Decision-Maker (DM) and then the pairwise comparison matrix and the eigenvector are derived to specify the weights of each parameter in the problem. The weights guide the DM in choosing the superior alternative.

The AHP was introduced by Saaty [49], but also utilized AHP in planning and anticipating for the first time [50]. He employed forward and backward process to determine logical future and then find promising control policies to attain the desired future. Application of AHP in mathematical optimization and operational research is widely practised and the weights gained by the AHP method are frequently employed as the coefficient of the objective function in linear and integer programming. The weights have also been applied for ranking multiple objectives in goal programming. The integrated AHP-ELECTRE method presented Kaya and Kahraman [28].

A number of studies have been carried out regarding AHP and its applications: Sinuany-Stern et al. [53] utilise AHP along with DEA (Date Envelopment Analysis) for ranking decision-making units. But it does eliminate the weaknesses of the above mentioned methods. In this article, AHP weights were employed as coefficients of the objective function and they were not used as the coefficients of the decision variables in constraints (technological coefficients). The literature review concerned with AHP and its applications was presented by Ho [24]. Raharjo et al. [48] presented modelling dynamic priorities in AHP using compositional data analysis. Ghazinoory et al. [17], Tiryaki and Ahlatcioglu [59] were concerned with the fuzzy AHP; Wu et al. [77] presented AHP-grey target theory systematic model. Skibniewski and Chao [56] were the first to apply the AHP method for construction problems. The AHP method is used for solving different problems e.g. Stein and Ahmad [57] constructed a measure of the magnitude of consequences component of moral intensity; Ginevicius and Podvezko

[20] evaluated the changes in economic and social development; Zavadskas et al. [70] evaluated the organisation of manufacturing and technological processes; Li and Li [36] gave the assessment of strategy under uncertainty; Vainiunas et al. [62] presented the evaluation managers for construction design projects; Tserng et al. [60] analysed risk management framework of construction projects through project life cycle; Bayraktar and Hastak [5] selected the optimal contracting strategy; Maskeliunaite et al. [40] analysed the quality of passenger railway transportation; Jaskowski et al. [27] assessed contractor selection criteria weights; Podvezko et al. [47] presented complex evaluation of contracts for construction; Sivilevicius [54] presented the interaction of transport system elements.

The expert judgment method proposed by Kendall [30] was used for determining criteria weights in the following research papers: Peldschus et al. [44] for construction site assessment, Sivilevicius [55] for determine the importance of operating asphalt mixing plant quality, Zavadskas et al. [67–69] for contractor selection.

4.2. Permutation method

The permutation method was developed by Paelnick [42]. The permutation method uses Jaquet-Lagreze's successive permutations of all possible rankings and alternatives [26]. When applying this MCDM method, all permutations of alternatives according to their preference ability are checked and compared among one another [61]. If there are m alternatives, then $m!$ permutations are available. The algorithm of this method is given in Figure 3 [72–73].

Suppose a number of alternatives a_i, $i=\overline{1,m}$ to be evaluated according to criterion x_j, when $j=\overline{1,n}$. The decision making matrix is set up according to the earlier adopted forms given in Equation (1):

$$P=\begin{array}{c} \\ a_1 \\ a_2 \\ \vdots \\ a_m \end{array}\begin{array}{|cccc} x_1 & x_2 & \cdots & x_n \\ x_{11} & x_{12} & \cdots & x_{1n} \\ x_{21} & x_{22} & \cdots & x_{2n} \\ \vdots & \vdots & \cdots & \vdots \\ x_{m1} & x_{m2} & \cdots & x_{mn} \end{array}; \tag{1}$$

For a solution of problems there exists an obligatory set of criteria weight coefficients q_j;

$$\sum_{j=1}^{n} q_j = 1.$$

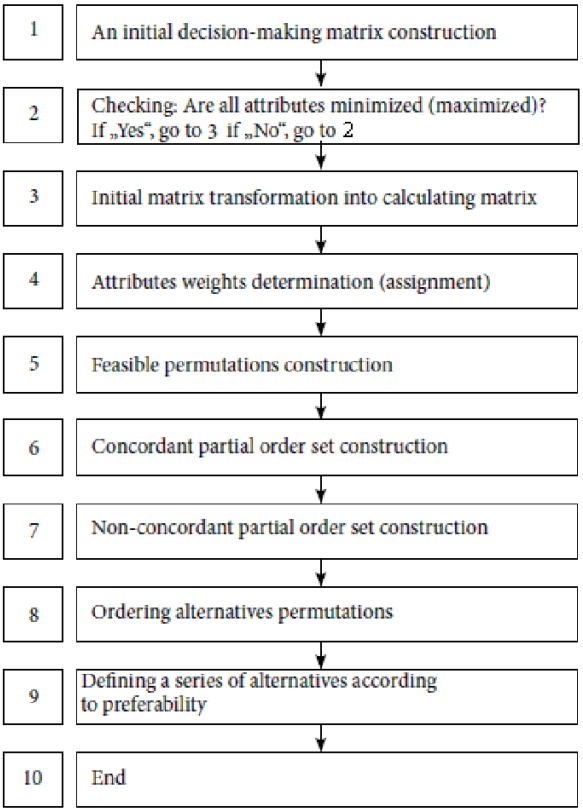

Fig. 3. Model of ordering feasible alternative solutions according to their preferability

From the given m alternatives the most appropriate need to be chosen, i.e., the preferability relationship must be assigned the set of alternatives which to best fit the system of values. Assume there are three total alternatives: a_1, a_2, a_3. Then, there exist six permutations in total (3! = 6):

$\pi_1 = \{a_1, a_2, a_3\}$, $\pi_2 = \{a_1, a_2, a_3\}$, $\pi_3 = \{a_1, a_2, a_3\}$,
$\pi_4 = \{a_1, a_2, a_3\}$, $\pi_5 = \{a_1, a_2, a_3\}$, $\pi_6 = \{a_1, a_2, a_3\}$.

Assume the checked order of alternatives is as follows: $\pi_5 = \{a_1, a_2, a_3\}$, then the set of the concordant partial order is $\{a_3 > a_1, a_3 > a_2, a_1 > a_2\}$ and the set of no concordant partial order is $\{a_3 < a_1, a_3 < a_2, a_1 < a_2\}$.

If in ranking (permutation) of the alternatives a partial order of $a_k > a_e$ it is evident that $x_{kj} \geq x_{ej}$ is evaluated by virtue of q_j, it is evident that $x_{ej} < x_{en}$ shows that it is evaluated by virtue of q_n.

The evaluation of ordering of the alternatives $\beta_g\,(g = \overline{1,m!})$, is carried out in the following way: suppose there is the g-th permutation $\pi_g = \{...,a_k,...,a_e\} \forall g, g = \overline{1,m!}$,

where a_k is preferable to a_e. Then, to this permutation the following estimate β_g is assigned is given as Equation (2):

$$\beta_g = \sum_{k,e=1}^{m} \sum_{j \in C_{ke}} q_j - \sum_{\substack{k,e=1 \\ k \neq e}}^{m} \sum_{j \in H_{ke}} q_j, \forall g; q = \overline{1,m}!, \tag{2}$$

where $C_{ke} = \{j / x_{kj} \geq x_{ej}\}, k,e = \overline{1,m}; k \neq e;\ H_{k,e} = \{j / x_{kj} < x_{ej}\}, k,e = \overline{1,m}; k \neq e.$

Then the following evaluation criterion is given to the permutation. The best concordant ordering is the one, for which the value of the evaluation criterion is the largest [61]. The best concordant ordering is the one for which value β_g is the largest. The considered method had has been tested quite a number of times in solving practical MCDM problems.

5. Practical example for the assessment of management effectiveness in construction enterprises

Feasible alternatives' rating is performed according to the criteria which determine strengths, weaknesses, opportunities and threats. The initial decision-making matrix has been formed according to the criteria values presented in Table 1. The weights w_j of criteria, presented in Table 2–8, were determined by applying the expert judgment method [30] and AHP [49].

Table 1. Criteria set for the assessment of management effectiveness in construction enterprises

Criteria group	Criteria		Optimum
C_1 – strengths	x_1	Technology skills	max
	x_2	Leading brands	max
	x_3	Customer relationship	max
	x_4	Management skills	max
	x_5	Products quality	max
C_2 – opportunities	x_6	Changing customer tastes	max
	x_7	Liberalization of geographic markets	max
	x_8	Technological advances	max
	x_9	Changes in government policies	max
C_3 – weaknesses	x_{10}	Absence of important skills	min
	x_{11}	Weak brands	min
	x_{12}	Low customer retention	min
	x_{13}	Management	min
	x_{14}	Unviable product	min
C_4 – threats	x_{15}	Changing customer tastes	min
	x_{16}	Closing of geographic markets	min
	x_{17}	Technological advances	min
	x_{18}	Changes of government policies	min

Table 2. Establishment weights *C* for criteria groups

		Criteria group				
		C_1	C_2	C_3	C_4	
Criteria	C_1		2	3	4	
	C_2			2	3	
	C_3				2	
	C_4					$\sum$
		0.46	0.28	0.16	0.10	1
CR = 0.011						

Table 3. Establishment of criteria weights *s* in the C_1 criteria group (by applying Expert Judgment method)

Criteria				
s_1	s_2	s_3	s_4	s_5
0.23	0.17	0.10	0.18	0.32

Table 4. Establishment of criteria weights *s* in the C_2 criteria group (by applying Expert Judgment method)

Criteria			
s_6	s_7	s_8	s_9
0.35	0.47	0.10	0.08

Table 5. Establishment of criteria weights *s* in the C_3 criteria group (by applying AHP method)

		Criteria				
		s_{10}	s_{11}	s_{12}	s_{13}	s_{14}
Criteria	s_{10}		2	0.5	2	0.5
	s_{11}			0.5	1	0.5
	s_{12}				2	0.5
	s_{13}					1
	s_{14}					
$\sum = 1$		0.19	0.12	0.25	0.15	0.29
CR = 0.062						

Table 6. Establishment of criteria weights *s* in the C_4 criteria group (by applying AHP method)

		Criteria				
		s_{15}	s_{16}	s_{17}	s_{18}	
Criteria	s_{15}		1	2	3	
	s_{16}			1	2	
	s_{17}				1	
	s_{18}					$\sum$
		0.37	0.28	0.20	0.15	1
CR = 0.03						

The majority of the respondents (72%) have university education, and 28% of respondents have college education. Next, the Kendall coefficient of concordance *W* was calculated to test the reliability of the responses, and significance testing was based on the Chi–square distribution at the level of 1% significance. The alternatives are rated by applying permutation method. The process of calculations is presented in Table 9.

Table 7. Final establishment of criteria weights w

Criteria group									
C_1					C_2				
0.46					0.28				
Criteria									
	s_1	s_2	s_3	s_4	s_5	s_6	s_7	s_8	s_9
	0.23	0.17	0.10	0.18	0.32	0.35	0.47	0.10	0.08
w_j	0.1	0.08	0.05	0.08	0.15	0.10	0.13	0.03	0.02
Criteria group									
C_3					C_4				
0.16					0.10				
Criteria									
	s_{10}	s_{11}	s_{12}	s_{13}	s_{15}	s_{16}	s_{17}	s_{18}	
	0.19	0.12	0.25	0.15	0.37	0.28	0.20	0.15	
w_j	0.03	0.02	0.04	0.02	0.04	0.03	0.02	0.02	

There $w_j = g_k \cdot s_l$; $k = 1, \ldots, 4$; $l = 1, \ldots, 18$; if $l < 6$ then $k=1$; if $5 < l < 10$ then $k = 2$; if $9 < l < 15$ then $k = 3$; if $14 < l$ then $k = 2$.

Table 8. Initial decision making matrix

Criteria									
	Optimum is maximum				Optimum is minimum				
w_j		A_1	A_2	A_3	w_j		A_1	A_2	A_3
w_1	0.11	7	6	8	w_{10}	0.03	2	3	4
w_2	0.08	5	6	6	w_{11}	0.02	1	1	2
w_3	0.05	4	5	4	w_{12}	0.04	3	4	5
w_4	0.08	4	4	5	w_{13}	0.02	2	3	3
w_5	0.15	7	5	5	w_{14}	0.05	2	4	3
w_6	0.10	7	8	6	w_{15}	0.04	5	3	6
w_7	0.13	9	8	7	w_{16}	0.03	6	7	6
w_8	0.03	9	7	9	w_{17}	0.02	5	4	5
w_9	0.02	4	5	4	w_{18}	0.02	7	8	7

Table 9. Permutations and calculations of evaluation criteria

	$\pi_1 = a_1 > a_2 > a_3$		
	a_1	a_2	a_3
a_1	0	**0.11 + 0.05 + 0.08 + 0.15 + 0.13 + 0.03 + 0.03 + 0.02 + 0.04 + 0.02 + 0.05 + 0.03 + 0.02 = 0.76**	**0.05 + 0.15 + 0.1 + 0.16 + 0.03 + 0.02 + 0.03 + 0.02 + 0.04 + 0.02 + 0.05 + 0.04 + 0.03 + 0.02 + 0.02 = 0.78**
a_2	0.08 + 0.08 + 0.1 + 0.02 + 0.02 + 0.04 + 0.02 = 0.36	0	**0.08 + 0.05 + 0.15 + 0.1 + 0.13 + 0.02 + 0.03 + 0.02 + 0.04 + 0.02 + 0.04 + 0.02 = 0.70**
a_3	0.11 + 0.08 + 0.05 + 0.08 + 0.03 + 0.02 + 0.03 + 0.02 + 0.02 = 0.44	0.11 + 0.08 + 0.08 + 0.15 + 0.03 + 0.02 + 0.05 + 0.03 + 0.02 = 0.57	0
Evaluation criterion β_1		**0.76+0.78+0.70 = 2.24**	0.36+0.44+0.57 = 1.37

	$\pi_2 = a_1 > a_3 > a_2$		
	a_1	a_3	a_2
a_1	0	**0.05 + 0.15 + 0.1 + 0.16 + 0.03 + 0.02 + 0.03 + 0.02 + 0.04 + 0.02 + 0.05 + 0.04 + 0.03 + 0.02 + 0.02 = 0.78**	**0.11 + 0.05 + 0.08 + 0.15 + 0.13 + 0.03 + 0.03 + 0.02 + 0.04 + 0.02 + 0.05 + 0.03 + 0.02 = 0.76**
a_3	0.11 + 0.08 + 0.05 + 0.08 + 0.03 + 0.02 + 0.03 + 0.02 + 0.02 = 0.44	0	**0.11 + 0.08 + 0.08 + 0.15 + 0.03 + 0.02 + 0.05 + 0.03 + 0.02 = 0.57**
a_2	0.08 + 0.08 + 0.1 + 0.02 + 0.02 + 0.04 + 0.02 = 0.36	0.08 + 0.05 + 0.15 + 0.1 + 0.13 + 0.02 + 0.03 + 0.02 + 0.04 + 0.02 + 0.04 + 0.02 = 0.70	0
Evaluation criterion β_2		**0.78 + 0.76 + 0.57 = 2.11**	0.44+0.36+0.70 = 1.50
	$\pi_3 = a_2 > a_1 > a_3$		
	a_2	a_1	a_3
a_2	0	**0.08 + 0.08 + 0.1 + 0.02 + 0.02 + 0.04 + 0.02 = 0.36**	**0.08 + 0.05 + 0.15 + 0.1 + 0.13 + 0.02 + 0.03 + 0.02 + 0.04 + 0.02 + 0.04 + 0.02 = 0.70**
a_1	0.11 + 0.05 + 0.08 0.15 + 0.13 + 0.03 + 0.03 + 0.02 + 0.04 + 0.02 + 0.05 + 0.03 + 0.02 = 0.76	0	**0.05 + 0.15 + 0.1 + 0.16 + 0.03 + 0.02 + 0.03 + 0.02 + 0.04 + 0.02 + 0.05 + 0.04 + 0.03 + 0.02 + 0.02 = 0.78**
a_3	0.11 + 0.08 + 0.08 + 0.15 + 0.03 + 0.02 + 0.05 + 0.03 + 0.02 = 0.57	0.11 + 0.08 + 0.05 + 0.08 + 0.03 + 0.02 + 0.03 + 0.02 + 0.02 = 0.44	0
Evaluation criterion β_3		**0.36 + 0.70 + 0.78 = 1.84**	0.76 + 0.57 + 0.44 = 1.77
	$\pi_4 = a_2 > a_3 > a_1$		
	a_2	a_3	a_1
a_2	0	**0.08 + 0.05 + 0.15 + 0.1 + 0.13 + 0.02 + 0.03 + 0.02 + 0.04 + 0.02 + 0.04 + 0.02 = 0.70**	**0.08 + 0.08 + 0.1 + 0.02 + 0.02 + 0.04 + 0.02 = 0.36**
a_3	0.11 + 0.08 + 0.08 + 0.15 + 0.03 + 0.02 + 0.05 + 0.03 + 0.02 = 0.57	0	**0.11 + 0.08 + 0.05 + 0.08 + 0.03 + 0.02 + 0.03 + 0.02 + 0.02 = 0.44**
a_1	0.11 + 0.05 + 0.08 + 0.15 + 0.13 + 0.03 + 0.03 + 0.02 + 0.04 + 0.02 + 0.05 + 0.03 + 0.02 = 0.76	0.05 + 0.15 + 0.1 + 0.16 + 0.03 + 0.02 + 0.03 + 0.02 + 0.04 + 0.02 + 0.05 + 0.04 + 0.03 + 0.02 + 0.02 = 0.78	0
Evaluation criterion β_4		**0.70 + 0.36 + 0.44 = 1.50**	0.57 + 0.76 + 0.78 = 2.11
	$\pi_5 = a_3 > a_1 > a_2$		
	a_3	a_1	a_2
a_3	0	**0.11 + 0.08 + 0.05 + 0.08 + 0.03 + 0.02 + 0.03 + 0.02 + 0.02 = 0.44**	**0.11 + 0.08 + 0.08 + 0.15 + 0.03 + 0.02 + 0.05 + 0.03 + 0.02 = 0.57**

a_1	0.05 + 0.15 + 0.1 + 0.16 + 0.03 + 0.02 + 0.03 + 0.02 + 0.04 + 0.02 + 0.05 + 0.04 + 0.03 + 0.02 + 0.02 = 0.78	0	**0.11 + 0.05 + 0.08 + 0.15 + 0.13 + 0.03 + 0.03 + 0.02 + 0.04 + 0.02 + 0.05 + 0.03 + 0.02 = 0.76**
a_2	0.08 + 0.05 + 0.15 + 0.1 + 0.13 + 0.02 + 0.03 + 0.02 + 0.04 + 0.02 + 0.04 + 0.02 = 0.70	0.08 + 0.08 + 0.1 + 0.02 + 0.02 + 0.04 + 0.02 = 0.36	0
Evaluation criterion β_5		**0.44 + 0.57 + 0.76 = 1.77**	0.78 + 0.70 + 0.36 = 1.84
	$\pi_6 = a_3 > a_2 > a_1$		
	a_3	a_2	a_1
a_3	0	**0.11 + 0.08 + 0.08 + 0.15 + 0.03 + 0.02 + 0.05 + 0.03 + 0.02 = 0.57**	**0.11 + 0.08 + 0.05 + 0.08 + 0.03 + 0.02 + 0.03 + 0.02 + 0.02 = 0.44**
a_2	0.08 + 0.05 + 0.15 + 0.1 + 0.13 + 0.02 + 0.03 + 0.02 + 0.04 + 0.02 + 0.04 + 0.02 = 0.70	0	**0.08 + 0.08 + 0.1 + 0.02 + 0.02 + 0.04 + 0.02 = 0.36**
a_1	0.05 + 0.15 + 0.1 + 0.16 + 0.03 + 0.02 + 0.03 + 0.02 + 0.04 + 0.02 + 0.05 + 0.04 + 0.03 + 0.02 + 0.02 = 0.78	0.11 + 0.05 + 0.08 + 0.15 + 0.13 + 0.03 + 0.03 + 0.02 + 0.04 + 0.02 + 0.05 + 0.03 + 0.02 = 0.76	0
Evaluation criterion β_6		**0.57 + 0.44 + 0.36 = 1.37**	0.70 + 0.78 + 0.76 = 2.24

Bold font – concordance values, Regular font - non-concordance values

Table 10. Summary of calculation results

	Permutation	**Concordance**	Non-concordance	β_g	β_g rank
1	$\pi_1 = a_1 > a_2 > a_3$	**0.36 + 0.70 + 0.78 = 1.84**	0.76 + 0.57 + 0.44 = 1.77	**1.84**–1.77 = **0.07**	2
2	$\pi_2 = a_1 > a_3 > a_2$	**0.78 + 0.76 + 0.57 = 2.11**	0.44 + 0.36 + 0.70 = 1.50	**2.11**–1.50 = **0.61**	1
3	$\pi_3 = a_2 > a_1 > a_3$	**0.36 + 0.70 + 0.78 = 1.84**	0.76 + 0.57 + 0.44 = 1.77	**1.84**–1.77 = **0.07**	3
4	$\pi_4 = a_2 > a_3 > a_1$	**0.70 + 0.36 + 0.44 = 1.50**	0.57 + 0.76 + 0.78 = 2.11	**1.50**–2.11 = –0.61	4
5	$\pi_5 = a_3 > a_1 > a_2$	**0.44 + 0.57 + 0.76 = 1.77**	0.78 + 0.70 + 0.36 = 1.84	**1.77**–1.84 = –0.07	5
6	$\pi_6 = a_3 > a_2 > a_1$	**0.57 + 0.44 + 0.36 = 1.37**	0.70 + 0.78 + 0.76 = 2.24	**1.37**–2.24 = –0.87	6

According to the results of Table 10, we can find the priority of considered alternatives is (permutation π_2). It can be concluded that the best alternative is the first alternative and the worst one is the second. The provided example suggests second one presented methods sixth are feasible to manage modern construction enterprises.

6. Conclusion

The algorithm of the effectiveness of construction enterprises management has been developed by applying SWOT and MCDM methods: AHP and permutation.

The algorithm describes a long-term goal which forms a solid framework for strategic planning in construction enterprises. Following the suggested algorithm, the evaluation criteria are selected by taking into consideration the objectives and interests of the stakeholders.

The algorithm presented in the research is a feasible tool to aid in decision making for alternatives ranking, when alternatives are described by cardinal and ordinal criteria. It has been found that the second enterprise is the best.

If they are numbered make sure that they are numbered consecutively. Place the numbers in parentheses flush with the right margin and level with the last line of the equation.

References

[1] Andreica M., Dobre I., Nitu B., Andreica R.: *A new approach of the risk project from managerial perspective*, Economic Computation and Economic Cybernetics Studies and Research, Vol. 42, No. 2, 2008, pp. 121–129.

[2] Arslan O., Er I.D.: *A SWOT analysis for successful bridge team organization and safer marine operations*, Process Safety Progress, Vol. 24, No. 1, 2008, pp. 21–28.

[3] Auruskeviciene V., Salciuviene L., Vanage J.: *Factors determining creation of competitive advantages in the subsidiaries of international enterprises*, Transformations in Business & Economics, Vol. 7, No. 3, 2008, pp. 31–46.

[4] Bartel-Kratochvil R., Leitner H., Axmann P.: *Success in local supply chains for organic products - strengths, weaknesses, opportunities and risks for local supply chains for organic cereals and bread*, Berichte uber Landwirtschaft, Vol. 87, No. 2, 2009, pp. 323–342.

[5] Bayraktar M.E., Hastak M.: *A decision support system for selecting the optimal contracting strategy in highway work zone projects*, Automation in Construction, Vol. 18, No. 6, 2009, pp. 834–843.

[6] Celik M., Cebi S., Kahraman C., Er I.D.: *Application of axiomatic design and TOPSIS methodologies under fuzzy environment for proposing competitive strategies on Turkish container ports in maritime transportation network*, Expert Systems with Applications, Vol. 36, No. 3, 2009, pp. 4541–4557.

[7] Celik Y., Peker K.: *Benefit/cost analysis of mushroom production for diversification of income in developing countries*, Bulgarian Journal of Agricultural Science, Vol. 15, No. 3, 2009, pp. 228–236.

[8] Cimpoeru S.S.: *Neural networks and their application in credit risk assessment. Evidence from the Romanian market*, Technological and Economic Development of Economy, Vol. 17, No. 3, 2011, pp. 519–534.

[9] Chintoanu M., Naghiu L., Roman C.: *National strategy for production and use of biofuels: a SWOT analysis*, Agricultura – Revista de Stiinta si Practica Agricola, Vol. 17, No. 4, 2008, pp. 5–10.

[10] Diskiene D., Galiniene B., Marcinskas A.: *A strategic management model for economic development*, Technological and Economic Development of Economy, Vol. 14, No. 3, 2008, pp. 375–387.

[11] Dwivedi P., Alavalapati J.R.R.: *Stakeholders' perceptions on forest biomass-based bioenergy development in the southern US*, Energy Policy, Vol. 37, No. 5, 2009, pp. 1999–2007.

[12] Jackson S.E., Joshi A., Erhardt N.L.: *Recent research on team and organizational diversity: SWOT analysis and implications*, Journal of Management, Vol. 29, No. 6, 2003, pp. 801–830.
[13] Ghazinoory S., Kheirkhah A.S.: *Transportation of hazardous materials in Iran: A strategic approach for decreasing accidents*, Transport, Vol. 23, No. 2, 2008, pp. 104–111.
[14] Ghazinoory S., Abdi M., Azadegan-Mehr M.: *SWOT Methodology: A state-of-the-art review for the past, a framework for the future*, Journal of Business Economics and Management, Vol. 12, No. 1, 2010, pp. 24–48.
[15] Ghazinoory S., Divsalar A., Soofi A.S.: *A new definition and framework for the development of a national technology strategy: The case of nanotechnology for Iran*, Technological Forecasting and Social Change, Vol. 76, No. 6, 2009, pp. 835–848.
[16] Ghazinoory S., Zadeh A.E., Memariani A.: *Fuzzy SWOT analysis*, Journal of Intelligent and Fuzzy Systems, Vol. 18, No. 1, 2007, pp. 99–108.
[17] Ghazinoory S., Aliahmadi A., Namdarzangeneh S., Ghodsypour S.H.: *Using AHP and LP for choosing the best alternatives based the gap analysis'*, Applied Mathematics and Computation, Vol. 184, No. 2, 2007, pp. 316–321.
[18] Ghosh S., Skibniewski M.J.: *Enterprise resource planning systems implementation as a complex project: a conceptual framework*, Journal of Business Economics and Management, Vol. 11, No. 4, 2010, pp. 533–549.
[19] Ginevicius R.: *The effectiveness of cooperation of industrial enterprises*, Journal of Business Economics and Management, Vol. 11, No. 2, 2010, pp. 283–296.
[20] Ginevicius R., Podvezko V.: *Evaluating the changes in economic and social development of Lithuanian counties by multiple criteria methods*, Technological and Economic Development of Economy, Vol. 15, No. 3, 2009, pp. 418–436.
[21] Grunig R., Kuhn R.: *Successful decision-making: a systematic approach to complex problems*, Springer, 2005.
[22] Gudas S.: *Enterprise knowledge modelling: domains and aspects*, Technological and Economic Development of Economy, Vol. 15, No. 2, 2009, pp. 281–293.
[23] Gudonavicius L., Bartoseviciene V., Saparnis G.: *Imperatives for enterprise strategists*, Inzinerine Ekonomika – Engineering Economics, Vol. 1, 2009, pp. 75–82.
[24] Ho W.: *Integrated analytic hierarchy process and its applications – a literature review*, European Journal of Operational Research, Vol. 186, 2008, pp. 211–228.
[25] Houben G., Lenie K., Vanhoof K.: *A knowledge-based SWOT-analysis system as an instrument for strategic planning in small and medium sized enterprises*, Decision Support Systems, Vol. 26, No. 2, 1999, pp. 125–135.
[26] Hwang C.L., Yoon K.: *Multiple attribute decision making, in lecture notes in economics and mathematical systems*, Springer-Verlag, Berlin, 1981.
[27] Jaskowski P., Biruk S., Bucon R.: *Assessing contractor selection criteria weights with fuzzy AHP method application in group decision environment,* Automation in Construction, Vol. 19, No. 2, 2010, pp. 120–126.
[28] Kaya T., Kahraman C.: *A fuzzy approach to e-banking website quality assessment based on an integrated AHP-ELECTRE method*, Technological and Economic Development of Economy, Vol. 17, No. 2, 2011, pp. 313–334.
[29] Kalibatas D., Zavadskas E.K., Kalibatiene D.: *The concept of the ideal indoor environment in Multi-attribute assessment of dwelling-houses*, Archives of Civil and Mechanical Engineering, Vol. 11, No. 1, 2011, pp. 89–101.

[30] Kendall M.G.: *Rank correlation methods* (4th ed.), London Griffin, 1970.
[31] Kheirkhah A.S., Esmailzadeh A., Ghazinoory S.: *Materials transportation in Iran using the method of fuzzy SWOT analysis*, Transport, Vol. 24, No. 4, 2009, pp. 325–332.
[32] Kong E.: *The development of strategic management in the non-profit context: Intellectual capital in social service non-profit organizations*, International Journal of Management Reviews, Vol. 10, No. 3, 2008, pp. 281–299.
[33] Lee C.T.: *Selecting technologies for constantly changing applications markets*, Research-Technology Management, Vol. 53, No. 1, 2010, pp. 44–54.
[34] Lee K.-L., Lin S.-C.: *A fuzzy quantified SWOT procedure for environmental evaluation of an international distribution centre*, Information Sciences, Vol. 178, No. 2, 2008, pp. 531–549.
[35] Lee S.-H., Jeon R.-K., Kim J.-H., Kim J.-J.: *Strategies for developing countries to expand their shares in the global construction market: phase-based SWOT and AAA analyses of Korea,* Journal of Construction Engineering and Management, Vol. 137, No. 6, 2011, pp. 460–471.
[36] Li S., Li J.Z.: *Hybridising human judgment, AHP, simulation and a fuzzy expert system for strategy formulation under uncertainty*, Expert Systems with Applications, Vol. 36, No. 3, 2009, pp. 5557–5564.
[37] Ling F.Y.Y., Gui Y.: *Strengths, weaknesses, opportunities, and threats: case study of consulting firms in shenzhen, China*, Journal of Construction Engineering and Management – ASCE, Vol. 135, No. 7, 2009, pp. 628–636.
[38] Ling F.Y.Y., Pham V.M.C., Hoang T.P.: *Strengths, weaknesses, opportunities, and threats for architectural, engineering, and construction firms: case study of Vietnam*, Journal of Construction Engineering and Management,-ASCE, Vol. 135, No. 10, 2009, pp. 1105–1113.
[39] Markovska N., Taseska V., Pop-Jordanov J.: *SWOT analyses of the national energy sector for sustainable energy development*, Energy, Vol. 34, No. 6, 2009, pp. 752–756.
[40] Maskeliunaite L., Sivilevicius H., Podvezko V.: *Research on the quality of passenger transportation by railway*, Transport, Vol. 24, No. 2, 2009, pp. 100–112.
[41] Maydl P., Passer A., Cresnik G.: *Stahl im Hochbau - ein nachhaltiger Werkstoff?* (in German), Stahlbau, Vol. 76, No. 4, 2007, pp. 241–249.
[42] Paelnick J.H.P.: *Qualitative multiple criteria analysis, environmental protection and multiregional development*, Papers of the Regional Science Association, Vol. 36, 1976, pp. 59–74.
[43] Pankratova N.D., Beznosik A.Y., Pankratov V.A.: *Definition of indicators of sustainable development of the coastal zone of the crimea autonomous republic with the context of regional priorities*, Journal of Automation and Information Sciences, Vol. 41, No. 9, 2009, pp. 63–73.
[44] Peldschus F., Zavadskas E.K., Turskis Z., Tamosaitiene J.: *Sustainable assessment of construction site by applying game theory*, Inzinerine Ekonomika–Engineering Economics, Vol. 21, No. 3, 2010, pp. 223–237.
[45] Peng Y., Kou G., Wang G., Wang H., Ko F.I.S.: *Empirical evaluation of classifiers for software risk management*, International Journal of Information Technology & Decision Making, Vol. 8, No. 4, 2009, pp. 749–767.
[46] Plebankiewicz E.: *Construction contractor prequalification from Polish clients' perspective*, Journal of Civil Engineering and Management, Vol. 16, No. 1, 2010, pp. 57–64.
[47] Podvezko V., Mitkus S., Trinkuniene E.: *Complex evaluation of contracts for construction*, Journal of Civil Engineering and Management, Vol. 16, No. 2, 2010, pp. 287–297.

[48] Raharjo H., Xie M., Brombacher A.C.: *On modeling dynamic priorities in the analytic hierarchy process using compositional data analysis*, European Journal of Operational Research, Vol. 194, No. 3, 2009, pp. 834–846.
[49] Saaty T.L.: *The Analytic hierarchy process: planning, priority setting, resource allocation*, McGraw-Hill, USA. 1980.
[50] Saaty T.L.: *Decision – making for leaders,* Pittsburg University Edition, 1990.
[51] Shi Y., Peng Y., Kou G., Chen Z.X.: *Classifying credit card accounts for business intelligence and decision making: A multiple-criteria quadratic programming approach*, International Journal of Information Technology & Decision Making, Vol. 4, No. 4, 2009, pp. 581–699.
[52] Shinno H., Yoshioka S., Marpaung S., Hachiga S.: *Qualitative SWOT analysis on the global competitiveness of machine tool industry*, Journal of Engineering Design, Vol. 17, No. 3, 2006, pp. 251–258.
[53] Sinuany-Stern Z., Mehrez A., Hadad Y.: *An AHP/DEA methodology for ranking decision making units*, International Transactions in Operational Research, Vol. 7, 2000, pp. 109–124.
[54] Sivilevicius H.: *Modelling the interaction of transport system elements*, Transport, Vol. 26, No. 1, 2011, pp. 20–34.
[55] Sivilevičius H.: *Application of expert evaluation method to determine the importance of operating asphalt mixing plant quality criteria and rank correlation*, The Baltic Journal of Road and Bridge Engineering, Vol. VI, No. 1, 2011, pp. 48–58.
[56] Skibniewski M.J., Chao L.-C.: *Evaluation of advanced construction technology with AHP method*, Journal of Construction Engineering and Management – ASCE, Vol. 118, No. 3, 1992, pp. 577–593.
[57] Stein E.W., Ahmad N.: *Using the analytical hierarchy process (AHP) to construct a measure of the magnitude of consequences component of moral intensity*, Journal of Business Ethics, Vol. 89, No. 3, 2009, pp. 391–407.
[58] Tamosaitiene J., Turskis Z., Zavadskas E.K.: *Modeling of contractor selection taking into account different risk level*, The 25th International Symposium on Automation and Robotics in Construction, Technika, Vilnius, 2008, pp. 676–681.
[59] Tiryaki F., Ahlatcioglua B.: *Fuzzy portfolio selection using fuzzy analytic hierarchy Process*, Information Sciences, Vol. 179, No. 1–2, 2009, pp. 53–69.
[60] Tserng H.P., Yin S.Y.L., Dzeng R.J., Wou B., Tsai M.D., Chen W.Y.: *A study of ontology-based risk management framework of construction projects through project life cycle*, Automation in Construction, Vol. 18, No. 7, 2009, pp. 994–1008.
[61] Turskis Z.: *Multi-attribute contractors ranking method by applying ordering of feasible alternatives of solutions in terms of preferability technique*, Technological and Economic Development of Economy, Vol. 14, No. 2, 2008, pp. 224–239.
[62] Vainiunas P., Zavadskas E.K., Peldschus F., Turskis Z., Tamosaitiene J.: *Model of construction design projects' managers qualifying by applying analytic hierarchy process and Bayes rule*, in the 5th International Conference EURO Mini Conference "Knowledge-Based Technologies and OR Methodologies for Strategic Decisions of Sustainable Development", Technika, Vilnius, 2009, pp. 154–158,
[63] Zaerpour N., Rabbani M., Gharehgozli A.H., Tavakkoli-Moghaddam R.: *Make-to-order or make-to-stock decision by a novel hybrid approach*, Advanced Engineering Informatics, Vol. 22, No. 2, 2008, pp. 186–201.

[64] Zavadskas E.K.: *Automation and robotics in construction: International research and achievements*, Automation in Construction, Vol. 19, No. 3, 2010, pp. 286–290.
[65] Zavadskas E. K., Turskis Z., Vilutiene T.: *Multiple criteria analysis of foundation installment alternatives by applying Additive Ratio Assessment (ARAS) method*, Archives of Civil and Mechanical Engineering, Vol. 10, 2010, pp. 123–141.
[66] Zavadskas E.K., Turskis Z., Tamosaitiene J.: *Multi-criteria decision making of management effectiveness of construction enterprises based on the SWOT and MCDM* in: The 6th International Scientific Conference Business and Management, Technika, Vilnius, 2010, pp. 1127–1132.
[67] Zavadskas E.K., Turskis Z., Tamosaitiene J.: *Risk assessment of construction projects*, Journal of Civil Engineering and Management, Vol. 16, No. 1, 2010, pp. 33–46.
[68] Zavadskas E.K., Vilutiene T., Turskis Z., Tamosaitiene J.: *Contractor selection for construction works by applying SAW-G and TOPSIS grey techniques*, Journal of Business Economics and Management, Vol. 11, No. 1, 2010, pp. 34–55.
[69] Zavadskas E.K., Kaklauskas A., Turskis Z., Tamosaitiene J.: *Multi-attribute decision-making model by applying grey numbers*, Informatica, Vol. 20, No. 2, 2009, pp. 305–320.
[70] Zavadskas E.K., Andruskevicius A., Podvezko V.: *Quantitative evaluation of the organisation of manufacturing and technological processes*, International Journal of Technology Management, Vol. 48, No. 4, 2009, pp. 544–55.
[71] Zavadskas E.K., Turskis Z., Tamošaitiene J.: *Contractor selection of construction in a competitive environment*, Journal of Business Economics and Management, Vol. 9, No. 3, 2008, pp. 181–187.
[72] Zavadskas E.K., Peldschus F., Kaklauskas A.: *Multiple criteria evaluation of projects in construction*, Technika Vilnius, 1994.
[73] Zavadskas E.K.: *Systems of estimation of technological solutions in building construction* (in Russian), St. Petersburg 1991.
[74] Zhao Z.Y., Shen L.Y., Zuo J.: *Performance and strategy of Chinese contractors in the international market*, Journal of Construction Engineering and Management – ASCE, Vol. 135, No. 2, 2009, pp. 108–118.
[75] Weihrich H.: *The TOWS matrix – a tool for situational analysis'*, Journal of Long Range Planning, Vol. 15, No. 2, 1982, pp. 54–66.
[76] Weihrich H.: *Analyzing the competitive advantages and disadvantages of Germany with the TOWS matrix – an alternative to Porter's model'*, European Business Review, Vol. 99, No. 1, 1999, pp. 9–22.
[77] Wu J., Tian X.G., Tang Y., Zhao Y.J., Hu Y.D., Fang Z.L.: *Application of analytic hierarchy process-grey target theory systematic model in comprehensive evaluation of water environmental quality*, Water Environment Research, Vol. 82, No. 7, 2010, pp. 633–641.
[78] Xu T.J., Smith N.J., Bower D.A.: *Forms of collaboration and project delivery in Chinese construction markets: Probable emergence of strategic alliances and design-build*, Journal of Management in Engineering, Vol. 21, No. 3, 2005, pp. 100–109.

Wybór strategii zarządzania przedsiębiorstwem budowlanym na podstawie metody SWOT i analizy wielokryterialnej

W pracy zaproponowano metodologie określania strategii zarządzania dla przedsiębiorstw budowlanych. W tym celu wykorzystywana jest analiza SWOT (mocnych stron,

słabych stron, szans, zagrożeń) jako narzędzie służące do formułowania odpowiedniej strategii zarządzania. Algorytm pomaga wybrać najbardziej korzystną strategie opartą na AHP, ekspertyzie i metodzie permutacyjnej dla prawdopodobnych scenariuszy. Perspektywa zarządzania przedsiębiorstwem budowlanym w ujęciu SWOT jest przeprowadzana na podstawie wybranych opisów stanu aktualnego oraz przyszłych możliwych scenariuszy. Finalnie wybrane scenariusze są oceniane w oparciu o metodę permutacyjną. Studium przypadku pokazuje możliwości zastosowania proponowanego modelu do rozwiązywania rzeczywisty problemów zarządzania.

Price 20 zł
(incl. 5% VAT)

Subscription orders should be addressed to:

Oficyna Wydawnicza Politechniki Wrocławskiej
Wybrzeże Wyspiańskiego 27
50-370 Wrocław